universität wien

DISSERTATION / DOCTORAL THESIS

Titel der Dissertation /Title of the Doctoral Thesis

„Generation and Detection of Quantum Entanglement in Optomechanical Systems“

verfasst von / submitted by

Jason Hoelscher-Obermaier

angestrebter akademischer Grad / in partial fulfilment of the requirements for the degree of

Doktor der Naturwissenschaften (Dr. rer. nat.)

Wien, 2017 / Vienna 2017

Studienkennzahl lt. Studienblatt / degree programme code as it appears on the student record sheet:	A 796 605 411
Dissertationsgebiet lt. Studienblatt / field of study as it appears on the student record sheet:	Physik
Betreut von / Supervisor:	Univ.-Prof. Dr. Markus Aspelmeyer

ABSTRACT

This thesis presents progress in two key areas in experimental quantum optomechanics: Optimal estimation of the state of an optomechanical system and generation and detection of optomechanical entanglement. In the first part of the thesis, I present the first experimental demonstration of optimal state estimation in cavity optomechanics. This is achieved by Kalman filtering based on a realistic model of the complete experiment. The accuracy of the Kalman filter for our experiment is demonstrated using statistical methods. Kalman filtering allows to systematically account for typical experimental limitations such as multiple mechanical modes, colored laser noise and detection inefficiencies. It is universally applicable to any cavity optomechanical system as long as the interaction is Gaussian. It works for classical systems as well as for systems dominated by quantum noise. Finally, Kalman filtering can be performed in real time and is therefore a suitable basis for optimal feedback control of quantum optomechanical systems.

The second part of the thesis deals with optomechanical entanglement. The optomechanical interaction between a light field and a mechanical mode can lead to entanglement between different temporal modes of the light field reflected from an optomechanical cavity—an effect which can be detected, for example, in pump–probe type experiments. This thesis establishes an alternative protocol for detecting such entanglement for a cavity driven by a continuous, resonant laser beam. Crucially, extensive and systematic simulations show that this protocol works even in the presence of multiple, closely spaced mechanical modes (which can be problematic in pump–probe type experiments) and assuming realistic levels of residual classical laser noise. In the novel protocol, extraction and correlation of different temporal light modes happen entirely in post-processing. The method is therefore highly flexible and can, in principle, be used to analyze correlations between arbitrary temporal modes of the reflected light field.

ZUSAMMENFASSUNG

Diese Dissertation behandelt zwei Schlüsselthemen der experimentellen Quantenoptomechanik: Optimale Schätzung des Zustandes eines optomechanischen Systems und Erzeugung und Nachweis von optomechanischer Verschränkung. Im ersten Teil der Dissertation präsentiere ich das erste Experiment zur optimalen Zustandsschätzung in der Cavity-Optomechanik. Die optimale Zustandsschätzung erfolgt durch einen Kalmanfilter, dem ein realistisches Modell des Experiments zu Grunde liegt. Die Anwendbarkeit des Kalmanfilters auf unser Experiment wird durch statistische Methoden nachgewiesen. Der Kalmanfilter ermöglicht eine systematische Behandlung typischer experimenteller Unzulänglichkeiten, wie etwa die gleichzeitige Kopplung an mehrere mechanische Moden, frequenzabhängiges Laserrauschen und ineffiziente Detektion. Der Kalmanfilter ist universell anwendbar für beliebige cavity-optomechanische Systeme, so lange die Wechselwirkung Gaußsch ist. Er kann sowohl auf klassische Systeme angewandt werden, als auch auf Systeme, die durch Quantenrauschen dominiert sind. Außerdem erlaubt der Kalmanfilter eine Echtzeit-Implementierung, so dass er als Grundlage für optimales Feedback-Kühlen quanten-optomechanischer Systeme dienen kann.

Der zweite Teil der Dissertation beschäftigt sich mit optomechanischer Verschränkung. Die optomechanische Wechselwirkung zwischen dem Lichtfeld und einer mechanischen Mode kann zu Verschränkung zwischen verschiedenen temporalen Moden des reflektierten Lichtfelds führen. Dieser Effekt kann beispielsweise in Pump-probe-Experimenten nachgewiesen werden. In dieser Arbeit analysiere ich ein alternatives Protokoll zur Detektion solcher Verschränkung für optomechanische cavities, die kontinuierlich und resonant getrieben werden. Ausführliche, systematische Simulationen zeigen, dass dieses Protokoll auch in Systemen mit mehreren mechanischen Moden und unter realistischen Annahmen an das klassische Laserrauschen Verschränkung nachweisen kann. Eine Besonderheit des Protokolls ist, dass die verschiedenen temporalen Lichtmoden vollständig im Postprocessing extrahiert und korreliert werden. Daher ist die Methode sehr flexibel und ermöglicht prinzipiell die Analyse von Korrelationen zwischen beliebigen temporalen Moden des reflektierten Lichtfelds.

Be grateful to everyone. — Atisha (982–1054 CE)

ACKNOWLEDGMENTS

I am very grateful to all my colleagues in the Aspelmeyer research group for their collegiality, openness and—most crucially—humor. In particular, I would like to thank: Witlef for being an incredibly reliable, patient and caring mentor, colleague and friend; my supervisor Markus for his unconditional support in scientific as well as personal matters; Sebastian for holding our discussions up to high standards of scientific rigor; Ramon, Claus, Ralf, Tobi, Karo, Thomas and Corentin for being very cheerful lab/office mates; Witlef, Sebastian, Corentin and Markus for helpful feedback on earlier versions of this text.

On the personal side (and not related to this work), the last years have been by far the most challenging of my life. Some people have been incredibly important for me: Milly, thank you for your constant support, warmth and tender humor. Tarik, thanks for being a reliable friend and having been such a fantastic flat mate. On the family side, I want to thank in particular: My sister Julia for always being there for me, personally or on the phone; my cute little nephew Xaver for cheering me up during the writing phase; my brother Jakob for providing a calm, peaceful space to meet; my father for being unconditionally supportive and doing his best to make things as easy as possible for me; my mother, who unfortunately did not live to see the conclusion of this period of my life, for her support and love.

I am also blessed with many good, old friends from pre-Vienna-times who provided emotional support in the form of a warm, welcoming place or a friendly conversation on the phone whenever I needed it. The two friends I have relied on most strongly are Jakob and Bine. Their enduring hospitality is simply amazing. The single thing I cherish most about the last years is how close they got me to many of the people mentioned above. The ties of friendship seem to become strongest when forged in times of crisis.

CONTENTS

1 INTRODUCTION

The experiments discussed in this thesis are motivated by the desire to achieve quantum control of macroscopic objects. Ultimately, this will enable precision tests of macroscopic quantum physics as well as novel quantum information applications based on mechanical systems [AKM14, sec. XI.]. To achieve quantum control of macroscopic objects we use cavity optomechanics. This allows us to apply the well-established and precise tools of quantum optics for controlling and measuring the state of massive mechanical systems. In the past decade, quantum control of massive objects has come a long way, including experiments such as strong coupling between mechanical and optical degrees of freedom [Grö+09a; Teu+11b], ground-state cooling [Teu+11a; Cha+11], optomechanical entanglement in microwave systems [Pal+13b], and squeezed lights produced by the optomechanical interaction [Saf+13; Pur+13].

towards macroscopic quantum physics

state of play

This thesis tackles two major challenges on the path to quantum control of macroscopic objects: Optimal state estimation of optomechanical systems and optomechanical entanglement using laser light.

goals of this thesis

Optimal state estimation in cavity optomechanics is the basis for feedback control of macroscopic mechanical objects, as well as system identification and optimal force estimation. This thesis presents the first experimental demonstration of optimal state estimation in cavity optomechanics, using Kalman filtering [Wie+15]. Kalman filtering is a universal and systematic method for optimal state estimation and it can be implemented in real-time.

optimal state estimation

Optomechanical entanglement, on the other hand, is interesting, first of all, as an unambiguous quantum effect involving macroscopic objects. But optomechanical entanglement can also serve as a resource for quantum information processing, for example to prepare quantum states of the mechanical subsystem via quantum teleportation [Hof+11; Hof+13; HH15]. In experimental practice, however, generation and detection of entanglement between a mechanical oscillator and laser light has been found to be challenging in the presence of classical laser noise and of multiple mechanical modes. Hence, a major part of this thesis is devoted to studying (using systematic, realistic simulations) the feasibility of entanglement detection in cavity optomechanics using a novel measurement protocol.

optomechanical entanglement

The theory literature usually assumes only a single mechanical mode. But in practice mechanical systems are multi-mode systems and often many of these modes interact significantly. Additional me-

multiple mechanical modes

chanical modes—if they are not properly taken into account—can prevent both optimal state estimation and entanglement detection. Fortunately, as demonstrated in this thesis, there are systematic ways to account for multiple mechanical modes in both cases, such that optimal state estimation and entanglement detection can be achieved for multimode optomechanical systems.

classical laser noise

Our mechanical devices operate at rather low mechanical frequencies, between some 100 kHz and some MHz. As it happens, classical laser noise is a common problem in this frequency range. In this thesis, I demonstrate two different approaches to this problem. In state estimation, laser noise can be dealt with by including an adequate model of the classical laser noise in the state space model of the experiment. In this way, we obtain state estimates which are optimal for the given experimental setup (though they could be improved by eliminating the classical laser noise). Regarding the entanglement experiment, I demonstrate that a filter cavity can suppress the laser noise to levels which are compatible with the generation and detection of entanglement.

1.1 OUTLINE

The remainder of the introduction (Section 1.2) is devoted to locating our experiments in the context of other work in optomechanics.

historical, theoretical, and experimental background

Chapter 2 presents the theoretical background for our experiments and introduces the notation. Chapter 3 describes the experimental setups, including the laser system, the mechanical devices and the optomechanical cavities.

optimal state estimation

Chapter 4 discusses state estimation in cavity optomechanics. I provide a pedagogical introduction to the Kalman filter and present experimental results (published in [Wie+15]) on optimal state estimation of a cavity-optomechanical system. I conclude with a discussion contrasting our work with previous work and an outlook regarding potential applications.

entanglement detection

Chapter 5 explores a novel protocol for the detection of entanglement between different modes of the light field arising from the interaction with a mechanical system. The experimental implementation of the protocol is still work in progress. In this thesis, I explore the protocol mainly using realistic simulations of the full experimental setup and I discuss the current experimental limitations. I close in Section 5.12 with a discussion of what has been achieved in this respect and an outlook discussing potential next steps.

appendix

In the appendix, I summarize the notation used throughout the thesis (Appendix A). I also add some more details regarding laser noise measurements (Appendix B) and simulations of the entanglement experiment (Appendix C).

1.2 HISTORICAL CONTEXT

Optomechanics in the most general sense—the study of the interaction of electromagnetic radiation and mechanical systems—has a long history [see AKM14, sec. I]. In classical physics, it was recognized early on that, if light carries a momentum in its direction of propagation (as suggested by corpuscular theories of light), then it should also exert a pressure on mechanical objects. Already in the early 1600s, Johannes Kepler proposed that this radiation pressure force could explain why comet tails point away from the sun, independent of the comet's direction of motion [Kep19].[1]

radiation pressure

[1] *This explanation is still accepted for the so-called 'dust tail' of comets.*

In 1873, Maxwell derived radiation pressure from his theory of electromagnetic waves [Max73, pp. 391-392], thus demonstrating that radiation pressure is not necessarily tied to a corpuscular theory of light. On the same pages, Maxwell proposed that radiation pressure might be measurable in a laboratory experiment. The first conclusive experiments were performed at the beginning of the 20th century by Lebedew and, independently, by Nichols and Hull, demonstrating the existence of radiation pressure in so-called light mills [Leb01; NH01]. Amusingly, already these early, purely classical, experiments with radiation pressure were plagued by unwanted effects due to heating by absorption, which—more than hundred years later—is still a major roadblock in many quantum optomechanics experiments.

radiation pressure from classical electro-dynamics

Only a few years later, in 1909, Einstein recognized that quantization implies stochastic fluctuations of the radiation pressure [Ein09]. In a similar way, fluctuating radiation pressure due to laser shot noise acts like a random noise force (also known as "backaction noise") on mechanical objects and imposes a lower limit on the accuracy of continuous position measurements, the standard quantum limit [Cav80].

quantum radiation pressure

backaction noise and SQL

It took almost a century to directly observe backaction noise in the laboratory. In 2008, Murch et al. observed backaction heating in a cloud of ultra-cold atoms [Mur+08]; the mechanical mode in this case was a collective mode of motion of the atom cloud. And the first direct observation of backaction noise on a macroscopic mechanical system (a thin, square SiN membrane of 0.5 mm lateral dimensions) had to wait till 2013 [PPR13].

experimental observation of backaction noise

Detecting quantum optomechanical effects (such as backaction noise) is challenging because it requires the optomechanical interaction to dominate other effects such as Brownian motion of the mechanical object. The first crucial step towards sufficiently large interaction strengths was the move to *cavity* optomechanics, i.e. embedding the mechanical objects in high-finesse cavities to amplify the optomechanical interaction. This idea dates back to the late 1960s when Braginsky and coworkers showed theoretically [BM67] and in experiments with microwave cavities [BMT70] that optomechanical effects

key ingredients for quantum optomechanics

cavity optomechanics

can be enhanced using cavities and that the nature of these effects depends drastically on the detuning of the radiation from the cavity resonance. The first cavity optomechanics experiment with laser light was performed a decade later by the quantum optics group of Herbert Walther in Munich [Dor+83].

microfabrication

A second important step towards large optomechanical coupling consisted in moving to micro-mechanical structures with favorable optical and mechanical properties. Because of their small mass, micro-mechanical structures allowed to reach high (bare) optomechanical coupling and enabled a new generation of experiments in the late 1990s.

towards optomechanical state estimation

The first of these more recent experiments focused on high sensitivity read-out of the mechanical motion. These experiments were able to measure the thermal fluctuations of the mechanical position at room temperature [Had+99] and at cryogenic temperatures [Tit+99]. Right at the start, the ability to precisely detect the mechanical position was recognized as a step towards mechanical state control. [CHP99], for example, used optical position readout to feedback cool a micro-mirror. More than a decade later, we continued this line of research and showed how to achieve optimal state estimation in cavity-optomechanical systems using a Kalman filter [Wie+15]. This opens the door to optimal feedback control of the mechanical state. In contrast to earlier approaches to mechanical state estimation, Kalman filtering is not only optimal (yielding the smallest possible estimation error) but also more systematic and more widely applicable (to any cavity optomechanical system, as long as the interaction is Gaussian).

towards optomechanical entanglement

Also in the 1990s, quantum effects in optomechanical systems were first investigated theoretically, among them squeezing of light, and QND measurements of the light intensity [see ref.s in AKM14, sec. I.]. Most importantly for us, also the generation of non-classical states of light and mechanics and, in particular, entanglement was explored theoretically [BJK97; MMT97]. More experimentalist-friendly proposals for the generation and detection of optomechanical entanglement appeared more than a decade later. [Vit+07] proposed a way to generate stationary entanglement between the intracavity light and the mechanical mode using a continuous laser drive. In contrast, [Hof+11] proposed a pulsed protocol which generates optomechanical entanglement in a first pulse and then swaps the mechanical state onto a second pulse. This reduces the problem of detecting entanglement between light and a mechanical system to the easier problem of detecting entanglement between two pulses of light. Two years after it was first proposed, the protocol of [Hof+11] was experimentally realized in a microwave electromechanical system [Pal+13b]. In contrast to most existing optomechanical systems, this electromechanical system has the advantage that only the fundamental mechanical mode

interacts significantly. This is due to the different nature of the coupling: In electromechanics, the coupling is capacitive and therefore depends on the average displacement of the mechanical oscillator. In optomechanics, on the other hand, the coupling results from the interaction of a focused laser beam with a mechanical structure. In this case, the coupling is strong for any mechanical mode which causes significant displacement in the region of the laser spot, and there are usually many modes which do.

Simultaneous coupling to a multitude of mechanical modes is a serious problem for entanglement detection in optomechanical systems, but also for optimal state estimation. This thesis shows how to systematically deal with the presence of multiple significantly interacting mechanical modes, if this cannot be avoided otherwise (which may be the experimenter's preferred option in many cases).

entanglement-based quantum control

The two main topics of this thesis—optomechanical state estimation and optomechanical entanglement—were recently connected in theory [Hof+13; HH15]. It was shown that optomechanical entanglement is a resource for time-continuous quantum control of the mechanical system. This shows that there is a close connection between optimal state estimation, which is the basis of optimal control, and the generation of optomechanical entanglement.

2

THEORY

This chapter reviews the basic theory for our cavity-optomechanical experiments and introduces the notation[2] for the subsequent chapters. Section 2.1 deals with one-dimensional mechanical oscillators, Section 2.2 with the mechanical motion of solid bodies. Section 2.3 discusses optical cavities. Section 2.4 treats the coupling between mechanical oscillators and optical cavities, both the case of end-mirror-coupling (Section 2.4.1), as well as the coupling of membranes inside cavities (Section 2.4.2). Section 2.5 describes the linearization of the optomechanical coupling for large amplitudes of the intracavity light field. This leads to the quantum Langevin equations for the coupled optomechanical system in the linearized regime (Section 2.6), which are the basis for the work described in this thesis.

[2] *The notation is also summarized in Appendix A*

outline

Note that the material presented in this chapter is not original and can be found in many other references. For a general review of cavity optomechanics see [AKM14], for more in-depth discussions of the coupling of membranes to optical cavities see [Wil12; Bia14], and for a careful discussion of the open quantum systems description of our experimental systems see [Hof15, ch. 1].

references

2.1 1D MECHANICAL OSCILLATORS

Let us begin with an undamped classical harmonic oscillator with mass m, spring constant k and angular frequency $\omega_m \equiv \sqrt{k/m}$. Its state of motion is described by its momentum p and position q, the so-called quadratures. Its equation of motion is given by:

undamped harmonic oscillator

$$\dot{p} = -kq = -m{\omega_m}^2 q,\ \dot{q} = p/m, \tag{2.1}$$

There are natural length scales q_0 and p_0 for this system, namely

ground state uncertainties

$$q_0 \equiv \sqrt{\hbar/2m\omega_m},\ p_0 \equiv m\omega_m q_0, \tag{2.2}$$

which, as we will see later, are the position and momentum uncertainty of the quantized system in the ground state. The quadratures q and p in (2.1) are in SI-units. We obtain dimensionless quantities, by expressing q and p as multiples of q_0 and p_0, i.e. by the substitutions

dimensionless units

$$q \to \sqrt{2}q_0 \cdot q, p \to \sqrt{2}p_0 \cdot p. \tag{2.3}$$

The equations of motion then simplify to

$$\dot{p} = -\omega_m q,\ \dot{q} = \omega_m p, \tag{2.4}$$

and the oscillator's energy $E = \left(p^2/m + kq^2\right)/2$ becomes

$$E = \hbar\omega_m \left(p^2 + q^2\right)/2. \tag{2.5}$$

complex amplitude

The oscillator's state of motion can now be expressed more simply in terms of a complex amplitude

$$b \equiv (q + ip)/\sqrt{2}. \tag{2.6}$$

The oscillator's energy is then given by

$$E = \hbar\omega_m |b|^2/2, \tag{2.7}$$

and the equation of motion simplifies to

$$\dot{b} = -i\omega_m b, \tag{2.8}$$

which is solved by a complex rotation $b(t) = b(0)\, e^{-i\omega_m t}$.

canonical quantization

To describe a quantum-mechanical oscillator, we impose the canonical commutation relation $[\hat{q}, \hat{p}] = i$ which, using the relations

$$\hat{q} \equiv \left(\hat{b} + \hat{b}^\dagger\right)/\sqrt{2}, \tag{2.9}$$

$$\hat{p} \equiv \left(\hat{b} - \hat{b}^\dagger\right)/i\sqrt{2}, \tag{2.10}$$

translates into $\left[\hat{b}, \hat{b}^\dagger\right] = 1$ and leads to an extra term $\hbar\omega_m/2$, the vacuum energy, in the Hamiltonian $\hat{H}_m$ for the mechanical oscillator:

$$\hat{H}_m = \hbar\omega_m \left(\hat{b}^\dagger\hat{b} + 1/2\right). \tag{2.11}$$

n-phonon states

The eigenstates of this Hamiltonian are the eigenstates $|n\rangle$ of the number operator $\hat{n} \equiv \hat{b}^\dagger\hat{b}$, which are defined by the condition

$$\hat{n}\,|n\rangle = \hat{b}^\dagger\hat{b}\,|n\rangle = n \cdot |n\rangle\,,\ n \in \mathbb{N}_0. \tag{2.12}$$

The state $|n\rangle$ is referred to as a Fock state or n-phonon state.

ground-state variance

The extra energy term $\hbar\omega_m/2$ in $\hat{H}_m$ is connected to the non-zero variance of position $\hat{q}$ and momentum $\hat{p}$ in the ground state $|0\rangle$:

$$\langle 0 \,|\, \hat{q}^2 \,|\, 0\rangle = \langle 0 \,|\, \hat{p}^2 \,|\, 0\rangle = 1/2. \tag{2.13}$$

(2.13) confirms that we have indeed expressed q and p in units of the ground-state uncertainty. More generally, for an n-phonon state $|n\rangle$,

$$\langle n \,|\, \hat{q}^2 \,|\, n\rangle = \langle n \,|\, \hat{p}^2 \,|\, n\rangle = n + 1/2. \tag{2.14}$$

In thermal equilibrium with an environment at temperature T, the probability for finding the system in the state $|n\rangle$ is given by the Bose-Einstein distribution

Bose-Einstein distribution

$$p(n) = (1 - \exp(-\beta\hbar\omega_m)) \cdot \exp(-\beta\hbar\omega_m)^n,\ \beta \equiv (k_\mathrm{B}T)^{-1}, \tag{2.15}$$

such that the thermal state can be written as

thermal state

$$\rho_\mathrm{th} \equiv \sum_{n=0}^{\infty} p(n)\,|n\rangle\,\langle n|\,. \tag{2.16}$$

Therefore, position and momentum variance in the thermal state are

thermal position and momentum variance

$$\mathrm{tr}\left(\rho_\mathrm{th}\,\hat{q}^2\right) = \mathrm{tr}\left(\rho_\mathrm{th}\,\hat{p}^2\right) = \sum_{n=0}^{\infty} p\,(n)\left(n + \frac{1}{2}\right) = \frac{1}{2}\coth\left(\frac{\hbar\omega_m}{2k_\mathrm{B}T}\right), \tag{2.17}$$

where $\mathrm{tr}\,(\hat{o})$ denotes the trace of an operator $\hat{o}$. The average phonon number $\bar{n}$ in the thermal state is

thermal occupation

$$\bar{n} \equiv \mathrm{tr}\,(\rho_\mathrm{th}\,\hat{n}) = \sum_{n=0}^{\infty} p(n)\cdot n = \frac{1}{\exp\,(\beta\hbar\omega_m) - 1}. \tag{2.18}$$

We typically deal with frequencies ω_m which are small compared to $k_\mathrm{B}T/\hbar$. Therefore, we can use the following limits for the average phonon number (2.18) and the thermal position and momentum variance (2.17):

high temperature limits

$$\mathrm{tr}\,(\rho_\mathrm{th}\,\hat{n})\,,\ \mathrm{tr}\left(\rho_\mathrm{th}\,\hat{q}^2\right)\,,\mathrm{tr}\left(\rho_\mathrm{th}\,\hat{p}^2\right) \overset{k_\mathrm{B}T \gg \hbar\omega_m}{\simeq} \frac{k_\mathrm{B}T}{\hbar\omega_m}. \tag{2.19}$$

2.1.1 *Dissipation*

Real mechanical oscillators are never undamped, however. A simple model of damping is velocity-damping (also known as Brownian motion damping)

Langevin equation

$$\dot{q} = \omega_m p,\ \dot{p} = -\omega_m q - \gamma_m p + F, \tag{2.20}$$

where the momentum-quadrature is damped with rate γ_m. In (2.20), F describes a stochastic thermal noise force, which— according to the fluctuation–dissipation theorem (FDT) [CW51; Sau90]—invariably arises for a damped system in contact with a thermal bath. Because of the

fluctuation

stochastic force F,[3] (2.20) is a stochastic differential equation, which is known as the *Langevin equation*.

[3] *Note that, in (2.20), F is in zero-point units (as $\dot{p}$).*

Note that there are damping mechanisms (such as damping due to internal materials loss) which are relevant for macroscopic mechanical oscillators but which are not well-described the velocity damping model (2.20) [Sau90]. But close to the mechanical resonance, (2.20) is a good approximation [see Wil12, sec. 2.2].

Written solely in terms of q, the Langevin eq. (2.20) is

$$\ddot{q} + \gamma_m \dot{q} + {\omega_m}^2 q = \omega_m F. \tag{2.21}$$

mechanical susceptibility

In Fourier space, (2.21) yields the following linear response function

$$\chi(\Omega) \equiv \tilde{q}(\Omega) / \tilde{F}(\Omega) = \omega_m / \left({\omega_m}^2 - \Omega^2 + i\Omega\gamma_m\right), \tag{2.22}$$

which describes the response of the position quadrature to the thermal noise force or any other external force. For small damping γ_m, the response (2.22) is very large at $\Omega \simeq \omega_m$. We can therefore strongly excite the oscillator using a piezo mounted close to the mechanical oscillator and driven at $\Omega \simeq \omega_m$. Then, q becomes so large that the thermal noise force F can be neglected in (2.21). If we then switch off the drive, the motion is (for a short time) governed by a freely decaying oscillation according to

resonant drive

$$\ddot{q} + \gamma_m \dot{q} + {\omega_m}^2 q = 0, \tag{2.23}$$

i.e. the system oscillates at frequency

$$\omega_m \cdot \sqrt{1 - {\gamma_m}^2/4{\omega_m}^2} \overset{\omega_m \gg \gamma_m}{\simeq} \omega_m \tag{2.24}$$

and its amplitude decays with the rate $\gamma_m/2$. The energy (when averaged over a mechanical cycle) is proportional to q^2, hence decays with rate γ_m. This energy decay can be measured directly using a spectrum analyzer with a sufficiently large bandwidth.

measuring γ_m via ringdowns

From a measurement of γ_m, we can calculate the *mechanical quality factor*, or Q-factor,

quality factor

$$Q \equiv \omega_m / \gamma_m, \tag{2.25}$$

which expresses the damping time of the system in units of the mechanical period. In this thesis, we always deal with mechanical modes with high quality factors in the range of 10^3 to 3×10^7. High Q-factors are crucial for quantum optomechanical experiments; but they are also quite convenient for the theory because they allows us to use high-Q approximations.

2.1.2 *Fluctuation*

If the mechanical oscillator is in contact with a thermal bath at temperature T, the FDT implies that the classical thermal noise force F in (2.20) and (2.21) is described by the following white (single-sided) noise power spectral density (NPS) [Sau90]:[4]

spectrum of thermal noise force

$$S_F(\Omega) = \frac{4k_B T}{\hbar\Omega}\,\mathrm{Im}\left(\chi\,(\Omega)^{-1}\right) = \frac{4k_B T}{\hbar\Omega}\frac{\gamma_m \Omega}{\omega_m} = \frac{4k_B T}{\hbar Q}. \tag{2.26}$$

[4] *Note that, in (2.26), F is again in zero-point units. To obtain SI-units, multiply by $\sqrt{2}p_0$.*

This NPS corresponds to a delta-correlated autocorrelation function

$$\mathbb{E}\left[F(t)F(t+\tau)\right] = 2\frac{k_B T}{\hbar Q}\delta(\tau), \tag{2.27}$$

where $\mathbb{E}\left[\ldots\right]$ denotes the ensemble average in the thermal state.

In (2.26), χ denotes the mechanical susceptibility (2.22). Hence, $S_F(\Omega)$ is non-zero if the mechanical susceptibility has a non-zero imaginary part, corresponding to a time lag between the driving force F and the response of the mechanical position q. Such a time lag is induced by mechanical damping. In this way, the FDT connects the damping of a system to the thermal noise forces acting on it.

thermal position NPS

Using (2.26) and (2.22), we can calculate the NPS of the mechanical position in thermal equilibrium

$$S_q(\Omega) = |\chi(\Omega)|^2 \cdot S_F(\Omega) = \frac{4k_B T \gamma_m \omega_m}{\hbar\left(\left({\omega_m}^2 - \Omega^2\right)^2 + {\gamma_m}^2\Omega^2\right)}. \tag{2.28}$$

This is the single-sided noise power spectral density of the position coordinate. It is related to the position variance $\mathbb{E}\left[q^2\,(t)\right]$ by

thermal position variance

$$\mathbb{E}\left[q^2\,(t)\right] = \int_0^\infty S_q\,(\Omega)\,\mathrm{d}\Omega/2\pi = k_B T/\hbar\omega_m \simeq \bar{n}. \tag{2.29}$$

The expectation value for the potential energy of the oscillator is therefore given by $\mathbb{E}\left[q^2\,(t)\right]\cdot\hbar\omega_m/2 = k_B T/2$, in accordance with the equipartition theorem. The noise power (2.28) peaks at

$$\Omega_0 = \omega_m\sqrt{1 - Q^{-2}/2} \overset{Q\gg 1}{\simeq} \omega_m \tag{2.30}$$

and has a full width at half maximum (FWHM) of

γ_m is FWHM of thermally driven position NPS

$$\gamma_m\left(1 + Q^{-2}/4 + \mathcal{O}\left(Q^{-4}\right)\right) \overset{Q\gg 1}{\simeq} \gamma_m. \tag{2.31}$$

Hence, for high Q factors, the power decay rate γ_m is also the FWHM-width of the thermal position NPS (or, equivalently, of the absolute square of the mechanical susceptibility).

Lorentzian approximation

When we fit measured spectra, we usually approximate the thermal noise power spectrum by a Lorentzian:

$$S_q(\Omega) \simeq \frac{4k_B T}{\hbar\omega\gamma_m}\left(1+4\left(\frac{\Omega-\omega_m}{\gamma_m}\right)^2\right)^{-1}. \tag{2.32}$$

This approximation is good for high Q-factors and close to resonance. Note again that, close to resonance, (2.32) is also a good approximation to the NPS resulting from forms of damping which are not well-described by a velocity damping model [see Wil12, eq. (2.19)].

2.1.3 *Quantum fluctuations*

By replacing the noise term F in (2.20) by $\sqrt{2\gamma_m}f$, we obtain the following set of equations describing the damped and thermally driven mechanical motion

$$\dot{q} = \omega_m p,\ \dot{p} = -\omega_m q - \gamma_m p + \sqrt{2\gamma_m}f, \tag{2.33}$$

$$\mathbb{E}\left[f(t)f(t+\tau)\right] = \frac{k_B T}{\hbar\omega_m}\delta(\tau) \simeq \bar{n}\delta(\tau). \tag{2.34}$$

This form is convenient because (as we will see) it is very similar to that of the Langevin equations for the optical intra-cavity mode. In (2.33), f has units of $\sqrt{\text{Hz}}$ and can be interpreted as the root of a phonon flux from the thermal bath.

To describe a quantum system, we now only need to interpret the classical random variables q, p (and f) as Heisenberg operators and reinterpret (2.33) as their stochastic equations of motion. This yields [Hof15, sec. 1.3.1]

quantum Langevin equations

$$\dot{\hat{p}} = -\omega_m\hat{q} - \gamma_m\hat{p} + \sqrt{2\gamma_m}\hat{f},\ \dot{\hat{q}} = \omega_m\hat{p}, \tag{2.35}$$

where $\hat{f}$ is now a self-adjoint noise operator satisfying[5]

[5] *$\langle\hat{o}\rangle$ denotes the expectation value of $\hat{o}$ with respect to the quantum state of the bath.*

$$\left\langle\hat{f}(t)\,\hat{f}(t') + \hat{f}(t')\,\hat{f}(t)\right\rangle/2 \simeq (\bar{n}+1/2), \tag{2.36}$$

Note the added term $1/2$ in (2.36) compared to (2.34), which arises because of the vacuum fluctuations of the quantized system. Note also that the thermal noise force $\hat{f}$ can only be treated as δ-correlated in the limit of high temperatures and high mechanical quality factors [see Hof15, sec. 1.3.1], which holds for our experiments.

mechanical decoherence at non-zero temperature

(2.35) and (2.36) imply that, for bath temperatures far above the ground state temperature, phonons enter the system at a rate $\bar{n}\gamma_m$ (where $\bar{n}$ is the mean phonon number of the bath at the mechanical frequency ω_m). This reduces the number of coherent oscillations from Q to $Q/\bar{n}$ [see AKM14, sec. II.B.2].

In our mechanical devices, clamping loss and material-intrinsic losses are the dominant damping mechanisms. The heat bath for these damping mechanisms is provided by the material of the support structure and of the oscillator itself, respectively. The thermal occupation number $\bar{n}$ for these heat baths is therefore determined by the temperature T of the support and the oscillator (and the frequency ω_m of the mechanical mode) via the Bose-Einstein-distribution (2.18).

thermal bath occupation

2.2 CONTINUOUS MECHANICAL OSCILLATORS

Let us link the simple 1D-model presented above to the mechanical behavior of solid bodies such as those used in our experiments. We use two different types of mechanical devices: Cantilevers carrying a Bragg mirror pad (for the state estimation experiment) and thin dielectric membranes (for the entanglement experiment). Both types of devices are roughly two-dimensional structures which are positioned perpendicular to an optical cavity mode.

cantilevers and membranes

I call[6] the axial direction (the direction along the cavity axis) z , and the transversal directions x and y. With this convention, our mechanical devices are essentially extended surfaces in the x-y-plane and only the motion of this surface in z direction couples optomechanically.

[6] *Coordinates for optomechanical cavities:*

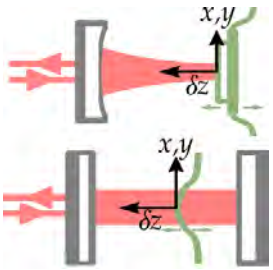

(top: mirror on cantilever; bottom: membrane)

We describe the surface motion of the mechanical device in z-direction using a displacement field $\psi(x,y,t)$. This scalar function gives the displacement in z-direction of the surface for every point (x,y) on the surface and for every time t. For small motional amplitudes, the devices behave linearly, which implies that their motion can be described via normal modes of the form

mechanical displacement field

$$\psi(x,y,t) = \sum_i q_i(t) \cdot u_i(x,y) \tag{2.37}$$

where $q_i(t)$ is the time-dependent amplitude of mode i and the mode function $u_i(x,y)$ describes the geometric shape of the mode. In the regime of linear motion, the mode amplitudes $q_i(t)$ satisfy the Langevin equations (2.33) for damped harmonic motion with a resonance frequency ω_i. The resonance frequencies ω_i and mode shapes $u_i(x,y)$ can be found either by solving the elastic wave equation for the mechanical device (in the simplest cases) or by finite-element modeling (for more complicated geometries).

Note that (2.37) defines q_i and u_i only up to a scaling factor since we can redefine $q_i \to \alpha \cdot q_i$ and $u_i \to (1/\alpha) \cdot u_i$ without changing (2.37). Hence, we have a freedom of normalization in the definition of u_i. One convenient option is to define u_i such that its maximum equals 1. With this choice, the coordinate q_i expresses the peak displacement of the given mode (the displacement of the point of maximum displacement on the surface of the mechanical device, for the given mode).

normalization of mode functions

2.2.1 *Modal mass*

The kinetic energy of motion in z-direction is given by [see e.g. Yan11]

$$T = \left(\iint \rho \cdot d \cdot \dot{\psi}(x,y,t)^2 \, \mathrm{d}x \, \mathrm{d}y \right) /2 \tag{2.38}$$

$$= \sum_i \left(\frac{\dot{q}_i(t)^2}{2} \iint \rho \cdot d \cdot u_i(x,y)^2 \, \mathrm{d}x \, \mathrm{d}y \right), \tag{2.39}$$

where $\rho = \rho(x,y)$ and $d = d(x,y)$ are the mass density and thickness of the oscillator. ρ and d are constant for the membranes, but depend on x and y for the cantilevers due to the mirror pad they are carrying. Note that, in (2.39), terms $u_i(x,y) \cdot u_j(x,y)$ drop out because of the orthogonality of the different eigenmodes.

By comparing (2.39) to the expression for the kinetic energy of a one-dimensional mechanical oscillator

$$T = \dot{q}(t)^2 m/2, \tag{2.40}$$

modal mass

we obtain the so-called modal mass m_i of mode i

$$m_i \equiv \iint \mathrm{d}x\mathrm{d}y \, \rho(x,y) d(x,y) u_i(x,y)^2. \tag{2.41}$$

This defines the mass parameter we must use to describe the motion of the coordinate $q_i(t)$ using the Langevin equations (2.33), or their quantum generalization (2.35). Note that the numerical value of m_i in (2.41) depends on the normalization of the mode functions $u_i(x,y)$.

2.3 OPTICAL CAVITIES

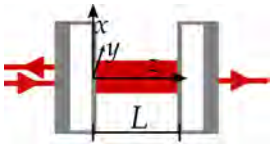

[7] *Optical cavity with adopted coordinate system.*

Consider an optical Fabry–Pérot cavity formed by two mirrors in vacuum separated by a distance L such that the round-trip path length for light inside the cavity is $p = 2L$. Call the direction along the cavity-axis (the longitudinal direction) z and the directions transversal to it x and y.[7]

eigenmodes

The spatial electro-magnetic field distributions for the eigenmodes of this cavity depend on curvature and shape of the mirrors. They are approximately given by Hermite–Gaussian (Laguerre–Gaussian) TEM-modes for square (round) mirrors [see KL66]. TEM is short for transverse electro-magnetic, which means that, for these modes, the electric and magnetic fields do not have components in the direction of propagation (z) but only in the transverse directions. The eigenmodes are labeled TEM_{mnq}: The first two subscripts $m, n \in \mathbb{N}_0$ count the nodes of the field in x and y (radial and azimuthal) direction for square (round) mirrors. The third and last subscript $q \in \mathbb{N}$ (which is usually omitted) counts the nodes in z-direction ($q \gg 1$).

For plane waves, constructive interference after a roundtrip in the cavity would occur for optical frequencies $2\pi \cdot q \cdot \nu_{\mathrm{FSR}}$ ($q \in \mathbb{N}$) where $\nu_{\mathrm{FSR}} = c/p$ is the inverse round-trip time in the cavity, also known as the free spectral range (FSR). But the resonance frequencies of the TEM_{mnq}-modes differ from those for plane waves due to an additional phase per round-trip, called the Gouy phase [see KL66]. Since the Gouy phase increases with the transversal mode numbers m, n, the different eigenmodes of the resonator are, in general, non-degenerate. However, because the Gouy phase does *not* depend on the longitudinal mode number q, the frequency spacing $\omega_{mnq} - \omega_{mnq'}$ of modes with the same transversal field distribution is still given by $(q - q') \cdot 2\pi \cdot \nu_{\mathrm{FSR}}$. Note that, for a cavity which is perfectly symmetric under exchange of x and y, the modes TEM_{mnq} and TEM_{nmq} will be degenerate (in the case of Hermite–Gaussian eigenmodes). In theory, if x and y can be interchanged, there should also be a degeneracy of horizontal and vertical polarization for a given TEM-mode. But in practice, they are usually slightly non-degenerate, probably due to an intrinsic birefringence of the Bragg mirrors [Bie+09].

resonance frequencies

In our experiments, we only use fundamental eigenmodes TEM_{00q}. Experimentally, we ensure that only TEM_{00q}-modes are significantly populated by mode-matching the driving laser to the transversal field distribution of the TEM_{00q}-modes at the input mirror. In addition, the frequency ω_{l} of the driving laser is always close to the resonance frequency ω_{c} of only one TEM_{00q}-mode. In other words, the detuning of the laser with respect to the cavity mode

mode-matching

detuning

$$\Delta \equiv \omega_{\mathrm{l}} - \omega_{\mathrm{c}} \tag{2.42}$$

satisfies $\Delta \ll 2\pi \cdot \nu_{\mathrm{FSR}}$. Because we work with resonators of high finesse, this implies that there is only a single fundamental eigenmode of the cavity, which we excite significantly—the one whose eigenfrequency is closest to the frequency of the driving laser. For this reason, I focus on only one eigenmode of the optical cavity in what follows.

single-mode case

2.3.1 *Classical description*

Let us now define[8] the relevant fields inside and outside the cavity and their couplings such that we can write down the Langevin equation for the intracavity mode: The mirrors 1 (input) and 2 have amplitude transmittivities t_1 and t_2, respectively. The corresponding amplitude reflectivities are denoted by $r_i = \sqrt{1 - t_i^2}$. The input field E_1^{in} has a carrier frequency ω_{l}, i.e. $E_1^{\mathrm{in}}(t) \propto \exp(-i\omega_{\mathrm{l}} t)$. This leads to the buildup of a stationary intracavity field E at the same frequency, whose amplitude depends on the detuning Δ, as we will see below.

[8] *Convention for electric fields and transmittivities:*

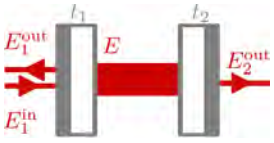

rotating frame at ω_1

For simplicity, we work in a frame rotating at the frequency ω_1 of the driving laser, such that we can simply write $E(t)$ or $E_1^{\text{in}}(t)$ instead of $E(t)\exp(-i\omega_1 t)$ or $E_1^{\text{in}}(t)\exp(-i\omega_1 t)$. Note that most of the expressions provided below regarding the time evolution of the intracavity mode depend both on the definition of Δ (here: $\Delta \equiv \omega_1 - \omega_c$) and on the convention regarding the rotation direction of the driving field (here $\propto \exp(-i\omega_1 t)$). In both cases, I follow the conventions in [AKM14; Hof15]. They deviate from [Wil12] (who uses a driving field $\propto \exp(+i\omega_1 t)$) and from [Grö10] (who defines $\Delta \equiv \omega_c - \omega_1$). Note that, for consistency with [Wie+15], I call the cavity amplitude decay rate κ (instead of $\kappa/2$ as in [AKM14; Hof15]).

conventions

one-sided cavities

We always work with strongly overcoupled cavities ($t_1 \gg t_2$). In this case, almost no light is transmitted. We therefore do not measure the transmitted field E_2^{out} but only the reflected field E_1^{out}. This allows us to treat transmission through the second mirror as a loss mechanism. For simplicity, we therefore include all other optical losses (scatter into other cavity modes or out of the cavity and absorption inside the cavity) in the definition of t_2.

Field amplitudes are (in analogy to the mechanical case) measured in units of ground state uncertainty. In these units, the absolute square of a traveling wave field amplitude expresses a photon flux. Correspondingly, the input field amplitude E_1^{in} is proportional to the root of the photon flux, hence has units of $\sqrt{\text{Hz}}$. But the intracavity field is more conveniently expressed in terms of the root of the intracavity photon number α. To achieve this, E should be multiplied by the root of the optical round-trip time $T \equiv 1/\nu_{\text{FSR}}$. Hence, we define $\alpha = \sqrt{T}E$. Then, for $\Delta \ll 2\pi \cdot \nu_{\text{FSR}}$, the following differential equation for the evolution of $\alpha(t)$ depending on the input field $E_1^{\text{in}}(t)$ can be derived [see Wil+09, sec. 2.3]:

equation of motion for intra-cavity amplitude

$$\dot{\alpha}(t) = (i\Delta - \kappa)\alpha(t) + \sqrt{2\kappa_1}E_1^{\text{in}}(t). \tag{2.43}$$

Here, the parameters κ_i, $(i = 1, 2)$ and κ are defined in terms of the power transmission t_i^2 as follows:

$$\kappa \equiv \sum_i \kappa_i \equiv \sum_i \nu_{\text{FSR}} \cdot t_i^2/2. \tag{2.44}$$

(2.43) is analogous to the evolution of a harmonic oscillator at frequency $-\Delta$ with damping κ and a driving term $E_1^{\text{in}}(t)$. Hence, the optical cavity mode and the mechanical modes behave very similarly, except that, in the case of the mechanical modes, we assumed an asymmetric damping (affecting only the momentum quadrature and not the full complex amplitude).

(2.43) implies that, without the drive E_1^{in}, the intracavity field amplitude $|\alpha|$ decays with rate κ. Hence, the intracavity photon number

decays with rate 2κ. For a continuous drive $E_1^{\text{in}} = \text{const}$, the intra-cavity field eventually acquires a steady-state value ($\dot{\alpha} = 0$) given by

$$\alpha = \frac{\sqrt{2\kappa_1}}{\kappa - i\Delta} E_1^{\text{in}}. \tag{2.45}$$

This the power buildup inside the cavity depends on the detuning and is given by

enhancement of intra-cavity power

$$\frac{|\alpha|^2/T}{|E_1|^2} = \frac{2\kappa_1 \nu_{\text{FSR}}}{\Delta^2 + \kappa^2}. \tag{2.46}$$

Hence, κ is not only the amplitude decay rate for the undriven cavity, but also the power half width at half maximum (HWHM) of the driven cavity.

On resonance, the power buildup (2.46) can be rewritten as

$$\frac{2\kappa_1 \nu_{\text{FSR}}}{\kappa^2} = \frac{2\mathcal{F}}{\pi} \cdot \frac{\kappa_1}{\kappa}, \tag{2.47}$$

where we introduced the finesse

finesse

$$\mathcal{F} \equiv \frac{2\pi \cdot \nu_{\text{FSR}}}{2\kappa}. \tag{2.48}$$

The finesse relates the full width 2κ of an individual cavity resonance to the frequency separation $2\pi \cdot \nu_{\text{FSR}}$ of neighboring modes. It is thus a dimensionless measure of the frequency resolution of the cavity as well as of the maximum power-buildup inside the cavity. Using the definition (2.44) for κ, we can also express the finesse as follows

$$\mathcal{F} = \frac{2\pi}{\sum_i t_i^2}. \tag{2.49}$$

Hence, the finesse depends only on the losses and not on the length of the cavity. This is why the finesse is useful for comparing cavities of very different dimensions.

Note that, for low transmission and for low scatter and absorption losses ($t_i \ll 1$), the round-trip optical power loss $1 - r^2 \equiv 1 - \prod_i r_i^2$ can be related to the power transmission t_i^2 as $1 - r^2 \simeq \sum_i t_i^2$. We can therefore relate the finesse to the round trip losses $1 - r^2$ as follows (for $\mathcal{F} \gg 1$):

$$\mathcal{F} \approx \frac{2\pi}{1 - r^2} \approx \frac{\pi}{1 - r}. \tag{2.50}$$

2.3.2 *Quantum description*

Quantum-mechanically, a cavity mode can be described as a harmonic oscillator—analogous to the mechanical case. In the frame

Hamiltonian

rotating at the frequency $\omega_l = \omega_c + \Delta$ of the driving laser, and without damping, its Hamiltonian $\hat{H}_o$ is given by [see AKM14, eq. (23)]

$$\hat{H}_o = -\hbar\Delta\hat{a}^\dagger\hat{a}. \tag{2.51}$$

I left out a zero-point contribution $-\hbar\Delta/2$, since it is not relevant in the following. The operators $\hat{a}^\dagger$ ($\hat{a}$) are the creation (annihilation) operators for photons in the cavity mode. They obey the canonical commutation relation $\left[\hat{a}, \hat{a}^\dagger\right] = 1$.

In close analogy to (2.43), the time-evolution of the mode operator $\hat{a}(t)$ in the Heisenberg picture in the presence of damping and under the influence of external fields is given by [GC85]

$$\dot{\hat{a}}(t) = (i\Delta - \kappa)\hat{a}(t) + \sqrt{2\kappa_1}\hat{a}_1^{\text{in}}(t) + \sqrt{2\kappa_2}\hat{a}_2^{\text{in}}(t), \tag{2.52}$$

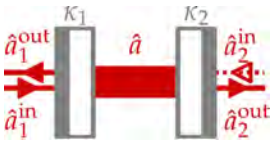

[9] *Convention for mode operators.*

where $\hat{a}_1^{\text{in}}$ describes the mode populated by the drive laser and $\hat{a}_2^{\text{in}}$ is a fictitious mode collecting all the loss channels.[9] All the modes lumped together in $\hat{a}_2^{\text{in}}$ are initially in the vacuum state. Their contribution to the dynamics of the intra-cavity mode $\hat{a}$ is therefore given by vacuum noise.

reflected field

As mentioned, we measure the reflected field. This field is described by a mode $\hat{a}_1^{\text{out}}$ which can be expressed as a sum of the directly reflected part of the input field plus a fraction $\sqrt{2\kappa_1}$ of the intracavity field, which is leaking out via the input coupling mirror [GC85]:

$$\hat{a}_1^{\text{out}}(t) = \sqrt{2\kappa_1}\hat{a}(t) - \hat{a}_1^{\text{in}}(t). \tag{2.53}$$

quadratures

It is convenient to define the amplitude quadrature $\hat{x}$ and phase quadrature $\hat{y}$ for the optical mode, in analogy to position and momentum for the mechanical mode:

$$\hat{x} \equiv \left(\hat{a} + \hat{a}^\dagger\right)/\sqrt{2},\ \hat{y} \equiv \left(\hat{a} - \hat{a}^\dagger\right)/\left(i\sqrt{2}\right). \tag{2.54}$$

The quadratures satisfy the canonical commutation relation $[\hat{x}, \hat{y}] = i$. Then (2.52) can be rewritten in terms of $\hat{x}$ and $\hat{y}$ as follows:

$$\dot{\hat{x}} = -\Delta\hat{y} - \kappa\hat{x} + \sqrt{2\kappa_1}\hat{x}_1^{\text{in}} + \sqrt{2\kappa_2}\hat{x}_2^{\text{in}}, \tag{2.55}$$

$$\dot{\hat{y}} = +\Delta\hat{x} - \kappa\hat{y} + \sqrt{2\kappa_1}\hat{y}_1^{\text{in}} + \sqrt{2\kappa_2}\hat{y}_2^{\text{in}}, \tag{2.56}$$

where $\hat{x}_1^{\text{in}}$, $\hat{y}_1^{\text{in}}$, $\hat{x}_2^{\text{in}}$, $\hat{y}_2^{\text{in}}$ are the quadratures of the input modes $\hat{a}_1^{\text{in}}$, $\hat{a}_2^{\text{in}}$, defined in analogy to (2.54).

2.4 OPTOMECHANICAL COUPLING

In an optomechanical cavity, the resonance frequency ω_c and, correspondingly, also the detuning Δ depend on the position quadrature $\hat{q}$ of a mechanical mode (generally, they depend on many mechanical

modes). In the simplest case of end-mirror-coupling (Section 2.4.1), this is due to the cavity length changing with $\hat{q}$. In the slightly more complicated case of a membrane inside a cavity (Section 2.4.2), it is due to the dependence of the membrane-induced phase shift on the membrane's position along the standing wave inside the cavity. In both cases, we get a parametric dependence of the optical cavity Hamiltonian $\hat{H}_o$ on $\hat{q}$:

parametric dependence of cavity resonance on mechanical position

$$\hat{H}_o = \hat{H}_o(\hat{q}) = -\hbar\Delta(\hat{q})\hat{a}^\dagger\hat{a}. \tag{2.57}$$

This parametric dependence of Δ on $\hat{q}$ implies a coupling of mechanical and optical degrees of freedom, which is referred to as *dispersive* coupling (in contrast to *dissipative* coupling, in which the cavity decay rate κ depends on $\hat{q}$ [see AKM14, sec. III.B.]).

The amplitude of mechanical motion in quantum optomechanical experiments is typically rather small compared to the optical length scales. The zero-point uncertainty of our mechanical oscillators is only on the order of $10^{-15}\,\mathrm{m}$, and, even at room temperature, the thermal position deviation is only on the order of $10^{-12}\,\mathrm{m}$, whereas the optical wave-length is on the order of $10^{-6}\,\mathrm{m}$. Therefore, the cavity detuning changes only very little for typical values of $\hat{q}$. Hence, the Hamiltonian (2.57) is very well approximated using a first-order expansion of Δ around the point $q = 0$:

small motional amplitudes

linearization in $\hat{q}$

$$\hat{H}_o(\hat{q}) \simeq -\hbar\left[\Delta(0) + \hat{q}\Delta'(0)\right]\hat{a}^\dagger\hat{a}, \tag{2.58}$$

where $\Delta'(q) \equiv \partial_q\Delta(q)$ is the derivative of the detuning with respect to q (with q in units of ground-state uncertainty).

We define the single-photon coupling strength

single-photon coupling

$$g_0 \equiv -\Delta'(0) = +\omega_c'(0) \tag{2.59}$$

which quantifies the frequency shift of the cavity due to an increase in the effective cavity length by an amount corresponding to the ground-state uncertainty. Introducing the derivative of the cavity resonance with respect to displacement z in SI-units

$$G \equiv \partial_z\omega_c(z) \tag{2.60}$$

and recalling that the conversion factor from ground-state uncertainty units to SI-units is $\sqrt{2}q_0$, we can also write

$$g_0 = \sqrt{2}q_0 \cdot G. \tag{2.61}$$

The optomechanical interaction is therefore, for the very small motional amplitudes typically achieved in micromechanical resonators, very well described by the following interaction term:

$$\hat{H}_i = \hbar g_o \, \hat{q} \, \hat{a}^\dagger \hat{a}. \tag{2.62}$$

non-linear interaction

Note that (2.62) is of third order in the mode operators which yields a nonlinear interaction between mechanical mode and cavity mode. As discussed in Section 2.5, (2.62) can be approximated by a linear interaction (quadratic in the mode operators), which is sufficient to describe all experiments of this thesis.

Note also that the sign of g_o in (2.62) depends on the definition of $\hat{q}$. In this thesis, I always use positive values for the coupling. (2.62) then implies that $\hat{q}$ is defined such that increases of $\hat{q}$ lead to increased energy, hence to an increased cavity frequency ω_c. In the case of end-mirror coupling this means positive $\hat{q}$ corresponds to a decreased cavity length.

2.4.1 *End-mirror coupling*

To calculate the coupling $g_0 = \omega_\mathrm{c}'(0)$, we have to calculate the dependence of the cavity resonance on the mechanical position q around its steady-state position (the origin of q by definition). The case of a Fabry–Pérot cavity with a movable mirror is particularly simple:

$$\omega_\mathrm{c}(q) = \frac{c}{2\left(L + \sqrt{2} q_0 q\right)}. \tag{2.63}$$

The single-photon coupling in this case is given by

$$g_0 = \partial_q \frac{c}{2\left(L + \sqrt{2} q_0 q\right)}\bigg|_{q=0} = \sqrt{2} q_0 \frac{\omega_\mathrm{c}}{L}, \tag{2.64}$$

which depends only weakly (via L) on the position of the oscillator.

The same type of coupling is observed in a variety of monolithic microcavities including microdisks, microtoroids, and silica spheres [see AKM14, section IV.C for an overview]. In these devices, mechanical deformations of the microcavity also change the optical round-trip path length, and therefore couple to the cavity mode.

2.4.2 *Membrane coupling*

A different type of dispersive optomechanical coupling is that of dielectric materials inside optical cavities. This can be experimentally realized in different ways [see AKM14, section IV.E for an overview],

for example, with dielectric particles trapped in the field of a cavity. Here we are interested in the case of thin dielectric films (membranes) inserted into a Fabry–Pérot cavity such that the cavity axis is normal to the membrane surface.

basic idea

The idea is almost as simple as for end-mirror coupling: Inserting a dielectric membrane into a Fabry–Pérot cavity changes the optical intracavity path length and, therefore, also the resonance frequency ω_c. But the membrane-induced phase shift and, correspondingly, also the cavity resonance frequency depend on the position of the membrane with respect to the standing wave inside the cavity. This leads to a coupling of membrane motion to the cavity mode.

[Wil12, sec. 3.3.1] provides the following approximate expression of the coupling $g_0(z)$ as a function of the membrane position z from the center of the cavity

$$g_0(z) \simeq -\frac{2q_0\omega_c}{L}\frac{|r_m|\,\xi(\lambda, z, r_m)}{1-2(z/L)\,|r_m|\,\xi(\lambda, z, r_m)}, \tag{2.65}$$

$$\xi(\lambda, z, r_m) \equiv \frac{\sin(4\pi z/\lambda)}{\sqrt{1-|r_m|^2\cos(4\pi z/\lambda)^2}}, \tag{2.66}$$

where $\lambda = 2\pi\cdot c/\omega_c$ is the optical wave length, L is the cavity length and r_m is the reflectivity of the membrane at wave length λ. Importantly, (2.65) implies that the membrane coupling g_0 is proportional to the coupling $\sqrt{2}q_0\omega_c/L$ in the end-mirror case. In particular, g_0 is inversely proportional to the cavity length.

periodicity of coupling

Note that, according to (2.65), the coupling g_0 is approximately periodic as a function of z with a period $\lambda/2$, i.e.

$$g_0(z+\lambda/2) \simeq g_0(z). \tag{2.67}$$

This is because also the intra-cavity field distribution is (up to sign) periodic in z with period $\lambda/2$. Therefore, inserting a membrane at z or at $z+\lambda/2$ has the same effect on the resonance frequency. Note, however, that the periodicity of the coupling as well as the intra-cavity field distribution is not perfect.

quadratic coupling

(2.65) also implies that there are positions z of the membrane at which the coupling $g_0(z)$ to the position $\hat{q}$ becomes zero. At these points, the light field couples predominantly to $\hat{q}^2$, which—under the right circumstances—allows to perform a QND-measurement of the mechanical phonon number [see AKM14, sec. VI.B.2].

calculating the coupling using transfer matrices

To calculate the coupling $g_0(z)$ of a membrane inside a Fabry–Pérot cavity from first principles, we have to find the cavity resonance frequency as a function of the membrane position z. This can be achieved using the transfer matrix formalism [see Wil+09, ch. 3], which allows to calculate the transmission and reflection of plane waves from parallel layers of differing index of refraction. This formalism

[10] *Membrane-cavity system (light enters from left):*

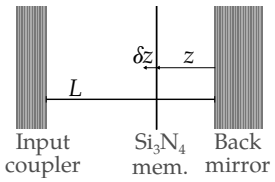

is sufficient to model the optomechanical system we are concerned with,[10] namely a cavity of length L with a membrane positioned at distance z from the back mirror: The input coupling mirror is modeled as a multilayer Bragg reflector, followed by a vacuum gap of length $L - z$, followed by the membrane of thickness d, followed by another vacuum gap of length z, followed by yet another multilayer for the back mirror.

Using the transfer matrix formalism, we can calculate the transmission through the whole structure as a function of membrane position z and laser frequency. The frequencies of maximal transmission, for a given membrane position z, are the resonance frequencies $\omega_c(z)$. Finally, we numerically differentiate the resonance frequencies $\omega_c(z)$ with respect to z to find $G(z) = \partial_z \omega_c(z)$ and $g_0(z) = \sqrt{2} q_0 \cdot G(z)$. Note that calculations can be sped up considerably by assuming the transmission of the multi-layer mirrors to be constant over the very small range of wave lengths considered here (which is an excellent approximation).

As an example, let us consider the latest iteration of our membrane optomechanical cavity, for which $L \simeq 5.5\,\mathrm{mm}$ and $z \simeq 0.5\,\mathrm{mm}$ such that the membrane sits close to the back mirror of the cavity. We chose to put the membrane close to the end of the cavity because it yields slightly higher coupling and because it increases stability and facilitates alignment, as explained in Section 3.5.2. The membrane thickness is $d \simeq 50\,\mathrm{nm}$, the real part of the refractive index of Si3N4 is $n \simeq 1.99$ (based on [Pol] and consistent with the spread of values quoted in [Wil12, sec. 3.1.1]). Here, I used input coupler and back mirror power transmissions of $\gtrsim 800\,\mathrm{ppm}$ and $\lesssim 1\,\mathrm{ppm}$, respectively, corresponding to a finesse of the empty cavity of $\mathcal{F} \simeq 7.8 \times 10^3$.

The results are plotted in Figure 2.1. As expected, both $\omega_c(z)$ as well as $G(z)$ are periodic with a period of $\lambda/2$. To deduce the single-photon coupling $g_0(z)$ from this plot, we need to know the ground-state uncertainty and the effective mass of the mechanical mode of the membrane we are interested in.

2.4.3 *Effective mass*

The above calculations of the coupling assumed that, by changing the position q of the mechanical mode, we change the cavity resonance frequency ω_c as if the whole oscillator (SiN-bridge or membrane) was uniformly displaced. The mechanical modes of real oscillators, however, do *not* lead to a uniform displacement. Therefore, the effect of a change of q on the cavity frequency ω_c depends on how those parts of the oscillator which are illuminated by the cavity mode are actually displaced. Consequently, also the optomechanical coupling g_0 depends on the overlap between mechanical and optical mode. With

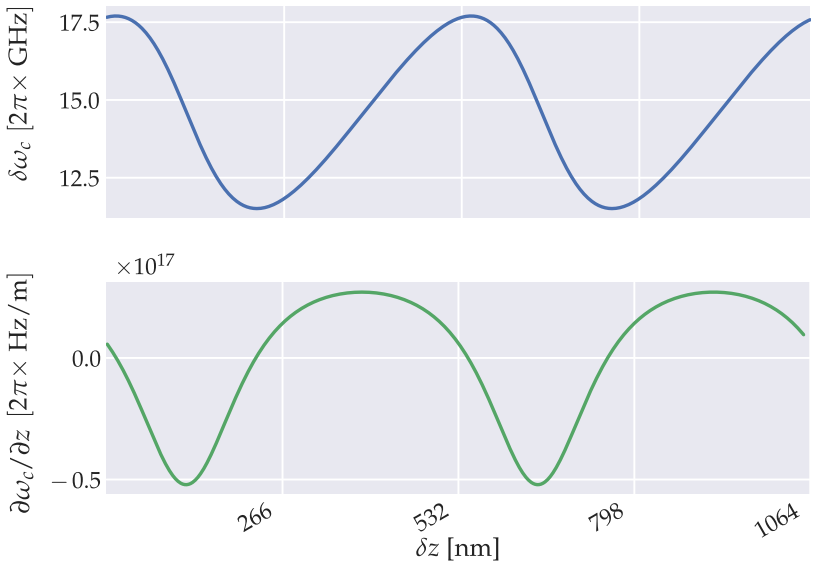

Figure 2.1. Shift $\delta\omega_c(z)$ of cavity resonance frequency (top panel) and its derivative $G(z)$ (bottom) as a function of membrane displacement δz (with respect to its nominal position at a distance of 0.5 mm from the back mirror of the cavity). The shift $\delta\omega_c(z)$ is given with respect to the nominal laser wave length of 1064 nm, but only its derivative matters for our purpose.

our definition of the mode function in Section 2.2.1, the mode amplitude measures peak displacement. But the light field does not always "see" the peak displacement. Hence, the coupling is generally smaller than suggested by above definitions.

The correction is, for high-finesse cavities, given by the overlap integral of normalized optical intensity $I(x,y)$ (at the position of the mechanical oscillator) and mechanical mode function $u(x,y)$ [PHH99]

overlap integral

$$g_0 \to g_0 \cdot \iint I(x,y)\cdot u(x,y)\,\mathrm{d}x\,\mathrm{d}y. \tag{2.68}$$

As expected, we get no correction for uniform displacement $u(x,y) = 1$, but a large correction if u differs significantly from 1 within the optical spot[11] or even oscillates within the optical spot (as for some high order membrane modes). (2.68) can be understood naively by noting that, in the mechanical ground state, only the light hitting the mechanical oscillator at points of maximum displacement (corresponding to $u = 1$) experiences the full shift corresponding to $\sqrt{2}q_0 \cdot G$ whereas at all other points the shift is suppressed by the factor u.

[11] *Illustration of (2.68) for the (3,3)-mode of a square membrane:*

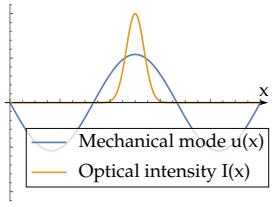

Note that historically, the correction $\iint I(x,y)\cdot u(x,y)\,\mathrm{d}x\,\mathrm{d}y$ has been absorbed into the definition of $q_0 = \sqrt{\hbar/2m\omega_m}$ by replacing the modal mass m in the definition of q_0 by the so-called *effective mass*

effective mass

$$m_{\mathit{eff}} = m/\left(\iint I(x,y)\cdot u(x,y)\,\mathrm{d}x\,\mathrm{d}y\right)^2. \tag{2.69}$$

This has the advantage of associating the mode-dependent correction (2.68) with a quantity which anyway depends on the mode. But it has, in my opinion, the disadvantage of obscuring the meaning of the zero-point uncertainty. Defined in this way, the zero-point motion does not measure the actual displacement of the membrane but only the "displacement seen by the optical beam".

To illustrate: For a 0.5 mm × 0.5 mm-membrane and an optical beam with a 45 µm waist at the membrane position and no lateral displacement, we get $\simeq 83.5\%$ for the overlap integral for the (3,3)-mode and correspondingly $m_{\mathrm{eff},33} \approx 1.43 \cdot m$ if m is the modal mass. For a 50 nm-thick SiN-membrane, this yields $m_{\mathrm{eff},33} \approx 9.9\,\mathrm{ng}$.

2.5 LINEARIZED HAMILTONIAN

In our experiments, the single-photon coupling g_0 is too small to yield observable effects. Fortunately, it can effectively be increased by drastically increasing the number of photons which interact with the mechanical oscillator. To this end, we drive the cavity with a coherent field with large amplitude. That is, the state of the input mode in the Langevin equation in (2.52) for the cavity mode satisfies

large coherent drive

$$\langle \hat{a}_1^{\mathrm{in}}(t) \rangle = \alpha_1^{\mathrm{in}} \in \mathbb{R},\ \alpha_1^{\mathrm{in}} \gg 1, \tag{2.70}$$

where the expectation value α_1^{in} is constant in the frame rotating at the drive frequency ω_1 and can be assumed real without loss of generality.

We know from (2.45), that—in the absence of optomechanical coupling—a constant drive leads to a steady state intracavity amplitude

intracavity steady state

$$\langle \hat{a} \rangle = \alpha,\ \alpha = \frac{\sqrt{2\kappa_1}}{\kappa - i\Delta}\alpha_1^{\mathrm{in}}. \tag{2.71}$$

With optomechanical coupling, the existence of a steady state depends on the detuning Δ and, due to the nonlinearity of the optomechanical interaction, also on the driving strength α_1^{in} [Hof15, fig. 12 (a)].[12] In what follows, I assume a stable steady state, since this is the case of interest in our experiments.

[12] *For some parameters, several stable steady states may exist [Dor+83].*

Assuming now that the intracavity field has acquired a large constant mean amplitude α due to the drive, it is useful to re-express the intracavity mode operators as

$$\hat{a} \equiv \alpha + \delta\hat{a},\ \alpha \equiv \langle \hat{a} \rangle \tag{2.72}$$

and expand the interaction Hamiltonian $\hat{H}_i$ in powers of α:

expansion of interaction Hamiltonian around mean intracavity amplitude

$$\hat{H}_i = \hbar g_o \hat{q} \left(\alpha + \delta\hat{a}\right)^\dagger \left(\alpha + \delta\hat{a}\right) \tag{2.73}$$

$$= \hbar g_o \hat{q} \left|\alpha\right|^2 + \hbar g_o \hat{q} \left(\alpha^* \delta\hat{a} + \alpha \delta\hat{a}^\dagger\right) + \mathcal{O}\left(\delta\hat{a}^\dagger \delta\hat{a}\right). \tag{2.74}$$

The first term $\hbar g_o \hat{q} |\alpha|^2$ in (2.74) represents a static radiation pressure force on the mechanical mode due to the DC part of the intracavity field. It leads to a constant non-zero mean displacement of the mechanical mode. We can drop this term by simply redefining the origin for $\hat{q}$ to coincide with the shifted mean position.

The last term in (2.74) can be neglected (compared to the second term) assuming that typical fluctuations $\delta\hat{a}$ are much smaller (in absolute value) than the mean amplitude α. Hence, the dominant interaction term becomes

$$\hat{H}_i \simeq \hbar g_o \hat{q} \left(\alpha^* \delta\hat{a} + \alpha \delta\hat{a}^\dagger \right) = \hbar g \hat{q} \left(\cos(\theta)\, \delta\hat{x} + \sin(\theta)\, \delta\hat{y} \right) \tag{2.75}$$

where the linearized optomechanical coupling is defined as *linearized coupling*

$$g \equiv \sqrt{2}\, |\alpha|\, g_o, \tag{2.76}$$

$\theta \equiv \arg(\alpha)$ and the quadratures $\delta\hat{x}$ and $\delta\hat{y}$ are defined as

$$\delta\hat{x} \equiv \left(\delta\hat{a} + \delta\hat{a}^\dagger \right) / \sqrt{2},\ \delta\hat{y} \equiv \left(\delta\hat{a} - \delta\hat{a}^\dagger \right) / \left(i\sqrt{2} \right).$$

Note that the derivation of the linearized coupling presented here is meant to be intuitive rather than rigorous. A rigorous derivation should take the open-system dynamics into account. For a much more thorough discussion of the linearization of the equations of motion around the steady state see [Hof15, sec. 1.3.1]. Note also that [Hof15] defines $g \equiv \alpha g_o / \sqrt{2}$, i.e. a factor two smaller than in our definition, which was chosen for consistency with [Wie+15].

(2.75) describes an interaction of the position quadrature $\hat{q}$ of the mechanical mode with a rotated quadrature $\cos(\theta)\, \delta\hat{x} + \sin(\theta)\, \delta\hat{y}$ of the intracavity mode. The interaction strength g is tunable via $|\alpha|$, the root of the mean intracavity photon number. For constant drive detuning Δ, we have *tunable coupling*

$$|\alpha| \exp(i\theta) = \frac{\sqrt{2\kappa_1}}{\kappa - i\Delta} \alpha_1^{\text{in}} = \frac{\sqrt{2\kappa_1}}{\kappa - i\Delta} \sqrt{\frac{P_{\text{opt}}}{\hbar\omega_l}}, \tag{2.77}$$

such that the linearized coupling g, defined by (2.76), is simply proportional to $\sqrt{P_{\text{opt}}}$. g can thus be adjusted via the optical power P_{opt} of the external drive. An upper limit on P_{opt} is, in current experiments, usually imposed either by the maximally tolerable amount of heating by absorption or the maximally tolerable level of classical laser noise, both of which increase with P_{opt}, or by in- or bi-stabilities of the cavity.

2.5.1 *Beam-splitter and two-mode-squeezer*

Since we always work in the linear regime, I now drop the δ in $\delta\hat{a}$, $\delta\hat{x}$, and $\delta\hat{y}$. Hence, the interaction Hamiltonian is now written simply as

$$\hat{H}_i = \hbar g \hat{q} \left(\cos\left(\theta\right)\hat{x} + \sin\left(\theta\right)\hat{y}\right). \tag{2.78}$$

To get an intuitive understanding of this interaction, we can rewrite $\hat{H}_i$ using the annihilation operators $\hat{a}$ (previously $\delta\hat{a}$) of the optical intracavity mode and $\hat{b}$ of the mechanical mode:

$$\hat{H}_i = \frac{\hbar g}{2}\left(\hat{b} + \hat{b}^\dagger\right)\left(e^{-i\theta}\hat{a} + e^{i\theta}\hat{a}^\dagger\right) \tag{2.79}$$

$$= \frac{\hbar g}{2}\left(e^{-i\theta}\hat{a}\hat{b} + +e^{i\theta}\hat{a}^\dagger\hat{b}^\dagger\right) + \frac{\hbar g}{2}\left(e^{-i\theta}\hat{a}\hat{b}^\dagger + e^{i\theta}\hat{a}^\dagger\hat{b}\right). \tag{2.80}$$

free evolution

The free evolution of the annihilation operators $\hat{a}$ and $\hat{b}$ (in the Heisenberg picture, in the frame rotating at the drive frequency $\omega_l = \omega_c + \Delta$, and neglecting damping) is given by

$$\hat{a}\left(t\right) = \hat{a}\left(0\right)\exp\left(+i\Delta t\right),\ \hat{b}\left(t\right) = \hat{b}\left(0\right)\exp\left(-i\omega_m t\right). \tag{2.81}$$

two-mode squeezer

Therefore, in an interaction picture which accounts for this free evolution, the first two terms in (2.80)

$$\frac{\hbar g}{2}\left(e^{-i\theta}\hat{a}\hat{b} + +e^{i\theta}\hat{a}^\dagger\hat{b}^\dagger\right) \equiv \hat{H}_{\mathrm{TMSS}} \tag{2.82}$$

oscillate with $\pm\left(\Delta - \omega_m\right)$. Hence, for a blue-detuned drive satisfying $\Delta \simeq \omega_m$, this part of the interaction is roughly stationary (in the interaction picture) and can therefore have a large effect, while the last two terms in (2.80) are rapidly oscillating (at $\simeq \pm 2\omega_m$) and are therefore effectively averaged out. (2.82) is called the two-mode squeezing Hamiltonian because it is analogous to the Hamiltonian describing optical down-conversion which yields entangled two-mode squeezed states. It describes joint creation and joint annihilation of phonons and photons and thereby produces states with strong phonon–photon-number correlations. For sufficiently low decoherence and sufficiently pure initial states, entanglement can result. In Chapter 5, I discuss different options for creation and detection of entanglement based on this part of the optomechanical interaction.

beam splitter

For a red-detuned drive $\Delta \simeq -\omega_m$, on the other hand, the last two terms in (2.80)

$$\frac{\hbar g}{2}\left(e^{-i\theta}\hat{a}\hat{b}^\dagger + e^{i\theta}\hat{a}^\dagger\hat{b}\right) \equiv \hat{H}_{\mathrm{BS}} \tag{2.83}$$

rotate (again in the interaction picture) with $\pm\left(\Delta + \omega_m\right)$ and, therefore, dominate the interaction. This part of the interaction is called

the beam-splitter Hamiltonian since it coherently exchanges excitations between the two modes, creating a phonon and destroying a photon or vice versa. This interaction can swap the state of the mechanical mode onto the optical mode and vice versa. If, as usual, the intracavity mode is much more weakly excited than the mechanical mode and the cavity decay is much faster than the interaction, the state swap (transferring mechanical excitations to the optical mode) is simply sideband cooling seen from a different point of view.

For more information on the rotating-wave approximation (RWA) which underlies the interpretation of the different terms in the Hamiltonian as beam-splitter and two-mode squeezer and the conditions under which the RWA can be applied see [Hof15, sec. 1.2].

2.6 QUANTUM LANGEVIN EQUATIONS

Let me summarize all of the preceding by presenting the linearized Langevin equations for the coupled optomechanical system. The basis are the quantum Langevin equations for the mechanical mode (2.35) and the optical mode (2.52) together with the linearized interaction. The resulting stochastic equations of motion for the Heisenberg quadrature operators of the mechanical mode are

mechanical part

$$\dot{\hat{q}} = +\omega_m \hat{p}, \tag{2.84}$$

$$\dot{\hat{p}} = -\omega_m \hat{q} - \gamma_m \hat{p} + g\left(\cos(\theta)\,\hat{x} - \sin(\theta)\,\hat{y}\right) - \sqrt{2\gamma_m}\hat{f}, \tag{2.85}$$

where the thermal noise force $\hat{f}$ satisfies (2.36).

Because it will be necessary for the discussion of the state estimation experiment and for the simulations of the entanglement experiment, I also include classical laser noise of the driving laser field [Abd+11] in the equations for the intracavity mode:

optical part

$$\begin{aligned}\dot{\hat{x}} &= -\kappa\hat{x} + \Delta\hat{y} + g\sin(\theta)\,\hat{q} + +\sqrt{2\kappa_1}\,\hat{x}_1^{\text{in}} + \sqrt{2\kappa_2}\,\hat{x}_2^{\text{in}} \\ &\quad \ldots + 2\sqrt{\kappa_1}\,\delta\alpha_1^{\text{in}} + |\alpha|\sin(\theta)\,\dot{\phi},\end{aligned} \tag{2.86}$$

$$\begin{aligned}\dot{\hat{y}} &= -\kappa\hat{y} - \Delta\hat{x} + g\sin(\theta)\,\hat{q} + \sqrt{2\kappa_1}\,\hat{y}_1^{\text{in}} + \sqrt{2\kappa_2}\,\hat{y}_2^{\text{in}} \\ &\quad \ldots + |\alpha|\cos(\theta)\,\dot{\phi},\end{aligned} \tag{2.87}$$

where $\delta\alpha_1^{\text{in}}(t)$ and $\dot{\phi}(t)$ are the classical amplitude and frequency fluctuations of the drive field $\alpha_1^{\text{in}}(t)$. To be more specific, in a frame rotating at the drive frequency ω_1, I assume

classical laser noise

$$\left\langle \hat{a}_1^{\text{in}}(t) \right\rangle = \left(\alpha_1^{\text{in}} + \delta\alpha_1^{\text{in}}(t)\right)\exp\left(-i\phi(t)\right), \tag{2.88}$$

where α_1^{in} is a constant mean amplitude and $\delta\alpha_1^{\text{in}}(t)$ and $\phi(t)$ are small, zero-mean fluctuations in amplitude and phase, respectively.

3

EXPERIMENTAL SETUP

In this thesis two experiments are discussed, optimal state estimation and entanglement generation. The setups for both of them can be broken down into four different functional blocks:[13]

LIGHT SOURCE: a laser, electro-optical modulators (EOMs) for creating optical sidebands, and optical filters (filter cavity for laser noise reduction and grating filters for sideband selection)

OM-CAVITY: a short, strongly over-coupled Fabry–Pérot cavity containing either a thin SiN membrane or a micromirror, operated in vacuum inside a refrigerator

DETECTION: photo-detectors, amplifiers, electronic filters, and fast AD-converters

LOCKING ELECTRONICS for locking the laser, the homodyne detectors, and the optical filters

[13] *Bird's eye view of an OM-experiment with flow of optical signals (red) and electrical signals (black).*

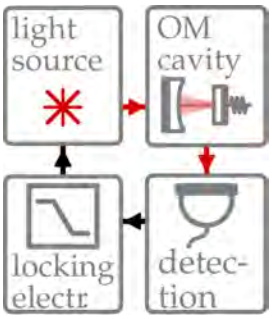

outline commonalities...

...and differences between the state estimation and the entanglement setup

In what follows, I first describe those aspects which are very similar in both experiments, namely the light source (Section 3.1), the detection (Section 3.2) and the locking (Section 3.3). Then, I explain differences between the two experimental setups—focusing first on the state estimation experiment (Section 3.4), then on the entanglement experiment (Section 3.5). The difference lies mainly in the mechanical resonators and optomechanical cavities—yielding wildly different mechanical quality factors and interaction strengths (see Section 3.4.3 and Section 3.5.2, respectively). Other differences concern the use of a second, detuned beam for laser cooling in the state estimation experiment (Section 3.4.1) and the use of a second homodyne detection setup for simultaneous monitoring of both phase and amplitude quadrature of the reflected light in the entanglement experiment.

3.1 LIGHT SOURCE

I first briefly describe our laser (Section 3.1.1) and the filter cavity (Section 3.1.2), which used for laser noise reduction in the entanglement experiment. Then, I present measurements of frequency noise (Section 3.1.4) and amplitude noise (Section 3.1.3) of the unfiltered and filtered laser.

3.1.1 *Laser*

Nd:YAG NPRO laser

We use a 1064 nm continuous-wave (CW) laser, the Prometheus from Innolight GmbH (now Coherent Inc.). We chose this model because of its good noise performance in the 0.1 to 10 MHz frequency range, which is the range we are mostly interested in. The Prometheus is a laser-diode-pumped Nd:YAG-laser [Bye88]. It delivers roughly 1 W of CW output at 1064 nm. In addition, it can provide roughly 100 µW at 532 nm (phase-coherent with the main beam at 1064 nm). The output of the Prometheus is single-mode in frequency, in transverse mode shape, and in polarization.

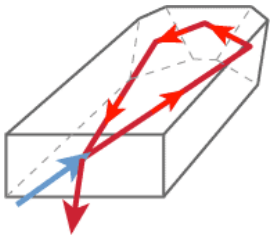

[14] *Sketch of NPRO laser crystal [from Pas] with* 808 nm *pump beam (blue in sketch) and* 1064 nm *laser beam (red)*

The Prometheus is designed as a so-called non-planar ring oscillator (NPRO)[14]. In this design [KB85], the laser cavity is perfectly monolithic, consisting only of the Nd:YAG laser-crystal with cut faces, one of which (the input/output coupler face) is convex and reflection-coated while all other faces are totally internally reflecting. The Nd:YAG laser-crystal is pumped with a laser diode at 808 nm.

single-mode

Because the laser cavity is a ring oscillator, its eigenmodes are traveling waves. This prevents spatial hole burning and allows single-mode operation in frequency and transverse mode shape. Because the beam hits the output coupler face under an oblique angle, the reflectivity of this face and, correspondingly, the finesse of the laser cavity are strongly polarization-dependent; this leads to a fixed polarization of the laser. Finally, the NPRO is also intrinsically unidirectional, i.e. can oscillate in only one of its two counter-propagating modes . This is important because backscattering of laser light into the counter-propagating cavity mode can introduce frequency noise. The NPRO is intrinsically unidirectional because it acts like an optical diode consisting of a polarizer, a wave plate and a Faraday rotator: The polarizer is the polarization-dependent output coupler reflectivity. The "wave plate" results from the beam path, which is non-planar and therefore yields a net polarization rotation. The "Faraday rotator" results from the Nd:YAG crystal (which has a positive Verdet constant) being placed in a static magnetic field.

fixed polarization

unidirectional

noise properties

Because of its monolithic design, the NPRO laser cavity is highly intrinsically stable. Correspondingly, also the laser frequency is highly stable on short time scales, i.e. characterized by low frequency noise at sideband frequencies of kHz or higher. Even on much slower timescales, the laser frequency is relatively stable: In my experience, the unlocked laser fluctuates by at most some MHz on a timescale of seconds. In addition, the temperature of the laser crystal is actively stabilized such that long-term drifts (over minutes) are also very small (again on the order of some MHz).

long-term stability

frequency tunability

In our experiments, we need to precisely control the laser frequency. First, to tune the laser to one of the resonances of the optomechanical

cavity. This requires slow (sub-Hz bandwidth) tunability over a range of some GHz. Then, to lock the laser to the jittering optomechanical cavity resonance, which requires fast (kHz bandwidth) tunability over a range of some MHz.

slow tuning via temperature

fast tuning via laser PZT

For slow tuning of the Prometheus (over a range of 30 GHz and with a bandwidth on the order of Hz) we change the temperature of the laser crystal. For fast tuning (over a range of 200 MHz and with a bandwidth of some 10 kHz) we apply high voltage to a PZT attached to the laser crystal [Gmb03].

further references

Nd:YAG NPROs such as the Prometheus are widely used, for example as seed lasers for gravitational wave detectors [Zaw+02]. The properties of Nd:YAG NPROs have therefore been studied in detail [KB85; KNB87; CK91], in particular, their noise performance, noise couplings [Que03] and stabilization [Bro99; Heu+04]. The specific design of the Prometheus is based on [Fre+93; FTW95].

3.1.2 *Filter cavity*

noise requirements for entanglement

Even though the classical laser noise of the Prometheus is intrinsically low, it is still too high for the purpose of the entanglement experiment. For this experiment, we need the amplitude quadrature x and phase quadrature y of the laser light to be dominated by photon shot noise.

Let us denote the NPS for the amplitude and phase quadrature of a hypothetical laser beam without classical noise by $S_{xx}^{(0)}(\Omega)$ and $S_{yy}^{(0)}(\Omega)$, respectively—in contrast to $S_{xx}(\Omega)$ and $S_{yy}(\Omega)$ for the actual beam which also carries classical laser noise. Using this terminology, we can define the "classical" amplitude and phase NPS $S_{xx}^{(\mathrm{cl})}(\Omega)$ and $S_{yy}^{(\mathrm{cl})}(\Omega)$ as the difference between the full NPS and that of the idealized beam:

$$S_{xx}^{(\mathrm{cl})}(\Omega) \equiv S_{xx}(\Omega) - S_{xx}^{(0)}(\Omega),\ S_{yy}^{(\mathrm{cl})}(\Omega) \equiv S_{yy}(\Omega) - S_{yy}^{(0)}(\Omega). \tag{3.1}$$

shot noise limitation

Then, we can express the requirement of shot noise limitation by

$$S_{xx}^{(\mathrm{cl})}(\Omega),\ S_{yy}^{(\mathrm{cl})}(\Omega) \overset{!}{\ll} S_{xx}^{(0)}(\Omega) = S_{yy}^{(0)}(\Omega). \tag{3.2}$$

power dependence

Note that, for both phase and amplitude quadrature, classical noise depends quadratically on the optical power, whereas quantum noise power depends only linearly on it:

$$S_{xx}^{(\mathrm{cl})}(\Omega),\ S_{yy}^{(\mathrm{cl})}(\Omega) \propto P_{\mathrm{opt}}^2, \tag{3.3}$$

$$S_{xx}^{(0)}(\Omega),\ S_{yy}^{(0)}(\Omega) \propto P_{\mathrm{opt}}. \tag{3.4}$$

Consequently, "shot noise limitation" as defined in (3.2) is a power-dependent property and is easier to achieve at low optical powers.

frequency dependence

The classical noise power $S_{xx}^{(\mathrm{cl})}(\Omega)$ and $S_{yy}^{(\mathrm{cl})}(\Omega)$ also depends strongly on the sideband frequency Ω and is typically highest at low frequencies, whereas shot noise is independent of sideband frequency. Therefore, shot noise limited beams are much easier to achieve at high sideband frequencies. Relevant for us are sideband frequencies close to the frequencies of the mechanical modes of interest (between some 100 kHz and several MHz).

laser noise suppression

For the optical powers we need to use in the entanglement experiment (some 100 µW) and at sideband frequencies below 1 MHz, the unfiltered laser is far from being shot-noise limited (see Figure 3.2). Therefore, we filter the laser using a narrow-band filter cavity with a HWHM-linewidth of $\kappa_{\mathrm{FC}} \simeq 50\,\mathrm{kHz}$. A single pass through the filter cavity yields, at sideband frequencies $\Omega \gg \kappa_{\mathrm{FC}}$, a quadratic suppression[15] of the classical laser noise power (proportional to $\kappa_{\mathrm{FC}}^2 \Omega^{-2}$).

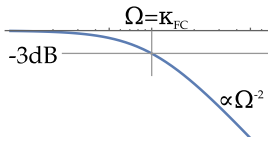

[15] *Quadratic suppression after single pass*

We use a triangular filter cavity,[16] whose design is described in detail in the PhD thesis of Hannes Böhm [Böh07]. The body of the cavity is machined from a monolithic block of Invar. It holds two flat mirrors which serve as in- and output coupling mirrors and a slightly curved end mirror, mounted on a PZT stack to allow locking the filter cavity to the laser.

[16] *Triangular filter cavity:*

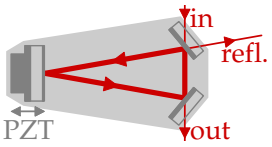

polarization-dependent transmission and finesse

Because, in this triangular design, the laser beam hits the in- and out-coupling mirrors under a highly oblique angle, the transmissivities of the in- and out-coupling mirrors differ by more than a factor of ten between H- and V-polarized light (see Table 3.1). This leads to a polarization-dependent finesse and linewidth (again, with differences of more than a factor of ten). Additionally, there is a birefringent splitting of the cavity resonances for the H- and V-polarization. Therefore, we can lock the filter cavity to one or the other polarization and thereby choose between two different filter cavity linewidths which we refer to as the "high finesse (HF) mode" and the "low finesse (LF) mode", respectively.

reduced transmission in high-finesse mode

For the entanglement experiment, we use the filter cavity in HF mode. Note that, in HF mode, power transmission is much smaller than in LF mode (see Table 3.1). This is because the ratio of transmission losses through the input-/output-coupling mirrors to the remaining round-trip losses is much smaller in HF than in LF mode.

alignment using the low-finesse mode

Fortunately, we can use the filter-cavity in the low-finesse mode during alignment because the transmitted beam of the low-finesse mode is geometrically indistinguishable from that of the high-finesse mode. Working in the low-finesse mode is more convenient for alignment because the filter cavity yields more optical power and is also easier to lock in this mode.

double-pass filtering

Another advantage of the triangular filter cavity is that it can easily be used in a double-pass configuration [HR05] in order to achieve an even stronger quartic suppression[17] of high-frequency noise. We im-

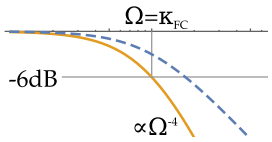

[17] *Quartic suppression after double pass*

PARAMETER	LOW-FINESSE	HIGH-FINESSE
Power transmission (resonant),		
single pass	69 %	21 %
double pass	43 %	4.7 %
HWHM-line width $\kappa_{FC}/2\pi$	650 kHz	48 kHz
Free spectral range ν_{FSR}	0.50 GHz	0.50 GHz
Finesse $\mathcal{F}$	380	5200
Power transmission $T_{in} = T_{out}$ of in- and output coupler	6.8 ‰	0.28 ‰
All other round-trip losses T_{loss}	2.8 ‰	0.65 ‰

Table 3.1. Parameters of the filter cavity. Power transmission was measured directly. κ_{FC} inferred from noise suppression measurements (see Figure 3.4). ν_{FSR} calculated from nominal round-trip length $p = 60\,\text{cm}$. $\mathcal{F}$ calculated from ν_{FSR} and κ_{FC}. Transmittivities T_{in}, T_{out} for in- and output coupling mirrors and remaining round-trip losses T_{loss} calculated from $\mathcal{F}$ and single-pass power transmission (assuming $T_{in} = T_{out}$).

plement double-pass filtering as sketched in Figure 3.1: We reflect the transmitted light back into the filter cavity using a flat mirror directly behind the output coupling mirror of the filter cavity. Thereby, we subject the laser light to a second independent filtering step. The reflected light propagates in the opposite direction inside the filter cavity and leaves the filter cavity in coincidence with the incoming beam but propagating in the opposite direction. A simple optical diode built from a quarter-wave plate, a Faraday rotator, and a polarizing beam splitter (PBS) is then sufficient to separate the (unfiltered) incoming beam, from the (doubly filtered) returning beam. In a linear cavity, we would not be able to implement double-pass filtering in this way because the returning beam would geometrically coincide with the directly reflected beam. In the triangular cavity, however, the directly reflected beam is reflected under an oblique angle and is therefore spatially separated from the doubly filtered beam.

In the following, I present measurements of the amplitude noise (Section 3.1.3) and frequency noise (Section 3.1.4) of the laser—unfiltered, as well after single- and double-pass through the filter cavity.

3.1.3 *Amplitude noise*

measurement technique

We measure the amplitude noise of our laser using direct detection on the photodetectors of our homodyne detectors. This yields the combined classical amplitude noise and shot noise. To obtain the NPS of only the classical amplitude noise we subtract the shot noise

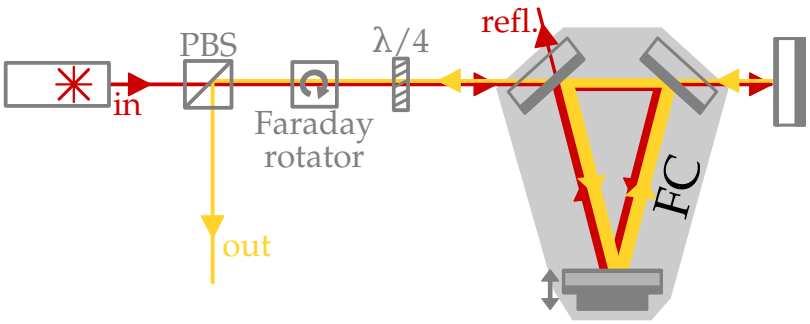

Figure 3.1. Triangular filter cavity in double-pass configuration. After the first pass (red lines) through the filter cavity (FC), the light is reflected back into the FC to complete a second filtering step (yellow). The doubly filtered beam is spatially separated from the incoming beam using an optical diode—a quarter wave plate ($\lambda/4$), a Faraday rotator, and a PBS. The error signal for locking the filter cavity is generated from the light reflected at the input coupler in the first pass.

NPS, which we measure separately using the difference current from two balanced detectors. After subtraction of the shot noise, we divide by the shot noise NPS to obtain the classical amplitude noise NPS in units of shot noise. This also takes care of frequency dependencies of the photodetector gain. All measurements are corrected for electronic dark noise. For more details on the amplitude noise measurements, see [Wie+15, Supplemental Material, sec. II.A.2].

classical amp. noise referenced to shot noise at 1 mW

Amplitude noise levels are reported in units of shot noise at 1 mW. A classical noise level of 10 dB at sideband frequency f, for example, means that classical amplitude noise is ten times stronger (in power density) at frequency f than shot noise, for a 1 mW beam. In fact, I measured at 15 mW optical power and rescaled the results to the noise level at 1 mW in order to increase measurement precision.

3.1.3.1 *Unfiltered amplitude noise*

unfiltered laser dominated by classical amplitude noise

The classical amplitude noise of the unfiltered, free-running (i.e., unlocked) laser is shown in Figure 3.2. For 1 mW optical power, classical amplitude noise of the unfiltered laser is much higher than shot noise from DC to around 5 MHz, even with the noise eater running. In the entanglement experiment, we typically use at most some 100 µW to drive the optomechanical cavity. But even for 100 µW—which corresponds to a factor of ten reduction in the ratio of classical to shot noise, compared to Figure 3.2—the unfiltered laser is not shot noise-limited below 4 MHz. Therefore, we need to filter our laser before we can hope to measure quantum entanglement. Below, I present measurements of the classical amplitude noise after single-pass and double-pass filtering (Section 3.1.3.3). These serve as input for constructing suitable noise models for the Kalman filter, as well as for simulations of the entanglement experiment. I also evaluate the trans-

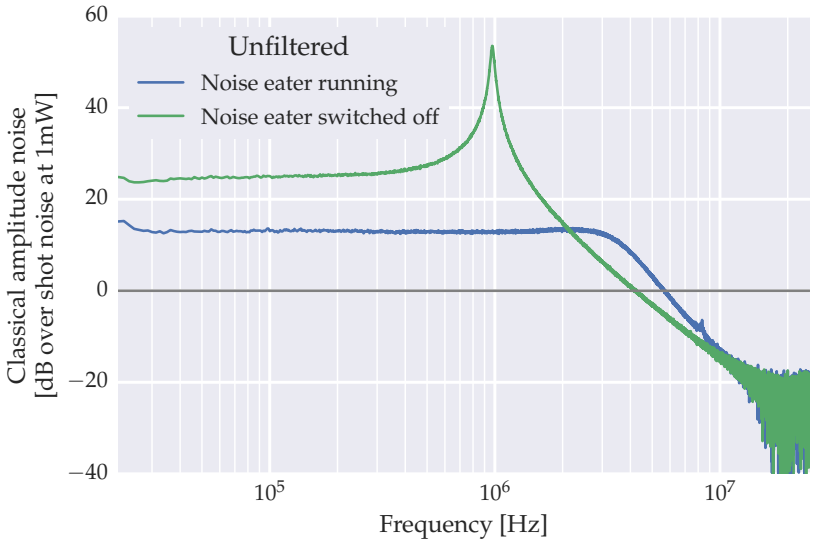

Figure 3.2. Classical amplitude noise of the unfiltered laser with noise eater (blue) and without it (green), in units of shot noise at 1 mW (gray line). Both with and without the noise eater, a broad classical noise background extends from DC to around 3 MHz. The noise eater reduces classical noise by around 10 dB at low frequencies and by around 40 dB at the frequency of the relaxation oscillation peak (roughly 1 MHz).

fer function of the filter cavity (Section 3.1.3.3). Some additional amplitude noise plots are provided in the appendix, in Section B.1.

3.1.3.2 *Amplitude noise suppression*

Figure 3.3 shows the effect of the filter cavity on the classical amplitude noise—for both the high-finesse and low-finesse mode, and for a single pass, as well as a double pass. As expected, noise at high sideband frequencies is removed most effectively by a double pass through the high finesse filter cavity;at 1 mW, the resulting beam is shot noise limited above 200 kHz. In theory, the double pass should significantly outperform the single pass at high sideband frequencies. In practice, however, the double pass is only slightly better than the single pass (see Section B.1.2 for more on this). Both high finesse filter options are significantly better than any of the low finesse filter options.

shot noise limited after high finesse filter cavity

In all cases, the filter cavity adds significant amounts of amplitude noise at very low frequencies (below 100 kHz). This is most likely due to an unstable lock of the filter cavity to the laser (see Section B.1.1 for some ideas regarding this effect).

added low-frequency noise

3.1.3.3 *Filter cavity transfer function*

Figure 3.4 shows the suppression of classical amplitude noise—defined

noise suppression curves

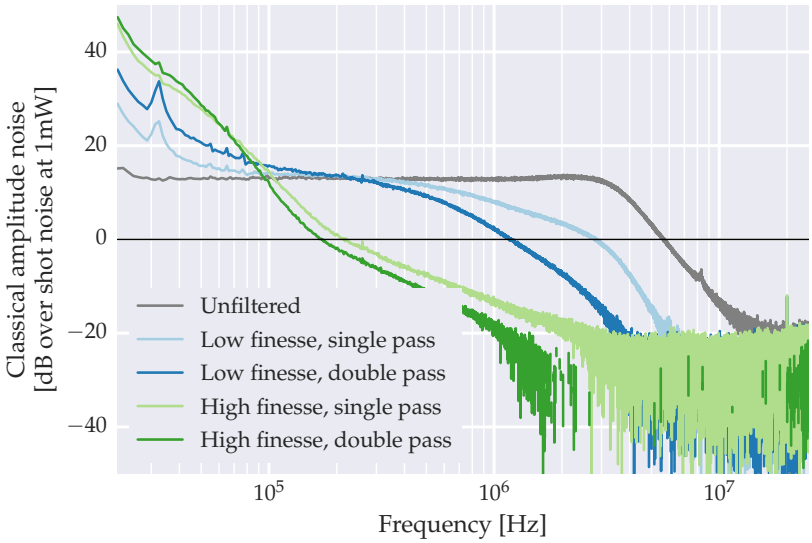

Figure 3.3. Classical amplitude noise for the unfiltered laser and the different filter options. At high frequencies, above roughly 100 kHz, amplitude noise is reduced by filtering and is smaller for high-finesse compared to low-finesse filtering and for double-pass compared to single-pass filtering. At low frequencies, amplitude noise is increased by filtering and the ordering of the different filter options with respect to resulting noise levels is exactly inverted. Note that the laser was free-running and the noise-eater was switched on. The measurement noise floor at around −20 dB results from shot noise.

as the ratio of filtered to unfiltered noise power spectral density—due to a single pass through the filter cavity. The theoretical expectation for the noise suppression at sideband frequency Ω assuming a cavity linewidth κ_{FC} is given by

$$\frac{1}{1+(\Omega/\kappa_{\mathrm{FC}})^2}, \tag{3.5}$$

which is the square of the magnitude of the filter cavity transfer function [see e.g. BTD01]. The filter cavity line width κ_{FC} (the only free parameter of the transfer function) has been determined by fitting the observed suppression at higher frequencies, yielding $\kappa_{\mathrm{FC}} = 2\pi \times 650\,\mathrm{kHz}$ for the low-finesse filter cavity and $\kappa_{\mathrm{FC}} = 2\pi \times 48\,\mathrm{kHz}$ for the high-finesse filter cavity. Expected and observed suppression agree very well above 200 kHz. At lower frequencies, we observe a deviation from the expected suppression due to added noise, which is likely caused by an unstable lock of filter cavity to laser (see Section B.1.1).

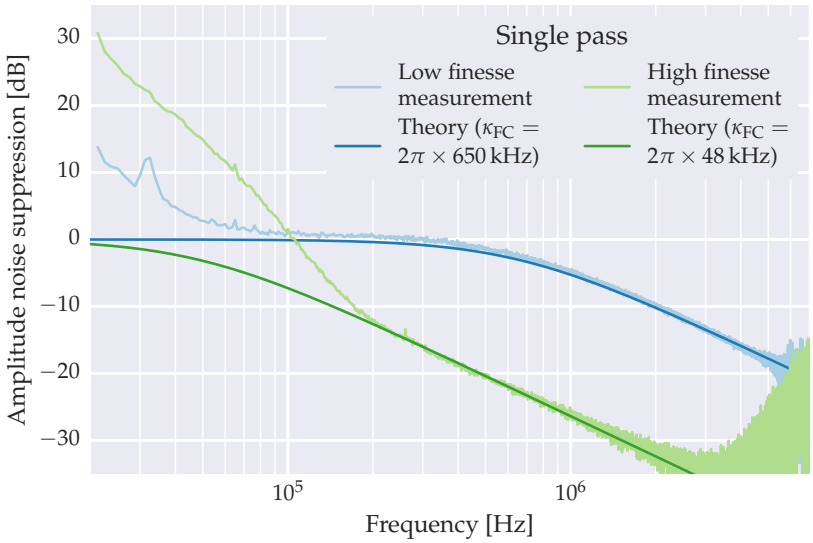

Figure 3.4. Amplitude noise suppression for single-pass filtering. Green and blue traces show measurements (light) and theory (dark) for the filter cavity in low-finesse and high-finesse mode, respectively. Below 200 kHz, the measured noise suppression is much smaller tan expected. Below 100 kHz, the filter cavity even adds amplitude noise, probably because of an imperfect lock of the filter cavity to the laser (see main text). At high frequencies, the measurements of the noise suppression are limited by shot noise.

3.1.4 *Frequency noise*

To measure the laser frequency noise we send the laser light onto a fiber-based Mach–Zehnder interferometer (MZI) with unequal arm lengths.[18] This interferometer converts frequency noise at its input into differential phase noise at its output. The measurement technique (sometimes also referred to as "delayed self-homodyning") is described in more detail in the appendix (Section B.3). Here, I present only the main results. Some additional plots of frequency noise and frequency noise suppression are provided in the appendix (Section B.2).

Note that frequency noise is given in units of $\mathrm{Hz}/\sqrt{\mathrm{Hz}}$ (hence as noise *amplitude* spectral densities), whereas noise suppression is given in units of dB (as suppression in noise *power*). Every measurement has been performed for up to three arm length differences of the MZI and independently calibrated. Hence, we obtain up to three independent measurements of the frequency noise. To give an idea of the systematic uncertainties, I plot all noise spectral densities in this section as a band between the minimal and maximal values across all measurements. Of course, this does not prove that there are no systematic errors larger than the indicated spread.

[18] *MZI with unequal arm lengths:*

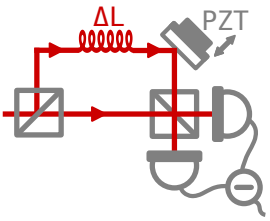

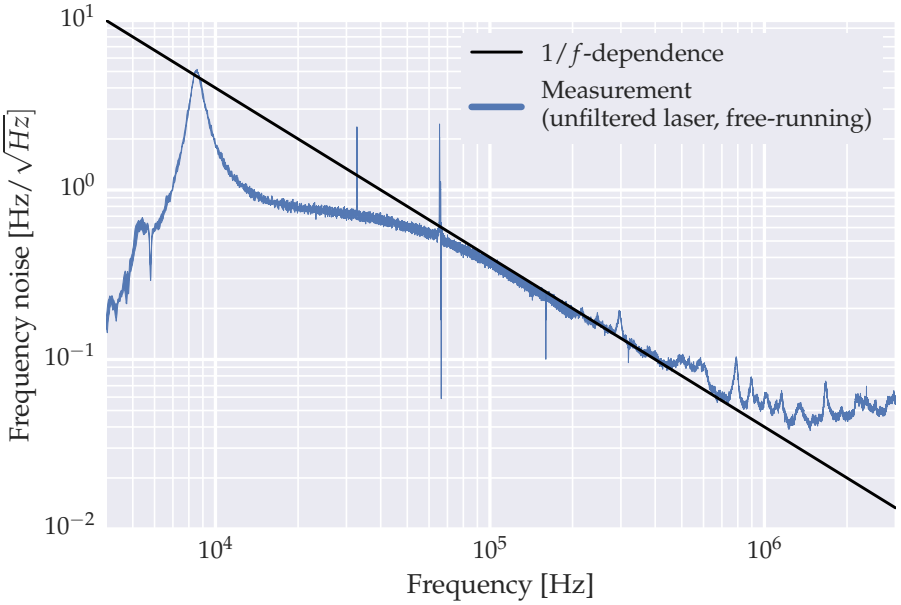

Figure 3.5. Frequency noise of the free-running laser (blue). Between 100 kHz and 1 MHz, the expected $1/f$-dependence (black) of the frequency noise is observed. Below 100 kHz the frequency noise is suppressed due to the interferometer lock, which acts as a high-pass filter.

3.1.4.1 *Unfiltered laser*

Figure 3.5 shows the frequency noise of the unfiltered (free-running) laser. Up to around 1 MHz we observe a $1/f$-dependence, consistent with the frequency dependence measured in [Trö+09].[19] At low frequencies ($\ll$ 100 kHz), this behavior is masked by the lock of the Mach-Zehnder-interferometer used for the frequency noise measurement. This lock stabilizes the relative phase difference between the two interferometer arms at low frequencies and thereby acts like a high-pass filter in our frequency noise measurement.

[19] *The measurements in [Trö+09] do not extend beyond* 1 MHz.

Note that I found the frequency noise to have roughly 4 times larger amplitude than specified by the manufacturer's customer support (the latter being consistent with measurements on a similar NPRO laser reported in [Trö+09]). As a consistency check, we can look at the sideband cooling performance which can be limited by classical frequency noise: A given frequency noise level (close to the mechanical resonance) implies a minimum for the phonon number which can be achieved by sideband cooling [RA09]. Our laser was previously used to demonstrate sideband cooling to about 30 thermal phonons [Grö+09b]. Assuming the experimental parameters of [Grö+09b], I obtain a frequency-noise limited thermal phonon number of $\sim$ 251, inconsistent with the cooling to $\sim$ 30 thermal phonons. Assuming instead the 4 times lower noise level specified by the manufacturer, I obtain a minimal phonon number of $\sim$ 16, consistent with [Grö+09b].

Unfortunately, I cannot resolve this inconsistency: I have performed the noise measurements and calibrations as carefully as possible but, of course, cannot completely exclude a systematic error in the measurement. On the other hand, our laser has been in heavy use for roughly ten years and it is not inconceivable that the noise performance did indeed degrade significantly over these years.

3.1.4.2 *Frequency noise suppression*

Figure 3.6 shows how the filter cavity reduces classical frequency noise. As expected, frequency noise at high sideband frequencies is reduced most effectively by a double pass through the high finesse filter cavity. Contrary to expectations, the double pass is only marginally better than the single pass (in high finesse mode), however, and the advantage vanishes for sideband frequencies larger than 200 kHz. At these frequencies, however, already the single pass (in high finesse mode) starts to deviate from the expectation (see plots of the measured and expected noise suppression in Figure B.5). This suggests that both high finesse measurements are limited by a common measurement noise background above 200 kHz. The measurement noise floor is likely given by background phase noise induced by the delay fiber.

Therefore, the measurements for the high-finesse filtered frequency noise are upper limits on the actual frequency noise above 200 kHz.[20] Since even with these (likely overly pessimistic) measured noise levels, entanglement detection is possible according to the simulations in Section 5.4.2.2, I did not investigate the limiting noise background further.

[20] *Note however that, for double-pass high-finesse filtering, also the amplitude noise suppression is weaker than expected (see Section B.1.2). Hence, it is possible that we also do not reach the expected suppression in phase noise.*

3.1.4.3 *Filtering of actuator inputs*

It is important to realize that the noise performance of a laser system can easily be spoiled. Particular attention has to be paid to all actuators: Their inputs must be carefully filtered such that only the desired feedback is achieved and no unwanted noise is introduced at higher frequencies. In general, the faster the actuator, the more critical for noise performance at high sideband frequencies.

The most critical actuator in our case is the laser PZT, which we actuate to lock the laser frequency to the optomechanical cavity. The actuation signal is produced by a digital PID, HV-amplified and then fed into the laser PZT using a BNC connection. Dark noise of the locking electronics or the HV amplifier can be enough to induce substantial added frequency noise.

As an illustration, Figure 3.7 compares the frequency noise of the laser with the laser PZT connected to the HV amplifier (without filters and without active feedback) to the case of a disconnected laser PZT.

locking electronics can add noise at PZT resonances

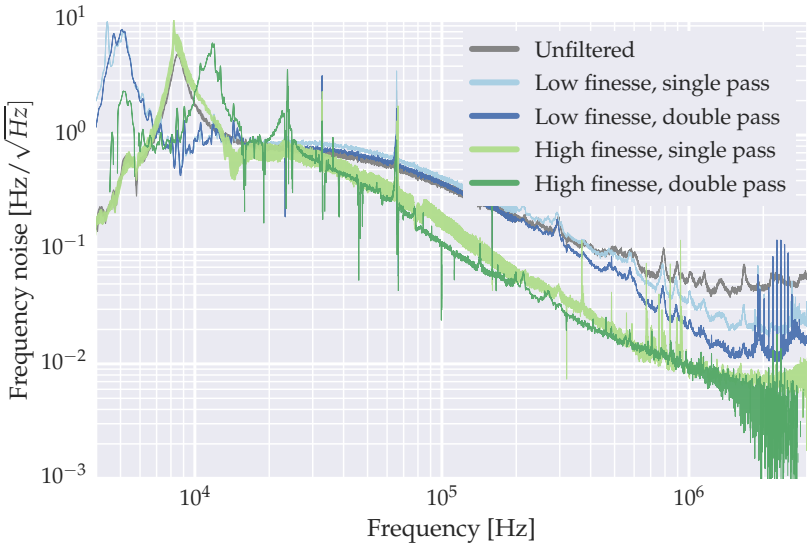

Figure 3.6. Classical frequency noise for the unfiltered laser and the different filter options in comparison. Above roughly 40 kHz (500 kHz), frequency noise is reduced by filtering with the high finesse (low finesse) filter cavity and is smaller for high-finesse compared to low-finesse and for double-pass compared to single-pass filtering. At frequencies above 200 kHz, the high finesse measurements are limited by a common measurement background, likely caused by phase noise induced in the delay fiber.

The difference is clearly visible and significant, with an added noise of more than 10 dB for some resonances of the laser PZT.

This added high-frequency noise must be taken care off by carefully filtering the feedback voltage right before the actuator. We implement a suitable filter by adding a large resistance (154 kΩ) before the laser PZT, which, together with the capacitance of the PZT (nominally 2.5 nF) forms a low-pass filter cutting off at roughly 0.4 kHz.

3.1.4.4 *Locking-induced noise*

Does filtering the actuation signal prevent the introduction of frequency noise when locking the laser to the optomechanical cavity? To answer this question, we compare the out-of-loop frequency noise for the locked and unlocked laser after a single pass through the high-finesse filter cavity. Figure 3.8 shows that we are not perfectly successful in filtering the feedback voltage such that some added noise remains in the range from 500 kHz to 1 MHz. Nevertheless, the discrepancy between locked and unlocked case is much less drastic than the discrepancy between the connected and the disconnected PZT in Figure 3.7. Hence, to a large extent, we achieve the desired effect by filtering the actuation signal.

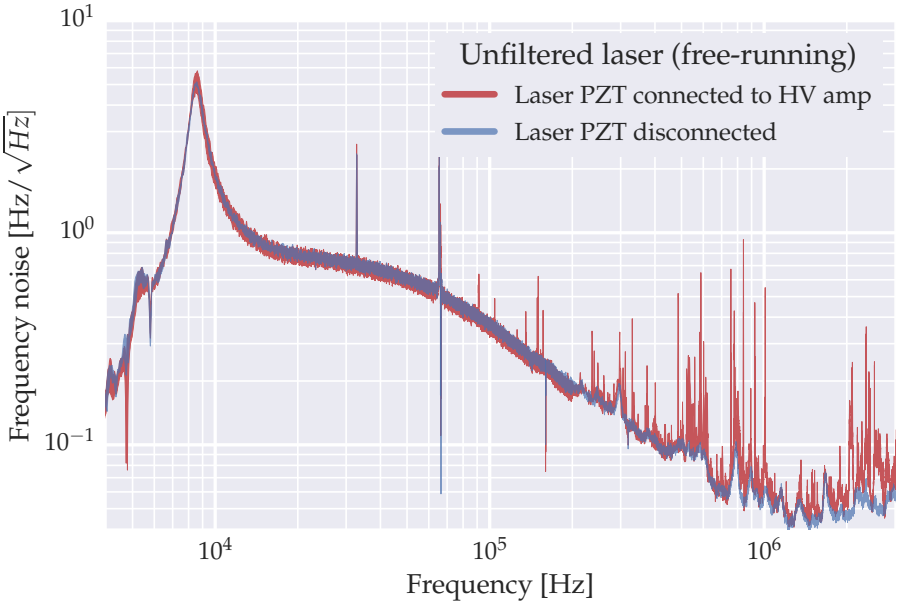

Figure 3.7. Effect of an unfiltered actuator input on the frequency noise of the unfiltered, free-running laser. When the laser PZT is connected to a high-voltage amplifier with nominally constant output (red), we observe many additional sharp noise peaks above 100 kHz compared to the case of a disconnected laser PZT (blue, semi-transparent). We attribute this added noise to mechanical resonances of the laser PZT being excited by the dark noise of the amplifier. Careful filtering of the feedback signals is therefore crucial.

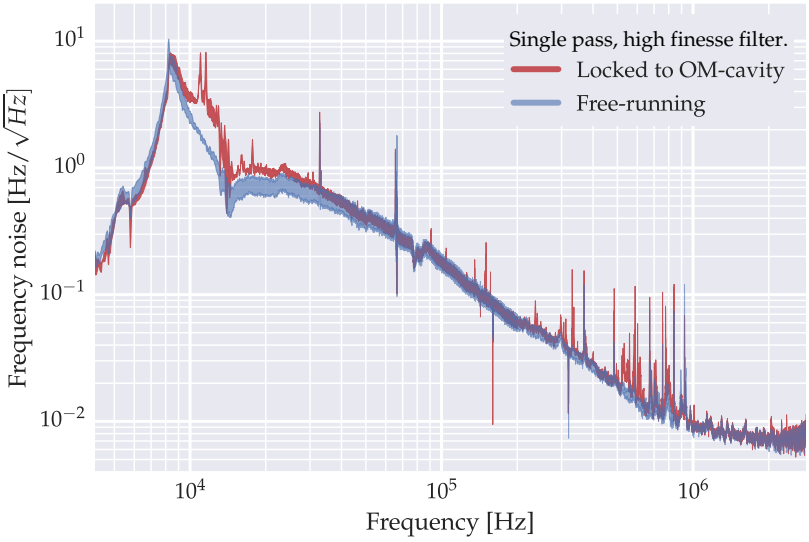

Figure 3.8. Effect of locking the laser to the optomechanical cavity on the out-of-loop frequency noise (after single-pass through the high-finesse filter cavity). Frequency noise for the locked (red) and unlocked (blue) laser coincides for most sideband frequencies. At low frequencies (around 10 kHz), acoustic vibrations lead to frequency fluctuations of the optomechanical cavity which are then imparted to the laser via the lock loop. At higher frequencies, between 500 kHz and 1 MHz, we observe some added noise due to excited resonances of the laser PZT.

3.1.5 *Noise models for simulations and state estimation*

For the simulations of the entanglement experiment (Section 5.4.2.2), as well as for the Kalman filter (Section 4.4), we need realistic models of the laser noise—state space models whose spectral response is designed such that their output (when driven with white Gaussian noise) has the measured frequency dependence [see Wie+15, Supplemental Material, sec. I.B., II.B., for more information]. For the simulations of the entanglement experiment, we use a model for the amplitude and frequency noise based on the measurements after double-pass high-finesse filtering (dark green spectra in Figure 3.3 and Figure 3.6). For the state estimation experiment, we worked with the unfiltered laser beam, hence the amplitude and frequency noise model in this case matches the measurements on the unfiltered beam (gray spectra in Figure 3.3 and Figure 3.6). Note that, for the Kalman filter, the noise models were actually identified using measured time traces not spectra, as explained in Section 4.3.2.

noise model for entanglement simulations

...and for Kalman filtering

3.2 DETECTION

[21] *Optical diode for separating incoming from reflected light*

To obtain information about the state of the mechanical oscillator, we measure light leaking out of the optomechanical cavity. Our optomechanical cavities are nearly one-sided (i.e. strongly over-coupled) such that most of the light leaks out on the input coupler side and almost no light is transmitted. Therefore, we measure only the light reflected from the input coupler, which we separate from the incoming light using a Faraday rotator, a quarter wave plate and a PBS.[21] A small fraction (usually, on the order of a µW) of the reflected light is split off and detected directly on a fast photo-diode to generate the PDH error signal (see Section 3.3.2). The rest of the reflected light is measured using homodyne detectors.

3.2.1 *Homodyne detectors*

Our homodyne detection setup are sketched in Figure 3.9. The signal beam (optical power between some µW and some 100 µW) is overlapped with a local oscillator (LO) beam (power typically 5 to 15 mW) on a 50:50 beam splitter. The relative phase of LO and signal is stabilized by feedback to a mirror mounted on a PZT—to 0° (90°) for measuring the amplitude (phase) quadrature. The interference of signal and LO is detected on two fast photodetectors (described in more detail in Section 3.2.2).

post-processing of detector signals

The photovoltages of the two detectors are subtracted with an analogue circuit, then amplified using a fast voltage amplifier (DHPVA-200 by FEMTO) with a bandwidth of 200 MHz and a (power) gain

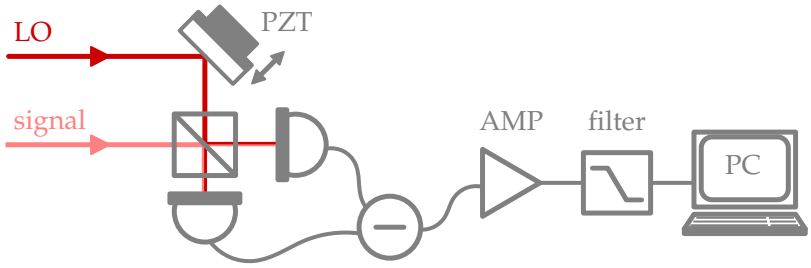

Figure 3.9. Homodyne detection setup. Two balanced photodetectors measure the interference of signal and local oscillator (LO) beam. The relative phase of the two beams is stabilized (at low frequencies) using a mirror mounted on a piezo (PZT). The difference of the photodetector outputs is amplified, low-pass-filtered and digitized.

between 10 dB and 60 dB. The resulting signal must be low-pass filtered to suppress a strong modulation at 20 MHz,[22] which would otherwise consume too much of the dynamic range of our data acquisition (DAQ)-system. Therefore, the amplifier output is filtered with a passive 12 MHz-low-pass filter. Finally, the filtered voltage is digitized with a fast DAQ system (PXIe5122 from National Instruments) at a sampling rate of roughly 100 MHz and a resolution of 14 bit and streamed to a RAID-system.

[22] *The 20 MHz modulation is required for the PDH error signal (see Section 3.3.2).*

Note that, for the state estimation experiment, the 50:50 beam splitter was emulated using polarization optics: In this scheme, LO and signal are initially orthogonally polarized—one in H, the other in V. Next, both beams are combined into the same spatial mode using a PBS. Using a half-wave plate (HWP), their polarizations are rotated by 45° to (H+V) and (H-V). The signal and LO beams, which are now both diagonally polarized, can then both be split 50:50 into H and V on a second PBS such that they interfere on both detectors.

beam recombination using polarization optics

3.2.1.1 *Phase quadrature measurement*

To measure relative phase fluctuations between LO and signal beam, we stabilize the relative phase of the two beams to 90° (at low frequencies). If the dominant contribution to the relative phase fluctuations is due to the signal beam, this amounts to a measurement of the phase quadrature of the signal beam. There are two relevant noise contributions in this measurement: Amplitude noise and common phase noise [see Wie+15, Supplemental Material, A.II.3].

relevant noise contributions

The contribution of amplitude noise to the measured signal is negligible if the two detectors are carefully balanced, i.e. if they detect exactly the same optical power. For careful balancing, amplitude noise is suppressed by more than 45 dB as compared to the unbalanced case. Note that balancing also requires equal photo-detector gains and photo-diodes with matching quantum efficiency [see Böh07, section 2.3.1].

amplitude noise

common phase noise

Common phase noise of LO and signal only contributes to the signal if there is a delay between LO and signal beam, i.e. if the optical path lengths of signal and LO are different. This is because common fluctuations in phase correspond to common fluctuations in instantaneous frequency and, without a delay between LO and signal, these fluctuations occur simultaneously and cannot be measured with a photodetector. By matching the relative path length of the LO and signal beam to within some cm, we can completely suppress the contribution of common phase noise in the frequency range of our interest. In practice, we minimize the path length difference as follows: We modulate the laser frequency by applying a modulation signal to the laser PZT, thereby creating a strong common phase noise signal on the LO and signal beam. Then we minimize the resulting modulation of the homodyne difference signal by adjusting the relative path length.

matching path lengths for signal and LO

3.2.1.2 *Amplitude quadrature measurement*

By locking the relative phase of LO and signal beam to 0°, we can measure the amplitude quadrature of the signal beam [see Wie+15, Supplemental Material, A.II.3]. In this case, we are not sensitive to common or relative phase noise. But we *are* sensitive to amplitude noise of the LO (which we were able to avoid in the phase quadrature measurement by balancing the detectors).

amplitude noise

For the state estimation experiment, this additional noise is not a problem as long as it is taken into account in the state space model describing the measurement. For the entanglement experiment, however, we want to avoid this noise. We therefore filter the laser such that its amplitude quadrature is shot noise limited at the optical power detected by the photodetectors (up to 10 mW) and for the frequency range of interest (above 400 kHz); see Figure B.2.

3.2.2 *Photodetectors*

Our photodetectors (consisting of photodiodes and detector electronics) have to satisfy two main requirements. They need to be fast enough to record the mechanical signals in the range from 0.1 to 10 MHz and they must provide a good signal-to-noise ratio. For the photodiodes, this means a large bandwidth and a high quantum efficiency. Large-area InGaAs photodiodes satisfy these requirements. For the state estimation experiment, we used the JDSU ETX 500, which have a large bandwidth (due to their low capacitance of nominally below 50 pF) and a reasonably high quantum efficiency (measured to be between 80 % and 90 % in [Grö10, Table 4.1]). For the entanglement experiment, we switched to different diodes from Laser Components which achieve even higher quantum efficiencies of around 95 %.

high-efficiency, high-bandwidth photodiodes

detector circuits with low NEP

The detector circuits, on the other hand, need to provide a low noise-equivalent power (NEP). Our detector circuits, which were designed by Hannes Böhm [Böh07, section 2.3.1], achieve this by splitting the photodiode voltage at ∼30 kHz into a DC and an AC component. This allows us to strongly amplify the weak AC component without saturating the amplification circuit with the DC component. Thereby, dark noise can be overcome already for low optical powers of around 1 mW (typically, we use at least 5 mW LO power).

3.3 LOCKING

In our experiments, there are two different types of locks: Homodyne locks which ensure a stable phase between local oscillator and signal light (Section 3.3.3) and cavity locks which ensure a stable relative frequency of the laser and the optical cavities. The cavity locks come in different forms—Pound–Drever–Hall (PDH) lock (Section 3.3.2), Hänsch–Couillaud lock (Section 3.3.1), and tilt lock—but they are all based on the same idea, which I will briefly explain.

basic idea of cavity locks

We want to stabilize the detuning $\Delta \equiv \omega_l - \omega_c$ between laser (frequency ω_l) and cavity (frequency ω_c) to a constant value. To do this, we need an error signal $\epsilon(\Delta)$ which satisfies

$$\epsilon(\Delta) = \text{const} \times \Delta + \mathcal{O}\left(\Delta^2\right), \tag{3.6}$$

i.e., which is proportional to Δ, at least for small Δ. Now consider the laser field before and after reflection at the cavity and, in particular, its carrier components E_0^{in} and E_0^{out} at frequency ω_l. From (2.45) and (2.53) we obtain (in the frame rotating at ω_l)

$$E_0^{\text{out}} / E_0^{\text{in}} = \left(\frac{2\kappa_1}{\kappa - i\Delta} - 1 \right) \tag{3.7}$$

The relative phase $\Delta\phi$ of E_0^{out} with respect to E_0^{in} is therefore[23]

$$\Delta\phi \equiv \arg\left(E_0^{\text{out}} / E_0^{\text{in}}\right) = \frac{\kappa}{\kappa_1^2 - \kappa^2/2}\Delta + \mathcal{O}\left(\Delta^3\right). \tag{3.8}$$

Hence, $\Delta\phi$ satisfies condition (3.6) and therefore qualifies as a good error signal.

But to measure $\Delta\phi$ we need a stable phase reference, i.e. a reference whose phase does not change with the detuning. Components of the reflected light field which are far off-resonant could provide such a stable reference, since their phase does not vary with the detuning. The different cavity locking schemes described below differ only in how they obtain the required off-resonant light fields.

[23] *Phase $\Delta\phi$ of reflected light versus detuning Δ:*

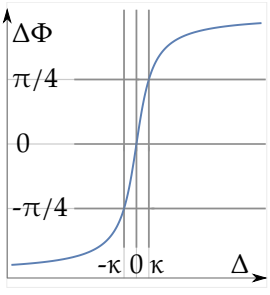

3.3.1 *Hänsch–Couillaud and tilt lock*

Hänsch–Couillaud lock

Our filter cavity (described in Section 3.1.2) is strongly birefringent. We can therefore lock it to the laser using the Hänsch–Couillaud technique [HC80], in which the phase reference is provided by an off-resonant linear polarization mode. If, for example, we lock on the vertically polarized cavity eigenmode, any horizontally polarized light is automatically off-resonant. Using a half-wave plate we can divert a small fraction of the incoming light into the unwanted horizontal polarization. In reflection, we can generate an error signal from the interference of the vertical (resonant) and horizontal (off-resonant) polarization components as follows. We rotate H and V by 45° using another half-wave plate and then project onto H and V again using a PBS. In the output ports of the PBS, the two components interfere dependent on Δ. We subtract the intensities measured in the two output ports which yields an error signal proportional to Δ.

tilt lock

In the state estimation experiment, we use a broad Fabry–Pérot filter cavity to select a particular optical sideband, which is separated from the carrier by several GHz (see Section 3.4.1). To lock this cavity to the desired sideband, we use a tilt lock. In contrast to the Hänsch–Couillaud lock, tilt locking does not rely on birefringence, but on the non-degeneracy of transversal eigenmodes of the cavity. In our case, TEM_{10} is off-resonant when TEM_{00} is resonant, such that we can use TEM_{10} as a phase reference when locking to TEM_{00}. To get some light into TEM_{10}, we displace the beam slightly after mode-matching it to TEM_{00}. To obtain an error signal, we need interference between the reflected TEM_{00}- and TEM_{10}-components. But TEM_{10} and TEM_{00} will not produce an interference signal on a regular detector, since their field distributions are orthogonal (in a plane perpendicular to the propagation direction). Interference between TEM_{00} and TEM_{10} can be observed, however, on a so-called split photodiode, which detects the difference in optical intensity between the left and right half of the diode. The tilt lock is described in more detail in [Grö10, sec. 4.3.2].

3.3.2 *Pound–Drever–Hall lock*

acoustic noise

We need to actively stabilize the laser frequency to the resonance frequency of the OM-cavity because the cavity resonance jitters strongly due to acoustic noise. In our cryostats, the main source of noise is the 1.5 kHz-rotation of the turbo vacuum pump. The resulting jitter of the cavity resonance can be as large as several line-widths of the OM-cavity.

We use a Pound–Drever–Hall lock (PDH) lock [Dre+83a; Dre+83b; Bla01] to stabilize the detuning between laser and optomechanical

cavity. The PDH lock works for any cavity, even if it is not birefringent and all transversal modes are degenerate. It uses optical sidebands at frequencies far from resonance (but in the same spatial and polarization mode) as a stable phase reference for the carrier phase. Since theory and some practical aspects of the PDH lock are discussed at length in [Grö10, sec. 4.3.2], I only sketch the basic idea.

off-resonant sideband as stable phase reference

The optical sidebands for PDH locking are generated by phase-modulating the light sent onto the cavity. If the laser is not resonant with the cavity, the phase-modulation of the incoming beam is partially converted into an amplitude modulation of the reflected beam. Now, crucially, the magnitude and phase of the resulting amplitude modulation depend on the magnitude and sign of the detuning, respectively. This allows us to generate an error signal in the following way. We measure the the amplitude modulation of the reflected beam on a photodetector and determine its phase and magnitude by mixing the photodetector output with the modulation signal which generated the sidebands. After low-pass filtering, this yields a suitable error signal for stabilizing the detuning between laser and cavity.

amplitude modulation dependent on detuning

In our setup, the phase-modulation is achieved using a resonant EOM at 20 MHz. This yields strong sidebands which contain up to 50 % of the optical power. After reflection at the optomechanical cavity, a small part (on the order of a µW) of the light is detected on a fast photodiode (ETX500) mounted directly on a FEMTO DHPCA current amplifier. The amplified detector output is then mixed with the 20 MHz-signal driving the EOM. The low-frequency component of the resulting signal is our PDH error signal: Its magnitude and sign depend on the detuning between carrier light and cavity resonance. Note that we also use the PDH-signal to infer the cavity linewidth: We scan the laser across the cavity resonance, record the PDH-signal and fit it to the expected error signal (with the cavity linewidth as the main free parameter).

implementation of the PDH lock

3.3.3 *Homodyne locks*

To measure the desired quadrature in homodyne detection, we need to stabilize the relative phase $\Delta\phi$ of signal and LO. We achieve this by feedback to a mirror mounted on a PZT in the LO path. Depending on the sign of the feedback, this mirror either shortens or lengthens the optical path of the LO and, thereby, changes $\Delta\phi$. The error signal used for this feedback loop depends on the quadrature we want to measure.

For the phase quadrature measurement, we can simply use the difference I_-^{DC} of the DC outputs of the photodetectors as the error signal. If $\Delta\phi \simeq 90°$ (corresponding to a measurement of the phase quadrature), the DC optical power is the same on both detectors,

phase quadrature

hence $I_-^{\mathrm{DC}} = 0$. If $\Delta\phi$ fluctuates away from 90°, the DC optical powers on the two photodetectors become different such that $I_-^{\mathrm{DC}} \neq 0$. Crucially, the sign of I_-^{DC} depends on the sign of the phase fluctuation which allows us to stabilize I_-^{DC} to zero and thereby stabilize $\Delta\phi$ to 90°. For subtracting the DC voltages from the two detectors, we use an active analogue add/subtract circuit as described in [Böho7, section 2.3.3].

amplitude quadrature

For the amplitude quadrature measurement, on the other hand, we need to stabilize $\Delta\phi$ to 0°. But for $\Delta\phi = 0°$, the interference of signal and LO is perfectly constructive on one detector and perfectly destructive on the other. Hence, $\Delta\phi = 0°$ corresponds to an extremum of I_-^{DC}. But we cannot lock to an extremum of the error signal: Assume $\Delta\phi$ fluctuates to $+1°$ or $-1°$. In both cases, the error signal I_-^{DC} is the same. Hence, we do not know whether to apply positive or negative feedback and, therefore, cannot use I_-^{DC} as the error signal.

PDH lock

Instead, we obtain an error signal using the PDH-technique. The signal beam already carries a 20 MHz phase modulation (for the PDH lock of the laser to the OM-cavity). The corresponding 20 MHz sidebands are far outside the linewidth of the OM-cavity and are therefore directly reflected at the input coupler mirror. These 20 MHz sidebands interfere with the carrier of the LO beam on the homodyne photo detectors. This can be used to stabilize $\Delta\phi$ to 0°, in complete analogy to the stabilization of the laser to the OM-cavity: If $\Delta\phi$ fluctuates away from 0°, the interference between the 20 MHz sidebands and the LO beam yields an amplitude modulation, whose phase and amplitude depend on $\Delta\phi$. By mixing this amplitude modulation with the 20 MHz modulation signal used to produce the PDH sidebands, we obtain an error signal which, for small fluctuations of $\Delta\phi$ around 0°, is proportional to $\Delta\phi$ and can therefore be used for stabilizing to the amplitude quadrature.

3.4 STATE ESTIMATION SETUP

In this section, I describe the specifics of the experimental setup used for the state estimation experiment. In Section 3.4.1, I explain how—in addition to a resonant laser beam—we incorporate a second, red-detuned beam, for which strong coupling can be achieved. I describe the mechanical device used for the state estimation experiment, in Section 3.4.2, and the optomechanical cavity in Section 3.4.3. The experimental setup is also described in some detail in the supplemental material of [Wie+15]. A quick overview of all relevant experimental parameters is provided in Table 3.2 at the end of this section.

3.4.1 *Detuned beam*

State estimation using a Kalman filter is universal in the sense that it is not limited to specific optomechanical parameter regimes (e.g. adiabatic or weak coupling), as long as the interaction is approximately linear (see Chapter 4). To demonstrate this versatility, we applied the Kalman filter to measurements in both the weak and strong coupling regime [Wie+15].

state estimation for weak and strong coupling

In the state estimation experiment, we use a resonant readout beam —a common feature of optomechanical experiments. The optical power of the resonant beam cannot be increased enough, however, to reach strong coupling without making the experiment unstable. To achieve strong coupling, we therefore add a second laser beam which is red-detuned by approximately the fundamental mechanical frequency $\omega_m \simeq 2\pi \times 1.278\,\mathrm{MHz}$. The optical power in this red-detuned beam can be varied from $20\,\mu\mathrm{W}$ to $1.4\,\mathrm{mW}$, corresponding to coupling strengths in between $0.2\,\kappa$ and $1.68\,\kappa$, without making the setup unstable.

detuned beam with tunable coupling

We create the detuned beam as a sideband to the resonant beam using a fiber EOM and optical filtering, as explained in Figure 3.10. The frequency difference of detuned and resonant beam is given by the modulation frequency of the fiber EOM. Hence, if the resonant beam is locked to the cavity resonance, the detuned beam also has a fixed detuning to the cavity resonance. At the same time, the detuning can be changed easily by changing the modulation frequency of the fiber EOM.

generation of the detuned beam

The full two-beam setup is sketched in Figure 3.11 (a). Note that the detuned beam is in the same spatial mode as the resonant beam but orthogonally polarized. After reflection at the optomechanical cavity, both beams are separated using polarization optics and sent to two different homodyne detection setups. A small fraction of the reflected resonant light is split off to generate an error signal for the PDH lock (see Section 3.3.2).

two-beam setup

Note that, in practice, orthogonal polarizations cannot be separated perfectly using polarization optics. Hence, a small fraction of the reflected detuned beam enters the homodyne detection and PDH lock detector of the resonant beam. This contribution from the detuned beam would disturb both the cavity lock as well as the homodyne detection of the resonant beam, if the two beams were only separated by ω_m. To avoid this, the detuning between detuned and resonant beam is set not to ω_m, but to ω_m plus one FSR of the optomechanical cavity (roughly $2\pi \times 15\,\mathrm{GHz}$). Because of this large frequency difference, unwanted interference effects between the two beams occur at frequencies which are not resolved by our detectors.

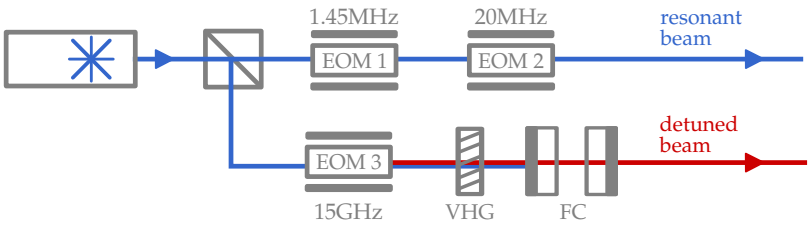

Figure 3.10. Laser beams used for the state estimation experiment. The 1064 nm-light is split into two beams. The resonant beam (blue) is sent through two free-space EOMs: The first (EOM 1) is modulated at 1.45 MHz to provide a calibration tone for the measurements; the second (EOM 2) is resonantly modulated at 20 MHz to create strong sidebands for the PDH-lock of the laser to the optomechanical cavity. The other part of the laser light is sent to a fiber EOM (EOM 3) which is strongly modulated at around 15 GHz. The detuned beam (red) is created there as one of several sidebands of the resonant beam. After filtering the emerging beam with a volume holographic grating (VHG) and a broad-band filter cavity (FC), only the desired sideband remains. The frequency difference of detuned and resonant beam of roughly $2\pi \times 15\,\mathrm{GHz}$ corresponds to the FSR of the optomechanical cavity. Hence, the detuned beam is close to the next longitudinal resonance of the optomechanical cavity, with the exact detuning being determined by the modulation frequency.

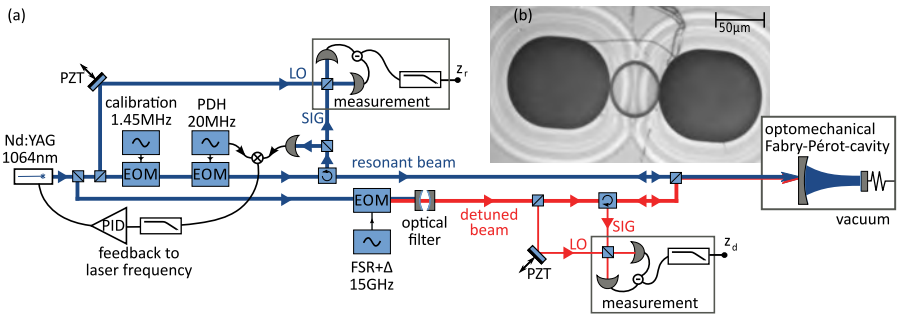

Figure 3.11. Sketch of the experimental setup for the state estimation experiment (a) and optical micrograph of the micro-mechanical oscillator (b). Taken from [Wie+15, Supplemental Material].

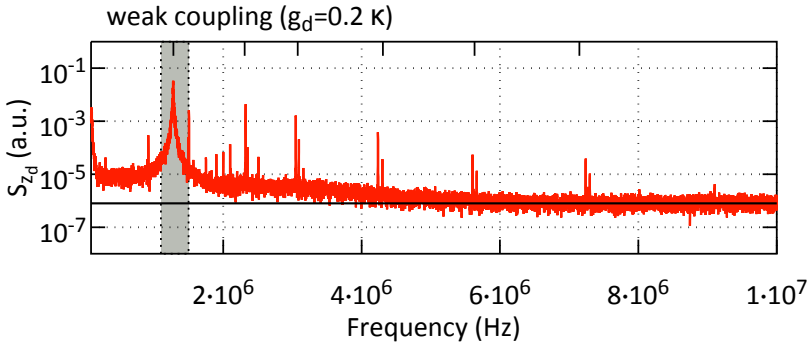

Figure 3.12. Noise power spectrum of the detuned beam showing several mechanical resonances of the doubly-clamped SiN bridge. The broad peak at 1.278 MHz (marked in gray) is caused by the fundamental mechanical mode. Other noise peaks (marked with ticks on the upper horizontal axis) can also be attributed to mechanical modes of the SiN bridge using finite element modeling (see Figure 3.13). The sharp peak at 1.45 MHz (to the right of the fundamental mechanical mode) is a calibration peak. Other unidentified noise peaks are probably due to laser noise. Taken from [Wie+15, Supplemental Material].

3.4.2 *Mechanical device*

SiN bridge with DBR on top

The mechanical device used in the state estimation experiment is a doubly-clamped SiN bridge, shown in Figure 3.11 (b). The SiN bridge carries a DBR with a diameter of 50 µm made from alternating layers of Ta_2O_5 and SiO_2. The device was fabricated by Simon Gröblacher. More details about the fabrication of this mechanical oscillator can be found in [Grö10, sec. 5.2].

mechanical mode structure

Figure 3.12 shows a NPS of the detuned beam. Several peaks can be attributed to mechanical modes: The fundamental mechanical mode at 1.278 MHz and higher mechanical modes at 2.325 MHz, 3.050 MHz, 4.237 MHz, 5.604 MHz, and 7.240 MHz. The fundamental mechanical mode couples most strongly to the intra-cavity mode and, consequently, contributes by far the largest band power to the NPS in Figure 3.12. But some higher mechanical modes between 2 MHz and 8 MHz also interact strongly enough to be relevant for Kalman filtering. In total, eight mechanical modes were taken into account in the Kalman filter.

finite element simulation

To attribute peaks in the NPS to mechanical modes, we use finite element (FEM) simulation of the mechanical device and match simulated eigen-frequencies of the device with observed peaks in the optical NPS. FEM results for some mechanical modes are visualized in Figure 3.13. Note that the FEM results can also be used to predict the coupling of the mechanical modes to the optical intracavity mode. To do this, we need to compute the effective mass of the mode according to (2.69). To this end, we average the displacement caused by a given mechanical mode over the region probed by the optical intra-cavity

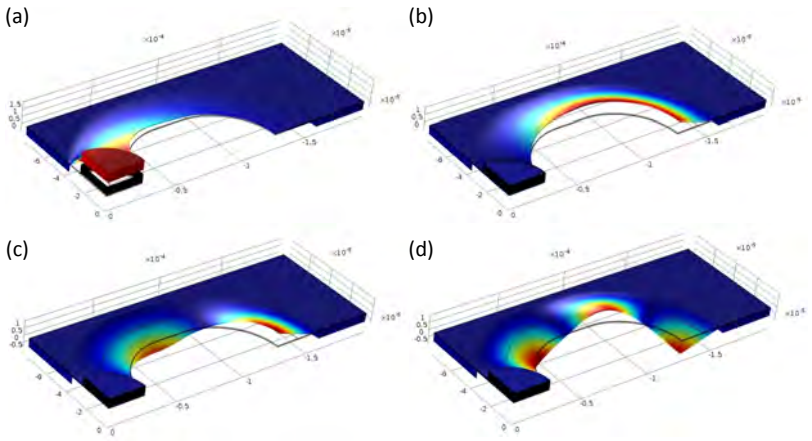

Figure 3.13. Mechanical displacement of the first four mechanical modes of the doubly-clamped SiN-bridge calculated by FEM. Due to two-fold mirror symmetry of these modes only a quarter of the device is shown. The full structure is obtained by mirroring with respect to the two edges facing the viewer. Color maps to absolute displacement with red corresponding to large (absolute) displacement and blue to small. The simulation predicts an eigen-frequency of 1.278 MHz for the fundamental mechanical mode (a) and of 2.31 MHz, 3.08 MHz, and 4.31 MHz for the next three higher modes (b) - (d). Taken from [Wie+15, Supplemental Material].

mode (a small part of the DBR surface). This average displacement is small for all but the fundamental mechanical mode (as illustrated by Figure 3.13), which explains why it shows a much larger optomechanical coupling than the other mechanical modes, and therefore yields the dominating contribution (measured in band power) to the NPS in Figure 3.12.

Note that the fundamental mechanical mode of this device has a very low quality factor of $Q \simeq 4800$ (at room temperature). Hence, this device is unsuitable for demonstrating conditional cooling to the ground state or any type of quantum effect, let alone quantum entanglement. For the restricted purpose of demonstrating optimal state estimation, however, the low quality factor is not a problem.

A big advantage of this device for the purpose of demonstrating optimal state estimation is its relatively small number of significantly interacting mechanical modes. This makes it comparatively easy to create a state space model suitable for Kalman filtering. In contrast, constructing a suitable state space model for a membrane-type oscillator (as used for the entanglement experiment) would be a much bigger challenge since, in this case, a huge number of mechanical modes (at least 50) interact significantly and would have to be taken into account.

3.4.3 *Optomechanical cavity*

cavity parameters

The optomechanical cavity consists of the micro-mirror (sitting on top of the SiN-bridge) as the end-mirror and a macroscopic mirror as the input coupler. The micro-mirror is a flat and highly reflective DBR with a power transmission on the order of a few ppm. The macroscopic input coupler has a radius of curvature of 10 mm and a power transmission of roughly 300 ppm. Total internal power losses except input coupler are below 70 ppm. The cavity is 1 cm long and has a free spectral range of $\nu_{\mathrm{FSR}} \simeq 15\,\mathrm{GHz}$. The HWHM-linewidth is $\kappa \simeq 2\pi \times 436\,\mathrm{kHz} \simeq 0.34 \times \omega_m$, corresponding to a finesse of $\mathcal{F} \simeq 17200$. The cavity is strongly over-coupled with $\kappa_1 \simeq 0.278 \times \omega_m$ and $\kappa_2 \simeq 0.064 \times \omega_m$. It is placed in vacuum ($p \simeq 10^{-5}\,\mathrm{mbar}$) inside a dilution refrigerator, but operated (for the experiment reported in [Wie+15]) at room temperature.

positioning of the mechanical oscillator

The SiN-bridge sits on a Si chip. The chip is mounted on a copper holder which can be moved independently along the cavity axis and laterally using three piezo-based positioners (ANPz101 from attocube). Positioning of the SiN-bridge along the cavity axis allows to fine-tune the cavity length and thereby to change the waist of the cavity mode at the position of the SiN-bridge. This is important because we need the waist to be much smaller ($\simeq 10\,\mu\mathrm{m}$) than the diameter (50 µm) of the DBR. Otherwise, we would lose a lot of light and could not achieve strong over-coupling of the cavity. Lateral positioning of the SiN-bridge ensures that the cavity mode hits the mechanical device as centrally as possible, resulting in minimal optical losses and optimal optomechanical coupling to the fundamental mechanical mode.

3.5 ENTANGLEMENT SETUP

The entanglement experiment (which is discussed in detail from a theory perspective in Chapter 5) is even simpler than the state estimation experiment, as far as the setup is concerned. There is only a single, resonant driving beam, which is read out using two separate homodyne detection setups. The main additional challenge, compared to the state estimation experiment, are the very stringent requirements on optical noise and mechanical decoherence. We reduce optical noise using a narrow-band filter cavity, as already discussed in Section 3.1.2. Mechanical decoherence is reduced by operating the experiment at cryogenic temperatures (which lowers the temperature of the mechanical bath) and working with mechanical modes with very high quality factors.

reducing optical noise & mechanical decoherence

The condition on the mechanical quality factors is indeed rather demanding. Simulations, such as Figure 5.5b, show that we need ap-

SYMBOL	DEFINITION	VALUE
ω_m	mechanical frequency	$2\pi \times 1.278\,\mathrm{MHz}$
γ_m	mechanical linewidth	$(1/4800) \times \omega_m$
q_0	mechanical ground state position	$2.73 \times 10^{-16}\,\mathrm{m}$
p_0	...and momentum uncertainty	$3.87 \times 10^{-19}\,\mathrm{kg\,m/s}$
κ	cavity HWHM-linew., $\kappa = \kappa_1 + \kappa_2$	$0.341 \times \omega_m$
κ_1	cavity linew. due to input coupler	$0.2775 \times \omega_m$
κ_2	cavity linew. due to other losses	$0.0635 \times \omega_m$
$g_{0,i}$	single-photon coupling	$2\pi \times 7.7\,\mathrm{Hz}$
g_d	coupling of detuned beam	$0.2 \ldots 1.68 \times \kappa$
g_r	coupling of resonant beam	$0.2 \times \kappa$
Δ_d	detuning of detuned beam	$-\omega_m$

Table 3.2. Values of important parameters in the state estimation experiment. The subscripts $i \in \{d, r\}$ denote the detuned and resonant laser beam, respectively. The mechanical parameters and optomechanical coupling rates refer to the fundamental mechanical mode. Adapted from [Wie+15, Supplemental Material].

requirements regarding mechanical quality factor

proximately $Q > 5 \times 10^6$ if we operate in a liquid helium flow cryostat ($T \simeq 5\,\mathrm{K}$). For this reason, we use high-stress SiN membranes as optomechanical devices for the entanglement experiment. Their suitability as OM-systems was demonstrated in [Jay+08; Tho+08; Wil+09] and they are known to yield sufficiently high quality factors [Ver+06; VCP08; Sou+09].

As an alternative to SiN membranes, high-stress InGaP membranes could be used in the future. They have already been shown to be high-Q mechanical oscillators [Col+14]. In addition, it should be possible to directly integrate InGaP membranes with semiconductor DBRs, via microfabrication. This would would remove the need for manual alignment of the membrane (with respect to the end mirror of a cavity) and allow to fine-tune the optomechanical coupling, which depends sensitively on the distance between membrane and end-mirror (see Section 2.4.2). It should also increase the stability of the resulting optomechanical cavity.

The remainder of this section discusses the mechanical and optomechanical properties of the SiN membranes (Section 3.5.1) and how we integrate them into an optomechanical cavity (Section 3.5.2).

3.5.1 *High-stress SiN membranes*

We work with thin, square, high-stress SiN-membranes which are either purchased from Norcada Inc or custom-made by Claus Gärtner (a PhD student in our group) in the clean room at TU Delft. They

are created by depositing a thin SiN layer ($d \simeq 50$ to $100\,\mathrm{nm}$) on a comparatively thick ($d_\mathrm{F} \simeq 200$ to $500\,\mu\mathrm{m}$) Si substrate.[24] The substrate, which we also refer to as the "frame", has lateral dimensions $L_\mathrm{F} \simeq 5$ to $10\,\mathrm{mm}$. By removing a square patch of the Si substrate in the center, a window is created, which is covered only by the thin SiN film and can move freely. This freely moving part of the SiN film is the mechanical oscillator we work with and it will be referred to simply as "the membrane". The frame provides the tensile stress for the membrane and is our handle for fixing the membrane at a desired position.

[24] *Sketch of SiN membrane on Si frame (top view and cut through center).*

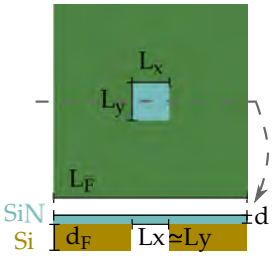

The membranes are almost perfectly square with lateral dimensions $L_x \simeq L_y \simeq 0.5$ to $1\,\mathrm{mm}$, much larger than their thickness $d \simeq 50$ to $100\,\mathrm{nm}$. The geometry of these membranes is therefore extremely well approximated by a two-dimensional square drum head, whose mechanical mode structure is well known. The mechanical modes of a square drum head can be labeled by two numbers $m, n \in \mathbb{N}$, the number of anti-nodes in the two transversal directions.[25] The frequencies $\omega_{m,n}$ and mode functions $u_{m,n}(x,y)$ of the mechanical modes are given by [see Wil+09, sec 4.2.1]

model of the mechanical motion

[25] *Mode structure of the $(3,3)$-mode of a square membrane, defined by three anti-nodes in both directions:*

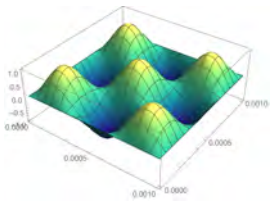

$$\omega_{m,n} = c\pi\sqrt{(n/L_x)^2 + (m/L_y)^2}, \tag{3.9}$$

$$u_{m,n}(x,y) = \sin(n\pi x/L_x) \cdot \sin(m\pi y/L_y), \tag{3.10}$$

where $c = \sqrt{\sigma/\rho} \simeq 550\,\mathrm{m/s}$ is the speed of sound for the membrane surface, $\sigma \simeq 1\,\mathrm{GPa}$ is the tensile stress of the membrane (assumed isotropic in x and y), and $\rho \simeq 3.44\,\mathrm{kg/m^3}$ is the mass density. $u_{m,n}(x,y)$ describes the peak displacement in z-direction of a point with coordinates (x,y) in the membrane plane due to mode (m,n). Note that (3.9) applies in the limit of high tensile stress σ, in which the contribution of flexural rigidity to the potential energy of the membrane can be neglected. In this limit, the frequencies $\omega_{m,n}$ depend only on the tensile stress and the lateral dimensions and not directly on the thickness.

For a sense of scale, according to (3.9), high-stress membranes of $1\,\mathrm{mm} \times 1\,\mathrm{mm}$ lateral dimensions should have a frequency of $\omega_{1,1} \simeq 2\pi \times 400\,\mathrm{kHz}$ for the fundamental mechanical mode and of $\omega_{3,3} \simeq 2\pi \times 1200\,\mathrm{kHz}$ for the $(3,3)$-mode. Figure 3.14 shows a mechanical NPS which demonstrates that this simple square drum model fits the measurements extremely well.

example spectrum

The main reason for using high-stress SiN membranes in optomechanical experiments are their potentially ultra-high mechanical quality factors [Ver+06; VCP08; Sou+09]. Even at room temperature, quality factors as large as $Q = 5 \times 10^7$ have been reported [Cha+14]. The large tensile stress is crucial for reaching very high quality factors: The quality factors of high-stress membranes have been shown to ex-

ultra-high Q-factors

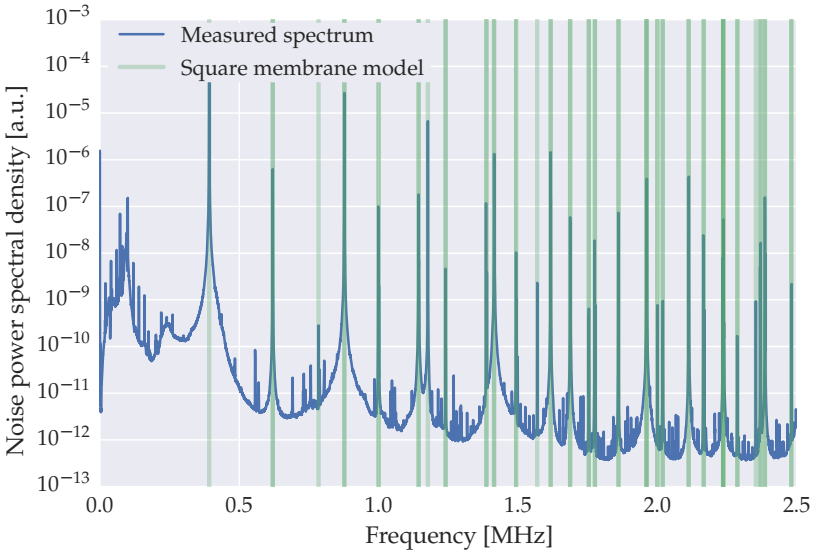

Assumed parameters: membrane side lengths $L_{x,y} = (1 \pm \epsilon) \cdot 1\,\mathrm{mm}$, density of Si_3N_4 $\rho = 3.44 \times 10^3\,\mathrm{kg/m^3}$; Fitted parameters: $\omega_{1,1} \simeq 2\pi \times 392\,\mathrm{kHz}$, tensile stress $\sigma = 1.06\,\mathrm{GPa}$, deviation from square form $\epsilon \simeq 1.4 \times 10^{-4}$.

Figure 3.14. Measured spectrum for a commercial SiN membrane. Semitransparent green vertical lines mark the theoretically expected frequencies of membrane modes (from the square membrane model (3.9), fitted to the measurement). The fundamental mechanical mode is at $\omega_{1,1} \simeq 2\pi \times 392\,\mathrm{kHz}$. As expected, all membrane modes are observed in the NPS. The additional broad noise peaks at low frequencies (between 10 kHz and 300 kHz) are due to laser noise. The many sharp small peaks at higher frequencies (with peak noise powers three to six orders of magnitude below typical membrane peaks) are mostly due to mirror substrate noise.

ceed those of corresponding unstressed devices by more than two orders of magnitude [Sou+09].

It is quite difficult to reproduce the highest reported quality factors within a cavity optomechanics experiment because the quality factors depend very sensitively on the "clamping", by which we mean, quite generally, the way the Si frame (which holds the membrane) is fixed to the optomechanical cavity; a discussion of this topic and a nice compilation of measurements of Q for different clamping methods are given in [Wil12, sec. 4.7]. The highest Q factors are usually recorded without any kind of rigid clamping, by letting the membrane simply rest on a surface, pushed down by its own gravity. In cavity optomechanical experiments, however, we need stable lateral and angular alignment of the membrane with respect to a cavity, which is hard to achieve without rigid clamping. Since the best way to position and clamp a membrane also depends on the cavity geometry, I will return to this topic when discussing the optomechanical cavity in Section 3.5.2. The reason for the large sensitivity of the mechanical quality factors to clamping is that the quality factors are usually limited by coupling of membrane modes to the surrounding support structure (the Si frame) via acoustic radiation [Wil+11; Cha+14]. The quality factor depends therefore very sensitively on the mechanical mode structure of the frame [Jöc+11], but the frame modes themselves can easily be disturbed—shifted in frequency as well as broadened—by clamping.

"clamping loss"

Figure 3.15 shows results of Q-measurements for a commercial $0.5 \times 0.5\,\mathrm{mm}$ SiN membrane mounted inside the MIM-cavity, both at room temperature and low temperature. Again, the measured mode frequencies agree extremely well with the simple formula (3.9).[26] The measured frequencies decrease by about 1 % by cooling from room temperature to 5 K. Importantly, we observe an increase in Q factors for the cooled sample by, on average, a factor 5. Increases in quality factor by cooling to liquid helium temperatures have been observed by many groups [see e.g. Sou+09].

Q measurements

[26] *Note that this membrane had a comparatively low tensile stress* $\sigma = 0.78\,\mathrm{GPa}$, *resulting in a fundamental frequency of only around* 680 kHz.

increased Q at low temperatures

For all membrane modes, the modal mass (2.41) is given by a fourth of the full membrane mass. For a $1\,\mathrm{mm} \times 1\,\mathrm{mm}$-membrane with thickness $d = 50\,\mathrm{nm}$ and mass density $\rho \simeq 3.44\,\mathrm{kg/m^3}$, the modal mass is $m \simeq 43\,\mathrm{ng}$, independent of the mechanical mode. This yields a zero-point position uncertainty of $q_0 \simeq 0.7\,\mathrm{fm}$ for the 11-mode, and $\sqrt{\omega_{11}/\omega_{mn}} \times 0.7\,\mathrm{fm}$ for a higher mechanical mode. If the laser is focused tightly onto an anti-node of the mechanical mode, the effective mass (2.69) of the membrane is roughly given by its modal mass. In this case, the coupling is proportional to $1/\sqrt{\omega_{mn}}$, hence depends only on the frequency ω_{mn} and not (directly) on the mode indices m, n.

modal mass

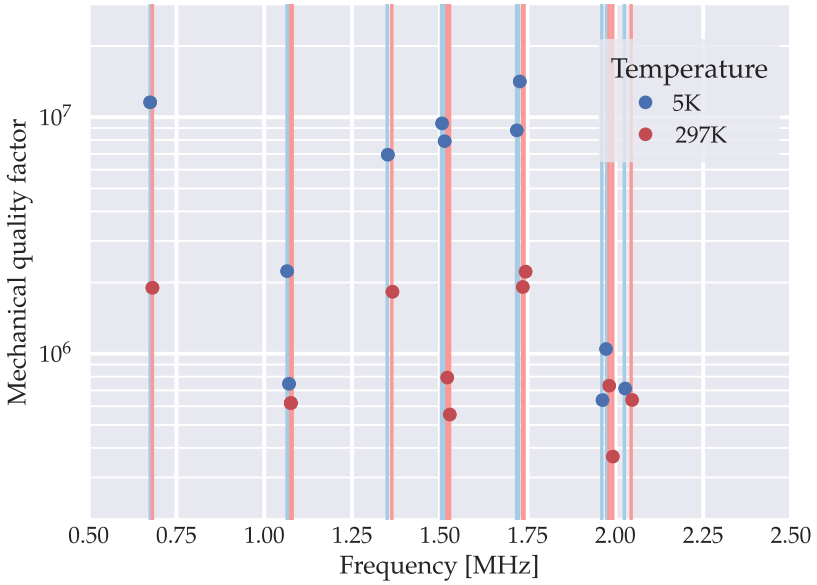

Assumed parameters: $L_{x,y} = (1 \pm \epsilon) \cdot 0.5\,\mathrm{mm}$ $\rho = 3.44 \times 10^3\,\mathrm{kg/m^3}$; Extract. parameters LT: $\omega_{1,1} \simeq 2\pi \times 675\,\mathrm{kHz}$, $\sigma = 0.78\,\mathrm{GPa}$, dev. from square form $\epsilon \simeq 4\,‰$; Extract. parameters RT: $\omega_{1,1} \simeq 2\pi \times 682\,\mathrm{kHz}$, $\sigma = 0.80\,\mathrm{GPa}$, $\epsilon \simeq 3\,‰$;

Figure 3.15. Measured Q and f at room temperature and low temperature (red and blue dots, respectively) for a commercial SiN membrane, mounted inside the MIM-cavity. The light red and blue vertical lines mark expected membrane frequencies according to (3.9) (parameters σ and ϵ are extracted from measurements, see margin) which fit the measurements excellently. For each data point, several mechanical ringdowns were recorded using optical readout at 1550 nm (for which the MIM-cavity is transparent, thus avoiding optical damping). Each mode was individually excited using a PZT mounted on the cavity corpus. The standard deviation across all ringdowns for a given mode is on the order of a %.

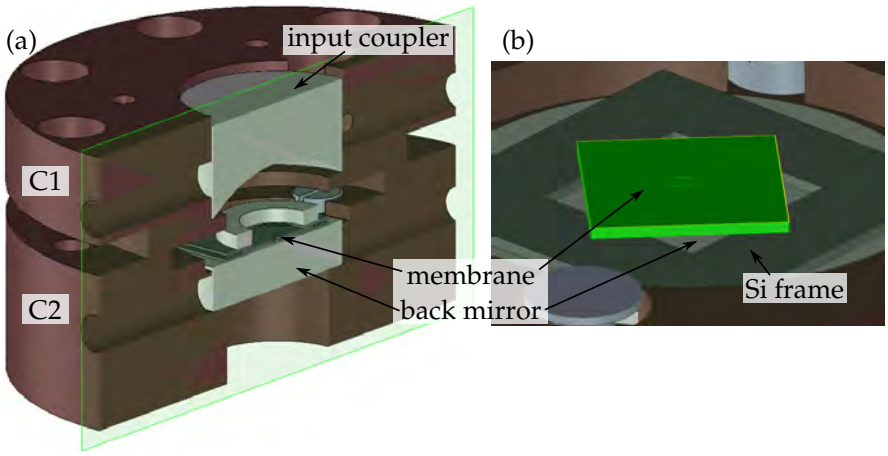

Figure 3.16. CAD drawing of the optomechanical cavity. (a) Cut through the center (along the axis) of the quasi-monolithic cavity body, consisting of two blocks of copper (C1 and C2) screwed tightly together. C1 holds the curved input coupler mirror, C2 holds the flat back mirror on which the membrane is fixed. (b) Zoom-in on the membrane shows how the membrane (green) is positioned on the back mirror: It rests on a Si frame (dark gray), rotated by 45° with respect to the membrane, and itself resting directly on the flat back mirror. Not shown are Teflon clamps which press the membrane down against the Si frame and back mirror.

3.5.2 *Optomechanical cavity*

To use high stress SiN membranes in optomechanical experiments, we have to integrate them into high finesse optomechanical cavities such that the membrane's mechanical motion couples significantly to an optical cavity mode (as discussed in Section 2.4.2). But can we insert a membrane into a high finesse cavity without introducing strong optical losses and ruining the finesse? Optical losses could result from absorption in the membrane or from scattering at the membrane surface (into other cavity modes or out of the cavity). Fortunately, the optical absorption of high stress SiN membranes is extremely low in the near infrared. [San+10] found $\lesssim 1.5 \times 10^{-6}$ for the imaginary part of the index of refraction at 1064 nm. Scatter into other cavity modes, on the other hand, could result from either surface roughness (not a problem for the membranes) or from a non-flat optical wave front at the position of the membrane. We avoid the latter by placing the membrane well within a Rayleigh range from the focus of the cavity mode. The third, and most pernicious, source of scattering losses is tilt, i.e. a non-zero angle between the membrane surface and the wave front of the cavity mode.

high finesse MIM cavity

low optical absorption

Tilt was a huge problems in the earliest cavity designs. It manifested in increased optical losses and a hybridization of different TEM-modes of the cavity; the latter lead to poor mode matching be-

avoiding tilt

tween laser and cavity. To avoid tilt, most groups align the membrane tilt actively using nano-positioners. We decided against such an approach and finally found a straightforward cavity design, shown in Figure 3.16, in which very good tilt alignment is possible without any active positioning. The idea is to use a flat back mirror (such that the cavity mode is perpendicular to the back mirror) and then lay the membrane directly on the back mirror (such that its surface is parallel to the back mirror and thereby perpendicular to the cavity axis). The only problem with that approach is that some air will be trapped in between the membrane and the mirror surface. When the cavity is evacuated, a pressure difference builds up which destroys the membrane. We therefore put the membrane on an auxiliary square Si frame (purchased from Norcada Inc.) of 10 mm side length and some 100 µm thickness and with a square window of 5 mm side length in the center. By rotating the membrane by 45° with respect to this window, we introduce air gaps through which the volume between the membrane surface and the mirror surface can be evacuated (see Figure 3.16 (b)). To keep the membrane in place, we clamp it down softly at the edges of the frame using clamps made from Teflon. In this design, tilt could still arise due to thickness variations of the auxiliary Si frame and of the Si frame of the membrane itself. But both of these are defined by microfabrication and therefore sufficiently smooth.

membrane positioning

lateral alignment

We also need good lateral alignment of the cavity mode with respect to the membrane, to avoid optical losses (from clamping of the cavity beam at the edges of the membrane) and to optimize the optomechanical coupling to the fundamental mechanical mode. We achieve lateral alignment as follows. We move the copper block C1 (which holds the input coupler) laterally with respect to C2 (which holds cavity and membrane) while they are only softly pressed together. We monitor the alignment on a CCD camera in transmission (behind the back mirror).[27] This camera detects both the small amount of infrared intracavity light leaking through the back mirror as well as a shadow of the membrane (the membrane is illuminated with white visible light through the input coupler). When we are satisfied with the relative position of membrane and cavity mode, we screw C1 tight against C2 which completely fixes the geometry of the cavity.

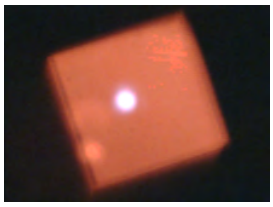

[27] *CCD image of membrane and cavity mode (bright spot).*

no longitudinal alignment

The biggest drawback of the current cavity design is that we cannot align the membrane longitudinally, i.e. we cannot fine-tune the distance z between membrane and back mirror. Fine-tuning of z with a precision of some nanometers would allow us to fine-tune the optomechanical coupling (as discussed in Section 2.4.2) and, therefore, to achieve the same coupling independent of temperature and from one cool-down to the next.

The decision for a manually pre-aligned quasi-monolithic cavity design without in-situ positioning was taken for stability reasons and to obtain a very compact design which allows us to fit the cavity into a small liquid Helium flow cryostat. The flow cryostat has the big advantage (compared to the large dilution refrigerator we were previously using) of allowing fast cool-downs and quick turn-around times. Regarding stability, we wanted to improve upon perceived flaws of an earlier cavity design (used for the state estimation experiment). This earlier design included active positioning and was therefore much more bulky, less monolithic and less stable in many respects: It required lateral and longitudinal realignment after cooling down and was much more susceptible to acoustic noise. In the current cavity, on the other hand, lateral and tilt alignment of the membrane are usually very well preserved when cooling down. Also the frequency stability of this cavity at acoustic frequencies is much better than previous designs. In this sense, the current cavity design is a success.

quasi-monolithic

Apart from stability, the main design goal for the cavity was to achieve strong cooperativity $\mathcal{C} = g^2/(\kappa\gamma_m\bar{n}) \overset{!}{>} 1$, which is needed for the entanglement experiment. To reduce the thermal phonon number $\bar{n}$, the membrane needs to be at low temperatures which requires a good thermalization of the cavity corpus. To this end, the cavity corpus is built from oxygen-free high thermal conductivity (OFHC) copper. γ_m can only be decreased by choosing high quality oscillators and taking good care to only introduce minimal clamping. This leaves us with the requirement of large g^2/κ. We have

high cooperativity

$$\frac{g^2}{\kappa} \propto \left(\frac{\kappa_1}{\kappa^2+\Delta^2} P_{\text{in}} g_0^2\right) / \kappa \overset{\kappa_1 \simeq \kappa}{\propto} \frac{g_0^2}{\kappa^2}. \tag{3.11}$$

Both κ and g_0 are proportional to $1/L$, hence the cooperativity is independent of the cavity length. But simulations of the entanglement experiment suggest that, at a given cooperativity, our protocol works better for decreasing sideband resolution ω_m/κ. We therefore decided to increase κ by shortening the optomechanical cavity to 5.5 mm. The cavity geometry is thus very similar to the one used in [Pur+12]. Note that, since we cannot fine-tune the cavity length, we must be able to tune the laser into resonance. Therefore, the tuning range of our laser of 30 GHz is the upper limit on the free spectral range. This translates into a minimum cavity length of 5 mm.

short cavity

For a given cavity length L, κ can of course be decreased by choosing higher mirror reflectivities. This is limited because we want to achieve strong over-coupling such that most of the light is reflected at the input coupler. We therefore choose a much higher transmission of $\simeq$ 950 ppm for the input coupler mirror, limiting the finesse to roughly 6600 (though we measured only $\simeq$ 6250; see Table 3.3).

one-sided cavity

membrane-at-the-end

Finally, the single-photon coupling g_0 can, for a given cavity length L, be increased a bit by moving the membrane as close to one of the mirrors as possible [Wil12, sec. 3.3.1]. This was another motivation for mounting the membrane more or less directly on the back mirror. Note again that the optomechanical coupling depends on the exact distance z of membrane and mirror (with a rough periodicity of $\lambda/2$). Since we cannot fine-tune z, we observe different couplings on each cool-down. The same is true for the finesse [Jay+08], [Wil12, sec. 3.3.2]. As an example, one set of optical and optomechanical parameters measured at low temperatures (5 K) is summarized in Table 3.3.

SYMBOL	DEFINITION	VALUE
L	cavity length	5.5 mm
ν_{FSR}	free spectral range	27 GHz
T_1	power transmission (nominal) of mirrors	950 ppm
T_2	(1: input coupler, 2: back mirror)	$\lesssim 1$ ppm
$R_1\,(R_2)$	radius of curvature of mirrors	10 mm (∞)
$w_1\,(w_2)$	waist of cavity mode at the mirrors	61 µm (41 µm)
$\mathcal{F}_{\mathrm{empty}}$	finesse of empty cavity (measured)	6250
$\mathcal{F}$	finesse of cavity with membrane (meas.)	5300
κ	cavity HWHM-linew. (incl. membrane)	$2\pi \times 2.6$ MHz
d	distance membrane to back mirror	0.5 mm
g_0	single-photon coupling of fundamental mode (measured at 5 K)	$2\pi \times 40$ Hz

Table 3.3. Optical and optomechanical parameters of the membrane cavity. Note that, the position of the membrane in axial direction (i.e. its distance from the back mirror) fluctuates from cool-down to cool-down. Therefore, also the finesse $\mathcal{F}$ of the optomechanical cavity and the single-photon coupling g_0 fluctuate from cool-down to cool-down; the values provided in the table are example values for one particular measurement. The sketch in the margin illustrates the naming conventions for the different length scales at play and the mirrors.

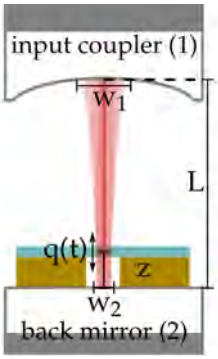

4

STATE ESTIMATION USING KALMAN FILTERING

4.1 INTRODUCTION

State estimation deals with the question: "If we know how two systems A and B interact and we observe system B, what can we say about the state of A?" This problem is very much ubiquitous in experimental physics where, more often than not, we are interested in physical quantities which are not directly observable.

ubiquity of state estimation

Consider photodetection: System A is the light field, system B is a photodetector. Light field and photodetector interact and we measure the photo-voltage—a property of the photodetector. Knowing the photo-voltage, what can we say about the state of the light field? What can we say about its intensity?

trivial example: photodetection

Photodetection can be framed as an instance of state estimation, but it is admittedly rather trivial: The measured observable (photovoltage) is simply proportional to the quantity of interest (light intensity) plus some added noise (electronic dark noise of the detector circuit, say). In this case, we can easily pretend to have directly measured light intensity. To add sophistication, we might add error bars to indicate that the measured photovoltage statistically fluctuates around the actual light intensity. This example is so simple that we may not even realize that we are, in fact, doing state estimation.

Often, however, the relationship between the quantity of interest and the measured observable is not that simple and state estimation becomes a real challenge. In cavity optomechanics, for example, we are interested in the position q of the mechanical element inside the cavity. Unfortunately, we generally cannot measure q directly. What we can measure is the phase y of the laser light reflected from the cavity, which in turn is influenced by q. But exactly how q influences y depends on experimental parameters such as laser detuning and intensity, mechanical properties etc. Furthermore, the transfer function from q to y is, in general, strongly frequency-dependent. Hence, we clearly cannot pretend anymore that y is proportional to q. The question is therefore: How do we get a good estimate of the mechanical position (and momentum) from the measured properties of the light? And how do we know how reliable (how close to the truth) our estimate is?

non-trivial example: optomechanics

This is the problem of *optimal state estimation*, which can be formulated in full generality as follows:

optimal state estimation

1. What is the *optimal estimate* of the full state of a system given observations on only a part of the system?
2. And how close to the true value is our optimal estimate? I.e., what is the *expected estimation error*?

assumptions: perfect system model...

We will answer these questions under the assumption that we have a perfect model of the system. This is, of course, never exactly true but is close enough to the truth for a physical system as well-studied as an optomechanical cavity. Furthermore, a single observation is usually not enough to learn much about the state of the system. Therefore, we consider repeated measurements in time and are concerned with the optimal estimate of the full system state given a set of, in general, multiple past observations.

...& repeated observations

conditional state

The optimal estimate together with the expected estimation error is encoded in the *conditional state*, which is the conditional probability distribution over all possible system states. This conditional probability distribution describes how likely you judge a certain system state to be given the history of observations. This is in contrast with the *unconditional state* which describes the probability of a given system state without taking any measurements into account. Specifying the full conditional probability is the most general and most informative way of expressing a state estimate, but often it is preferable to condense this information further by defining:

EXPECTED ESTIMATION ERROR Expected deviation between the optimal estimate of the system state and its true value, where the expectation value is taken with respect to the conditional probability distribution.

OPTIMAL ESTIMATE System state which minimizes the expected estimation error. This might (but need not) be the the same as the expectation value of the conditional probability distribution.

state estimation as an optimization problem

Hence, state estimation is an optimization problem: The expected estimation error is the so-called cost function, which we want to minimize. Note that the expected estimation error will here be defined as the root mean square (RMS) deviation from the true state. This is a common choice but other cost functions can be just as legitimate, depending on what we want to do with the estimate (i.e. which types of errors we most desperately want to avoid). Changing the cost function means changing the definition of "estimation error" and will, in general, lead to a different optimal estimate.

4.1.1 *State estimation for Gaussian systems*

To calculate the optimal estimate and the expected estimation error, we generally need to know the full conditional probability distribu-

tion after each measurement. But the conditional probability distribution is generally described by an infinite number of parameters. This is one reason why optimal state estimation is, in general, computationally expensive or even impossible in practice.

computationally expensive

Fortunately, our experimental system is Gaussian. This means:

Gaussian systems

- The unconditional state is given by a Gaussian distribution.
- The system dynamics is linear.
- The driving noise processes are described by Gaussians random processes.

These three properties imply that the conditional state of a Gaussian system is always given by a Gaussian distribution—at least as long as only linear measurements are considered, which is the case in all our experiments. This drastically simplifies optimal state estimation because it implies that the conditional state is fully described by the first and second moments (vector of means and covariance matrix) of the conditional probability distribution; hence, by $N + N(N+1)/2$ real numbers if the system is described by N state variables.

conditional state is Gaussian

It might therefore be not too surprising that, for Gaussian systems, a practical solution to the problem of state estimation is known, called the *Kalman filter.* As explained in Section 4.2, the Kalman filter can be understood as recursive Bayesian updating applied to Gaussian systems or as a time-dependent version of linear regression.

Kalman filter

What are the advantages of the Kalman filter?

advantages of Kalman filtering

- It is provably optimal for Gaussian systems. Hence, no other systematic procedure for estimating the system state fares better in a statistical sense (yields a smaller RMS estimation error).
- In addition to an optimal estimate for the current system state it also yields an estimate of the estimation error. Hence, for Gaussian systems, it yields the complete conditional state.
- The Kalman filter is completely recursive: It produces its state estimate based only on the previous state estimate and the current measurement. Hence, the memory requirements are low and it is, in principle, amenable to real-time implementation.
- The Kalman filter can be "debugged" systematically (as explained in more detail in Section 4.4.1) by analyzing the so-called innovation sequence, which is the difference between expected and actually observed measurement values.
- This "debugging procedure" can be used as a tool for system identification: If the innovation sequence behaves (statistically) as expected, we can be confident that we have found a reasonable system model.

What are the main challenges we have to overcome when we implement a Kalman filter?

challenges of Kalman filtering

- The Kalman filter requires an accurate state space model for the experimental system. Identifying a suitable model is, generally, not trivial! Section 4.3 explains how to construct a suitable state space model for a cavity optomechanical experiment.
- The Kalman filter assumes that the system is driven by white noise. But in practice, the driving noise often has a strong frequency-dependence. In this case, we need to find an equivalent model which is driven by white noise only. This is achieved by adding a model for the driving noise process to the actual state space model, as explained in Section 4.3.2. Identifying a suitable model for the driving noise can, again, be non-trivial.

In [Wie+15], we demonstrated that these challenges can be overcome and that Kalman filtering can be applied to real-world cavity optomechanical systems—even in the presence of colored laser noise and multiple mechanical modes, both of which are typical features of current cavity optomechanical setups. While Kalman filtering itself has been used successfully for a long time in many science and engineering disciplines, [Wie+15] was the first application of Kalman filtering to cavity optomechanical systems, thereby opening a door to a wide range of potential applications: From quantum state reconstruction over conditional cooling and real-time optimal control to improved mechanical force sensing. This chapter of the thesis is devoted to explaining these results in some detail.

4.1.2 *Outline*

I start, in Section 4.2, with a general introduction to Kalman filtering from a Bayesian point of view. In Section 4.3, I explain the state space model for our experimental system, which is the basis of the Kalman filter. Section 4.3.2 focuses specifically on how to incorporate colored laser noise into the state space model. Section 4.4 presents the results of applying a Kalman filter to our measurement data. We showed that our state space model is accurate by analyzing the innovation sequence (Section 4.4.1). We demonstrated that the Kalman filter is applicable in very different optomechanical parameter regimes by varying the optomechanical coupling (Section 4.4.2). Finally, we demonstrated conditional cooling of the mechanical subsystem by analyzing the so-called estimation error covariance (Section 4.4.3). In Section 4.5, I briefly contrast the Kalman filter with earlier approaches to optomechanical state-estimation and provide an outlook regarding potential applications.

4.2 RECURSIVE BAYESIAN ESTIMATION & KALMAN FILTER

Note that some notation and some straightforward calculation rules used throughout this section are collected in Section A.4.

4.2.1 *Bayesian estimation*

Consider a measurement of a variable z which depends linearly on another variable x (the *system state*) but with some added measurement noise v

linear measurement with noise

$$z = Cx + v,\ v \sim \mathcal{N}(v; 0, V), \tag{4.1}$$

where v is white and distributed according to a Gaussian with zero mean and variance V (denoted by $\mathcal{N}(v; 0, V)$). For example: x = light intensity at detector, v = amplifier dark noise, z = photovoltage.

Our goal is to arrive at an optimal estimate of x, based on the measurement outcome z. This is the problem of *state estimation*. Because of the measurement noise v we clearly cannot know x exactly. Hence, the question really is: *Given the measurement result z, which probabilities should we assign to different possible values of x?*

state estimation

In addition to the measurement result z, we generally also have some prior information about x, usually from earlier measurements. In general, these two pieces of information—current measurement and prior information—will point to different values of x. Hence, we need to reconcile two conflicting pieces of information, by attaching relative weights to them. How to best do this depends on:

weighing information

- The quality of the prior knowledge: The more we trust it, the less weight we attach to a conflicting measurement result.
- The quality of our measurement: The more reliable our measurement is, the more weight we will attach to it.

These intuitions can be made precise using Bayesian concepts:

Bayesian terminology

PRIOR $\rho^{(-)}(x)$: probability[28] we assign to x before the measurement.

POSTERIOR $\rho^{(+)}(x)$=$\rho(x|z)$: probability we assign to x conditional on a measurement outcome z.

LIKELIHOOD $\rho(z|x)$: conditional probability to observe the actual measurement outcome z as a function of the system state x.

[28] *Note that we are actually dealing with probability densities, but refer to them simply as "probabilities" for the sake of brevity.*

Note that the prior and posterior are simply the *conditional states* for x before and after a measurement, respectively.

Using these concepts, *Bayes' theorem* provides a comprehensive solution to the problem of state estimation:

Bayes' theorem

$$\rho^{(+)}(x|z) = \frac{\rho(z|x)}{\rho(z)}\rho^{(-)}(x) \propto \rho(z|x) \cdot \rho^{(-)}(x). \tag{4.2}$$

(4.2) tells us how to update the conditional state when we obtain a measurement outcome z: The posterior $\rho^{(+)}$ (the new conditional state) is proportional to the prior $\rho^{(-)}$ (the old conditional state) times the likelihood $\rho(z|x)$ for obtaining result z.

application to our experiment

To apply this to our experiment, we need to evaluate (4.2) for a multidimensional linear measurement (with Gaussian errors) on a multidimensional Gaussian system.[29] In addition, since in our experiment the system state x is not constant but evolves in time between measurements, we need to amend (4.2) by another equation specifying how the conditional state changes in between measurements.

[29] *"Multidimensional" means that system state and measurements are both described by vectors.*

Kalman filter

The Kalman filter is nothing more than this: A rule for updating conditional probabilities recursively for Gaussian systems subject to linear measurements—alternating between *measurement-induced updates* according to Bayes' theorem (4.2) and *updates due to the regular time-evolution of the system*. In what follows, I will slowly build up towards the full Kalman filter equations by a sequence of generalizations starting from recursive estimation of a constant state.

4.2.2 *Bayesian estimation for Gaussian probabilities*

Consider repeated measurements of a variable z, linearly related to the system state x, but subject to measurement noise v:

$$z_i = Cx + v_i,\ i = 1, \ldots, N. \tag{4.3}$$

z_i and v_i denote the measurement outcome and strength of the noise for the i-th measurement, respectively. v is assumed white and Gaussian with zero mean and (time-independent) variance V:

$$\mathbb{E}\left[v_i v_j\right] = V \cdot \delta_{ij},\ v_i \sim \mathcal{N}\left(v_i; 0, V\right). \tag{4.4}$$

prior

Assume the prior probability is Gaussian, i.e.

$$\rho^{(-)}(x) = \mathcal{N}\left(x;\, \hat{x}^{(-)}, P^{(-)}\right), \tag{4.5}$$

where $\hat{x}^{(-)}$ and $P^{(-)}$ are the expectation value and variance of $\rho^{(-)}(x)$. This means that $\hat{x}^{(-)}$ and $P^{(-)}$ can be interpreted as our "prior best guess" of x and our "prior uncertainty" about x, respectively.

likelihood

(4.3) implies the following likelihood function for measuring z_i:

$$\rho\left(z_i|x\right) = \mathcal{N}\left(z_i;\, Cx, V\right) \propto \mathcal{N}\left(x;\, z_i/C,\, V/C^2\right). \tag{4.6}$$

posterior

Using Bayes' theorem (4.2) together with the simple rules (A.1), (A.2), and (A.3), we see that the posterior probability $\rho^{(+)}$ after a single

measurement with outcome z is also Gaussian:

$$\rho^{(+)}(x|z) = \frac{\rho(z|x)}{\rho(z)}\rho^{(-)}(x) = \mathcal{N}\left(x;\, \hat{x}^{(+)}, P^{(+)}\right), \tag{4.7}$$

where the posterior expectation value and variance $\hat{x}^{(+)}$ and $P^{(+)}$ (our "new best guess for x" and our "new uncertainty about x") are:

new optimal estimate

$$\hat{x}^{(+)} = P^{(+)}\left(\hat{x}^{(-)}/P^{(-)} + (z/C) \,/\, \left(V/C^2\right)\right), \tag{4.8}$$

$$1/P^{(+)} = 1/P^{(-)} + C^2/V. \tag{4.9}$$

Note that, for a Gaussian conditional probability $\rho(x) = \mathcal{N}(x;\, \hat{x}, P)$, $\hat{x}$ is indeed the best estimate for x because, for any other estimate $\hat{x}'$, the expected mean square estimation error (with respect to ρ) is larger

interpretation of $\hat{x}$ as "best guess"...

$$\mathbb{E}\left[\left(x - \hat{x}'\right)^2\right] \equiv \int_{-\infty}^{+\infty} \left(x - \hat{x}'\right)^2 \mathcal{N}(x;\, \hat{x}, P)\, \mathrm{d}x \geq \mathbb{E}\left[(x - \hat{x})^2\right], \tag{4.10}$$

and P is indeed the mean square estimation error for the estimate $\hat{x}$:

...and P as "estimation uncertainty"

$$\mathbb{E}\left[(x - \hat{x})^2\right] = P. \tag{4.11}$$

4.2.2.1 *Repeated measurements and relation to linear regression*

Suppose the system state x does not change with time (as implicitly expressed in (4.3)). Then we can simply measure repeatedly to obtain a more accurate state estimate. Using (4.8) and (4.9) recursively we get

recursive Bayesian estimation

$$\hat{x}_i = P_i\left(\hat{x}_{i-1}/P_{i-1} + (z_i/C) \,/\, \left(V/C^2\right)\right), \tag{4.12}$$

$$1/P_i = 1/P_{i-1} + C^2/V, \tag{4.13}$$

where z_i is the measurement outcome for the i-th measurement and where $\hat{x}_i$ and P_i define the posterior after the i-th measurement (which is the same as the prior before the measurement $i+1$).

Assume now that we have no prior knowledge about x. We can model this by letting $P_0 \to \infty$ in (4.12) and (4.13) (the value of $\hat{x}_0$ does not matter in this case). This yields:

prior knowledge

$$\hat{x}_N = (1/N) \times \sum_{i=1}^{N} (z_i/C) = \overline{z}/C, \tag{4.14}$$

$$P_N = (1/N) \times V/C^2, \tag{4.15}$$

where $\overline{z} \equiv \left(\sum_{i=1}^{N} z_i\right)/N$ denotes the sample mean.

Equations (4.14) and (4.15) show that repeated application of Bayesian updating for time-independent systems without prior knowledge yields

linear regression

the ordinary least squares estimator, which is also known as linear regression. Note that the expected (mean square) estimation error is simply the variance P_N of the posterior distribution (as it should be):

$$\mathbb{E}\left[(\hat{x}_N - x)^2\right] \overset{(4.14)}{=} \mathbb{E}\left[\left(\frac{1}{N}\sum_{i=1}^{N}(z_i/C) - x\right)^2\right] \tag{4.16}$$

$$\overset{(4.3)}{=} \mathbb{E}\left[\left(\frac{1}{N}\sum_{i=1}^{N}\frac{v_i}{C}\right)^2\right] \overset{(*)}{=} \frac{V}{NC^2} = P_N, \tag{4.17}$$

where we used the assumption of white measurement noise in $(*)$:

$$\mathbb{E}\left[\left(\frac{1}{N}\sum_{i=1}^{N}\frac{v_i}{C}\right)^2\right] = \frac{1}{N^2C^2}\sum_{i,j=1}^{N}\underbrace{\mathbb{E}\left[v_i v_j\right]}_{V\cdot\delta_{ij}} = \frac{V}{NC^2}. \tag{4.18}$$

Using $P_N = V/\left(NC^2\right)$, we can simplify (4.12) to

$$\hat{x}_N = \hat{x}_{N-1} + \frac{1}{NC} \times \left(z_N - C\hat{x}_{N-1}\right). \tag{4.19}$$

Hence, the new state estimate $\hat{x}_N$ is simply the old estimate $\hat{x}_{N-1}$ plus a correction proportional to the difference between the measurement z_N and the expected measurement $C\hat{x}_{N-1}$.

"innovation" and "Kalman gain"

The term $z_N - C\hat{x}_{N-1}$ will later be referred to as the "innovation", while the proportionality constant $1/NC$ will be called the "Kalman gain". The Kalman gain generally depends on the relative uncertainty of measurement and previous estimate. In our example, the Kalman gain decreases with the number N of observations. This is intuitively reasonable because it means that less and less weight is given to new observations as the number of past observations (and thus the certainty of the previous estimate) increases.

4.2.2.2 *Vector case*

linear measurement

The generalization to a (column) vector of state variables $\boldsymbol{x}$ and measurement variables $\boldsymbol{z}$ is, in principle, straightforward. The measurements $\boldsymbol{z}$ are now related to the system state $\boldsymbol{x}$ via a measurement matrix $\boldsymbol{C}$ plus some (white, Gaussian, zero-mean) measurement noise $\boldsymbol{v}$:

$$\boldsymbol{z}_i = \boldsymbol{C}\boldsymbol{x} + \boldsymbol{v}_i, \tag{4.20}$$

$$\boldsymbol{v}_i \sim \mathcal{N}\left(\boldsymbol{v}_i; 0, \boldsymbol{V}\right), \mathbb{E}\left[\boldsymbol{v}_i \boldsymbol{v}_j^{\mathsf{T}}\right] = \boldsymbol{V}\cdot\delta_{ij}. \tag{4.21}$$

A small added subtlety arises because, in general, we cannot simply invert the measurement matrix $\boldsymbol{C}$ to get an estimate of the state vector $\boldsymbol{x}$ from the measurement vector $\boldsymbol{z}$. Instead we have to use the right

pseudoinverse and (A.4) to infer information about $\boldsymbol{x}$ from $\boldsymbol{z}$. The likelihood function therefore takes a slightly more complicated form:

likelihood function

$$\rho(\boldsymbol{z}|\boldsymbol{x}) \propto \mathcal{N}\left(\boldsymbol{x};\, \boldsymbol{C}^\mathsf{T}\left(\boldsymbol{C}\boldsymbol{C}^\mathsf{T}\right)^{-1}\boldsymbol{z}, \left(\boldsymbol{C}^\mathsf{T}\boldsymbol{V}^{-1}\boldsymbol{C}\right)^{-1}\right). \tag{4.22}$$

I define the prior and posterior distributions in complete analogy to the scalar case such that $\hat{\boldsymbol{x}}^{(-)}$ ($\hat{\boldsymbol{x}}^{(+)}$) and $\boldsymbol{P}^{(-)}$ ($\boldsymbol{P}^{(+)}$) are expectation value and covariance matrix of the prior (posterior) distribution, respectively. Then a simple application of Bayes' theorem (4.2) shows that the posterior is characterized by the following covariance matrix and expectation value (using (A.4), (A.2), and (A.3))

posterior covariance & expectation value

$$\begin{aligned}
{\boldsymbol{P}^{(+)}}^{-1} &= {\boldsymbol{P}^{(-)}}^{-1} + \boldsymbol{C}^\mathsf{T}\boldsymbol{V}^{-1}\boldsymbol{C}, && (4.23)\\
\hat{\boldsymbol{x}}^{(+)} &= \boldsymbol{P}^{(+)}\left({\boldsymbol{P}^{(-)}}^{-1}\hat{\boldsymbol{x}}^{(-)} + \boldsymbol{C}^\mathsf{T}\boldsymbol{V}^{-1}\boldsymbol{z}\right) && (4.24)\\
&= \hat{\boldsymbol{x}}^{(-)} + \boldsymbol{P}^{(+)}\boldsymbol{C}^\mathsf{T}\boldsymbol{V}^{-1}\left(\boldsymbol{z} - \boldsymbol{C}\hat{\boldsymbol{x}}^{(-)}\right) && (4.25)\\
&\equiv \hat{\boldsymbol{x}}^{(-)} + \boldsymbol{K}\left(\boldsymbol{z} - \boldsymbol{C}\hat{\boldsymbol{x}}^{(-)}\right) \equiv \hat{\boldsymbol{x}}^{(-)} + \boldsymbol{K}\boldsymbol{\nu}. && (4.26)
\end{aligned}$$

The inverse covariance matrix $\boldsymbol{P}^{-1}$ is a measure of information about the system. Therefore, we can interpret $\boldsymbol{C}^\mathsf{T}\boldsymbol{V}^{-1}\boldsymbol{C}$ in (4.23) as the information gained in the measurement. If measurement errors are big, $\boldsymbol{V}^{-1}$ is small and only little information is gained. Similarly, little information is gained if the measurement variables $\boldsymbol{z}$ couple only weakly to the state variables $\boldsymbol{x}$, i.e. if the measurement matrix $\boldsymbol{C}$ is small.

information gain

The expectation value $\hat{\boldsymbol{x}}$ shifts, according to (4.26), by $\boldsymbol{K}\boldsymbol{\nu}$, where the *innovation*

change in $\hat{\boldsymbol{x}}$ = innovation...

$$\boldsymbol{\nu} \equiv \left(\boldsymbol{z} - \boldsymbol{C}\hat{\boldsymbol{x}}^{(-)}\right) \tag{4.27}$$

is defined as the difference between actual and expected measurement outcome, and the *Kalman gain*

...times Kalman gain

$$\boldsymbol{K} \equiv \boldsymbol{P}^{(+)}\boldsymbol{C}^\mathsf{T}\boldsymbol{V}^{-1}, \tag{4.28}$$

is the weight that we accord to the new information.

The Kalman gain (4.28) can be rewritten in terms of the prior uncertainty $\boldsymbol{P}^{(-)}$ as follows [Ste94, pp. 312-314]

Kalman gain

$$\boldsymbol{K} = \boldsymbol{P}^{(-)}\boldsymbol{C}^\mathsf{T}\left(\boldsymbol{C}\boldsymbol{P}^{(-)}\boldsymbol{C}^\mathsf{T} + \boldsymbol{V}\right)^{-1}. \tag{4.29}$$

Note that, for $\boldsymbol{V} \ll \boldsymbol{C}\boldsymbol{P}^{(-)}\boldsymbol{C}^\mathsf{T}$, i.e. if the measurement errors are small compared to the prior uncertainty, we get

negligible measurement errors...

$$\boldsymbol{K} \simeq \boldsymbol{P}^{(-)}\boldsymbol{C}^\mathsf{T}\left(\boldsymbol{C}\boldsymbol{P}^{(-)}\boldsymbol{C}^\mathsf{T}\right)^{-1}, \tag{4.30}$$

such that $\boldsymbol{C}\boldsymbol{K} \simeq \mathbb{1}$. In this case, we have

$$\boldsymbol{C}\hat{\boldsymbol{x}}^{(+)} = \boldsymbol{C}\boldsymbol{K}\left(\boldsymbol{z} - \boldsymbol{C}\hat{\boldsymbol{x}}^{(-)}\right) + \boldsymbol{C}\hat{\boldsymbol{x}}^{(-)} \tag{4.31}$$

$$\simeq \mathbb{1}\left(\boldsymbol{z} - \boldsymbol{C}\hat{\boldsymbol{x}}^{(-)}\right) + \boldsymbol{C}\hat{\boldsymbol{x}}^{(-)} = \boldsymbol{z}. \tag{4.32}$$

Hence, for negligible measurement uncertainty, the estimate changes such that the new estimate $\hat{\boldsymbol{x}}^{(+)}$ perfectly predicts the measurement outcome.

...and large measurement errors

For very large measurement uncertainty $\boldsymbol{V} \gg \boldsymbol{C}\boldsymbol{P}^{(-)}\boldsymbol{C}^{\mathsf{T}}$, on the other hand, the gain (4.29) is small. Hence, only little weight is attached to the measurement result and the estimate $\hat{\boldsymbol{x}}$ changes little.

Bayesian update (vector case)

To sum up, given a measurement result $\boldsymbol{z}$, the the estimation uncertainty $\boldsymbol{P}$ and the state estimate $\hat{\boldsymbol{x}}$ are updated according to:

$$\boldsymbol{P}^{(+)-1} = \boldsymbol{P}^{(-)-1} + \boldsymbol{C}^{\mathsf{T}}\boldsymbol{V}^{-1}\boldsymbol{C}, \tag{4.33}$$

$$\hat{\boldsymbol{x}}^{(+)} = \hat{\boldsymbol{x}}^{(-)} + \boldsymbol{K}\left(\boldsymbol{z} - \boldsymbol{C}\hat{\boldsymbol{x}}^{(-)}\right), \tag{4.34}$$

$$\boldsymbol{K} = \boldsymbol{P}^{(-)}\boldsymbol{C}^{\mathsf{T}}\left(\boldsymbol{C}\boldsymbol{P}^{(-)}\boldsymbol{C}^{\mathsf{T}} + \boldsymbol{V}\right)^{-1}. \tag{4.35}$$

4.2.2.3 *Joseph's form of the covariance update*

It will prove useful to rewrite (4.33), which specifies how to update the estimation uncertainty $\boldsymbol{P}$, in a slightly more general form. Recall that $\boldsymbol{P}$ quantifies our expectation for the estimation error:

$$\boldsymbol{P}_i^{(+)} = \mathbb{E}\left[\boldsymbol{\epsilon}_i^{(+)}\boldsymbol{\epsilon}_i^{(+)\mathsf{T}}\right], \text{ where} \tag{4.36}$$

$$\boldsymbol{\epsilon}_i^{(+)} \equiv \boldsymbol{x}_i - \hat{\boldsymbol{x}}_i^{(+)}, \tag{4.37}$$

and analogously for $\boldsymbol{P}_i^{(-)}$ and $\boldsymbol{\epsilon}_i^{(-)}$. A simple calculation [Ste94, p. 355] shows that, during the measurement, the estimation error changes as:

$$\boldsymbol{\epsilon}_i^{(+)} = \left(\mathbb{1} - \boldsymbol{K}_i\boldsymbol{C}_i\right)\boldsymbol{\epsilon}_i^{(-)} - \boldsymbol{K}_i\boldsymbol{v}_i. \tag{4.38}$$

Joseph form

Using (4.36) and (4.38), as well as $\mathbb{E}\left[\boldsymbol{v}_i\boldsymbol{v}_i^{\mathsf{T}}\right] = \boldsymbol{V}$, we obtain the so-called *Joseph form* of the covariance update:

$$\boldsymbol{P}_i^{(+)} = \left(\mathbb{1} - \boldsymbol{K}_i\boldsymbol{C}_i\right)\boldsymbol{P}_i^{(-)}\left(\mathbb{1} - \boldsymbol{K}_i\boldsymbol{C}_i\right)^{\mathsf{T}} + \boldsymbol{K}_i\boldsymbol{V}\boldsymbol{K}_i^{\mathsf{T}}. \tag{4.39}$$

Note that, to derive (4.39), we used $\mathbb{E}\left[\boldsymbol{\epsilon}_i^{(-)}\boldsymbol{v}_i^{\mathsf{T}}\right] = \mathbb{E}\left[\boldsymbol{v}_i\boldsymbol{\epsilon}_i^{(-)\mathsf{T}}\right] = 0$. This holds because $\boldsymbol{v}_i$ is white and therefore uncorrelated to everything before measurement i (hence also uncorrelated to $\boldsymbol{\epsilon}_i^{(-)}$).

The Joseph form (4.39) has two advantages over (4.33):

applicable to other gains

First, it is more general since it also tells us how the estimation error changes if we do not use the gain (4.35) in the measurement update. In fact, we will have to change the gain to account for correlations of process and measurement noise. We could, however, also be forced to

use a different (suboptimal) gain because the optimal gain might be hard to compute or we might not know the correct state space model.

Second, the Joseph form explicitly preserves symmetry and positive definiteness of the estimation error covariance matrix [Ste94, p. 355]. If the Kalman filter is implemented on a computer, using the Joseph form ensures that these properties are preserved even in the presence of numerical rounding errors [see Ste94, p. 354]. For this reason, the Joseph form of the covariance update is sometimes also called the "stabilized Kalman filter".

numerically stable

4.2.3 *State space models*

Only one ingredient is missing for the full Kalman filter: The system state $\boldsymbol{x}$ evolves in time between successive measurements and this needs to be taken into account when calculating the state estimate. In our experiment, both the time evolution and the measurements are linear and subject to white, zero-mean Gaussian noise. Hence, the full experiment can be described by a *state space model* of the form

state space model

$$\boldsymbol{x}_i = \boldsymbol{A}\boldsymbol{x}_{i-1} + \boldsymbol{w}_{i-1}, \tag{4.40}$$

$$\boldsymbol{z}_i = \boldsymbol{C}\boldsymbol{x}_i + \boldsymbol{v}_i. \tag{4.41}$$

(4.40) describes the time evolution of the system state $\boldsymbol{x}$. The *process matrix* $\boldsymbol{A}$ describes the deterministic part of the time evolution. A stochastic element is included in the form of the so-called *process noise* $\boldsymbol{w}$ which is assumed to be a zero-mean Gaussian white-noise process with covariance matrix $\boldsymbol{W} = \mathbb{E}\left[\boldsymbol{w}\boldsymbol{w}^\mathsf{T}\right]$:

process matrix & process noise

$$\boldsymbol{w}_i \sim \mathcal{N}\left(\boldsymbol{w}_i; 0, \boldsymbol{W}\right), \mathbb{E}\left[\boldsymbol{w}_i \boldsymbol{w}_j^\mathsf{T}\right] = \boldsymbol{W} \cdot \delta_{ij}. \tag{4.42}$$

(4.41) describes measurements. The *measurement noise* $\boldsymbol{v}$ satisfies

measurement noise

$$\boldsymbol{v}_i \sim \mathcal{N}\left(\boldsymbol{v}_i; 0, \boldsymbol{V}\right), \mathbb{E}\left[\boldsymbol{v}_i \boldsymbol{v}_j^\mathsf{T}\right] = \boldsymbol{V} \cdot \delta_{ij}. \tag{4.43}$$

We assume, for now, uncorrelated measurement and process noise:

$$\mathbb{E}\left[\boldsymbol{v}_i \boldsymbol{w}_j^\mathsf{T}\right] = 0. \tag{4.44}$$

Suppose we know the conditional state $\rho_{i-1}^{(+)}$ after a measurement at time $i-1$. Assuming that the system evolves according to (4.40): What is the conditional state $\rho_i^{(-)}$ at time i? What are $\hat{\boldsymbol{x}}_i^{(-)}$ and $\boldsymbol{P}_i^{(-)}$?

time evolution of conditional states

We find, for the evolution of the state estimate $\hat{\boldsymbol{x}}$,

$$\hat{\boldsymbol{x}}_i^{(-)} = \mathbb{E}\left[\boldsymbol{x}_i\right] = \mathbb{E}\left[\boldsymbol{A}\boldsymbol{x}_{i-1} + \boldsymbol{w}_{i-1}\right] \tag{4.45}$$

$$= \boldsymbol{A}\,\mathbb{E}\left[\boldsymbol{x}_{i-1}\right] + \mathbb{E}\left[\boldsymbol{w}_{i-1}\right] = \boldsymbol{A}\hat{\boldsymbol{x}}_{i-1}^{(+)}, \tag{4.46}$$

where expectation values $\mathbb{E}[\ldots]$ refer to the posterior $\rho_{i-1}^{(+)}$.

Therefore, the estimation error $\boldsymbol{\epsilon}$ evolves as follows:

$$\begin{aligned}\boldsymbol{\epsilon}_i^{(-)} &\equiv \boldsymbol{x}_i - \hat{\boldsymbol{x}}_i^{(-)} \overset{(4.46)}{=} \boldsymbol{x}_i - \boldsymbol{A}\hat{\boldsymbol{x}}_{i-1}^{(+)} && (4.47)\\ &\overset{(4.40)}{=} \boldsymbol{A}\left(\boldsymbol{x}_{i-1} - \hat{\boldsymbol{x}}_{i-1}^{(+)}\right) + \boldsymbol{w}_{i-1} && (4.48)\\ &\overset{(4.36)}{=} \boldsymbol{A}\boldsymbol{\epsilon}_{i-1}^{(+)} + \boldsymbol{w}_{i-1}. && (4.49)\end{aligned}$$

Hence, the estimation error covariance matrix $\boldsymbol{P}$ evolves as

$$\boldsymbol{P}_i^{(-)} = \mathbb{E}\left[\boldsymbol{\epsilon}_i^{(-)}\boldsymbol{\epsilon}_i^{(-)\mathsf{T}}\right] = \boldsymbol{A}\boldsymbol{P}_{i-1}^{(+)}\boldsymbol{A}^\mathsf{T} + \boldsymbol{W}. \tag{4.50}$$

To derive (4.50), we used $\mathbb{E}\left[\boldsymbol{\epsilon}_{i-1}^{(+)}\boldsymbol{w}_{i-1}^\mathsf{T}\right] = \mathbb{E}\left[\boldsymbol{w}_{i-1}\boldsymbol{\epsilon}_{i-1}^{(+)\mathsf{T}}\right] = 0$, which holds since $\boldsymbol{w}$ is a white-noise process and $\boldsymbol{w}_{i-1}$ only influences the system state at time i (and later), according to (4.40).

effect of time evolution

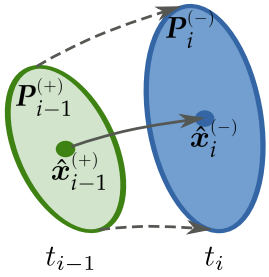

Hence, the effect of time evolution on the conditional state is

$$\begin{aligned}\hat{\boldsymbol{x}}_i^{(-)} &= \boldsymbol{A}\hat{\boldsymbol{x}}_{i-1}^{(+)}, && (4.51)\\ \boldsymbol{P}_i^{(-)} &= \boldsymbol{A}\boldsymbol{P}_{i-1}^{(+)}\boldsymbol{A}^\mathsf{T} + \boldsymbol{W}. && (4.52)\end{aligned}$$

The process matrix $\boldsymbol{A}$ describes a deterministic, linear evolution, hence rotations in phase space plus, potentially, damping or amplification. Correspondingly, the effect of $\boldsymbol{A}$ on the error covariance matrix $\boldsymbol{P}$ is a rotation and/or contraction or expansion. The additional term $\boldsymbol{W}$ leads to an increased error covariance, hence describes a loss of information due to the unknown process noise $\boldsymbol{w}$.

effect of measurement

We have seen before (in (4.34), (4.39), (4.35)) that the effect of the measurement on the conditional state is

$$\begin{aligned}\hat{\boldsymbol{x}}_i^{(+)} &= \hat{\boldsymbol{x}}_i^{(-)} + \boldsymbol{K}_i\left(\boldsymbol{z}_i - \boldsymbol{C}\hat{\boldsymbol{x}}_i^{(-)}\right), && (4.53)\\ \boldsymbol{P}_i^{(+)} &= \left(\mathbb{1} - \boldsymbol{K}_i\boldsymbol{C}_i\right)\boldsymbol{P}_i^{(-)}\left(\mathbb{1} - \boldsymbol{K}_i\boldsymbol{C}_i\right)^\mathsf{T} + \boldsymbol{K}_i\boldsymbol{V}\boldsymbol{K}_i^\mathsf{T}, && (4.54)\\ \boldsymbol{K}_i &= \boldsymbol{P}_i^{(-)}\boldsymbol{C}^\mathsf{T}\left(\boldsymbol{C}\boldsymbol{P}_i^{(-)}\boldsymbol{C}^\mathsf{T} + \boldsymbol{V}\right)^{-1}. && (4.55)\end{aligned}$$

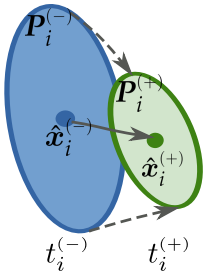

Hence, the effect of the measurement on the expectation value is a shift in phase space by $\boldsymbol{K}_i\left(\boldsymbol{z}_i - \boldsymbol{C}\hat{\boldsymbol{x}}_i^{(-)}\right)$.

Using the optimal gain (4.55), we can rewrite (4.54) as

$$1/\boldsymbol{P}_i^{(+)} = 1/\boldsymbol{P}_i^{(-)} + \boldsymbol{C}^\mathsf{T}\boldsymbol{V}^{-1}\boldsymbol{C}. \tag{4.56}$$

Hence, due to the measurement, $1/\boldsymbol{P}_i^{(+)}$ increases by $\boldsymbol{C}^\mathsf{T}\boldsymbol{V}^{-1}\boldsymbol{C}$, which represents the information gain due to the measurement.

4.2.4 *Kalman filter*

The five equations (4.51)–(4.55) taken together represent the full discrete-time Kalman filter [Kal60]. By substituting (4.53) and (4.54) into (4.51) and (4.52) or vice versa, and using (4.56), we can reduce these five equations to three equations for the evolution of the prior states

evolution of priors

$$\hat{\boldsymbol{x}}_{i+1}^{(-)} = \boldsymbol{A}\left(\hat{\boldsymbol{x}}_i^{(-)} + \boldsymbol{K}_i\left(\boldsymbol{z}_i - \boldsymbol{C}\hat{\boldsymbol{x}}_i^{(-)}\right)\right), \tag{4.57}$$

$$\boldsymbol{P}_{i+1}^{(-)} = \boldsymbol{A}\left(1/\boldsymbol{P}_i^{(-)} + \boldsymbol{C}^\mathsf{T}\boldsymbol{V}^{-1}\boldsymbol{C}\right)^{-1}\boldsymbol{A}^\mathsf{T} + \boldsymbol{W}, \tag{4.58}$$

$$\boldsymbol{K}_i = \boldsymbol{P}_i^{(-)}\boldsymbol{C}^\mathsf{T}\left(\boldsymbol{C}\boldsymbol{P}_i^{(-)}\boldsymbol{C}^\mathsf{T} + \boldsymbol{V}\right)^{-1}, \tag{4.59}$$

or, alternatively, three evolution equations for the posterior states:

evolution of posteriors

$$\hat{\boldsymbol{x}}_i^{(+)} = \boldsymbol{A}\hat{\boldsymbol{x}}_{i-1}^{(+)} + \boldsymbol{K}_i\left(\boldsymbol{z}_i - \boldsymbol{C}\boldsymbol{A}\hat{\boldsymbol{x}}_{i-1}^{(+)}\right), \tag{4.60}$$

$$1/\boldsymbol{P}_i^{(+)} = \left(\boldsymbol{A}\boldsymbol{P}_{i-1}^{(+)}\boldsymbol{A}^\mathsf{T} + \boldsymbol{W}\right)^{-1} + \boldsymbol{C}^\mathsf{T}\boldsymbol{V}^{-1}\boldsymbol{C}, \tag{4.61}$$

$$\boldsymbol{K}_i = \boldsymbol{P}_i^{(+)}\boldsymbol{C}^\mathsf{T}\boldsymbol{V}^{-1}, \tag{4.62}$$

where (4.62) follows from the identity $\boldsymbol{P}^{(+)}=(\mathbb{1} - \boldsymbol{K}\boldsymbol{C})\,\boldsymbol{P}^{(-)}$ (which can be obtained from (4.33) using the Woodbury identity [P+08, eq. 156]) together with $1/\boldsymbol{P}^{(-)} = \left(1/\boldsymbol{P}^{(+)} - \boldsymbol{C}^\mathsf{T}\boldsymbol{V}^{-1}\boldsymbol{C}\right)$, which follows from (4.33).

The interplay between information gain due to the measurement and information loss due to the process noise can, under certain conditions, imply the existence of a steady state $\boldsymbol{P}_\infty^{(+)}$ for the uncertainty $\boldsymbol{P}$, characterized by the condition[30]

steady state

[30] *Also known as the discrete-time algebraic Riccati equation.*

$$1/\boldsymbol{P}_\infty^{(+)} = \left(\boldsymbol{A}\boldsymbol{P}_\infty^{(+)}\boldsymbol{A}^\mathsf{T} + \boldsymbol{W}\right)^{-1} + \boldsymbol{C}^\mathsf{T}\boldsymbol{V}^{-1}\boldsymbol{C}, \tag{4.63}$$

$1/\boldsymbol{P}_\infty^{(+)}$ can then be interpreted as the maximum amount of information we can gather by an arbitrary number of observations on the system. (4.63) is a non-linear matrix equation which can, in general, only be solved numerically (if a steady state solution exists).

4.2.4.1 *Correlated measurement and process noise*

Contrary to our assumptions so far, process and measurement noise are correlated in our experiment. Therefore, we need to generalize the previous equations slightly. If process and measurement noise are correlated, the measurement also provides information about the process noise. This additional information about the process noise must be incorporated in the state estimate. This is achieved by adapting the Kalman gain as follows.

Assume that process noise w and measurement noise v are white and jointly Gaussian with correlation matrix

$$\boldsymbol{M} \equiv \mathbb{E}\left[\boldsymbol{w}_{i-1}\boldsymbol{v}_i^{\mathsf{T}}\right]. \tag{4.64}$$

Then, the correct Kalman gain (4.55) is given by [Ste94, eq. 4.4-17]

$$\boldsymbol{K}_i = \left(\boldsymbol{P}_i^{(-)}\boldsymbol{C}^{\mathsf{T}} + \boldsymbol{M}\right)\left(\boldsymbol{C}\boldsymbol{P}_i^{(-)}\boldsymbol{C}^{\mathsf{T}} + \boldsymbol{C}\boldsymbol{M} + \boldsymbol{M}^{\mathsf{T}}\boldsymbol{C}^{\mathsf{T}} + \boldsymbol{V}\right)^{-1}. \tag{4.65}$$

To correctly incorporate the cross-correlation between measurement and process noise in the full Kalman filter equations, we can use the Joseph form (4.39) of the update equation for the estimation error together with the gain (4.65).

4.2.4.2 *Continuous-time systems*

Our experimental system is described by a continuous-time linear state space model which can, most generally, be written as:

$$\dot{\boldsymbol{x}}_t = \boldsymbol{A}_t\boldsymbol{x}_t + \boldsymbol{w}_t, \tag{4.66}$$

$$\boldsymbol{z}_t = \boldsymbol{C}_t\boldsymbol{x}_t + \boldsymbol{v}_t, \tag{4.67}$$

Here, the process matrix $\boldsymbol{A}_t$ and measurement matrix $\boldsymbol{C}_t$ are indexed with a subscript t, indicating a possible time-dependence. Process noise $\boldsymbol{w}_t$ and measurement noise $\boldsymbol{v}_t$ are, again, zero-mean Gaussian white-noise processes with covariance matrices $\boldsymbol{W}$ and $\boldsymbol{V}$ and correlation-matrix $\boldsymbol{M}$:

$$\mathbb{E}\left[\boldsymbol{w}_t\boldsymbol{w}_\tau^{\mathsf{T}}\right] = \boldsymbol{W}\delta(t-\tau),\ \mathbb{E}\left[\boldsymbol{v}_t\boldsymbol{v}_\tau^{\mathsf{T}}\right] = \boldsymbol{V}\delta(t-\tau), \tag{4.68}$$

$$\mathbb{E}\left[\boldsymbol{w}_t\boldsymbol{v}_\tau^{\mathsf{T}}\right] = \boldsymbol{M}\delta(t-\tau). \tag{4.69}$$

The time-continuous Kalman filter for a state space model of the form (4.66)–(4.67) was first derived in [KB61] and can be obtained from the discrete version presented above by letting $t_i - t_{i-1} \to 0$. The time-continuous Kalman filter is a set of differential equations which yields the optimal estimate $\hat{\boldsymbol{x}}_t$ and estimation error covariance $\boldsymbol{P}_t$ as a function of time t:

$$\dot{\hat{\boldsymbol{x}}}_t = \boldsymbol{A}_t\hat{\boldsymbol{x}}_t + \boldsymbol{K}_t(\boldsymbol{z}_t - \boldsymbol{C}_t\hat{\boldsymbol{x}}_t), \tag{4.70}$$

$$\dot{\boldsymbol{P}}_t = \boldsymbol{A}_t\boldsymbol{P}_t + \boldsymbol{P}_t\boldsymbol{A}_t^{\mathsf{T}} + \boldsymbol{W} - \boldsymbol{K}_t\boldsymbol{V}\boldsymbol{K}_t^{\mathsf{T}}, \tag{4.71}$$

$$\boldsymbol{K}_t = (\boldsymbol{P}_t\boldsymbol{C}_t^{\mathsf{T}} + \boldsymbol{M})\boldsymbol{V}^{-1}. \tag{4.72}$$

If measurements start at $t = 0$, the values $\hat{\boldsymbol{x}}_0$ and $\boldsymbol{P}_0$ are the initial conditions for the differential equations above. They are defined by the prior at $t = 0$, i.e. the unconditional state of the system. The

same is true, of course, for the discrete Kalman filter, which is a set of recursive equations in which $\hat{\boldsymbol{x}}_0$ and $\boldsymbol{P}_0$ (again defined by the unconditional state) are the initial conditions. For a continuously driven optomechanical system, the unconditional state is the steady state solution of the quantum Langevin equations (4.77)–(4.80).

4.2.4.3 *Discrete sampling*

The observations $\boldsymbol{z}_t$ in our experiment are, however, not continuous in time but discrete (sampled with a finite sampling rate), so that the continuous-time Kalman filter (4.70)–(4.72) is not directly applicable. Therefore we actually use the discrete-time Kalman filter presented in Section 4.2.4 using a discretized version of the continuous-time state space model of the optomechanical system. We proceed as follows:

1. We determine a suitable continuous-time model of the form (4.66)–(4.67) describing the state evolution and measurements of the optomechanical system. Section 4.3 explains how a suitable model can be found.

2. We discretize the continuous model. For more information regarding the relation of discretely sampled continuous systems to discrete-time systems see [Ste94, pp. 326-329].

3. Finally, we use the discretized state space model to implement the discrete-time Kalman filter according to the equations presented in Section 4.2.4.

4.2.4.4 *Quantum interpretation*

So far, we considered classical Gaussian systems, i.e. classical systems which are subject to a linear time evolution, driven by white noise, and on which linear, noisy measurements are performed. The class of systems fitting this description is very large. Therefore, the Kalman filter has been widely applied since the 1960s in many fields of engineering and applied science, from aeronautics [GA10] to noise cancellation in gravitational wave detectors [FM01].

application to classical systems

But in fact, the Kalman filter is applicable not only to classical systems but also to open quantum systems such as the cavity optomechanical systems used in our experiments. Assume the time-dependent Heisenberg operators $\boldsymbol{x}_t$ of an open quantum system—I leave out the operator "hats" on $\boldsymbol{x}_t$ in what follows to avoid confusion with the state estimate $\hat{\boldsymbol{x}}_t$—obey a set of quantum Langevin equations of the form (4.66), (4.67). Then the solution $\hat{\boldsymbol{x}}_t$ and $\boldsymbol{P}_t$ to the corresponding Kalman filter equations (4.70)–(4.72) is equivalent

relation of Kalman filter to stochastic master equation

to the conditional quantum state ρ_t (conditioned on the previous measurement outcomes $\boldsymbol{z}_\tau$, $0 \leq \tau \leq t$), in the following sense:

$$\hat{\boldsymbol{x}}_t = \mathrm{tr}\left(\boldsymbol{x}\rho_t\right), \tag{4.73}$$

$$\boldsymbol{P}_t = \mathrm{Re}\left\{\mathrm{tr}\left(\boldsymbol{x}\boldsymbol{x}^\mathsf{T}\rho_t\right)\right\} - \hat{\boldsymbol{x}}_t\hat{\boldsymbol{x}}_t^\mathsf{T}, \tag{4.74}$$

where $\boldsymbol{x}$ are the (time-independent) Schrödinger operators corresponding to the (time-dependent) Heisenberg operators $\boldsymbol{x}_t$. $\mathrm{Re}\{\ldots\}$ denotes the real part and is necessary to obtain a symmetric covariance matrix, since the Schrödinger operators $\boldsymbol{x}$ generally do not commute with themselves.

(4.73)–(4.74) means that the optimal estimate $\hat{\boldsymbol{x}}_t$ is the expectation value of the Schrödinger operators $\boldsymbol{x}$ for the system in the conditional state ρ_t and the estimation uncertainty $\boldsymbol{P}_t$ is the symmetrized covariance matrix of the system in the conditional state ρ_t [Bel80]. Since the system is Gaussian and the measurements linear, the conditional quantum state ρ_t is a Gaussian state. Hence, ρ_t is uniquely parametrized by the solutions $\hat{\boldsymbol{x}}_t$ and $\boldsymbol{P}_t$ to the corresponding classical optimal estimation problem [Bel80]. Note that the conditional state ρ_t is the solution to the stochastic master equation, a generalization of the Schrödinger equation which gives the time evolution of the conditional system state including the influence of noise and conditioned on continuous measurements of the system. In this sense, the classical optimal estimation problem solves the corresponding stochastic master equation (at least for Gaussian systems).

non-commutative noise

Note that, in the quantum case, the noise processes $\boldsymbol{w}_t$ and $\boldsymbol{v}_t$ are generally non-commutative. Strictly speaking, the covariance matrices $\boldsymbol{V}, \boldsymbol{W}$ and the correlation matrix $\boldsymbol{M}$ in equations (4.66), (4.67), should therefore in the quantum case be defined as

$$\mathrm{Re}\left\{\mathbb{E}\left[\boldsymbol{w}_t\boldsymbol{w}_\tau^\mathsf{T}\right]\right\} = \boldsymbol{W}\delta(t-\tau),\ \mathrm{Re}\left\{\mathbb{E}\left[\boldsymbol{v}_t\boldsymbol{v}_\tau^\mathsf{T}\right]\right\} = \boldsymbol{V}\delta(t-\tau), \tag{4.75}$$

$$\mathrm{Re}\left\{\mathbb{E}\left[\boldsymbol{w}_t\boldsymbol{v}_\tau^\mathsf{T}\right]\right\} = \boldsymbol{M}\delta(t-\tau). \tag{4.76}$$

4.3 STATE SPACE MODEL FOR OUR EXPERIMENT

In the following section, I explain how to obtain a suitable continuous-time state space model of the form (4.66), (4.67) as the basis for the Kalman filter. The experimental setup used for the Kalman filter experiment was presented in Section 3.4. It consists of a laser source driving two optical cavity modes at different frequencies which interact with a mechanical oscillator. One of the cavity modes is driven weakly and on resonance; the other is driven red-detuned by ω_m (the frequency of the fundamental mechanical mode) and with variable optical power. The reflected light for both cavity modes is detected

using two different homodyne detection setups. The digitized measurement signals from these homodyne detections are the raw data on which our Kalman filter operates.

For simplicity, I will decompose the full state-space model into three separate parts and explain each of them in turn. These are: *overview*

- The core cavity-optomechanical system (Section 4.3.1) consisting of two optical intra-cavity modes (driven by shot noise and classical laser noise) and, coupled to the optical intra-cavity modes, several mechanical modes (driven by white thermal noise).
- Loss and detection (Section 4.3.3). This models the optical losses in between the optomechanical cavity and the homodyne detection as well as the homodyne detection itself, which is affected by shot noise and classical laser noise.
- The colored laser noise (Section 4.3.2) which drives the optical intra-cavity modes (in addition to the white shot noise).

Since a very detailed discussion of the state space model was presented in [Wie+15, Supplemental Material], I will keep the discussion here brief and limited to the essential ideas.

4.3.1 *Cavity optomechanical model*

The basis of the state space model are the quantum Langevin equations for the coupled optomechanical system. The equations were introduced in Section 2.6 for the case of a single optical mode; they have to be extended to account for the simultaneous coupling of the mechanical system to two optical cavity modes, which we distinguish by subscripts r and d for "resonant" and "detuned", respectively: *quantum Langevin equations for optical intracavity modes and mechanical mode(s)*

$$\dot{q} = +\omega_m p, \tag{4.77}$$

$$\dot{p} = -\omega_m q - \gamma_m p + \sum_{i=r,d} g_i \left(\cos\left(\theta_i\right) x_i - \sin\left(\theta_i\right) y_i\right) - \sqrt{2\gamma_m} f, \tag{4.78}$$

$$\begin{aligned}\dot{x}_i = &-\kappa x_i + \Delta_i y_i + g_i \sin\left(\theta_i\right) q + \sqrt{2\kappa_1} x_{i,1}^{\text{in}} + \sqrt{2\kappa_2} x_{i,2}^{\text{in}} \\ &\ldots + 2\sqrt{\kappa_1}\delta\alpha_{i,1}^{\text{in}} + |\alpha_i| \sin\left(\theta_i\right) \dot{\phi}_i,\end{aligned} \tag{4.79}$$

$$\begin{aligned}\dot{y}_i = &-\kappa y_i - \Delta_i x_i + g_i \sin\left(\theta_i\right) q + \sqrt{2\kappa_1} y_{i,1}^{\text{in}} + \sqrt{2\kappa_2} y_{i,2}^{\text{in}} \\ &\ldots + |\alpha_i| \cos\left(\theta_i\right) \dot{\phi}_i,\end{aligned} \tag{4.80}$$

where Δ_i and g_i are the detuning and optomechanical coupling of the optical mode with index i, respectively, and $\theta_i \equiv \arctan\left(\frac{\Delta_i}{\kappa}\right)$. x_i and y_i are the amplitude and phase quadrature of the optical intracavity mode i ($i \in \{r, d\}$), which satisfy canonical commutation relations $[x_k, y_l] = i\delta_{kl}$, and q and p are mechanical position and momentum quadrature, respectively, satisfying $[q, p] = i$. In principle, q and p

should also carry subscripts since, in our experiment, multiple mechanical modes couple significantly to the optical modes. To explicitly include these additional mechanical modes, we simply append the equations (4.77)–(4.78) for each additional mode and replace coupling terms like $\sin(\theta_i)\, g_i q$ by sums of the form $\sin(\theta_i)\,(g_{i1}q_1 + \ldots + g_{im}q_m)$, where g_{im} is the linearized coupling of the m-th mechanical mode to the cavity mode with index i.

Suppressing again the additional mechanical modes for the sake of legibility, the system's state vector can be written as

$$\boldsymbol{x}_t \equiv (q, p, x_d, y_d, x_r, y_r)^{\mathsf{T}}. \tag{4.81}$$

process matrix

Using the definition (4.81) of the state space vector, we can now directly read off the process matrix $\boldsymbol{A}$ describing the time evolution of the optomechanical system according to (4.66) from the quantum Langevin equations (4.77)–(4.80). The results are provided in [Wie+15, Supplemental Material, (12)–(16)].

white driving noise

The driving noise forces in (4.77)–(4.80) are: Optical shot noise ($x^{\text{in}}_{i,1}$, $y^{\text{in}}_{i,1}$, $x^{\text{in}}_{i,2}$, and $y^{\text{in}}_{i,2}$) with variance $1/2$ acting on the optical intracavity quadratures. And white thermal noise f acting on the mechanical momentum quadrature; f has variance $\bar{n} + 1/2$, where $\bar{n} \simeq k_{\text{B}}T/\hbar\omega_m$ is the mean occupation number of the bath at temperature T and the frequency of the mechanical mode ω_m. This defines the process noise vector $\boldsymbol{w}_t$ and its covariance matrix $\boldsymbol{W}$ in (4.40) and (4.42).

colored laser noise

There are two additional noise terms $\dot{\phi}_i$ and $\delta\alpha^{\text{in}}_{i,1}$ in (4.77)–(4.80), which describe the classical frequency and amplitude noise of the driving laser fields (the subscript i again distinguishes between resonant and detuned beam). Unfortunately, these noise terms are not white but strongly frequency-dependent, as discussed in Section 3.1.5. But the Kalman filter as presented above requires a state space model which is exclusively driven by white-noise terms. To correctly account for these noise terms, we therefore have to extend the state space model as described in the next section.

4.3.2 *Colored noise model*

original state space model

Our original system can be written in the form

$$\dot{\boldsymbol{x}}_t = \boldsymbol{A}_t \boldsymbol{x}_t + \boldsymbol{w}_t + \boldsymbol{\xi}_t, \tag{4.82}$$

where $\boldsymbol{w}_t$ denotes the white noise forces and $\boldsymbol{\xi}_t$ is a (vector-valued) noise term with a non-white spectral dependence. Note that the colored noise term $\boldsymbol{\xi}_t$ in (4.82) is related to the colored laser noise terms $\dot{\phi}_i$ and $\delta\alpha^{\text{in}}_{i,1}$ in (4.77)–(4.80) by a simple linear transformation, which I will not spell out here.

state space model for colored noise

Assume now that $\boldsymbol{\xi}_t$ is itself described by a state space model

$$\dot{\boldsymbol{\xi}}_t = \boldsymbol{F}\boldsymbol{\xi}_t + \boldsymbol{\zeta}_t, \tag{4.83}$$

where the driving noise $\boldsymbol{\zeta}_t$ is white with covariance matrix $\boldsymbol{W}$. Then the spectrum of the noise $\boldsymbol{\xi}_t$ is given by

$$S_{\boldsymbol{\xi}}(\Omega) = \boldsymbol{H}(\Omega)\boldsymbol{W}\boldsymbol{H}(-\Omega)^{\mathrm{T}}, \tag{4.84}$$

where $\boldsymbol{H}(\Omega) = -(i\Omega + \boldsymbol{F})^{-1}$ is the process's transfer function. If we can find a process matrix $\boldsymbol{F}$ such that (4.84) matches the experimentally measured spectrum of the noise $\boldsymbol{\xi}_t$, we have a state space model which is driven only by white noise and reproduces the spectral characteristics of the colored noise.

Then, we can simply add up the two state space models (4.82) and (4.83) by defining an extended state vector $\boldsymbol{y}_t \equiv (\boldsymbol{x}_t^{\mathrm{T}}, \boldsymbol{\xi}_t^{\mathrm{T}})^{\mathrm{T}}$ whose time evolution is given by the following extended state space model

extended state space model

$$\dot{\boldsymbol{y}}_t = \begin{pmatrix} \boldsymbol{A}_t & \mathbb{1}_n \\ 0 & \boldsymbol{F} \end{pmatrix} \boldsymbol{y}_t + \begin{pmatrix} \boldsymbol{w}_t \\ \boldsymbol{\zeta}_t \end{pmatrix}. \tag{4.85}$$

Note that this model is now driven only by the white noise process $(\boldsymbol{w}_t^{\mathrm{T}}, \boldsymbol{\zeta}_t^{\mathrm{T}})$. By simply disregarding the extra components $\boldsymbol{\xi}_t$ in the extended state space vector $\boldsymbol{y}_t = (\boldsymbol{x}_t^{\mathrm{T}}, \boldsymbol{\xi}_t^{\mathrm{T}})^{\mathrm{T}}$, we end up with a state space model which describes the time evolution of the state space vector $\boldsymbol{x}_t$ but nevertheless is only driven by white noise. This extended state space model can therefore be used as the basis for the Kalman filter.

Hence, we only need to find suitable state space models of the form (4.83) which reproduce the (experimentally measured) spectral characteristics of the driving classical laser noise $\dot{\phi}_i$ and $\delta\alpha_{i,1}^{\mathrm{in}}$ in our experiment. We identified suitable models with the MATLAB system identification toolbox, using experimentally recorded time traces of the amplitude and frequency noise as input [see Wie+15, SM, II.B.]. Corresponding spectra were presented in the experimental chapter (see Section 3.1.5). We separately modeled three different types of laser noise: Broadband amplitude and phase noise, narrow-band low-frequency noise due to the laser lock, and the strong narrow-band phase modulation of the resonant beam at 20 MHz (used for PDH-locking of the laser to the optomechanical cavity).

model identification for colored laser noise

4.3.3 *Loss and detection model*

The measurements to which we apply the Kalman filter are homodyne measurements of generalized quadratures $z_{\phi,d}$ and $z_{\phi,r}$ of the reflected light field for the detuned and resonant beam, respectively. These are defined by

input to the Kalman filter: homodyne measurements

$$z_{\phi,i} \equiv \cos(\phi)\, x_i + \sin(\phi)\, y_i \;\; (i = \{r, d\}).$$

For the resonant beam, the homodyne detector was locked to the phase quadrature ($\phi_d \simeq 90°$). For the detuned beam, on the other hand, the homodyning phase was actually slowly scanned in time. This time-dependent homodyning phase can easily be incorporated in the Kalman filter. For the plots presented below, however, only data corresponding to a homodyne measurement of the amplitude quadrature of the detuned beam (i.e. $\phi_r \simeq 0°$) was selected.

extra-cavity quadratures

The generalized quadratures of the optical modes after reflection at the optomechanical cavity are, according to the cavity input-output relations (2.53), given by

$$z_i' = \left(\sqrt{2\kappa_1}\, x_i + x_{i,1}^{\text{in}} + \delta\alpha_{i,1}^{\text{in}}\right)\cos\phi_i + \left(\sqrt{2\kappa}\, y_i + y_{i,1}^{\text{in}}\right)\sin\phi_i, \quad (4.86)$$

In principle, (4.86) also contains a classical phase noise term proportional to ϕ_i. But this classical phase noise is common between local oscillator and signal and is therefore invisible in homodyning. We therefore do not need to include it in (4.86). The amplitude noise $\delta\alpha_{i,1}^{\text{in}}$, on the other hand, contributes to the homodyning signal and must therefore be included. $x_{i,1}^{\text{in}}$ and $y_{i,1}^{\text{in}}$ are shot noise terms which are perfectly correlated with the corresponding shot noise terms driving the intracavity modes according to (4.79) and (4.80). They are δ-correlated in time and have variance $1/2$.

colored measurement noise

The Kalman filter assumes the measurement noise to be white (see (4.41) and (4.43)). This is true for the noise terms $x_{i,1}^{\text{in}}$ and $y_{i,1}^{\text{in}}$. The laser amplitude noise term $\delta\alpha_{i,1}^{\text{in}}$, on the other hand, is—in the context of the extended state space model (4.85)—not considered a noise term, but part of the state vector. The noise term $\delta\alpha_{i,1}^{\text{in}}$ is therefore automatically taken into account by the correct choice of the measurement matrix (which relates the state vector to the measured variables).

optical losses and inefficient detection

Some of the light which is reflected from the optomechanical cavity is lost on its way to the homodyne detection setups. These optical losses, together with the inefficiencies of the photodetectors, can be modeled by beam splitter losses of strength η_i. The signals we actually measure are therefore described by

$$z_i = \sqrt{1-\eta}\, z_i' + \sqrt{\eta}\, z_i^{\text{in}}, \quad (4.87)$$

where z_i^{in} describes the additional shot noise (with variance $1/2$) associated with the optical losses. Note that the shot noise term z_i^{in} is statistically uncorrelated to the shot noise terms x_i^{in} and y_i^{in}.

detector characteristics

The response of our homodyne detectors is itself frequency-dependent. The frequency dependence of the detection is partially due to a band pass intrinsic to the detector circuits and partially due to an additional passive 12 MHz low pass filter in the signal path. The latter is necessary to suppress a very strong signal at 20 MHz (due to the PDH-modulation) far enough to prevent it from saturating our DAQ

system. To model the frequency dependent detector response, we resort once more to an extension of the state space model as discussed in Section 4.3.2. The measured quadratures are now considered part of an extended state space vector

$$\boldsymbol{y}_t' \equiv (\boldsymbol{x}_t^\mathrm{T}, \boldsymbol{\xi}_t^\mathrm{T}, \boldsymbol{z}_t^\mathrm{T}, \boldsymbol{\zeta}_t^\mathrm{T})^\mathrm{T}, \tag{4.88}$$

where $\boldsymbol{z}_t$ are the quadratures we would measure with perfect (frequency-independent) detectors and $\boldsymbol{\zeta}_t$ are the actually measured quadratures. If the transfer function of the detector is given by $\boldsymbol{H}(\Omega) = -(i\Omega + \boldsymbol{F})^{-1}$, then real and ideal measurements are related by

$$\dot{\boldsymbol{\zeta}}_t = \boldsymbol{F}\boldsymbol{\zeta}_t + \boldsymbol{z}_t. \tag{4.89}$$

Combining (4.86)–(4.89) for the measurements with the extended model (4.85) for the time evolution of the state vector, we can now write the complete state space model for our experiment in the form (4.66)–(4.67). A suitably discretized version of this model then completely defines the Kalman filter which we apply to the measurements which are digitized at a rate of 50 MHz.

complete state space model

4.4 RESULTS FROM KALMAN FILTERING

In this section, I explain the main results of the experiment published in [Wie+15]. I first explain how we assessed the accuracy of the filter (Section 4.4.1), then present example traces for the estimated quadratures in the weak and strong coupling regime (Section 4.4.2), and finally discuss the covariances of estimated quadratures and conditional cooling of the mechanical subsystem (Section 4.4.3).

4.4.1 *Innovation sequence*

Figure 4.1 shows measurements z_r and z_d and the corresponding Kalman filter predictions $\hat{z}_r$ and $\hat{z}_d$ (together with their expected uncertainties) over a period of 2 µs (100 sample points), for the resonant and detuned beam. In this figure (and all subsequent ones in this section), two different coupling regimes for the detuned beam are compared: weak coupling ($g_d \simeq 0.2 \times \kappa$; left panels) and strong coupling ($g_d \simeq 1.68 \times \kappa$; right panels).[31] For both weak and strong coupling, the Kalman filter predictions match the measurements very well within the expected uncertainty. To assess the quality of the filter more quantitatively, we analyzed the innovation sequence.

[31] *Note that the resonant beam is weakly coupled in both cases ($g_r \simeq 0.2 \times \kappa$).*

The innovation sequence (plotted below the main plots in Figure 4.1) is defined as the difference between actual and predicted measure-

innovation sequence

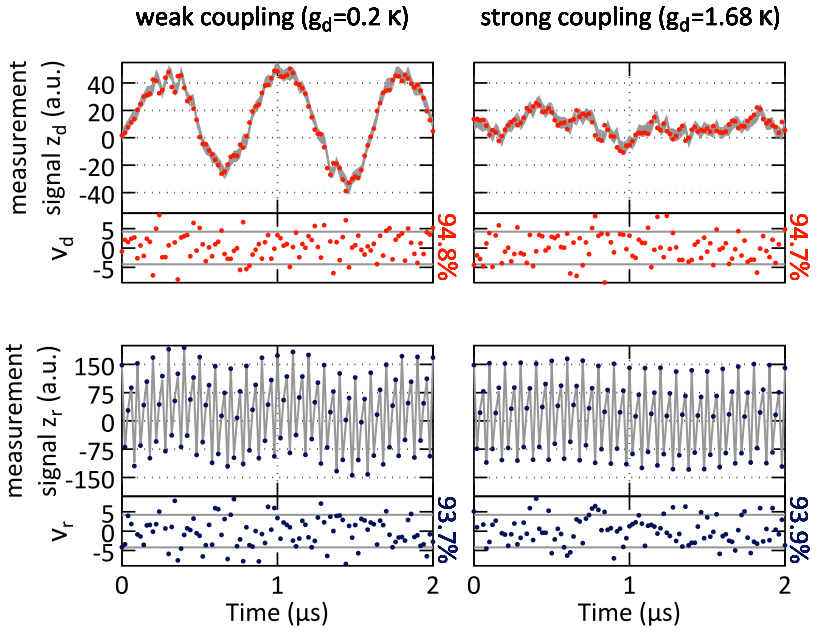

Figure 4.1. Observed and predicted measurement signals for weak coupling (left) and strong coupling (right). The top panels (red) refer to the detuned beam, bottom panels (blue) to the resonant beam. The actual measurements z_d and z_r are marked with colored dots, the Kalman filter predictions $\hat{z}_d$ and $\hat{z}_r$ are drawn as gray lines in the background; the width of the lines indicates the $\pm 2\sigma$-uncertainty of the predictions. The innovations $\nu_i = z_i - \hat{z}_i$ are shown below the main plots. If the system model is accurate, the innovations are a zero-mean, white, Gaussian noise. The expected variance σ^2 of the innovations can be predicted from the system parameters. The percentage of measured innovations which fall within $\pm 2\sigma$ around zero (indicated by horizontal gray lines) is displayed next to the innovation-plots; theoretically, the ratio should be $\simeq 95\,\%$, the measured values are all close to 95 %. The statistics of the innovations is analyzed in more detail in Figure 4.2. Note that observed and predicted measurements for the resonant beam (z_r and $\hat{z}_r$) are dominated by the 20 MHz-modulation for the PDH-lock. This modulation is well incorporated in our state space model as evidenced by the good fit of the innovations $\nu_r = z_r - \hat{z}_r$. Plots taken from [Wie+15].

ment outcome

$$\boldsymbol{\nu}_t \equiv \boldsymbol{z}_t - \hat{\boldsymbol{z}}_t \equiv \boldsymbol{z}_t - \boldsymbol{C}_t \hat{\boldsymbol{x}}_t \tag{4.90}$$
$$= \boldsymbol{C}_t \boldsymbol{x}_t + \boldsymbol{v}_t - \boldsymbol{C}_t \hat{\boldsymbol{x}}_t. \tag{4.91}$$

Using the definition of the estimation error $\boldsymbol{\epsilon}_t \equiv \boldsymbol{x}_t - \hat{\boldsymbol{x}}_t$, the innovations can be written as $\boldsymbol{\nu}_t = \boldsymbol{C}_t \boldsymbol{\epsilon}_t + \boldsymbol{v}_t$. Since the measurement error $\boldsymbol{v}_t$ and state estimation error $\boldsymbol{\epsilon}_t$ are uncorrelated and Gaussian with zero-mean, also the innovation $\boldsymbol{\nu}_t$ is Gaussian with zero-mean [Hei04, sec. 8.4.1]. Its covariance matrix $\boldsymbol{S}_t$ is given by

statistics of innovation sequence

$$\boldsymbol{S}_t \equiv \mathbb{E}\left[\boldsymbol{\nu}_t \boldsymbol{\nu}_t^\mathsf{T}\right] = \boldsymbol{C}_t \, \mathbb{E}\left[\boldsymbol{\epsilon}_t \boldsymbol{\epsilon}_t^\mathsf{T}\right] \boldsymbol{C}_t^\mathsf{T} + \mathbb{E}\left[\boldsymbol{v}_t \boldsymbol{v}_t^\mathsf{T}\right] = \boldsymbol{C}_t \boldsymbol{P}_t \boldsymbol{C}_t^\mathsf{T} + \boldsymbol{V}. \tag{4.92}$$

In addition, the innovation sequence is also white [Hei04, sec. 8.4.1].

Using the Cholesky decomposition $\boldsymbol{L}_t \boldsymbol{L}_t^\mathsf{T} = \boldsymbol{S}_t$ of the innovation covariance $\boldsymbol{S}_t$, we can define a normalized innovation sequence (NIS)

normalized innovation sequence (NIS)

$$\tilde{\boldsymbol{\nu}}_t \equiv \boldsymbol{L}_t^{-1} \boldsymbol{\nu}_t. \tag{4.93}$$

The normalized innovation sequence is a Gaussian zero-mean, unit-variance, white-noise process:

$$\tilde{\boldsymbol{\nu}}_t \sim \mathcal{N}\left(\tilde{\boldsymbol{\nu}}_t; 0, 1\right), \, \mathbb{E}\left[\tilde{\boldsymbol{\nu}}_t \tilde{\boldsymbol{\nu}}_\tau^\mathsf{T}\right] \propto \delta\left(t - \tau\right). \tag{4.94}$$

(4.94) holds only if the state space model accurately describes the experiment. We can therefore check the quality of the implemented filter—and therefore, indirectly, of the underlying state space model—by analyzing the distribution of the NIS and comparing it to (4.94).

statistics of innovations as consistency check

For our experiment, the measured NIS is, indeed, almost perfectly distributed according to a zero-mean, unit-variance Gaussian (see Figure 4.2 (a)). Also, the spectra of the NIS are indeed approximately white, over a wide frequency range (see Figure 4.2 (b)). The main deviations of the NIS spectra from a white spectrum are well understood: The broadband suppression at low frequencies can be attributed to an imperfect model of the detector response. And the very sharp noise peaks at frequencies of a few MHz correspond to unmodeled laser noise due to excited resonances of the laser cavity piezo. Since remaining errors of the model can often be identified based on their frequency-dependence, the spectra of the NIS are very helpful for improving the system model.

spectra of innovations

Apart from these checks based on the experimentally measured NIS, we also checked the Kalman filter using simulations. Such simulation-based tests obviously say nothing about the quality of the system model, but they can help to detect problems with the numerical implementation of the Kalman filter. We simulate time traces of the system state and the corresponding measurements using the state

simulation based tests

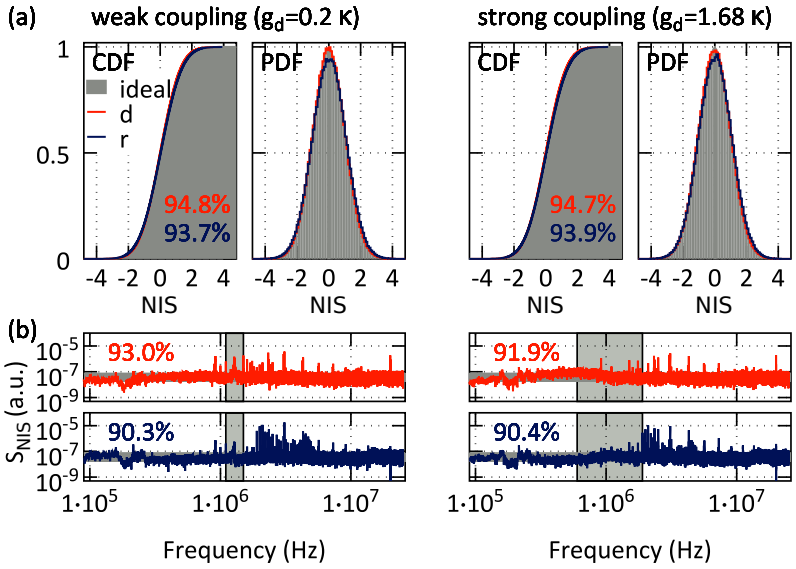

Figure 4.2. Statistics of the normalized innovation sequence (NIS). (a) Cumulative distribution functions (CDF) and histograms (PDF) of the experimentally measured NIS; red and blue for detuned and resonant beam) in comparison to the theoretical expectations (in gray) for a zero-mean, unit-variance Gaussian noise. (b) Noise power spectrum of the NIS (which is expected to be white). Horizontal shaded areas indicate the $\pm 2\sigma$ band around the expected noise power. This band should contain roughly 95 % of the data points of the measured noise power spectrum. The actual percentages (displayed in color next to the spectra) are around 90 % for the resonant and around 93 % (92 %) for the detuned beam in weak (strong) coupling. Vertical shaded areas around 1.28 MHz indicate the regions, where the measurements are dominated by the fundamental mechanical mode. Plots taken from [Wie+15, Supplemental Material].

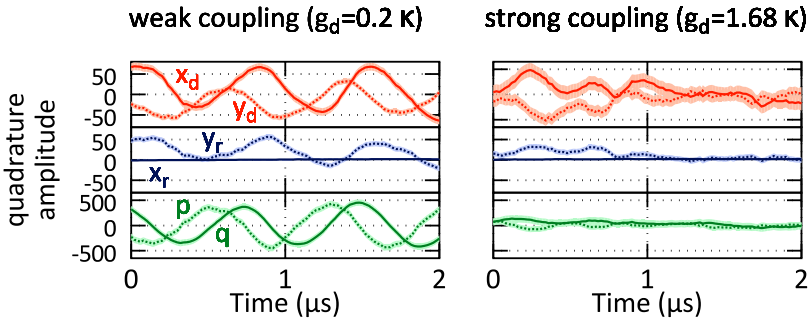

Figure 4.3. Kalman filter estimates of intracavity quadratures. The estimates are in units of ground state uncertainty, the shaded areas around the estimated traces indicate the $\pm 1\sigma$ estimation uncertainty. The top and middle panels show estimates for the detuned beam (red) and resonant beam (blue), respectively, for both the amplitude quadratures $\hat{x}_i$ (solid lines) and the phase quadratures $\hat{y}_i$ (dotted). Note that $\hat{x}_r$ is a horizontal line close to zero; this is expected since the mechanical motion does not couple to the amplitude quadrature for a resonant beam. The bottom panels shows the estimated position $\hat{q}$ and momentum $\hat{p}$ for the fundamental mechanical mode, which oscillate at the mechanical frequency $\omega_m \simeq 2\pi \times 1.278\,\mathrm{MHz}$. In the strong coupling regime (right panels), the mechanical motion is strongly suppressed due to sideband cooling. Plots taken from [Wie+15].

space model of the experiment. Then we apply the Kalman filter to the simulated measurements. This yields predicted measurements and predicted state variables. Using the predicted measurements, we calculate the NIS and check that it is indeed distributed as expected. Using the predicted state variables, on the other hand, we calculate the estimation errors and check that they are also distributed as expected (zero-mean with covariance $\boldsymbol{P}_t$). The latter is possible only in simulations, of course, since the state variables are unknown in the actual experiments.

Note that simulations are useful not only for guarding against possible mistakes in the implementation of the Kalman filter; they can also help to build intuition for the model and the Kalman filter since they allow us to directly compare the estimated and simulated state variables.

4.4.2 *Weak and strong coupling*

Figure 4.3 shows the optimal estimates of the intracavity quadratures for the optical modes and the fundamental mechanical mode. These estimates are the result of applying the Kalman filter to the measurement data shown in Figure 4.1. Again, we compare two regimes—weak coupling and strong coupling of the detuned beam—which yield markedly different results.

weak coupling

In the weak coupling regime, the fundamental mechanical mode oscillates coherently, driven by thermal noise. The quadratures of the detuned beam, $\hat{x}_d$ and $\hat{y}_d$, are strongly correlated with the mechanical quadratures, $\hat{q}$ and $\hat{p}$, respectively. This is a signature of the beam-splitter interaction, which swaps the mechanical state onto the detuned beam. For the resonant beam, on the other hand, only the phase quadrature $\hat{y}_r$ oscillates coherently, while the amplitude quadrature $\hat{x}_r$ is dominated by shot noise. This is because for a resonant beam, only the phase quadratures couples to the mechanical motion.

strong coupling

For strong coupling of the detuned beam, the amplitudes of motion for the mechanical mode and the resonant beam are much smaller due to sideband cooling of the mechanical mode. Nevertheless, the resonant phase quadrature $\hat{y}_r$ and the mechanical position $\hat{q}$ are still correlated. The quadratures of the detuned beam, on the other hand, fluctuate more strongly than the mechanical quadratures now. This is because thermal energy of the oscillator is dumped into the detuned beam. Note that the estimation uncertainty for the detuned beam is larger for strong coupling than for weak coupling. This is an experimental artifact. For technical reasons, we had to attenuate the detuned beam before the detection for the strong coupling measurements. Consequently, the signal to noise ratio was worse in this case.

Despite these clear differences between weak and strong coupling regarding the system dynamics, the Kalman filter innovations clearly fit the expectations in both cases (see Figure 4.2). This illustrates the versatility of the Kalman filter, which can be applied independently of the system parameters (as long as the system is in the Gaussian regime). Note that we do not need a new system model to achieve optimal state estimation for a different coupling regime. We only have to change the coupling strength g_d in the existing model. In practice, we also need to fine-tune some other parameters, such as the strength of the low-frequency phase and amplitude noise (changes with the lock condition of the laser), the exact value of the detuning, plus permille-level adjustments to the frequencies of some mechanical modes.

4.4.3 *Conditional cooling*

phase space trajectories

Figure 4.4 shows examples of estimated phase-space trajectories of the intracavity system state. Since the estimated system state $\hat{\boldsymbol{x}}_t$ is more than two-dimensional, we have to project down to two quadratures to be able to plot phase space trajectories. The top panels show trajectories $(\hat{q}_t, \hat{p}_t)$ for the fundamental mechanical mode during 100 µs. These trajectories illustrate the Brownian motion of the

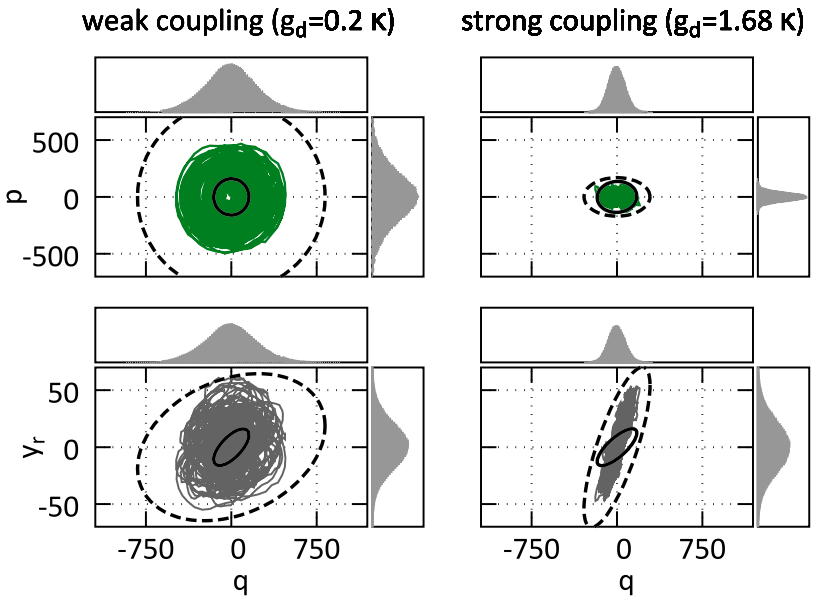

Figure 4.4. Kalman filter estimates in phase space for weak coupling (left) and strong coupling (right). Top panels show estimates $(\hat{q}_t, \hat{p}_t)$ of the mechanical position and momentum for a 100 µs-trace; bottom panels show analogous plots for $\hat{y}_r$ and $\hat{q}$. Everything in units of ground state uncertainty. Histograms of the estimated quadratures (from 10 ms-traces) are shown on top and to the right of the phase-space plots. The covariances of the unconditional (conditional) state are displayed on top of the trajectories as a dashed (solid) ellipse. Note that the the unconditional state ellipses are not filled by the estimated trajectories because of their limited duration of only 100 µs. Plots taken from [Wie+15].

mechanical oscillator, i.e. thermally driven damped motion with a strong harmonic component. The marginal distribution of $\hat{q}_t$ and $\hat{p}_t$ are illustrated by histograms on top and to the right of the phase space plots (histograms are based on 10 ms-traces to gather sufficient statistics). As expected for thermally driven mirror motion, the marginal distributions are Gaussian.

The plots in Figure 4.4 should be compared to analogous plots in the pioneering experiment on reconstruction of the mechanical phase space [Bri+03, fig. 3]. A clear advance over earlier experiments such as [Bri+03] is that the Kalman filter also provides the estimation error covariance matrix $\boldsymbol{P}_t$. Recall that estimation errors are distributed according to a Gaussian with zero mean and covariance matrix $\boldsymbol{P}_t$. The estimation error $\boldsymbol{P}_t$ can therefore, when projected onto a two-dimensional subspace, be illustrated by ellipses (solid lines in the phase space plots in Figure 4.4). In general, the estimation errors for different components of the state vector can be correlated, corresponding to ellipses which are skewed with respect to the coordinate axes.

estimation error

conditional cooling

The estimation error is our uncertainty about the system state after the measurements, i.e. conditional on the measurements ("conditional uncertainty"). The variance of the unconditional state (i.e., the steady state), on the other hand, is our uncertainty about the system state prior to any measurement ("unconditional uncertainty"). Comparing the conditional and unconditional uncertainty therefore yields a measure of the information we gained in the measurements. Figure 4.4 compares the conditional uncertainties (solid line ellipses) to the unconditional uncertainties (dashed ellipses). The conditional uncertainty is significantly reduced compared to the unconditional one, corresponding to a reduction in effective temperature by a factor of 27 in the case of weak coupling. Because the Kalman filter is optimal, this reduction in uncertainty is the optimum given our experimental setup. Note that the reduced effective mode temperature for the conditional state is closely related to (but not identical with) the steady-state mode temperature which can be achieved via optimal feedback cooling using the Kalman filter estimates [see HH15].

unconditional cooling

The unconditional uncertainty of the mechanical system is much smaller for strong coupling than for weak coupling. This is a result of the (unconditional) sideband cooling due to the detuned beam. The conditional uncertainty, however, is very similar in both coupling regimes. Correspondingly, the conditional cooling effect is much weaker for strong coupling than for weak coupling. This is an artifact of our measurement: For technical reasons, we had to attenuate the detuned beam to the same optical power in both coupling regimes before the detection.[32] Therefore, the detuned beam cannot provide more information in the strong coupling case (which it normally would).

[32] *This attenuation has been taken into account in the state space model.*

The bottom panels in Figure 4.4 show estimated trajectories of the resonant phase quadrature $\hat{y}_r$and the position $\hat{q}$ of the fundamental mechanical mode. This illustrates another clear advantage of the Kalman filter over [Bri+03]: The Kalman filter allows us to estimate the not only mechanical quadratures, but also the intracavity light quadratures themselves (and any other modeled system variable). The uncertainty ellipses in Figure 4.4 show that the resonant phase quadrature and the position of the fundamental mechanical mode are correlated both unconditionally (as expected from the optomechanical interaction) as well as conditionally. Note that the unconditional correlation of these quadratures is far from perfect. This makes sense since multiple mechanical modes as well as classical laser noise influence the resonant phase quadrature. Despite this underwhelming correlation, the Kalman filter can salvage a surprising amount of information about the position of the fundamental mechanical mode from the resonant phase quadrature by systematically taking into account the full system dynamics. In previous experiments, estimation

of the mechanical position from measurements of the light quadratures was only achieved in an ad-hoc fashion, by band-pass filtering the measurement signals around the mechanical resonance.

4.5 DISCUSSION AND OUTLOOK

As mentioned, state estimation has been realized in cavity optomechanics already a long time ago. Let me therefore quickly summarize previous experimental work and the main advances of our approach over it. Some of the earliest experiments in optomechanics demonstrated real-time estimation of the mechanical position in the weak coupling regime: [Had+99] observed the Brownian motion of the fundamental mechanical mode of a macroscopic mirror using a weak, resonant readout beam, while [Tit+99] achieved the same at cryogenic temperatures for a microscopic mirror. In principle, these experiments yield real-time state estimates which can be used for feedback cooling, as demonstrated by [CHP99]. However, the state estimates achieved in these experiments are in general suboptimal, which translates into suboptimal cooling performance. The Kalman filter provides a provably optimal estimate and correspondingly the optimal feedback cooling performance. In fact, Kalman filtering would, for suitable experimental parameters, allow feedback cooling to the quantum ground state [HH15]. This requires a measurement in the regime of strong cooperativity $g^2 > \kappa\gamma_m\bar{n}$, which has been achieved in a couple of recent experiments [Bre+08; Mur+08; PPR13; Wil+15]. The experimental parameters of the early experiments (as well as of the experiment presented here) are not sufficient for feedback control at the quantum level, however.

previous work

real-time estimation and feedback cooling

feedback cooling to the ground state

The experiments of the late 1990s estimated only the mechanical position. [Bri+03] improved on this by simultaneously monitoring both the position and momentum quadrature of a mirror mode. In this way they provided a complete reconstruction of the mechanical phase space of the oscillator. Here again, the Kalman filter represents an important generalization since it allows the complete reconstruction of not only the mechanical quadratures but all modeled variables including the optical intracavity quadratures and the position and momentum of all significantly interacting mechanical modes.

advantages of the Kalman filter...

...estimation of the complete system state

Note that [Bri+03] uses a band-pass filter to suppress the effects of other mechanical modes. Such ad-hoc methods can work (as long as the modes are well separated) but they are suboptimal and the resulting estimation errors are usually not quantified. In contrast, the Kalman filter allows a systematic treatment of multiple mechanical modes (as well as many other experimental imperfections) and provides us with a theoretically well-founded estimate of the estimation error.

...optimal and systematic

...universal

The early estimation experiments were restricted to the weak coupling regime. The plots in Figure 4.1 and Figure 4.2 demonstrate that the Kalman filter works equally well for both weak and strong coupling—even though the dynamics and correlations of the optomechanical system changes significantly (see Figure 4.4).

...time-domain estimation

Other earlier work has aimed at a full characterization of the mechanical state in the frequency-domain: [Pat+06] show (theoretically) how the noise power spectrum of the position of a mechanical mode can be inferred from measurements of the phase quadrature of the reflected field. They do so for arbitrary detuning, which makes the method more general than the experiments discussed before. But this work does not yield a real-time estimate of the mechanical position. Hence, in contrast to our approach, it is unsuitable as a basis for real-time feedback.

...real-time

In this experiment, we have applied the Kalman filter off-line to previously recorded data. Hence, while demonstrating the suitability of the filter for cavity optomechanical systems, we have not implemented the Kalman filter in real-time. But the recursive nature of the Kalman filter makes a real-time implementation possible in principle. In practice, this requires suitably fast hardware which can read the measurement signals fast enough and at sufficient precision and perform the required matrix computations fast enough (much faster than a mechanical period). The requirements are discussed in more detail in [Wie+15, Supplemental Material, V.]. For our experimental parameters, currently available field programmable gate arrays (FPGAs) would allow the implementation of real-time estimation (using the Kalman filter) and feedback.

5

TOWARDS PULSED-CONTINUOUS ENTANGLEMENT

5.1 INTRODUCTION

How can we entangle a mechanical oscillator with laser light? In cavity optomechanics, entanglement between a mechanical oscillator and laser light ("light–mechanics entanglement") can be produced via the two-mode squeezing part of the optomechanical interaction [see Hof15, p. 14], as discussed in Section 2.5.1. In an optomechanical cavity with mechanical frequency ω_m and driven with laser light at frequency ω_l, the two-mode squeezing interaction simultaneously creates photons (at frequency $\omega_l - \omega_m$) and phonons (at frequency ω_m). This interaction can produce a state with a strong correlation between photon-number and phonon-number. For the right parameters (sufficiently strong coupling together with sufficiently low decoherence), the mechanical oscillator can even become entangled with the laser light. The dependence of the light-mechanics entanglement on the optomechanical parameters has been presented systematically in [Hof15]. For continuously driven optomechanical systems, light-mechanics entanglement can—due to stability requirements—only be achieved with red-detuned laser drives, and it requires large coupling or cooperativity [Hof15, sec. 1.4]. In pulsed protocols, on the other hand, light–mechanics entanglement can also be created by driving on the blue side [see Hof15, sec. 2.1, and references therein].

How to create light–mechanics entanglement?

But how can we detect light–mechanics entanglement? The only way of reading out the mechanical position with sufficient precision is to rely on the cavity-optomechanical interaction once again, this time on the beam splitter part of the interaction. The beam-splitter interaction destroys phonons (frequency ω_m) to create photons at frequency $\omega_l + \omega_m$, thereby swapping the state of the mechanical oscillator onto the cavity light, as discussed in Section 2.5.1. If the mechanical oscillator was entangled with another system X before, then the cavity light will become entangled with X as a consequence of the beam-splitter interaction.

How to detect light–mechanics entanglement?

By suitably combining the creation of light–mechanics entanglement (using the two-mode squeezing interaction) with a mechanics-to-light state swap (using the beam-splitter interaction) we are able to generate "mechanically mediated" entanglement between different modes of the returning light field ("light-light entanglement"). Detection of this light-light entanglement can serve as an indirect way

light-light entanglement

of detecting light–mechanics entanglement. Two different protocols which achieve this—one pulsed and one continuous—are described in the following.

5.2 PULSED ENTANGLEMENT GENERATION AND DETECTION

A conceptually simple way of combining entanglement creation with a state swap was proposed by [Hof+11] and has been realized experimentally using microwaves by [Pal+13b]. The basic idea of this protocol is to use distinct pulses, first a blue-detuned pulse, then a red-detuned pulse, to implement a sequence of entanglement generation and state swap. Finally, homodyne measurements are performed on the returning pulses to verify that light-light entanglement has indeed been created.

[33] *Pulsed entanglement protocol*

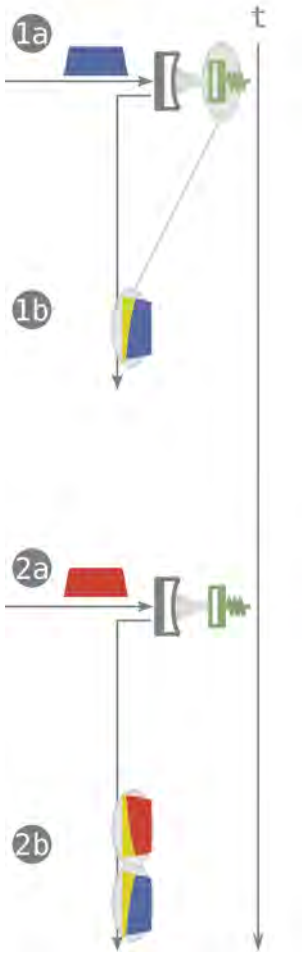

The steps of the pulsed protocol are sketched in the margin:[33]

1. Entanglement generation
   a) A blue-detuned pulse is sent onto an optomechanical cavity. The pulse is at frequency $\omega_c + \omega_m$, where ω_c is the resonance frequency of the optomechanical cavity and ω_m the frequency of the mechanical mode. The cavity enhances the (down-)scattering onto the cavity resonance which is equivalent to a two-mode squeezing interaction acting on the mechanical mode and the cavity mode.
   b) The returning blue pulse contains light scattered onto resonance (yellow in the drawing in the margin) via the two-mode squeezing interaction. This light has become entangled with the mechanical oscillator (green in the drawing).
2. Entanglement swap
   a) A red-detuned pulse (at frequency $\omega_c - \omega_m$) is sent onto the optomechanical cavity. Again, the cavity enhances the scattering onto the cavity resonance, but this time the scattering is upward in frequency. This means a beam-splitter interaction is taking place which swaps the mechanical state onto the second pulse.
   b) The returning red pulse contains a resonant sideband (yellow in the sketch in the margin) onto which the state of the mechanical oscillator has been partially swapped. Therefore (the resonant part of) the returning red pulse is now entangled with (the resonant part of) the returning blue pulse and mechanically mediated light-light entanglement has been created.

verification of light-light entanglement

To verify the entanglement, homodyne measurements are performed on both pulses. The full covariance matrix of the two-pulse system is then reconstructed by correlating the measurement outcomes on the individual pulses. Finally, the entanglement of the two-pulse system is calculated on the basis of the measured covariance matrix.

essence of pulsed entanglement detection

The heart of the pulsed protocol for entanglement detection is to measure a correlation between *down-scattered light* (resulting from the two-mode squeezing part of the interaction) *at earlier times and up-scattered light* (from the beam-splitter part) *at later times*. Under the right conditions (sufficiently strong interaction, sufficiently low decoherence), entanglement can be detected in this way. In the following section, I will demonstrate that this idea for entanglement detection is more generally applicable and not restricted to the pulsed protocol of [Hof+11]. In particular, I will show how—using a very similar correlation measurement between down-scattered light at earlier times and up-scattered light at later times—we can detect mechanically-mediated light-light entanglement even for a continuously driven optomechanical system, where the drive can be on resonance or red-detuned.

The protocol which is presented in the following was first proposed by Klemens Hammerer (University of Hannover) and Sebastian Hofer (University of Vienna). The extension of the protocol to the case of multiple mechanical modes is due to myself. This extension (as well as other improvements to the original proposal) was developed in collaboration with Hofer and Hammerer as well as the people involved in the experimental effort at the university of Vienna (Witlef Wieczorek, Ramon Moghadas Nia, Claus Gärtner, and Corentin Gut).

5.3 PULSED-CONTINUOUS ENTANGLEMENT GENERATION AND DETECTION

In the remainder of this chapter, I discuss the generation of entanglement via the optomechanical interaction in a continuously driven optomechanical cavity (as sketched in the margin).[34] I will demonstrate that already this simplest possible setup can give rise to entanglement and to an astonishingly rich correlation structure.

[34] *Experimental setting: Continuously driven optomechanical system*

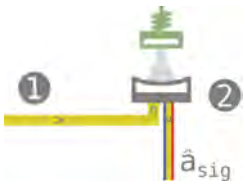

1. We drive an optomechanical cavity continuously with resonant laser light at frequency $\omega_l = \omega_c$ (yellow in the sketch).

2. The optomechanical interaction of the laser light with the mechanical device (green in the sketch) leads to the creation of red and blue sidebands (at $\omega_l - \omega_m$ and $\omega_l + \omega_m$, respectively) inside the cavity. The returning light (mode operator $\hat{a}_{sig}$) contains a contribution from the intra-cavity light. Therefore, it also carries the red and blue sidebands.

distinguishing contributions from two-mode squeezing and beam-splitter interaction

Because we drive continuously and on resonance, both the two-mode squeezing interaction (down-scattering) and the beam-splitter interaction (up-scattering) take place continuously and at the same time. Therefore,—in sharp contrast to the pulsed protocol discussed above —we cannot anymore distinguish the contributions from the two-mode squeezing and the beam-splitter interaction based on timing. But these contributions can of course be distinguished based on frequency: light at $\omega_l - \omega_m$ arises from the two-mode squeezing interaction, while light at $\omega_l + \omega_m$ arises from the beam-splitter interaction. The general idea, therefore, is to correlate light at frequencies close to $\omega_l - \omega_m$ at earlier times with light at frequencies close to $\omega_l + \omega_m$ at later times.

5.3.1 *Correlations in time and frequency*

To correlate the different frequency components (upper and lower sidebands) in the returning light field $\hat{a}_{\mathrm{sig}}$ during different time intervals, we have to perform a time–frequency analysis of $\hat{a}_{\mathrm{sig}}$.

mode functions

To this end, we define the following so-called "mode functions"

$$\alpha(t) \equiv \mathcal{N}_\alpha \cdot \exp(i\omega_m t) \times \exp(\Gamma t) \ (\text{for } t \leq 0), \tag{5.1}$$

$$\beta(t) \equiv \mathcal{N}_\beta \cdot \exp(-i\omega_m t) \times \exp(-\Gamma t) \ (\text{for } t \geq 0). \tag{5.2}$$

$\mathcal{N}_\alpha$ and $\mathcal{N}_\beta$ are real normalization constants to be determined later. This leaves two free (real) parameters in the above definitions, ω_m and Γ, which need to be adapted to the experiment we want to analyze. In the mode functions above, $\pm\omega_m$ parametrizes a complex rotation and $\pm\Gamma$ an exponential envelope. The basic idea, explained in more detail later, is to set ω_m to the mechanical frequency and Γ to, roughly, the mechanical decoherence time.

The mode functions (5.1) and (5.2) can be used to implement bandpass filtering of a complex signal $c(\tau)$ around the upper and lower mechanical sideband. The signal $c(\tau)$ we are interested in results, as explained in more detail later, from homodyne measurements on the returning light field $\hat{a}_{\mathrm{sig}}$. Since the local oscillator in the homodyne measurement is at the drive frequency ω_l, the signal $c(\tau)$ will consist of a carrier at frequency 0 and sidebands at at $\pm\omega_m$. Therefore, $c(\tau)$ is roughly of the following form:

$$c(\tau) = c_0(\tau) + c_+(\tau) \cdot \exp(i\omega_m\tau) + c_-(\tau) \cdot \exp(-i\omega_m\tau), \tag{5.3}$$

where c_0, c_+, and c_- are the slowly varying amplitudes of the carrier and upper and lower sideband, respectively. c_0, c_+, and c_- are assumed to vary slowly on the time-scale of the mechanical frequency ω_m, hence to be approximately constant over one mechanical period

$T = 1/\omega_m$. This implies that, for any integration period $[t, t+T]$ of duration T, the following holds:

$$\left| \int_t^{t+T} \mathrm{d}\tau \, \exp\left(\pm i\omega_m \tau\right) \cdot c_{0,+,-}\left(\tau\right) \right| \ll \left| \int_t^{t+T} \mathrm{d}\tau \, c_{0,+,-}\left(\tau\right) \right| . \tag{5.4}$$

If we multiply $c\left(\tau\right)$ by the mode function $\alpha\left(\tau\right)$ and integrate, we obtain (assuming $\Gamma \ll \omega_m$)

$$\begin{aligned} a_0 &\equiv \int_{-\infty}^{0} \alpha\left(\tau\right) \, c(\tau) \mathrm{d}\tau && (5.5)\\ &\propto \int_{-\infty}^{0} \mathrm{d}\tau \, \exp\left(\Gamma\tau\right) \cdot \Big(c_-(\tau) + \ldots && (5.6)\\ &\ldots \exp\left(i\omega_m\tau\right) \cdot c_0(\tau) + \exp\left(2i\omega_m\tau\right) \cdot c_+(\tau) \Big) && (5.7)\\ &\simeq \int_{-\infty}^{0} \mathrm{d}\tau \, \exp\left(\Gamma\tau\right) \cdot c_-(\tau), && (5.8) \end{aligned}$$

where the last approximate equality is justified by (5.4). Hence, a_0 is (roughly) an exponentially weighted mean of the amplitude of the lower sideband $c_-(\tau)$ in the time interval $[-1/\Gamma, 0]$. Analogously, integration of $c\left(\tau\right)$ with $\beta(\tau)$ yields roughly an exponentially weighted mean of the amplitude $c_+\left(\tau\right)$ of the upper sideband. Figure 5.1 sketches the mode functions $\alpha\left(t\right)$ and $\beta\left(t\right)$ in the time domain and their filter effect in frequency.

5.3.1.1 *Pulse modes*

We can use the mode functions $\alpha\left(t\right)$ and $\beta\left(t\right)$ to define new mode operators $\hat{a}_t$ and $\hat{b}_t$ based on our signal field $\hat{a}_{\mathrm{sig}}$, as follows:

canonical transformation to new light modes

$$\hat{a}_t \equiv \int_{-\infty}^{t} \alpha\left(\tau - t\right) \, \hat{a}_{\mathrm{sig}}(\tau) \mathrm{d}\tau, \tag{5.9}$$

$$\hat{b}_t \equiv \int_{t}^{+\infty} \beta\left(\tau - t\right) \, \hat{a}_{\mathrm{sig}}(\tau) \mathrm{d}\tau. \tag{5.10}$$

This defines light modes which are localized both in time and frequency. In time, they are restricted to times before (after) time t, respectively. In frequency, they are centered (relative to the carrier frequency of the light field) at $-\omega_m$ ($+\omega_m$), hence at the lower (upper) sideband. This is illustrated in Figure 5.1 (b).

candidate light modes for mechanically mediated entanglement

These new modes have similar properties to the modes analyzed in the pulsed protocol. They are populated predominantly via the two-mode squeezing (beam-splitter) interaction and are adjacent in time. They can therefore become entangled analogously to the way two light pulses can become entangled in the pulsed protocol via a

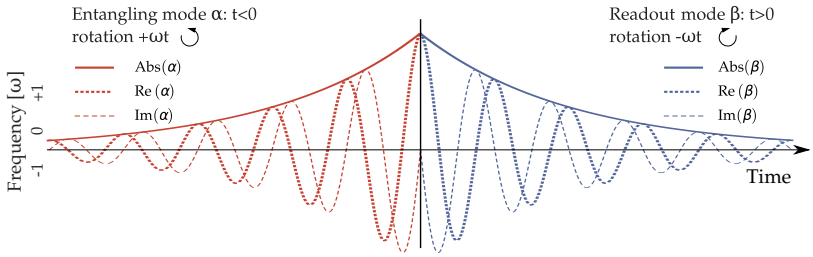

(a) Mode functions in the time domain.

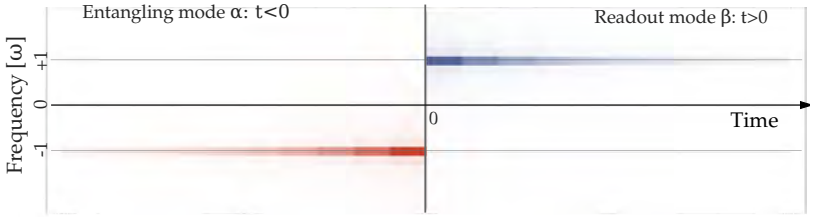

(b) Time–frequency representation of filter effect of the mode functions.

Figure 5.1. Mode functions (5.1) and (5.2) in the time-domain (Figure 5.1a) and their filter effect in time and frequency (Figure 5.1b). For $t < 0$, the rotation of the mode function is $+\omega t$ which means that, by integrating a signal with the mode function as defined in (5.9), contributions from the red sideband (frequency $\omega_l - \omega_m$, originating from the two-mode squeezing interaction) are picked out. For $t > 0$, the rotation is in the opposite direction such that contributions from the blue sideband (frequency $\omega_l + \omega_m$, originating from the beam-splitter interaction) are picked out. Figure 5.1b illustrates which frequency components at which time contribute most strongly to the entangling mode (5.9) and readout mode (5.10) (calculated based on a windowed Fourier transform).

sequence of light–mechanics entanglement generation and mechanics–light entanglement swap.

If we want to calculate entanglement between the light modes defined by the mode operators $\hat{a}_t$ and $\hat{b}_t$, we need them to obey canonical commutation relations:

canonical commutation relations

$$\left[\hat{a}_t, \hat{a}_t^\dagger\right] = \left[\hat{b}_t, \hat{b}_t^\dagger\right] = 1, \tag{5.11}$$

$$\left[\hat{a}_t^{(\dagger)}, \hat{b}_t^{(\dagger)}\right] = 0. \tag{5.12}$$

The commutators in (5.12) vanish trivially since $\hat{a}_t^{(\dagger)}$ and $\hat{b}_t^{(\dagger)}$have no overlap in time and $\left[\hat{a}_{\mathrm{sig}}(\tau_1), \hat{a}_{\mathrm{sig}}^\dagger(\tau_2)\right] = 0$, for all $\tau_1 \neq \tau_2$. Regarding (5.11), we have

$$\left[\hat{a}_t, \hat{a}_t^\dagger\right] = \iint_{-\infty}^{t} \mathrm{d}\tau_1 \, \mathrm{d}\tau_2 \, \alpha(\tau_1 - t)\alpha^*(\tau_2 - t) \underbrace{\left[\hat{a}_{\mathrm{sig}}(\tau_1), \hat{a}_{\mathrm{sig}}^\dagger(\tau_2)\right]}_{=\delta(\tau_1-\tau_2)} \tag{5.13}$$

$$= \int_{-\infty}^{t} \mathrm{d}\tau \, |\alpha(\tau - t)|^2, \tag{5.14}$$

$$\left[\hat{b}_t, \hat{b}_t^\dagger\right] = \ldots = \int_{t}^{+\infty} \mathrm{d}\tau \, |\beta(\tau - t)|^2. \tag{5.15}$$

Hence, $\hat{a}_t$ and $\hat{b}_t$ are legitimate quantum-mechanical mode operators exactly if the mode functions $\alpha(t)$ and $\beta(t)$ are normalized. The normalization constants $\mathcal{N}_\alpha$ and $\mathcal{N}_\beta$ are therefore chosen to be:

normalization of the mode functions

$$\mathcal{N}_\alpha = 1/\sqrt{\int_{-\infty}^{t} \mathrm{d}\tau \, |\alpha(\tau - t)|^2}, \tag{5.16}$$

$$\mathcal{N}_\beta = 1/\sqrt{\int_{t}^{+\infty} \mathrm{d}\tau \, |\beta(\tau - t)|^2}. \tag{5.17}$$

5.3.1.2 *Pulse quadratures*

Next, we define amplitude and phase quadratures for these new modes:

amplitude and phase of entangling and readout mode

$$\hat{Q}_t \equiv \mathrm{Re}(\hat{a}_t), \; \hat{P}_t \equiv \mathrm{Im}(\hat{a}_t), \tag{5.18}$$

$$\hat{X}_t \equiv \mathrm{Re}\left(\hat{b}_t\right), \; \hat{Y}_t \equiv \mathrm{Im}\left(\hat{b}_t\right). \tag{5.19}$$

We collect these quadrature operators into a column vector $\hat{\boldsymbol{R}}^{(t)} \equiv \left(\hat{Q}_t, \hat{P}_t, \hat{X}_t, \hat{Y}_t\right)^{\mathsf{T}}$ to define the covariance matrix $\boldsymbol{\sigma}$ of the two-mode system consisting of the entangling and the readout mode [see AI07, p. 7827] with matrix entries

covariance matrix of entangling and readout mode

$$\boldsymbol{\sigma}_{ij} \equiv {}^1\!/_2 \left\langle \hat{\boldsymbol{R}}_i \hat{\boldsymbol{R}}_j + \hat{\boldsymbol{R}}_j \hat{\boldsymbol{R}}_i \right\rangle - \left\langle \hat{\boldsymbol{R}}_i \right\rangle \left\langle \hat{\boldsymbol{R}}_j \right\rangle. \tag{5.20}$$

Here, $\langle \hat{O} \rangle \equiv \mathrm{tr}\left(\rho_{\mathrm{sig}} \hat{O}\right)$ denotes the quantum-mechanical expectation value of an operator $\hat{O}$ with respect to the quantum state ρ_{sig} of the output light field $\hat{a}_{\mathrm{sig}}$.

Note that the covariance matrix (5.20) still implicitly refers to the "split moment" t which separates the two modes $\hat{a}_t$ and $\hat{b}_t$ defined

stationarity of the covariance matrix

above. But if we calculate the matrix elements σ_{ij} (using the definitions of the pulse modes) we find that they are all sums of integrals of the form

$$\iint_{-\infty}^{t} \mathrm{d}\tau_1 \mathrm{d}\tau_2\, \alpha(\tau_1 - t)\, \alpha(\tau_2 - t)\, \langle \hat{a}_{\mathrm{sig}}(\tau_1)\, \hat{a}_{\mathrm{sig}}(\tau_2) \rangle = \dots \tag{5.21}$$

$$\underbrace{\tau_{1/2} \to \tau_{1/2} + t}_{=} \iint_{-\infty}^{0} \mathrm{d}\tau_1 \mathrm{d}\tau_2\, \alpha(\tau_1)\, \alpha(\tau_2)\, \langle \hat{a}_{\mathrm{sig}}(\tau_1 + t)\, \hat{a}_{\mathrm{sig}}(\tau_2 + t) \rangle$$

or similar with one or both of the α replaced by α^*, β, or β^* (with suitably adjusted integration limits in the case of β or β^*) and one or both of the $\hat{a}_{\mathrm{sig}}$ replaced by its Hermitian conjugate. Hence, the implicit t-dependence of σ_{ij} can always be reduced to the t-dependence of expressions like $\langle \hat{a}_{\mathrm{sig}}^{(\dagger)}(\tau_1 + t)\, \hat{a}_{\mathrm{sig}}^{(\dagger)}(\tau_2 + t) \rangle$, where the expectation value $\langle \dots \rangle$ is with respect to the quantum state ρ of the returning light field. Experimentally, there is only one potential reason for an explicit time-dependence of these expectation values: the switching on of the laser at a time t_0. But since, in the experiment, we are always working in a stable regime,[35] such switching effects are exponentially damped out such that, for times $t_1, t_2 \gg t_0$ (which are the only times relevant for our measurement) we have

$$\langle \hat{a}_{\mathrm{sig}}^{(\dagger)}(\tau_1 + t_1)\, \hat{a}_{\mathrm{sig}}^{(\dagger)}(\tau_2 + t_1) \rangle \simeq \langle \hat{a}_{\mathrm{sig}}^{(\dagger)}(\tau_1 + t_2)\, \hat{a}_{\mathrm{sig}}^{(\dagger)}(\tau_2 + t_2) \rangle\,. \tag{5.22}$$

[35] *Note that, for this reason, the laser drive is never perfectly resonant in the experiment but always at least slightly red-detuned.*

Hence, the covariance matrix of the pulse quadratures (5.20) is, for all practical purposes, stationary.

Summing up, we can consider $\hat{a}_t$ and $\hat{b}_t$ as annihilation operators for two new light modes, the "entangling mode" and the "readout mode", respectively. The entangling mode is restricted to times $\tau < t$ and centered at the lower sideband, while the readout mode is restricted to times $\tau > t$ and centered at the upper sideband. These modes can become entangled via the optomechanical interaction as will be shown below in Section 5.4. The quantum state of the new modes $\hat{a}_t$ and $\hat{b}_t$ is Gaussian since they are linear combinations of the operators $\hat{a}_{\mathrm{sig}}(\tau)$ at different times and $\hat{a}_{\mathrm{sig}}(\tau)$ is in a Gaussian state at all times. Therefore, the entanglement of the new modes $\hat{a}_t$ and $\hat{b}_t$ is completely determined by their covariance matrix σ. In what follows, I will explain how we can actually measure the covariance matrix σ of the pulse modes $\hat{a}_t$ and $\hat{b}_t$ in our experiment.

5.3.2 *Dual-rail homodyne detection*

We can measure the returning light field $\hat{a}_{\mathrm{sig}}$ approximately—with a known statistical error—using "dual-rail homodyning". In the liter-

ature, this is also known as "8 port homodyning", "8 port junction", "4×4 directional coupler" or, in the microwave domain, as a "dual balanced receiver" [see Wal87, p. 42].

In the margin, the full experiment including the dual-rail homodyning is sketched:[36]

[36] *Pulsed-continuous entanglement protocol: dual rail homodyning*

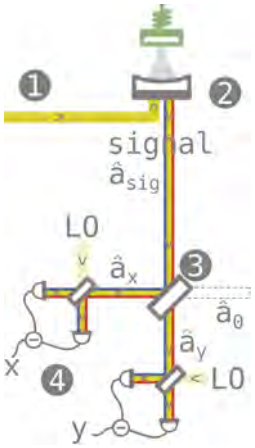

1. An optomechanical cavity is driven continuously with resonant laser light (frequency $\omega_l = \omega_c$; yellow in the sketch).

2. The optomechanical interaction of the laser light with the mechanical device (green in the sketch) creates red and blue sidebands sidebands at $\omega_l - \omega_m$ and $\omega_l + \omega_m$ inside the cavity and on the returning light (mode operator $\hat{a}_{sig}$).

3. We split the returning light on a 50/50 beam splitter. We obtain two fields $\hat{a}_x$ and $\hat{a}_y$ which are given by

$$\begin{pmatrix} \hat{a}_x \\ \hat{a}_y \end{pmatrix} = \frac{1}{\sqrt{2}} \begin{pmatrix} 1 & 1 \\ 1 & -1 \end{pmatrix} \begin{pmatrix} \hat{a}_{sig} \\ \hat{a}_0 \end{pmatrix}. \tag{5.23}$$

   The mode operator $\hat{a}_0$ corresponds to the unused port of the beam splitter, which is in the vacuum state.

4. We continuously measure the amplitude quadrature $\hat{x} \equiv \left(\hat{a}_x + \hat{a}_x^\dagger\right)/\sqrt{2}$ on the field $\hat{a}_x$ and the phase quadrature $\hat{y} \equiv \left(\hat{a}_y - \hat{a}_y^\dagger\right)/i\sqrt{2}$ on $\hat{a}_y$ using homodyne detection and obtain as measurement results $x(t)$ and $y(t)$, respectively.

estimate of the complex amplitude of the signal beam

By combining the measurement results x and y into $c \equiv \sqrt{2}(x + iy)$, we obtain an estimate for the full complex field amplitude of the signal mode $\hat{a}_{sig}$. Correspondingly, we can define an operator

$$\hat{c} \equiv \sqrt{2}(\hat{x} + i\hat{y}) = \ldots = \left(\hat{x}_{sig} + i\hat{y}_{sig}\right) + \left(\hat{x}_0 - i\hat{y}_0\right), \tag{5.24}$$

where $\hat{x}_{sig} \equiv \left(\hat{a}_{sig} + \hat{a}_{sig}^\dagger\right)/\sqrt{2}$ and $\hat{y}_{sig} \equiv \left(\hat{a}_{sig} - \hat{a}_{sig}^\dagger\right)/i\sqrt{2}$ are the amplitude and phase quadrature of the returning signal beam, respectively, and $\hat{x}_0$ and $\hat{y}_0$ analogously for the unused port of the 50/50 beam splitter (vacuum input). We have

$$\hat{c} = \hat{a}_{sig} + \hat{a}_0^\dagger. \tag{5.25}$$

Hence, $\hat{c}$ is almost the field operator of the returning signal field but not exactly. The added vacuum term is crucial: $\hat{x}_{sig}$ and $\hat{y}_{sig}$ are non-commuting observables and therefore a simultaneous perfect measurement of these observables is ruled out by Heisenberg uncertainty. $\hat{x}$ and $\hat{y}$, on the other hand, can be measured simultaneously and combined into an estimate for the operator $\hat{c}$. The added vacuum operator $\hat{a}_0^\dagger$ ensures that $\hat{c}$ only corresponds to $\hat{a}_{sig}$ up to one unit of shot

added measurement noise consistent with Heisenberg uncertainty

noise in both quadratures. In this way, this "measurement" of $\hat{a}_{\text{sig}}$ complies with Heisenberg uncertainty. Effectively, we perform a measurement of the Husimi Q function of the returning light field. For a good discussion of this measurement scheme see [Leo97, pp. 6.1-2], and references therein.

We can estimate the covariance matrix σ of (5.20) by replacing the operator $\hat{a}_{\text{sig}}$ (which cannot be measured directly) by $c \equiv \sqrt{2}\,(x + iy)$ in the calculation of the pulse modes (5.9) and (5.10). Hence, we calculate:

$$a_t \equiv \int_{-\infty}^{t} \alpha\,(\tau - t)\; c(\tau)\mathrm{d}\tau, \tag{5.26}$$

$$b_t \equiv \int_{t}^{+\infty} \beta\,(\tau - t)\; c(\tau)\mathrm{d}\tau. \tag{5.27}$$

From these we calculate, the values of the pulse quadratures via (5.18) and (5.19). Note that this is not a direct measurement of the pulse quadratures because, as pointed out above, $\hat{c}$ only approximates $\hat{a}_{\text{sig}}$ up to one unit of shot noise per quadrature. Luckily, we are interested only in the statistics of the pulse quadratures, and—on a statistical level—we can subtract this additional noise as described by 5.3.3.

5.3.2.1 *Connection to the sample covariance matrix*

discrete version of pulsed modes

In the experiment, we sample the output of our homodyne detectors at discrete times t_i $(i = 1 \ldots N)$ with a sampling rate $f_s = 1/\,(t_i - t_{i-1}) \simeq 100\,\text{MHz}$. For the sake of brevity, we are going to denote quantities like $x(t_i)$ which refer to a sampling time t_i simply by x_i (analogously for y_i, c_i, a_i, b_i). The definition of a_i and b_i (and its corresponding quadratures Q_i, P_i, X_i, and Y_i) now read:

$$a_i \equiv Q_i + iP_i \equiv \sum_{k=i-M+1}^{i} \alpha_{k-i} c_k \left(= \sum_{k=-M+1}^{0} \alpha_k c_{k+i} \right), \tag{5.28}$$

$$b_i \equiv X_i + iY_i \equiv \sum_{k=i+1}^{i+M} \beta_{k-i} c_k \left(= \sum_{k=1}^{M} \beta_k c_{k+i} \right), \tag{5.29}$$

where

$$\alpha_k \propto \exp\left(i\omega_m \Delta t\, k\right) \times \exp\left(\Gamma \Delta t\, k\right), \; (k = -M+1, \ldots, 0), \tag{5.30}$$

$$\beta_k \propto \exp\left(-i\omega_m \Delta t\, k\right) \times \exp\left(-\Gamma \Delta t\, k\right), \; (k = 1, \ldots, M), \tag{5.31}$$

$$\Delta t \equiv 1/f_s = t_i - t_{i-1}. \tag{5.32}$$

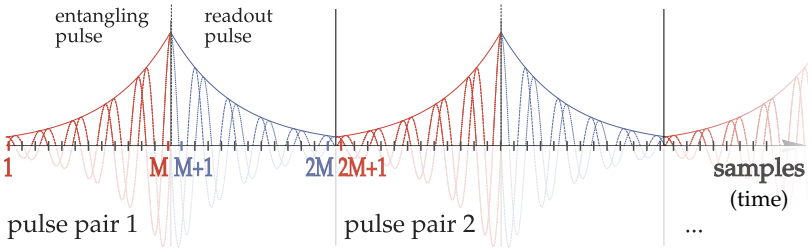

Figure 5.2. Illustration of the selection of pulse pairs from the measured time traces. The first M samples of the x- and y-trace are selected to calculate the entangling mode for the first pulse pair. The next M samples ($M+1$ to $2M$) are used to calculate the readout mode for the first pulse pair. Samples $2M+1$ to $3M$ and $3M+1$ to $4M$ are the input for the entangling and readout mode, respectively, of the second pulse pair, and so on.

In (5.28) and (5.29), we have restricted the summation per pulse to M samples before and after sample i, respectively. The number of samples per pulse M should be chosen large enough to satisfy

$$|\alpha_0| \overset{!}{\gg} |\alpha_{-M+1}|\,, \; |\beta_1| \overset{!}{\gg} |\beta_M|\,. \tag{5.33}$$

Condition (5.33) ensures that multiplication with the mode function still acts approximately like a bandpass filter of width Γ around $-\omega_m$ or $+\omega_m$ as previously discussed.

The normalization condition for the mode functions then reads

$$\sum_{k=-M+1}^{0} |\alpha_k|^2 \overset{!}{=} 1, \; \sum_{k=1}^{M} |\beta_k|^2 \overset{!}{=} 1. \tag{5.34}$$

If we restrict the summation to M samples per pulse, we can extract $\lfloor N/2M \rfloor$ non-overlapping pulse pairs from a trace containing N samples:[37] The first pulse pair extends from samples 1 to M (entangling pulse) and $M+1$ to $2M$ (readout pulse), the second pulse pair extends from samples $2M+1$ to $3M$ (entangling pulse) and from $3M+1$ to $4M$ (readout pulse), and so on, as sketched in Figure 5.2.

[37] $\lfloor x \rfloor$ *denotes the floor of* x.

For each of these pulse pairs, we obtain a vector of four quadratures $\boldsymbol{R}_i \equiv (Q_i, P_i, X_i, Y_i)^\intercal$ where the index i now runs over all pulse pairs, i.e. $i = 1, \ldots, \lfloor N/2M \rfloor$. This ensemble $\{\boldsymbol{R}_i | i = 1, \ldots, \lfloor N/2M \rfloor\}$ of pulse pairs can be used to calculate a sample covariance matrix $\tilde{\boldsymbol{\sigma}}$ as follows:

$$\tilde{\boldsymbol{\sigma}} \equiv \begin{pmatrix} \overline{Q_i^2} & \overline{Q_i P_i} & \overline{Q_i X_i} & \overline{Q_i Y_i} \\ \overline{Q_i P_i} & \overline{P_i^2} & \overline{P_i X_i} & \overline{P_i Y_i} \\ \overline{Q_i X_i} & \overline{P_i X_i} & \overline{X_i^2} & \overline{X_i Y_i} \\ \overline{Q_i Y_i} & \overline{P_i Y_i} & \overline{X_i Y_i} & \overline{Y_i^2} \end{pmatrix} - \begin{pmatrix} \overline{Q_i}^2 & \overline{Q_i} \cdot \overline{P_i} & \cdots \\ \overline{Q_i} \cdot \overline{P_i} & \ddots & \\ \vdots & & \end{pmatrix}, \tag{5.35}$$

where $\overline{O} \equiv \frac{1}{\lfloor N/2M \rfloor - 1} \sum_{i=1}^{\lfloor N/2M \rfloor} O_i$ denotes the sample mean of pulse quadrature O over all pulse pairs. Here and in what follows, I use the tilde (as in $\tilde{\sigma}$) to denote measured quantities, in this case the sample covariance matrix—in contrast to the ensemble covariance matrix σ defined by (5.20).

Assuming Gaussianity and stationarity of the underlying process, (5.35) is the best estimator of the quantum-mechanical covariance matrix (5.20). We will therefore calculate the entanglement of the output light field based on (5.35). We use the logarithmic negativity as a measure of entanglement because it can be calculated easily from the covariance matrix [see AI07, p. 7842]. Note that we use a slightly modified definition of the logarithmic negativity; see Section C.1 for details.

effect of long mechanical coherence times

Note also that (5.35) is the optimal estimator of the covariance matrix of the underlying random process only if the samples (pulse *pairs*) are statistically independent. It turns out that, for a resonantly driven system, this assumption is not met: There are strong correlations between different pulse pairs which persist for very long times. This is because the time scale of these correlations is set by the coherence time (i.e. the mechanical quality factor) of the mechanical oscillator which can be extremely high. In the experiment, however, we always operate with a slightly red-detuned laser drive. This leads to optical damping of the mechanical oscillator and reduces its coherence time drastically. The coherence time is actually reduced so strongly that the autocorrelation of the pulse-pairs becomes essentially zero in the experiment; see Section 5.9.2 for a discussion of this point. Therefore, we are justified in treating each pulse pair like an independent random draw from the underlying distribution when analyzing our experimental data.

5.3.3 *Post-processing steps*

Once we have calculated $\tilde{\sigma}$ according to (5.35) using (5.28) and (5.29), we need to apply some post-processing steps in order to calibrate and correct for known systematic errors:

1. Subtract contributions due to the detector dark noise.
2. Correct signal and shot noise data for sub-optimal quantum efficiency and homodyning visibility of our detection setup.
3. Calibrate our data to shot noise units (the raw data recorded in our experiment is in units of Volt).
4. Subtract the extra shot noise contribution due to the dual-rail homodyning setup.

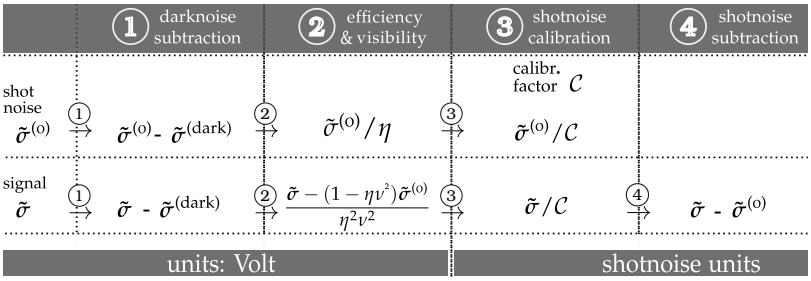

Figure 5.3. Sequence of post-processing steps. $\tilde{\sigma}$ is the covariance matrix of pulsed quadratures defined by (5.35), $\tilde{\sigma}^{(o)}$ and $\tilde{\sigma}^{(dark)}$ are the covariance matrices calculated on the basis of shot noise and dark noise measurements, respectively. η is the detection efficiency, ν is the homodyning visibility. $\mathcal{C}$ denotes a calibration factor (see main text for details). Note that in each correction step, the result of the previous correction is meant to be used as input. Hence, $\sigma \to f(\sigma) \to g(\sigma)$ means $\sigma \to g(f(\sigma))$, i.e. apply f to σ, then g to $f(\sigma)$.

These steps are sketched in Figure 5.3 and will be explained in more detail below.

Note that correcting our measurement results for detector dark noise, sub-unit quantum efficiency and sub-unit homodyning visibility (steps 1 and 2 above) is justified since these imperfections are only a feature of our measurement of the state, not of its generation. The same is true for the subtraction of the extra shot noise contribution due to the dual-rail homodyning (step 4).

1. Dark noise subtraction

The measurement output from our homodyne detectors contains—on top of the signal—a contribution due to the dark noise of our detectors. Hence, the signal we measure can be written as

$$x(t) + iy(t) = x^{(\text{ideal})}(t) + iy^{(\text{ideal})}(t) + x^{(\text{dark})}(t) + iy^{(\text{dark})}(t), \tag{5.36}$$

where $x^{(\text{ideal})}$ and $y^{(\text{ideal})}$ are the signals we would have measured in the absence of dark noise and $x^{(\text{dark})}$ and $y^{(\text{dark})}$ are due to detector dark noise.

Since the dark noise signals are statistically independent from the ideal signals, the sample covariance matrix $\tilde{\sigma}$ calculated on the basis of the noisy signals is given by

$$\tilde{\sigma} = \tilde{\sigma}^{(\text{ideal})} + \tilde{\sigma}^{(\text{dark})}, \tag{5.37}$$

where the dark noise contribution $\tilde{\sigma}^{(\text{dark})}$ is simply the result of our evaluation procedure applied to dark noise signals.

Hence, we can proceed as follows:

1. We measure dark noise traces $x^{(\mathrm{dark})}(t)$ and $y^{(\mathrm{dark})}(t)$ by recording the output from the x- and y-homodyne detector, respectively, with all light (local oscillator as well as signal) blocked.

2. We perform the data evaluation procedure (calculation of pulsed quadratures, calculation of the sample covariance matrix of the pulsed quadratures) using the measured dark noise traces and obtain the matrix $\tilde{\sigma}^{(\mathrm{dark})}$.

3. We subtract $\tilde{\sigma}^{(\mathrm{dark})}$ from the sample covariance matrix $\tilde{\sigma}$ for the measured signal to obtain the sample covariance matrix $\tilde{\sigma}^{(\mathrm{ideal})}$ for the noise-free signal $x^{(\mathrm{ideal})}(t) + iy^{(\mathrm{ideal})}(t)$.

4. Finally, we also need to subtract $\tilde{\sigma}^{(\mathrm{dark})}$ from the covariance matrix $\tilde{\sigma}^{(0)}$ calculated for pure shot noise input. The matrix $\tilde{\sigma}^{(0)}$ is needed for the calibration of the measurement data in shot noise units as explained below.

2a. Detector efficiency

Our photodetectors have a quantum efficiency $\eta \simeq 95\,\%$. This means that, on average, around 95 % of the arriving photons create a photoelectron, while 5 % of the arriving photons are effectively lost. The effect is the same as if the optical power was attenuated by 5 %. Since the variance of a classical signal scales with the square of the optical power, while the variance due to quantum fluctuations scales only linearly with power, the effect of inefficient detection is different for the shot noise and the signal measurements. To correct for inefficient detection, the shot noise covariance matrix $\tilde{\sigma}^{(0)}$ must be multiplied by $1/\eta$, while the signal covariance matrix $\tilde{\sigma}$ must be multiplied by $1/\eta^2$. However, since the measured signal also contains a shot noise contribution, the full correction for the signal is actually a little bit more complex. It will be given below together with the correction for sub-unit homodyne visibility. The required corrections are derived in the appendix, in Section C.5.

2b. Homodyning visibility

The visibility ν of the interference between local oscillator and the signal mode is usually limited to $\nu \simeq 90\,\%$, due to imperfect spatial mode-matching. We measure the homodyning visibility ν as follows: We set signal and local oscillator to the same optical power and scan the relative phase between local oscillator and signal using a PZT-mounted mirror in the local oscillator path. The DC output of the photodetector will show oscillations resulting from the interference

of signal and local oscillator. Defining $V_{\min}$ and $V_{\max}$ as the minimum and maximum of the interference signal, we calculate the visibility as

$$v = \frac{V_{\max} - V_{\min}}{V_{\max} + V_{\min}}. \tag{5.38}$$

The effect of sub-unit visibility on our measurement is as follows: In the shot noise measurement, only the local oscillator beam is used. Hence, clearly, the reduced interference visibility does not make a difference in the shot noise measurement. Measurements with a signal beam, however, are affected by the reduced visibility. The effect is the same as if the amplitude of the local oscillator field were reduced by a factor η. This reduces the measured signal variance by η^2.

combined correction for visibility and efficiency

The full correction for both detector inefficiency and sub-unit homodyning visibility is given by (see Section C.5 for the calculation):

$$\tilde{\sigma} \to \frac{\tilde{\sigma} - (1 - \eta v^2)\tilde{\sigma}^{(o)}}{\eta^2 v^2}, \tag{5.39}$$

$$\tilde{\sigma}^{(o)} \to \frac{\tilde{\sigma}^{(o)}}{\eta}. \tag{5.40}$$

Here, $\tilde{\sigma}^{(o)}$ and $\tilde{\sigma}$ refer to the measured covariance matrices of shot noise and signal, respectively. Note that the term $\tilde{\sigma}^{(o)}$ on the right-hand side of (5.39) refers to the measured shot noise matrix before the correction described by (5.40).

3. Shot noise calibration

Our raw measurement data is in units of Volt. But to calculate entanglement based on the covariance matrix $\tilde{\sigma}$ of pulsed quadratures, we need our data to be expressed in shot noise units, i.e. in units in which the variance of shot noise is $1/2$. This can be achieved by calculating the covariance matrix $\tilde{\sigma}^{(o)}$ of pulsed quadratures for shot noise inputs, finding a scale factor $\mathcal{C}$ such that the resulting matrix has a mean diagonal value of $1/2$ and applying the same scale factor to the signal data. Hence, we proceed as follows:

1. We block the signal to record shot noise traces $x^{(o)}(t)$ and $y^{(o)}(t)$ with the x- and y-homodyne detector, respectively.

2. We perform the data evaluation (calculation of pulsed quadratures (5.28) and (5.29) and their covariance matrix (5.35)) based on the shot noise traces $x^{(o)}(t)$ and $y^{(o)}(t)$ to obtain the shot noise covariance matrix $\tilde{\sigma}^{(o)}$.

3. We calculate the calibration factor $\mathcal{C} \equiv 2 \cdot \sum_{i=1}^{4} \tilde{\sigma}^{(o)}{}_{ii}$ from the shot noise matrix $\tilde{\sigma}^{(o)}$ (hence, the calibration factor is twice the mean value of the diagonal).

4. Finally, we redefine the covariance matrices $\tilde{\sigma}$ and $\tilde{\sigma}^{(o)}$ (for signal and shot noise, respectively) as follows

$$\tilde{\sigma} \to \tilde{\sigma}/\mathcal{C}, \tag{5.41}$$

$$\tilde{\sigma}^{(o)} \to \tilde{\sigma}^{(o)}/\mathcal{C}. \tag{5.42}$$

4. Added noise due to dual-rail homodyning

There is one further subtlety: What we want to characterize is the entanglement of the light field $\hat{a}_{\text{sig}}$ returning from the cavity.[38] What we actually characterize in our dual rail homodyning setup, however, are the two light fields $\hat{a}_x$ and $\hat{a}_y$ which result from mixing the signal field $\hat{a}_{\text{sig}}$ on a 50:50 beam splitter with a mode $\hat{a}_0$ in the vacuum state:

$$\begin{pmatrix} \hat{a}_x \\ \hat{a}_y \end{pmatrix} = \frac{1}{\sqrt{2}} \begin{pmatrix} 1 & 1 \\ 1 & -1 \end{pmatrix} \begin{pmatrix} \hat{a}_{\text{sig}} \\ \hat{a}_0 \end{pmatrix}. \tag{5.43}$$

[38] *Recall the setup:*

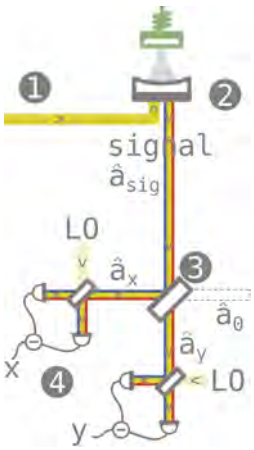

As explained above, our post-processing procedure amounts to estimating the operator

$$\hat{c} \equiv \sqrt{2}\,(\hat{x} + i\hat{y}) = \ldots = \hat{a}_{\text{sig}} + \hat{a}_0^\dagger, \tag{5.44}$$

where $\hat{x}$ and $\hat{y}$ are the amplitude and phase quadrature of the fields $\hat{a}_x$ and $\hat{a}_y$, respectively. Hence, in addition to $\hat{a}_{\text{sig}}$, we also measure an extra unit of shot noise $\hat{a}_0^\dagger$ which can be attributed to the splitting of the signal on the beam splitter.

On the level of the pulse modes, this additional shot noise contribution implies

$$\hat{a}_t \equiv \int_{-\infty}^{t} \alpha\,(\tau - t)\,\hat{c}(\tau)\mathrm{d}\tau \tag{5.45}$$

$$= \int_{-\infty}^{t} \alpha\,(\tau - t)\,\hat{a}_{\text{sig}}\,(\tau)\,\mathrm{d}\tau + \int_{-\infty}^{t} \alpha\,(\tau - t)\,\hat{a}_0^\dagger\,(\tau)\,\mathrm{d}\tau, \tag{5.46}$$

$$\hat{b}_t \equiv \int_{t}^{+\infty} \beta\,(\tau - t)\,\hat{c}(\tau)\mathrm{d}\tau \tag{5.47}$$

$$= \int_{t}^{+\infty} \beta\,(\tau - t)\,\hat{a}_{\text{sig}}\,(\tau)\,\mathrm{d}\tau + \int_{t}^{+\infty} \beta\,(\tau - t)\,\hat{a}_0^\dagger\,(\tau)\,\mathrm{d}\tau. \tag{5.48}$$

Recall that the pulse quadratures $\hat{Q}_t, \hat{P}_t, \hat{X}_t, \hat{Y}_t$ are defined as the real and imaginary parts of the mode operators $\hat{a}_t$ and $\hat{b}_t$:

$$\hat{Q}_t \equiv \mathrm{Re}\,(\hat{a}_t)\,, \hat{P}_t \equiv \mathrm{Im}\,(\hat{a}_t)\,, \tag{5.49}$$

$$\hat{X}_t \equiv \mathrm{Re}\left(\hat{b}_t\right), \hat{Y}_t \equiv \mathrm{Im}\left(\hat{b}_t\right). \tag{5.50}$$

Analogously, we define pulse quadratures $\hat{Q}_t^{(\mathrm{sig})}, \ldots$, and $\hat{Q}_t^{(\mathrm{o})}, \ldots$ based only on the fields $\hat{a}_{\mathrm{sig}}$ and $\hat{a}_0^\dagger$, respectively:

$$\hat{Q}_t^{(\mathrm{sig})} \equiv \mathrm{Re}\left(\int_{-\infty}^{t} \alpha\left(\tau - t\right) \hat{a}_{\mathrm{sig}}\left(\tau\right) \mathrm{d}\tau\right), \ldots \tag{5.51}$$

$$\hat{Q}_t^{(\mathrm{o})} \equiv \mathrm{Re}\left(\int_{-\infty}^{t} \alpha\left(\tau - t\right) \hat{a}_0^\dagger\left(\tau\right) \mathrm{d}\tau\right), \ldots \tag{5.52}$$

The vector $\hat{\boldsymbol{R}}_t \equiv \left(\hat{q}_t, \hat{p}_t, \hat{x}_t, \hat{y}_t\right)^{\mathsf{T}}$ of (actually measured) pulse quadratures can then be written as

$$\boldsymbol{R}_t = \boldsymbol{R}^{(\mathrm{sig})}{}_t + \boldsymbol{R}^{(\mathrm{o})}{}_t, \text{ where} \tag{5.53}$$

$$\hat{\boldsymbol{R}}_t^{(\mathrm{sig})} \equiv \left(\hat{q}_t^{(\mathrm{sig})}, \hat{p}_t^{(\mathrm{sig})}, \hat{x}_t^{(\mathrm{sig})}, \hat{y}_t^{(\mathrm{sig})}\right)^{\mathsf{T}} \tag{5.54}$$

$$\hat{\boldsymbol{R}}_t^{(\mathrm{o})} \equiv \left(\hat{q}_t^{(\mathrm{o})}, -\hat{p}_t^{(\mathrm{o})}, \hat{x}_t^{(\mathrm{o})}, -\hat{y}_t^{(\mathrm{o})}\right)^{\mathsf{T}}. \tag{5.55}$$

We can define covariance matrices $\tilde{\sigma}^{(\mathrm{sig})}$ and $\tilde{\sigma}^{(\mathrm{o})}$ for both $\hat{\boldsymbol{R}}^{(\mathrm{sig})}$ and $\hat{\boldsymbol{R}}^{(\mathrm{o})}$, respectively. Since the contributions $\hat{\boldsymbol{R}}^{(\mathrm{o})}$ due to the added shot noise are statistically uncorrelated with the contributions $\hat{\boldsymbol{R}}^{(\mathrm{sig})}$ due to the signal light field, the covariance matrix $\tilde{\sigma}$ of the measured pulse quadratures is simply a sum of the covariance matrix $\tilde{\sigma}^{(\mathrm{sig})}$ due to the signal light field $\hat{a}_{\mathrm{sig}}$ alone and the covariance matrix $\tilde{\sigma}^{(\mathrm{o})}$ resulting from the added shot noise $\hat{a}_0^\dagger$:

$$\tilde{\sigma} = \tilde{\sigma}^{(\mathrm{sig})} + \tilde{\sigma}^{(\mathrm{o})}. \tag{5.56}$$

Note that the expectation value for $\tilde{\sigma}^{(\mathrm{o})}$ is

$$\mathbb{E}\left[\tilde{\sigma}^{(\mathrm{o})}\right] = \mathbb{E}\left[\left(\hat{q}_t^{(\mathrm{o})}, -\hat{p}_t^{(\mathrm{o})}, \hat{x}_t^{(\mathrm{o})}, -\hat{y}_t^{(\mathrm{o})}\right)^{\mathsf{T}} \left(\hat{q}_t^{(\mathrm{o})}, -\hat{p}_t^{(\mathrm{o})}, \hat{x}_t^{(\mathrm{o})}, -\hat{y}_t^{(\mathrm{o})}\right)\right] \tag{5.57}$$

$$= \mathbb{E}\left[\left(\hat{q}_t^{(\mathrm{o})}, \hat{p}_t^{(\mathrm{o})}, \hat{x}_t^{(\mathrm{o})}, \hat{y}_t^{(\mathrm{o})}\right)^{\mathsf{T}} \left(\hat{q}_t^{(\mathrm{o})}, \hat{p}_t^{(\mathrm{o})}, \hat{x}_t^{(\mathrm{o})}, \hat{y}_t^{(\mathrm{o})}\right)\right], \tag{5.58}$$

since there are no correlations between different quadratures for shot noise. Hence, the relative sign between the quadratures $\hat{q}_t^{(\mathrm{o})}, \hat{x}_t^{(\mathrm{o})}$ and $\hat{p}_t^{(\mathrm{o})}, \hat{y}_t^{(\mathrm{o})}$ does not matter.

measuring $\tilde{\sigma}^{(\mathrm{o})}$

As described above, we can measure the shot noise contribution $\tilde{\sigma}^{(\mathrm{o})}$ simply by performing the data evaluation for shot noise measurements, i.e. measurements with only the local oscillator light but no signal light. Then we can subtract $\tilde{\sigma}^{(\mathrm{o})}$ from $\tilde{\sigma}$ to obtain

$$\tilde{\sigma}^{(\mathrm{sig})} \equiv \tilde{\sigma} - \tilde{\sigma}^{(\mathrm{o})}. \tag{5.59}$$

This final covariance matrix $\tilde{\sigma}^{(\mathrm{sig})}$ is our best estimate for the quantum state of the entangling and readout mode in the returning light

field. We will therefore use $\tilde{\sigma}^{(\mathrm{sig})}$ to asses the light-light entanglement created via the optomechanical interaction.

logarithmic negativity as entanglement measure

We use the logarithmic negativity as an entanglement measure because it can be calculated easily on the basis of the covariance matrix. Note, that we use a slightly modified definition of the logarithmic negativity. Usually, separable states are assigned a logarithmic negativity of zero. In this thesis, however, we extend the definition of the logarithmic negativity and assign negative values to separable states such that negative values close to zero correspond to states which are (in some sense) close to being entangled while negative values far from zero correspond to states which are far from being entangled. See Section C.1 for more details.

5.4 SINGLE-MODE SIMULATIONS

To check that mechanically mediated light–light entanglement can indeed be detected by the measurement protocol described above, I performed simulations of the experiment and apply our entanglement detection protocol to the simulated measurement data. I start with the simplest case: simulations with a single mechanical mode and neglecting (for now) classical laser noise.

5.4.1 *Entanglement as a function of pulse width* Γ

In the simulations presented below, I fix the optomechanical parameters g, κ, ω_m, Q, and T. For the evaluation, I vary the pulse width Γ in the definition of the pulse modes (5.1) and (5.2), but keep the central frequency of the pulses fixed at $\mp\omega_m$.

Figure 5.4 demonstrates that, for the right set of optomechanical parameters, it is indeed possible to detect entanglement using our protocol. It also shows that entanglement can only be detected if the pulse width Γ (in the frequency domain) is chosen appropriately. If the pulse duration is too long (hence pulse width too narrow in the frequency domain) mechanical decoherence destroys the correlations between the pulses. Therefore the lower limit for the pulse width is roughly given by $\bar{n}\gamma$ ($2\pi \times 21\,\mathrm{kHz}$ in this example). If the pulses are too short, on the other hand, there is not enough time for correlations to build up. The critical time is given by κ/g^2, which is the inverse of the effective interaction rate (in the adiabatic approximation). Therefore, the upper limit for the pulse width is roughly given by g^2/κ ($2\pi \times 240\,\mathrm{kHz}$ in this example).

optimal pulse width

dependence on Q/T

Another important insight from Figure 5.4 is that the entanglement created in this protocol does not depend on the mechanical quality factor Q or the temperature T independently but only via the ratio T/Q. This is demonstrated by the nearly perfect coincidence of the

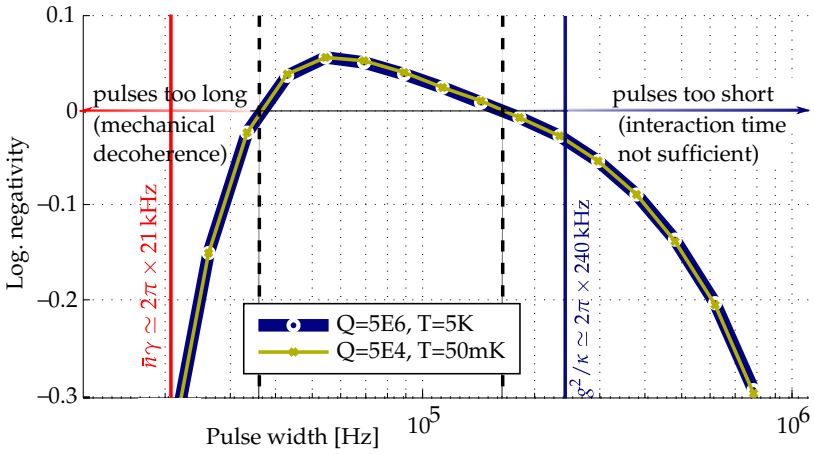

Figure 5.4. Logarithmic negativity $E_\mathcal{N}$ versus pulse width Γ for single-mode simulations. We observe entanglement for $40\,\text{kHz} < \Gamma < 163\,\text{kHz}$ (dashed vertical lines). These limits are tighter than but on the same order as the mechanical decoherence rate $\bar{n}\gamma \simeq 2\pi \times 21\,\text{kHz}$ (red, vertical line) and $g^2/\kappa \simeq 0.24 \times \omega_m = 2\pi \times 240\,\text{kHz}$ (blue vertical line), respectively. The two coinciding entanglement curves (thick blue and thin yellow line) correspond to simulations with different mechanical quality factors $Q = 1 \times 10^6$, $Q = 1 \times 10^4$ and temperatures $T = 5\,\text{K}$, $T = 50\,\text{mK}$, respectively, but constant thermal cooperativity $\mathcal{C} \simeq 1.26$ and constant mechanical decoherence rate $\bar{n}\gamma \simeq 2\pi \times 21\,\text{kHz}$.

Parameters:
$\omega_m = 2\pi \times 1\,\text{MHz}$,
$\kappa \simeq 2.73 \times \omega_m$,
$g_0 = 65 \times 10^{-6} \times \omega_m$,
$g \simeq 0.27 \times \omega_m$,
$Q = 1 \times 10^4$ (1×10^6),
$T = 50\,\text{mK}$ (5 K),
$P_\text{in} = 20\,\mu\text{W}$,
$\mathcal{C} \simeq 1.26$,
without optical noise.

curves $E_\mathcal{N}(\Gamma)$ for two simulations which differ by two orders of magnitude in Q and T but have identical T/Q. The physical reason for this coincidence is that the quality factor and the temperature only influence the entanglement via the mechanical decoherence rate which is (for $k_\text{B}T \gg \hbar\omega_m$) given by

$$\bar{n}\gamma \simeq \frac{k_\text{B}T}{\hbar\omega_m} \times \frac{\omega_m}{Q} = \frac{k_\text{B}T}{\hbar Q} \propto \frac{T}{Q}. \tag{5.60}$$

choice of parameters for simulations

Note that the values of the optomechanical parameters in the simulations are generally chosen such that they agree with measured or expected values for our experimental setup (with the exception of $T = 50\,\text{mK}$ in Figure 5.4 which was chosen to illustrate that $E_\mathcal{N}$ depends on $\bar{n}\gamma$ but not $\bar{n}$ or γ individually).

5.4.2 *Systematic exploration of parameter-space*

To explore the feasibility of the proposed protocol for entanglement generation and detection, I systematically studied the dependence of the expected entanglement on key parameters such as the linearized optomechanical coupling g, the mechanical frequency ω_m, and the mechanical quality factor Q. The coupling g is proportional to the square root of the intracavity power and can therefore be increased easily by increasing the optical input power. The mechanical fre-

quency ω_m can be varied by changing the dimensions of the mechanical device using microfabrication. For MIM-cavities, the possible range for the fundamental mechanical frequency extends from some hundred kHz to a few MHz (limited at the upper end by the requirement that the lateral dimensions of the membrane should be larger than the optical spot size). The mechanical quality factor Q is much harder to control but improving and controlling it is a focus of much recent work on microfabricated optomechanical devices [Ver+06; VCP08; Cha+14; Col+14; NMG16; Rei+16].

choice of mechanical frequency

In Figure 5.5, I present results from simulations regarding the generated entanglement as a function of the optomechanical coupling g and mechanical quality factor Q within experimentally accessible parameter ranges. The mechanical frequency was set to $\omega_m = 2\pi \times 920\,\mathrm{kHz}$ which can be easily achieved with high tensile stress SiN membranes (lateral dimensions $l_x = l_y \simeq 430\,\mu\mathrm{m}$, tensile stress $\sigma \simeq 1\,\mathrm{GPa}$, density $\rho \simeq 3.18 \times 10^3\,\mathrm{kg/m^3}$). I repeated the same simulations with a mechanical frequency of $\omega_m = 2\pi \times 1.5\,\mathrm{MHz}$ (lateral dimensions $l_x = l_y \simeq 265\,\mu\mathrm{m}$). The results are so similar that I do not include them here. I conclude that for the proposed experiment, membranes with fundamental mechanical frequencies in the range 900 kHz to 1.5 MHz should all work and yield quite similar results. Frequencies much higher than 1.5 MHz are excluded because it would require shrinking the membrane close to or even below the waist of the cavity mode which would lead to significant optical losses. Frequencies much lower than 900 kHz are also problematic because of the laser noise which rises strongly with decreasing frequency.

optomechanical parameters

cavity parameters

The optomechanical bare coupling is fixed at $g_0 = 2\pi \times 65\,\mathrm{Hz}$, which is the optimal value for the coupling of the fundamental mechanical mode in our MIM-cavity geometry (recall that the coupling g_0 depends on the exact position of the membrane along the cavity axis). The cavity parameters are set to the values we achieve in our current setup, namely $\kappa_{\mathrm{in}} = 2\pi \times 1.7\,\mathrm{MHz}$, $\kappa_{\mathrm{out}} = 2\pi \times 810\,\mathrm{kHz}$. The term κ_{out} accounts for losses due to transmission through the cavity end mirror but also for losses due to scatter and absorption inside the cavity.

optical losses

Optical losses in between the optomechanical cavity and the detection setup (on the order of 15 to 20 %) are not taken into account in the simulations. These losses will lower the detected entanglement values but will not make the entanglement disappear. Furthermore, we can in principle easily correct for these losses in the data evaluation to obtain the entanglement of the light field directly after the optomechanical cavity. The simulations also do not account for detector efficiency (roughly 95 %) and homodyning visibility (roughly 90 %). In the experiment we correct for the latter two effects; see Section 5.3.3 and Section C.5 for a discussion of this correction. The

temperature

temperature is set to 5 K in the following simulations, which is readily achievable in a liquid helium flow cryostat.

5.4.2.1 *Simulations without optical noise*

Figure 5.5a presents the results for simulations without optical noise. To generate this plot (and the following one), 45 different simulations were run with all combinations of optical input powers P_{in} from the set $\{2.5, 5, 7.5, 10, 15, 20, 30, 40, 50\}$ µW (corresponding to couplings g in the range $[0.1, \ldots, 0.48] \times \omega_m$) and mechanical quality factors Q from the set $\{5 \times 10^5, 5 \times 10^{5.5}, 5 \times 10^6, 5 \times 10^{6.5}, 5 \times 10^7\}$; these simulated parameter combinations are marked with a cross in the plot. For each of these simulations, the logarithmic negativity $E_{\mathcal{N}}$ was optimized with respect to the pulse width Γ.[39] The resulting optimal entanglement values were then interpolated linearly to other values of g and Q to generate the contour plots below.

[39] *The pulse widths Γ for which the optimal amount of entanglement is extracted are plotted in the appendix (Section C.6), in Figure C.7a.*

The linearized optical coupling is proportional to $\sqrt{P_{\text{in}}}$ and varies in the range $g = [0.1, \ldots, 0.48] \times \omega_m$ in these simulations. Therefore, all simulations satisfy $g < \omega_m$ and $g < \kappa$. We observe that, in this regime, entanglement increases with both coupling strength g as well as mechanical quality factor Q. Only for large mechanical quality factors and for large coupling, a decrease of entanglement for a further increase in coupling is observed.

increase with g and Q

The cooperativity $\mathcal{C} \equiv g^2/(\kappa\bar{n}\gamma)$ varies between $\mathcal{C} \simeq 1.9 \times 10^{-2}$ for $g \simeq 0.1 \times \omega_m$ and $Q = 5 \times 10^5$ (lower left corner) and $\mathcal{C} \simeq 37$ for $g \simeq 0.48 \times \omega_m$ and $Q = 5 \times 10^7$ (upper right corner). Two lines of equal cooperativity at $\mathcal{C} = 1$ (red dashed) and $\mathcal{C} = 0.25$ (blue dashed) are drawn. For a large part of the parameter space, curves of equal entanglement coincide roughly with lines of equal cooperativity. Entanglement appears roughly for $\mathcal{C} \gtrsim 0.25$.

dependence on cooperativity

5.4.2.2 *Simulations including optical noise*

Figure 5.5b shows results of simulations for the same parameters as in Figure 5.5a but including optical noise—phase noise as well as amplitude noise—as measured for our setup.[40] Note that the noise model need not be perfect for reliable simulations. This is demonstrated in Section C.9 where the effects of different noise models on the entanglement are compared.

[40] *The pulse widths Γ for which the optimal amount of entanglement is extracted are again shown in the appendix (Section C.6), in Figure C.7b.*

As before, the entanglement increases with the mechanical quality factor. The main difference to the noise-free case (Figure 5.5a) is that, in the presence of noise, lines of equal entanglement do not coincide anymore with lines of equal cooperativity. Instead, for all quality factors considered here, entanglement decreases again once the coupling becomes too large, i.e. once the optical power becomes too large. This is due to the fact that the effects of classical laser noise scale quadrat-

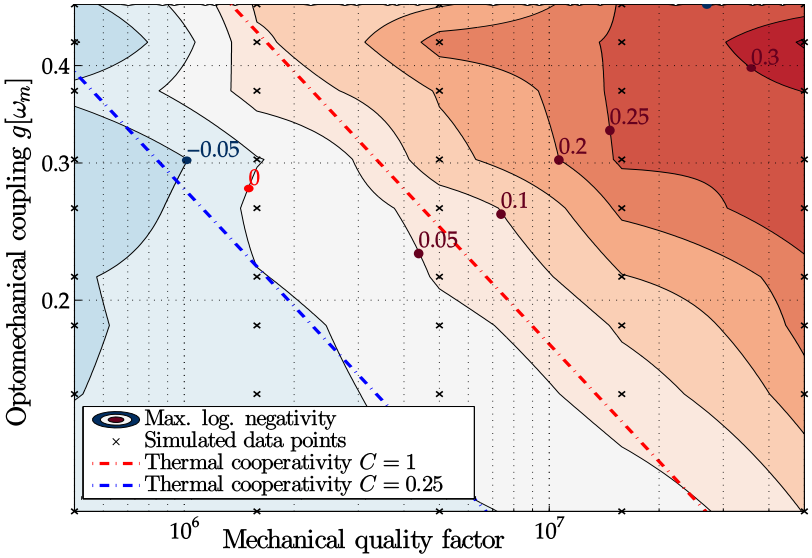

(a) Optimal logarithmic negativity $E_{\mathcal{N}}(\Gamma_{\text{opt}})$ versus quality factor Q and optomechanical coupling g for single-mode simulations *without optical noise*.

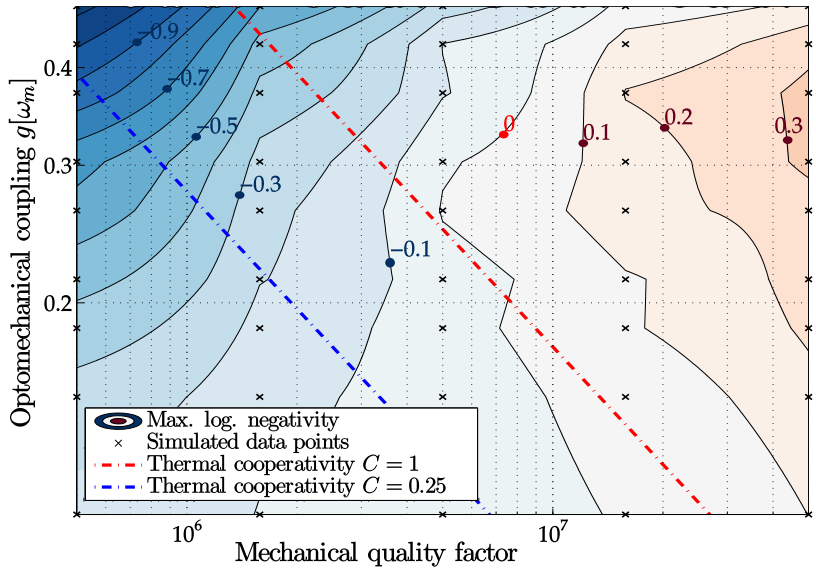

(b) Optimal logarithmic negativity $E_{\mathcal{N}}(\Gamma_{\text{opt}})$ versus quality factor Q and optomechanical coupling g for single-mode simulations *with optical noise* as measured for our setup.

Parameters:
$\omega_m = 2\pi \times 0.92\,\text{MHz}$,
$\kappa \simeq 2.73 \times \omega_m$,
$g_0 = 65 \times 10^{-6} \times \omega_m$,
$T = 5\,\text{K}$.

Figure 5.5. Optimal logarithmic negativity $E_{\mathcal{N}}(\Gamma_{\text{opt}})$ versus quality factor Q and optomechanical coupling g for single-mode simulations with optical noise (Figure 5.5b) and without it (Figure 5.5a). Crosses mark the parameters which were simulated. For these parameters, entanglement was evaluated for different pulse widths Γ and then optimized with respect to Γ. In between the simulated parameters, the optimized entanglement values were interpolated linearly. Lines of equal cooperativity $\mathcal{C} = 1$ ($\mathcal{C} = 0.25$) are marked with a red (blue) dashed line.

ically with the optical power and thus become more detrimental for higher optical powers.

5.5 MULTIMODE EFFECTS

So far, we assumed that we are dealing with a single mechanical mode. Unfortunately, this could not be further from the truth. On the contrary, in a MIM cavity, there are a large number of membrane mechanical modes which interact with comparable coupling strengths with the optical cavity mode. Hence, MIM cavities are genuinely multimode optomechanical systems. This is in sharp contrast to the electromechanical membranes used in the experiments of [Pal+13a; Pal+13b]. In the electro-mechanical case, the coupling is capacitive and therefore depends on the average displacement over the full membrane surface. Therefore, in electro-mechanical membrane setups, the fundamental mechanical mode couples much more strongly than all other modes, since it is the only mode which has a large displacement when averaged over the full membrane surface.

electromechanical membrane setups are effectively single-mode

In a MIM-cavity, on the other hand, we are probing the membrane displacement in only a very small region on the membrane surface. But, for any small region on the membrane surface, there are many membrane modes with non-negligible average displacement over that region. Hence, there are many membrane modes with comparable optomechanical coupling in a MIM-cavity. The experimentally measured membrane spectrum in Figure 3.14 illustrates this point quite drastically. In the frequency band from DC to 2.5 MHz, there are roughly 50 mechanical modes and most of them are clearly observable in the spectrum of the cavity light.

optomechanical membrane setups are multi-mode

The important question is: Does the multimode character of our MIM-cavity matter for our entanglement experiment? Below, we will answer this question affirmatively using multimode simulations. But the following simple back-of-the-envelope estimate also shows that the multimode character of the MIM-cavity could make a big difference for the proposed experiment.

5.5.1 *Relevant frequency scale for mode separation*

The relevant frequency scale regarding the separation of mechanical modes in our entanglement detection protocol is given by the optimal width Γ_{opt} of our pulse mode functions (5.1), (5.2). A pulse mode with central frequency $\omega_m/2\pi$ and width $\Gamma/2\pi$ defines a window $[\omega_m - \Gamma, \omega_m + \Gamma]/2\pi$ in frequency space. Signals at frequencies within this window contribute strongly to the pulse quadratures extracted by this pulse mode function. Signals at frequencies outside this window contribute only weakly. Therefore, we expect that the

presence of higher mechanical modes matters for our experiment if the separation of mechanical modes $\Delta\omega_m$ is smaller than or similar to the typical optimal width Γ_{opt} of pulse mode functions in frequency space. Note however that, since the pulse shape is exponential in time, we are dealing with a Lorentzian in frequency space which does not have a clear cut-off but rolls off with $1/\Omega^2$ towards high sideband frequencies. Therefore, it is impossible to conclude solely on the basis of the pulse shape that signals outside this frequency window will not prevent entanglement detection.

Recall that the optimal pulse width Γ_{opt} is restricted by $\bar{n}\gamma \ll \Gamma_{\text{opt}} \ll g^2/\kappa$ and that, in simulations with realistic parameters (see e.g. Figure 5.4), Γ_{opt} turned out to be on the order of $0.1 \times \omega_m$. This optimal pulse width is on the same order of magnitude as the typical separation of mechanical mode frequencies for our membranes: For square membranes (such as the 1 mm × 1 mm Norcada SiN membrane whose spectrum is shown in Figure 3.14), the expected mean separation between neighboring modes in the range from DC to 2.5 MHz is $0.1 \times \omega_m$ ($0.2 \times \omega_m$ if we exclude quasi-degenerate modes). The difference between the fundamental mechanical mode and the next mechanical mode is quite a bit larger than that ($0.58 \times \omega_m$) but still on the same order of magnitude as the optimal pulse width. Hence, the single-mode assumption is not well satisfied in our system in the context of the pulsed-continuous entanglement experiment (the conclusion would actually be no different if we employed actual pulses as in the original protocol of [Hof+11]).

Hence, if we want to detect entanglement, we cannot analyze only the signal caused by the fundamental mechanical mode. For better or worse, the closest higher-order mechanical modes will also contribute to the signal we analyze (i.e. the pulse quadratures). This amounts to a form of additional noise which can mask the entanglement.

Below, I demonstrate using simulations that higher mechanical modes can indeed prevent the detection of entanglement (see Figure 5.6). All is not lost, however. We can generalize our protocol such that the contributions of higher mechanical modes are properly taken into account, as explained in Section 5.6. The contributions of higher mechanical modes are then seen to be not random noise, but part of a larger correlation structure. With this extended protocol, we are indeed able to detect entanglement in the output light even in the presence of multiple closely spaced and strongly interacting mechanical modes, as demonstrated in Section 5.7.1 (see, in particular, Figure 5.6).

5.6 MULTIMODE PROTOCOL

The guiding idea for a multimode generalization of our entanglement detection protocol is as follows. We want to extract simultaneously the contribution of several mechanical modes to the output light field. To this end we define, for each mechanical mode i, mode functions in analogy to Section 5.3.1: *mode functions*

$$\tilde{\alpha}^{(\mathrm{i})}(t) \equiv \exp(i\omega_i t) \times \exp(\Gamma_i t) \ (\text{for } t \leq 0), \tag{5.61}$$

$$\tilde{\beta}^{(\mathrm{i})}(t) \equiv \exp(-i\omega_i t) \times \exp(-\Gamma_i t) \ (\text{for } t \geq 0). \tag{5.62}$$

The mode function $\tilde{\alpha}^{(\mathrm{i})}$ ($\tilde{\beta}^{(\mathrm{i})}$) with label i is meant to extract the lower (upper) sideband due to the i-th mechanical mode during the first (second) pulse. Therefore, the central frequency of the mode functions is chosen to be $\pm\omega_i$, respectively, where ω_i is the frequency of the i-th mechanical mode. The pulse widths Γ_i (=inverse decay time / width in frequency space) of the mode functions must be chosen carefully to allow detection of entanglement. In principle, the Γ_i could be chosen differently for each mechanical mode to optimize the detected amount of entanglement. In practice, however, we cannot scan each of the Γ_i individually since the data evaluation procedure is (computationally) quite time-intensive. For this reason, in all evaluations presented below, all Γ_i are set to the same value and scanned collectively (unless otherwise noted). *choice of parameters*

Next, we have to ensure that the mode functions (5.61) and (5.62) are mutually orthonormal. To this end, we numerically orthonormalize (using either modified Gram-Schmidt or Householder reflections) the set of mode functions $\left\{\tilde{\alpha}^{(i)}(t),\, \tilde{\beta}^{(i)}(t)\right\}_{i=1\ldots m}$ in order to obtain a new orthonormal set of mode functions $\left\{\alpha^{(i)}(t),\, \beta^{(i)}(t)\right\}_{i=1\ldots m}$ which satisfies *orthonormalization*

$$\int_{-\infty}^{0} \alpha^{(i)}(t)\, \alpha^{(\mathrm{j})*}(t)\, \mathrm{d}t = \delta_{ij}, \tag{5.63}$$

$$\int_{0}^{+\infty} \beta^{(i)}(t)\, \beta^{(\mathrm{j})*}(t)\, \mathrm{d}t = \delta_{ij}. \tag{5.64}$$

Note that any mode function $\alpha^{(i)}(t)$ is automatically orthogonal to any mode function $\beta^{(\mathrm{j})}(t)$ since they have no overlap in time. In Section C.2, an example of a set of mode functions used for multi-mode evaluations is given.

These mode functions allow us to define the following mode operators:

$$\hat{a}_t^{(\mathrm{i})} \equiv \int_{-\infty}^{t} \alpha^{(\mathrm{i})}(\tau - t)\, \hat{a}_{\mathrm{sig}}(\tau)\, \mathrm{d}\tau, \tag{5.65}$$

$$\hat{b}_t^{(\mathrm{i})} \equiv \int_{t}^{+\infty} \beta^{(\mathrm{i})}(\tau - t)\, \hat{a}_{\mathrm{sig}}(\tau)\, \mathrm{d}\tau. \tag{5.66}$$

pulse modes

The operators $\hat{a}_t^{(i)}$ and $\hat{b}_t^{(i)}$ define light modes, which we refer to as "pulse modes". These modes allow us to describe the quantum state of the output light field before and after time t, respectively. We call the set of modes $\left\{\alpha^{(i)}(t)\right\}_{i=1\ldots m}$ the "entangling pulse" and the modes $\left\{\beta^{(i)}(t)\right\}_{i=1\ldots m}$ the "readout pulse".

Because the mode functions $\left\{\alpha^{(i)}(t), \beta^{(i)}(t)\right\}_{i=1\ldots m}$ are mutually orthonormal, the multiplication and integration of (5.65) and (5.66) amounts to a unitary transformation from the operators $\left\{\hat{a}_{\mathrm{sig}}(t)\right\}_{t\in\mathbb{R}}$ to the operators $\left\{\hat{a}_t^{(i)}, \hat{b}_t^{(i)}\right\}_{i=1\ldots m}$. Hence, the resulting operators $\hat{a}_t^{(i)}$ and $\hat{b}_t^{(i)}$ are legitimate quantum mode operators in the sense that they satisfy the same canonical commutation relations as the operators $\left\{\hat{a}_{\mathrm{sig}}(t)\right\}_{t\in\mathbb{R}}$. As in the single-mode case, we proceed by defining corresponding quadrature operators, which we will also refer to as "pulse quadratures":

pulse quadratures

$$\hat{Q}_t^{(\mathrm{i})} \equiv \mathrm{Re}\left(\hat{a}_t^{(\mathrm{i})}\right), \hat{P}_t^{(\mathrm{i})} \equiv \mathrm{Im}\left(\hat{a}_t^{(\mathrm{i})}\right), \tag{5.67}$$

$$\hat{X}_t^{(\mathrm{i})} \equiv \mathrm{Re}\left(\hat{b}_t^{(\mathrm{i})}\right), \hat{Y}_t^{(\mathrm{i})} \equiv \mathrm{Im}\left(\hat{b}_t^{(\mathrm{i})}\right). \tag{5.68}$$

application to experimental data

How can we measure these pulse quadratures? In complete analogy to the single-mode case, we substitute our measurement $c(\tau) \equiv \sqrt{2}\,(x(\tau) + iy(\tau))$ for $\hat{a}_{\mathrm{sig}}(\tau)$ in (5.65) and (5.66) and use the results to compute measurement results for the pulse quadratures (5.67) and (5.68). Recall that x and y are the measurement signals from the amplitude and phase homodyne detection, respectively, and $c(\tau) \equiv \sqrt{2}\,(x(\tau) + iy(\tau))$ is our estimate for the complex field state of the light mode $\hat{a}_{\mathrm{sig}}(\tau)$ returning from the optomechanical cavity.

covariance matrix of pulse quadratures

To gather statistics regarding the pulse quadratures, we repeat this process by cutting our measurement trace $c(\tau)$ into N non-overlapping pieces and calculating the pulse quadratures for each of these pieces as described in Section 5.3.2.1. In this way, we can collect an ensemble of pulse quadratures $\left\{{Q^{(\mathrm{i})}}_t, {P^{(\mathrm{i})}}_t, {X^{(\mathrm{i})}}_t, {Y^{(\mathrm{i})}}_t\right\}_{t=t_1,\ldots,t_N}^{i=1\ldots m}$ measured for N different times t. We calculate the covariance matrix $\tilde{\sigma}$ for this ensemble of measured pulse quadratures, in order to evaluate the entanglement between the pulse modes $\left\{\hat{a}_t^{(i)})\right\}_{i=1\ldots m}$ and $\left\{\hat{b}_t^{(i)}\right\}_{i=1\ldots m}$. Note

that, if we analyze the contributions of m mechanical modes, $\tilde{\sigma}$ is a $4m \times 4m$ matrix.

Finally, we calculate the logarithmic negativity $E_{\mathcal{N}}$ of $\tilde{\sigma}$ with respect to the bipartition formed by the entangling and readout pulse, hence the bipartition formed by the set of quadrature operators

measuring the entanglement

$$\hat{\boldsymbol{R}}_{\text{entangling}} \equiv \left\{ \hat{Q}_t^{(\text{i})}, \hat{P}_t^{(\text{i})} \right\}_{i=1\ldots m}, \tag{5.69}$$

$$\hat{\boldsymbol{R}}_{\text{read-out}} \equiv \left\{ \hat{X}_t^{(\text{i})}, \hat{Y}_t^{(\text{i})} \right\}_{i=1\ldots m}. \tag{5.70}$$

Note that, in this thesis, I use a slightly extended definition of the logarithmic negativity which allows to ascribe different negative values to different separable states (while the standard definition always yields zero for separable states). This extension, which is subtly ambiguous in the multi-mode case, is explained in Section C.1.

As discussed in 5.3.3, $c(\tau)$ is an estimate of $\hat{a}_{\text{sig}}(\tau)$ only up to an additional shot noise term. This is unavoidable because we simultaneously measure x and y on the same field. But the additional shot noise is statistically uncorrelated with $\hat{a}_{\text{sig}}(\tau)$ and we can independently characterize its effects on our results. Therefore, we can subtract the effect of the additional shot noise on the level of covariance matrices as described in 5.3.3. Also the other post-processing steps (correction for dark noise, homodyne visibility, and detector efficiency, and calibration) should be performed in analogy to the single-mode case as described in Section 5.3.3.

added noise due to dual-rail homodyning

5.7 MULTIMODE SIMULATIONS

5.7.1 *Single-mode vs multimode*

Let us first check that the multi-mode generalization of the protocol described in Section 5.6 can indeed reveal entanglement in the output light of our optomechanical cavity. To this end, we analyze multi-mode simulations using the single-mode and the multi-mode protocol and compare the results. For simplicity, let us look at the simplest case: a resonantly driven two-mode system with a moderate mode spacing (roughly 400 kHz) and without optical noise. Figure 5.6 shows the results of applying a two-mode and a single-mode evaluation in this situation. Indeed, the two-mode evaluation reveals entanglement which the single-mode evaluation does not detect.

For comparison, the plot also shows the result for the corresponding single-mode case (i.e. a simulation with only the first of the two simulated modes). Over a wide range of pulse widths, the entanglement obtained in the single-mode simulation is quite similar to that obtained in the two-mode evaluation of the two-mode simula-

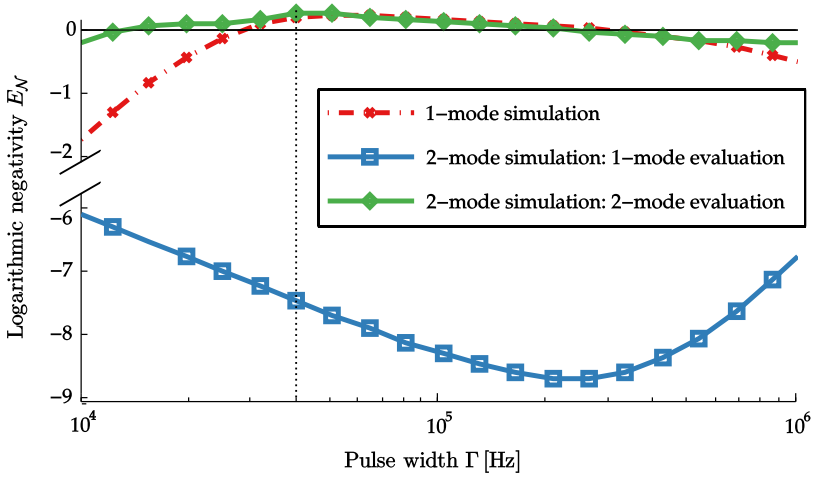

Parameters: without optical noise, $\omega_{m1} = 2\pi \times 920\,\mathrm{kHz}$, $\omega_{m2} = 2\pi \times 1.3\,\mathrm{MHz}$, $\kappa \simeq 2.73 \times \omega_{m1}$, $g_0 \simeq 71 \times 10^{-6} \times \omega_{m1}$, $P_{\mathrm{in}} = 30\,\mu\mathrm{W}$, $g \simeq 0.37 \times \omega_{m1}$, $Q \simeq 15.8 \times 10^6$, $T = 5\,\mathrm{K}$.

Figure 5.6. Logarithmic negativity $E_{\mathcal{N}}$ versus pulse width Γ for single- and two-mode evaluations of a two-mode simulation. The two-mode evaluation (green line, diamond markers) reveals entanglement for a wide range of pulse widths (chosen identically for the first and the second mode function), while the single-mode evaluation (blue line, square markers) does not reveal entanglement. Note that the y-axis has been broken in order to fit both curves into the same plot. For comparison, the entanglement for a simulation with only the first of the two modes is also plotted (red dashed-dotted line).

tion. Hence, even though the second mechanical mode can, if it is not accounted for, completely destroy the entanglement, it does not add significantly to the amount of detected entanglement for most pulse widths in this scenario. (For very long pulses, i.e. very small pulse widths, however, the two-mode evaluation/simulation yields significantly higher entanglement.) Note also that going from the single-mode case to the two-mode case does not affect the optimal pulse width very much; the optimum shifts only slightly towards narrower pulses.

5.7.1.1 *Correlation structure in the multi-mode case*

To understand better why the single-mode evaluation fails to reveal the entanglement if multiple mechanical modes are present, we can analyze the states produced in the evaluations presented in Figure 5.6. For simplicity, we fix the pulse width at $\Gamma \simeq 40\,\mathrm{kHz}$ (at the value yielding the maximum entanglement; dotted vertical line in Figure 5.6) and compare the following states:

σ_1: single-mode simulation (green, diamond marker in Figure 5.6).

σ_2: two-mode evaluation of two-mode simulation (red, cross marker).

σ_{21}: single-mode evaluation of two-mode simulation (blue, square).

STATE	SIMULATION	EVALUATION	$E_{\mathcal{N}}$	n_{EFF}
σ_1	1-mode	1-mode	0.23	5.59×10^2
σ_2	2-mode	2-mode	0.27	5.62×10^2
σ_{21}	2-mode	1-mode	-7.5	3.39×10^4

Table 5.1. Comparison of entanglement and effective occupation number for different numbers of modes used in the simulation and in the evaluation.

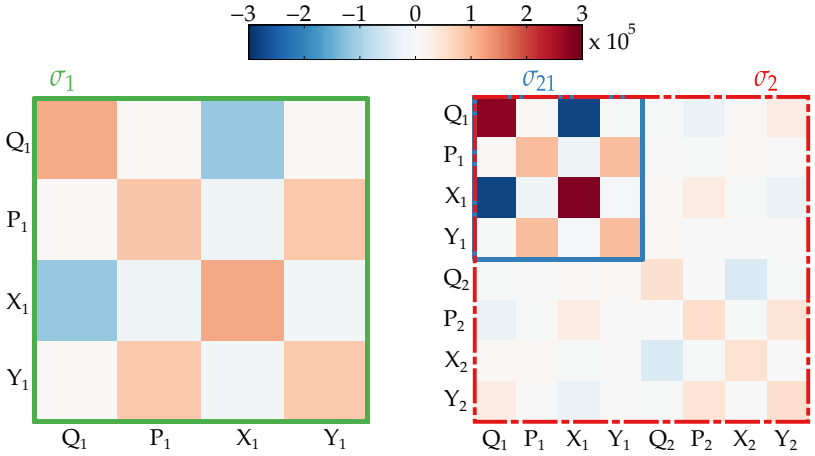

Figure 5.7. Density plot of covariance matrices resulting from different types of evaluations. The colors of the frames for the different matrix plots correspond to those in the corresponding plots of $E_{\mathcal{N}}$ versus Γ in Figure 5.6. Note that σ_{21} (right panel, blue frame; corresponding to the 1-mode evaluation of a 2-mode simulation) is a submatrix of σ_2 (right panel, red frame; corresponding to the 2-mode evaluation of the same simulation). σ_{21} should be compared with σ_1 (left panel, green frame) which is the same evaluation but applied to a single-mode simulation.

Parameters: as in Figure 5.6, $\Gamma = \Gamma_{\text{opt}} \simeq 40\,\text{kHz}$.

Figure 5.7 shows a density plot of the covariance matrices corresponding to these states, while some key characteristics of these states are listed in Table 5.1.

As pointed out above, only σ_1 and σ_2 are entangled (with similar values of $E_{\mathcal{N}}$), while σ_{21} (single-mode evaluation of the two-mode simulation) is separable. At the same time, σ_1 and σ_2 have almost the same effective occupation number n_{eff},[41] whereas σ_{21} has an effective occupation number which is almost two orders of magnitude larger. Hence, the purity and the entanglement of σ_1 and σ_2 are almost the same, whereas σ_{21} is much less pure and separable.

[41] *Defined as the occupation number of a thermal state with the same purity.*

This can be interpreted as follows. In the multi-mode case, the light modes $\hat{a}^{(1)}$, $\hat{b}^{(1)}$ corresponding to a single mechanical mode are, in general, strongly correlated with light modes $\hat{a}^{(j)}$, $\hat{b}^{(j)}$ corresponding to other mechanical modes. In the single-mode evaluation, where

single-mode evaluation

we only look at $\hat{a}^{(1)}$, $\hat{b}^{(1)}$, this correlation looks like random noise, i.e. it drastically decreases the purity of the modes $\hat{a}^{(1)}$, $\hat{b}^{(1)}$. This decreased purity, in turn, prevents entanglement between $\hat{a}^{(1)}$ and $\hat{b}^{(1)}$. The multi-mode evaluation, on the other hand, includes all light modes $\hat{a}^{(j)}$, $\hat{b}^{(j)}$ which are correlated with the light modes $\hat{a}^{(1)}$ and $\hat{b}^{(1)}$ of primary interest in the evaluation. What looked like random noise on the modes $\hat{a}^{(1)}$ and $\hat{b}^{(1)}$ before, can thereby be seen as correlations with other light modes. In this way, the (global) purity is restored to the original level and entanglement can be detected.

multi-mode evaluation

5.7.2 *Full multi-mode case*

The results of Section 5.7.1 establish the in-principle-suitability of our entanglement detection protocol in a multi-mode setting. There may still remain doubts, however, about the feasibility of this idea in a MIM-cavity setting in which there are on the order of 50 mechanical modes in a frequency range of only a few MHz. To check that we can detect entanglement also in this situation, I performed simulations with 45 mechanical modes with realistic parameters (frequencies ω_m and coupling rates g) for liquid Helium temperatures ($T = 5\,\mathrm{K}$) and including optical noise as measured for our setup. I fixed all mechanical quality factors at $Q = 5 \times 10^6$, such that the mechanical decoherence rate for all mechanical modes in this simulation is given by

$$\bar{n}\gamma = \frac{kT}{\hbar Q} \simeq 2\pi \times 21\,\mathrm{kHz}. \tag{5.71}$$

The result is presented in Figure 5.8. Entanglement appears for pulse widths $\Gamma \geq 44\,\mathrm{kHz}$. Hence, we can detect entanglement also in an extreme multi-mode setting and, as expected, the entanglement persists for pulse durations up to the order of the mechanical decoherence time. In contrast to the single- and two-mode case, however, entanglement appears already for much shorter pulses (larger pulse widths). The maximum amount of entanglement achieved in this example is $E_{\mathcal{N}}^{(\mathrm{opt})} \simeq 0.074$.

5.7.2.1 *Per-mode analysis of the full multi-mode case*

Using the 45-mode simulation presented above, we can explore how individual mechanical modes contribute to the entanglement in an extreme multi-mode case. Figure 5.9 shows the logarithmic negativity (optimized over pulse width Γ) after tracing out one mode. This optimum is plotted against the index of the mode which has been traced out. The index refers to the position of the mode if modes are ordered by ascending frequency.

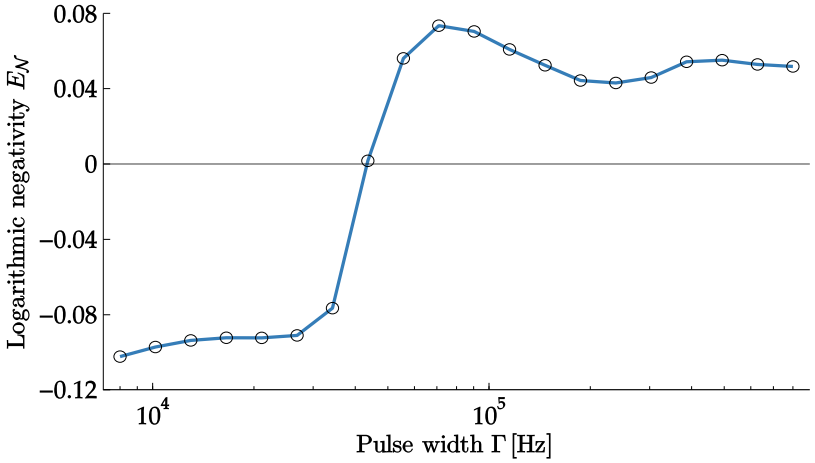

Figure 5.8. Logarithmic negativity $E_{\mathcal{N}}$ versus pulse width Γ for a simulation of the first 45 modes of a SiN membrane of roughly 490 µm side length. We assume a relative difference of the side lengths of below 1 ‰. This slight asymmetry introduces a relative frequency difference of 0.03 ‰ to 0.5 ‰ between the otherwise degenerate modes $\omega_{i,j}$ and $\omega_{j,i}$. Couplings were calculated assuming optimal positioning along the axial cavity direction and a slight misalignment of some µm along the transversal directions yielding $g_1 \simeq 0.37 \times \omega_1$ for the fundamental mechanical mode and in between $7.4 \times 10^{-3} \times \omega_1$ and $0.22 \times \omega_1$ for the higher mechanical modes. For lack of a good model for the clamping loss, we set all mechanical quality factors to $Q = 5 \times 10^6$.

Parameters:
with optical noise,
$\omega_1 = 2\pi \times 800\,\mathrm{kHz}$,
$\omega_{2,\ldots,45}/(2\pi \cdot \mathrm{MHz}) \simeq \{1.26, \ldots, 4.56\}$,
$Q = 5 \times 10^6$ (all modes),
$g_1 \simeq 0.37 \times \omega_1$,
$g_{2,\ldots,45}/\omega_1 \in [7.4 \times 10^{-3}, \ldots, 0.22]$
$\kappa \simeq 2.73 \times \omega_1$,
$P_{\mathrm{in}} = 20\,\mu\mathrm{W}$,
$T = 5\,\mathrm{K}$.

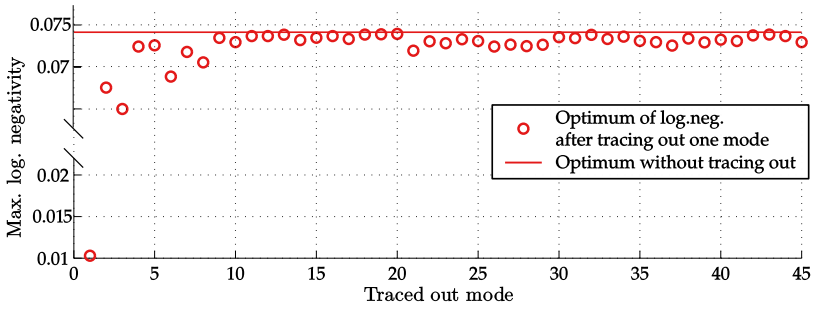

Figure 5.9. Logarithmic negativity $E_{\mathcal{N}}$ for a 45-mode simulation with all but one mode taken into account in the evaluation. Plotted is the optimum of the logarithmic negativity against the index of the mechanical mode which has been traced out (i.e. not taken into account in the evaluation). The red horizontal line marks the optimum for the full evaluation which takes all modes into account ($E_{\mathcal{N}}^{(\mathrm{opt})} \simeq 0.074$). Note that the y-axis has been split to also show the outlier at index 1.

Parameters as in Figure 5.8.

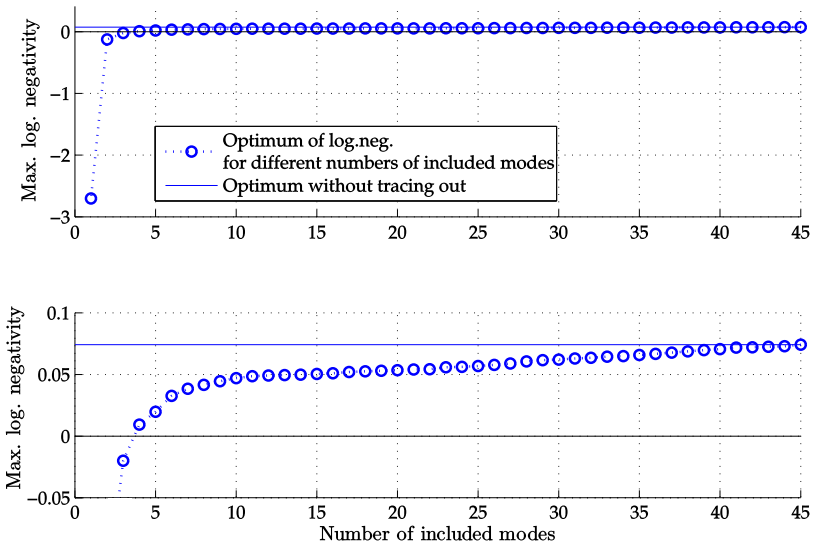

Parameters as in Figure 5.8

Figure 5.10. Logarithmic negativity $E_{\mathcal{N}}$ for a 45-mode simulation with a varying number of modes taken into account in the evaluation. Plotted is the optimum of the logarithmic negativity against the index of the last mechanical mode which has been taken into account (equivalently, the number of modes taken into account). For example, the third data-point corresponds to an evaluation which includes the first three mechanical modes. The lower panel is a zoom-in of the upper panel. The blue horizontal line marks the optimum for the full evaluation which takes all 45 modes into account ($E_{\mathcal{N}}^{(\mathrm{opt})} \simeq 0.074$).

Figure 5.9 shows that there is only one mode we absolutely should not forget, namely the fundamental mode (index 1): If we leave out the fundamental mode, the entanglement persists but the logarithmic negativity drops by almost 90 %. The next most important modes are those with indices 3, 2, 6, 8, and 7, which correspond to the following frequencies (in $2\pi \times$ MHz): 1.2651, 1.2647, 1.7892, 2.0398, and 2.0394 (membrane mode indices $(1,2)$, $(2,1)$, $(1,3)$, $(2,3)$, and $(3,2)$). If one of these five modes is not taken into account, the logarithmic negativity drops by around 5 % to 10 %. For most other higher order modes it does not make a big difference whether we take them into account or not.

Note, however, that this does not mean that we can neglect *all* higher order modes. This is demonstrated in Figure 5.10 which shows the optimum of the logarithmic negativity as a function of the number of modes which are taken into account for the evaluation.

small number of modes is sufficient in the evaluation

Figure 5.10 shows that, in this example, we need to take, at least, the first four modes into account to detect entanglement. Including the first ten modes is sufficient to reap two thirds of the maximum amount of entanglement. This demonstrates clearly that we can limit the evaluation to a small number of modes, which is good news be-

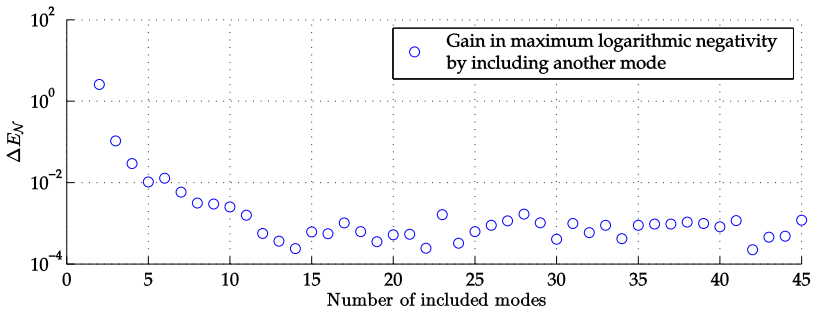

Figure 5.11. Increase $\Delta E_{\mathcal{N}}$ in logarithmic negativity when taking more and more modes into account (in a 45-mode simulation). Plotted is the change in the optimum of the logarithmic negativity against the index of the last mechanical mode which has been taken into account (equivalently, the number of modes taken into account). Note the logarithmic y-axis.

Parameters as in Figure 5.8

cause it would be impossible to include all membrane modes (which interact significantly) in the evaluation.

Figure 5.10 also shows that, with increasing number of added modes, the marginal improvement in logarithmic negativity from adding more modes becomes quite small. This can be seen even more clearly in Figure 5.11 which shows the gain in logarithmic negativity from adding the next mode as a function of the number of included modes. Figure 5.11 also shows that even though the marginal improvement becomes quite small, it does not converge to zero. This suggests that there is no in-principle saturation of the entanglement for an increasing number of mechanical modes. We should keep in mind however that, for all simulated modes, the sideband resolution ω_m/κ was relatively small (the highest frequency is $\omega_{45} \simeq 2\pi \times 4.56\,\mathrm{MHz} \simeq 2.1 \times \kappa$). If we add mechanical modes at increasingly high frequencies, we expect to see diminishing entanglement returns because, eventually, for $\omega_m \gg \kappa$ sideband creation is suppressed by the cavity envelope.

marginal entanglement gain from adding modes

5.8 TWO-SIDEBAND PROTOCOL

In this section, I discuss an extension of the entanglement detection protocol which I refer to as the "two-sideband protocol". This protocol is more efficient in the sense of detecting significantly more entanglement. For certain parameters, it even allows entanglement detection where we could not detect entanglement without it.

Recall that the protocol for detecting mechanically mediated light-light entanglement discussed so far relies on the analysis of only one sideband per pulse and mechanical mode: We extract the lower sideband in the first pulse and the upper sideband in the second pulse.

This protocol was motivated as follows: The lower sideband is caused by the two-mode squeezing interaction while the upper side-

band is caused by the beam-splitter interaction. Hence, first extracting the lower sideband and then the upper sideband amounts to entanglement creation (between the mechanical mode and the lower sideband) followed by an entanglement swap (from the mechanical mode onto the upper sideband).

continuous production of both sidebands

In reality, however, both processes take place continuously. Hence, a partial swap from the mechanical oscillator onto the upper sideband takes place within each pulse. This means that there is a correlation between the lower and the upper sideband not only in between two subsequent pulses (inter-pulse correlation), but also within each pulse (intra-pulse correlation). If we evaluate the *inter-pulse* correlation by taking only one sideband into account in a given pulse, the *intra-pulse* correlation with the other sideband (which is not accounted for in the evaluation) translates into increased mixedness of the inter-pulse quantum state and, correspondingly, lower entanglement. Note that this is in very close analogy to the discussion in Section 5.7.1.1 regarding the increase in mixedness and corresponding decrease in entanglement due to correlations with sidebands caused by other mechanical modes.

intra-pulse correlations

5.8.1 *Definition of the two-sideband protocol*

This suggests that we can improve our entanglement detection protocol significantly by taking, within each pulse, both sidebands into account. To this end, we define four mode functions per mechanical mode:

extended set of mode functions

$$\tilde{\alpha}^{(\mathrm{i})}_{(\pm)}(t) \equiv \exp\left(\pm i\omega_{mi}t\right) \times \exp\left(\Gamma_i t\right) \text{ (for } t \leq 0\text{)}\,, \tag{5.72}$$

$$\tilde{\beta}^{(\mathrm{i})}_{(\mp)}(t) \equiv \exp\left(\mp i\omega_{mi}t\right) \times \exp\left(-\Gamma_i t\right) \text{ (for } t \geq 0\text{)}\,. \tag{5.73}$$

$\tilde{\alpha}^{(\mathrm{i})}_{(+)}$ and $\tilde{\beta}^{(\mathrm{i})}_{(-)}$ are the two mode functions which were previously considered. They extract the lower sideband for the first pulse and the upper sideband for the second pulse, respectively. To these, we add two additional mode functions $\tilde{\alpha}^{(\mathrm{i})}_{(-)}$ and $\tilde{\beta}^{(\mathrm{i})}_{(+)}$ which extract exactly the opposite sidebands: the upper sideband for the first pulse and the lower sideband for the second pulse, respectively. Hence, in this extended protocol, we analyze four light modes per mechanical mode. The application of these mode functions to the actual measurement data is exactly as described in detail in Section 5.3.1.

Again, we have to ensure that the mode functions are mutually orthonormal. To this end, we apply a numerical orthonormalization procedure to the extended set of mode functions

orthonormalization

$$\left\{\tilde{\alpha}^{(\mathrm{i})}_{(+)}(t),\, \tilde{\alpha}^{(\mathrm{i})}_{(-)}(t),\, \tilde{\beta}^{(\mathrm{i})}_{(-)}(t),\, \tilde{\beta}^{(\mathrm{i})}_{(+)}(t)\right\}_{i=1\ldots m}$$

in order to obtain a an orthonormal set of mode functions. Note that mode functions belonging to different pulses are automatically mutually orthogonal to each other since they have no overlap in time. Hence, we do not need to orthonormalize any of the β-functions to any of the α-functions. In Section C.4, an example of a set of mode functions used for a two-sideband evaluation is given.

As mentioned above, this extension of the protocol will increase the purity of the reconstructed state of the light field and should thereby also increase the entanglement. Note that, in the two-sideband protocol, we will always detect at least as much entanglement as in the "single-sideband" protocol considered so far. This is because, with the two-sideband protocol as defined above, switching back to a "single-sideband" evaluation simply amounts to tracing out the added modes $\tilde{\alpha}^{(\mathrm{i})}_{(-)}$ and $\tilde{\beta}^{(\mathrm{i})}_{(+)}$ and tracing out can only decrease the amount of entanglement.

expected effect on entanglement

5.8.2 *Single-mode case*

To verify that we can indeed profit from extending the protocol as described in Section 5.8.1, we turn to simulations. For simplicity, we consider only a single mechanical mode at first. Figure 5.12 shows the entanglement as a function of pulse width for a single-mode simulation without optical noise and a mechanical quality factor of only $Q = 5 \times 10^5$. The plot compares the results of a two-sideband evaluation to those of an evaluation which takes only one sideband per pulse into account. Remarkably, entanglement can be detected with the two-sideband evaluation despite the poor mechanical quality factor and a very small cooperativity of only $\mathcal{C} \simeq 3.7 \times 10^{-2}$, whereas no entanglement is detected with the single-sideband evaluation.

5.8.2.1 *Structure of the covariance matrix*

Figure 5.13 demonstrates why the two-sideband evaluation is beneficial: There are indeed very strong correlations between the light modes $\tilde{\alpha}_{(+)}$ and $\tilde{\beta}_{(-)}$ we considered before Section 5.8 (upper left submatrix) and the light modes $\tilde{\alpha}_{(-)}$ and $\tilde{\beta}_{(+)}$ (lower right submatrix) which were added in Section 5.8.1. Because of these correlations, the effective occupation number of the quantum state of only the modes $\tilde{\alpha}_{(+)}$ and $\tilde{\beta}_{(-)}$ is much higher ($n_{\mathrm{eff}} \simeq 63.1$) than that of the quantum state of the full two-sideband evaluation ($n_{\mathrm{eff}} \simeq 8.7$). Because of this increased mixedness there is no entanglement between the modes $\tilde{\alpha}_{(+)}$ and $\tilde{\beta}_{(-)}$ ($E_{\mathcal{N}} \simeq -0.07$), but there is entanglement between the set of modes $\tilde{\alpha}_{(+)}$, $\tilde{\alpha}_{(-)}$ and the set of modes $\tilde{\beta}_{(-)}$, $\tilde{\beta}_{(+)}$ ($E_{\mathcal{N}} \simeq 0.013$).

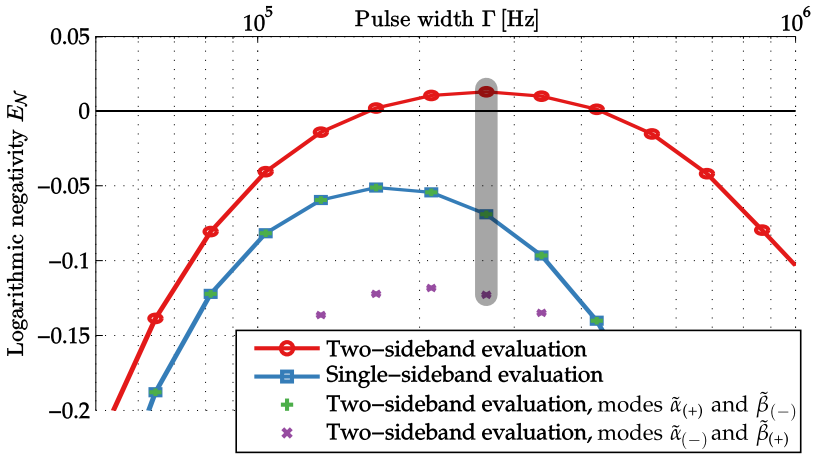

Parameters: without optical noise, $\omega_m = 2\pi \times 920\,\mathrm{kHz}$, $\kappa \simeq 2.73 \times \omega_m$, $g_0 \simeq 7.1 \times 10^{-5} \times \omega_m$, $g \simeq 0.15 \times \omega_m$, $Q = 5 \times 10^5$, $T = 5\,\mathrm{K}$, $\mathcal{C} \simeq 3.7 \times 10^{-2}$.

Figure 5.12. Logarithmic negativity $E_\mathcal{N}$ versus pulse width Γ for a single-mode simulation. The two-sideband evaluation (red, circle markers) yields entanglement while the single-sideband evaluation (blue, square markers) does not. Keeping only the modes $\tilde{\alpha}_{(+)}$ and $\tilde{\beta}_{(-)}$ from the two-sideband evaluation (green, plus markers) yields the same results as the single-sideband evaluation, as expected. Keeping only the modes $\tilde{\alpha}_{(-)}$ and $\tilde{\beta}_{(+)}$ (purple, cross markers) yields even smaller values of $E_\mathcal{N}$. Figure 5.13 shows covariance matrices corresponding to the values marked by the gray beam (at $\Gamma \simeq 266\,\mathrm{kHz}$).

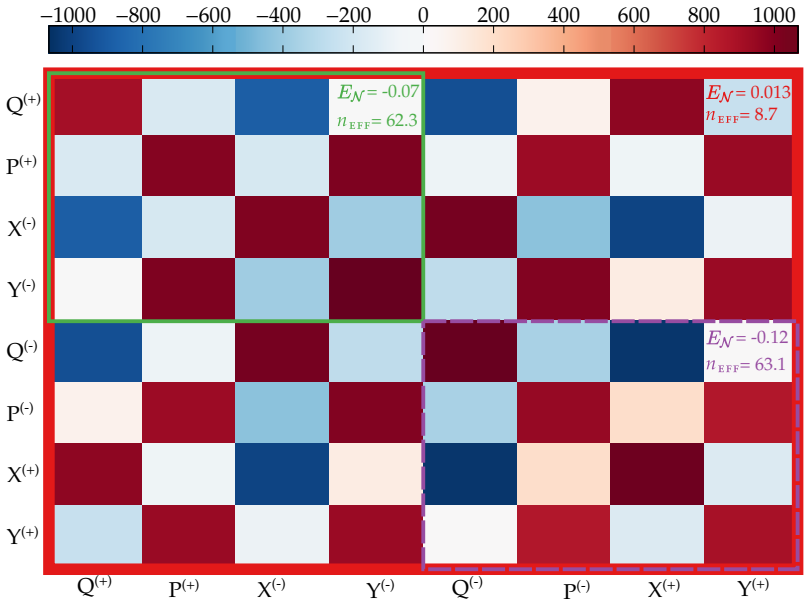

Parameters: as in Figure 5.12. $\Gamma = \Gamma_{\mathrm{opt}} \simeq 266\,\mathrm{kHz}$ (marked with a gray beam in Figure 5.12).

Figure 5.13. Covariance matrix (CM) for two-sideband evaluation of a single-mode simulation without optical noise. The full CM (red frame) results from the two-sideband evaluation, yielding entanglement ($E_\mathcal{N} \simeq 0.013$) and a low effective occupation number $n_{\mathrm{eff}} \simeq 8.7$. The upper left CM (green frame) corresponds to the single-sideband evaluation discussed before Section 5.8, which takes only the light modes $\tilde{\alpha}_{(+)}$ and $\tilde{\beta}_{(-)}$ into account. This yields $E_\mathcal{N} \simeq -0.07$ and $n_{\mathrm{eff}} \simeq 62.3$. The lower right CM (purple, dashed frame) corresponds to the light modes $\tilde{\alpha}_{(-)}$ and $\tilde{\beta}_{(+)}$ which yields $E_\mathcal{N} \simeq -0.12$ and $n_{\mathrm{eff}} \simeq 63.1$.

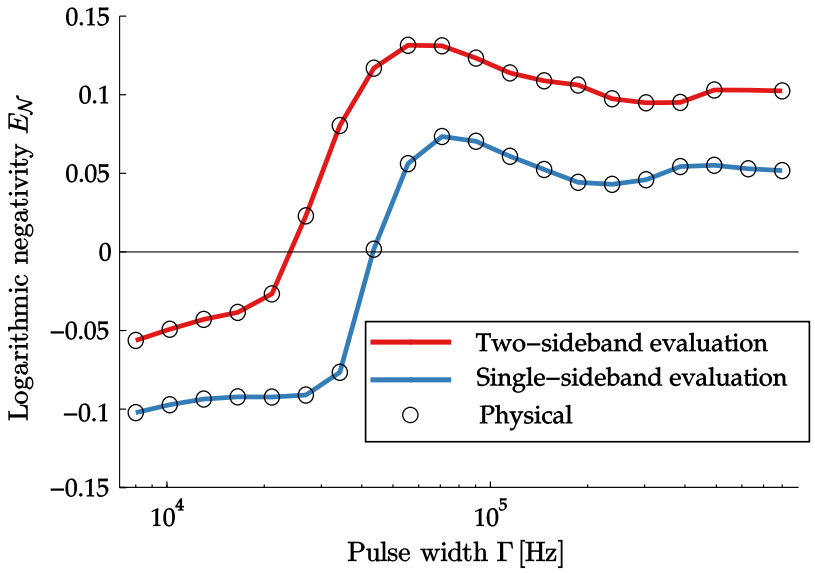

Figure 5.14. Logarithmic negativity $E_{\mathcal{N}}$ versus pulse width Γ for a simulation of the first 45 modes of a SiN membrane of roughly 490 µm side length. For all pulse widths Γ, the two-sideband evaluation (red line) yields more entanglement than the single-sideband evaluation (blue line). The maximum of the two-sideband evaluation ($E_{\mathcal{N}}^{(\max)} \simeq 0.13$) is almost twice as large as the maximum of the single-sideband evaluation ($E_{\mathcal{N}}^{(\max)} \simeq 0.07$).

Parameters: as in Figure 5.8.

5.8.3 *Multi-mode case*

Finally, let us check whether the encouraging results of Section 5.8.2 also hold in a multi-mode setting. To this end, we reevaluate the data from the 45-mode simulation presented in Figure 5.8 using the two-sideband evaluation. The result is presented in Figure 5.14. The 45-mode simulation confirms that, also in an extreme multi-mode setting, the two-sideband evaluation yields significantly more logarithmic negativity ($E_{\mathcal{N}}^{(\max)} \simeq 0.13$ compared to $E_{\mathcal{N}}^{(\max)} \simeq 0.07$ for the single-sideband evaluation). Note that, in Figure 5.14 and in some of the following plots, black circle markers denote the pulse widths at which the corresponding covariance matrix is physical, where "physical" means that the covariance matrix satisfies generalized Heisenberg uncertainty relations (sometimes referred to as the Robertson–Schrödinger uncertainty relations); see e.g. [AI07, eq. (18)].

5.8.3.1 *Structure of the covariance matrix*

Let us step back for a moment: We have seen that under experimentally realistic conditions, pulsed-continuous entanglement can be detected if a suitable set of light modes is analyzed. I covered two ways of extending the set of light modes under consideration. First, in Section 5.6 and Section 5.7, I showed how to deal with multiple me-

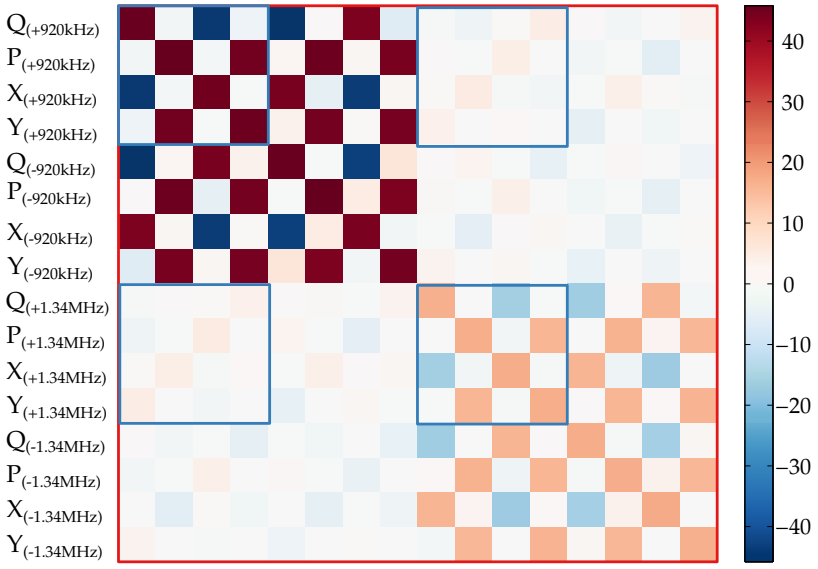

Parameters: without optical noise, $\omega_1 = 2\pi \times 920\,\mathrm{kHz}$, $\omega_2 \simeq 1.45 \times \omega_1$, $\kappa \simeq 2.73 \times \omega_1$, $g_1 = g_2 \simeq 0.37 \times \omega_1$, $Q_1 = Q_2 \simeq 15.8 \times 10^6$, $T = 5\,\mathrm{K}$.

Figure 5.15. Covariance matrix (CM) for two-sideband evaluation of a two-mode simulation without optical noise. The full CM (red frame) results from the two-sideband evaluation and yields $E_\mathcal{N} \simeq 0.3$. The blocks surrounded by blue frames correspond to the single-sideband evaluation discussed before Section 5.8, which yields $E_\mathcal{N} \simeq 0.09$. The upper left block, corresponds to a single-mode, two-sideband evaluation, which does not yield entanglement ($E_\mathcal{N} \simeq -0.22$). In this simulation, a slight red-detuning of the laser of $\Delta = 2\pi \times 25\,\mathrm{kHz}$ has been assumed (see Section 5.9).

chanical modes. Next, in Section 5.8, I showed that including both sidebands for each pulse (and each mechanical mode) can improve the protocol even further.

Figure 5.15 brings both of these extensions together in one plot. It shows the covariance matrix for a two-sideband evaluation of a two-mode simulation. The quadratures have been arranged such that the light modes pertaining to each mechanical mode form a connected block.

It is immediately apparent from the resulting very clear block structure that there are strong correlations between all the light modes pertaining to the same mechanical mode. In particular, there are also very strong correlations between the light modes corresponding to the same mechanical mode within the same pulse (intra-pulse correlations). And we have seen that the two-sideband protocol, by taking these intra-pulse correlations into account, indeed yields much more logarithmic negativity (in the example plotted here: $E_\mathcal{N} \simeq 0.3$ instead of $E_\mathcal{N} \simeq 0.09$).

intra-pulse correlations

In addition, we see some correlations between these blocks: These are the correlations which connect light modes pertaining to different mechanical modes. Surprisingly, neglecting these correlations between light modes related to different mechanical modes has a much

correlations between light-modes corresponding to different mechanical modes

bigger effect on the entanglement than neglecting the intra-pulse correlations for each mechanical mode. In fact, it leads to a complete loss of entanglement ($E_{\mathcal{N}} \simeq -0.22$ instead of $E_{\mathcal{N}} \simeq 0.3$).

In this sense, the multi-mode protocol of Section 5.6 is absolutely essential for detection of entanglement in a multi-mode setting, while the two-sideband extension is very beneficial but, in general, not strictly necessary.

5.9 DETUNED DRIVE

So far, we assumed a resonant laser drive. In a real experiment, however, this assumption cannot be met exactly because the laser detuning is always fluctuating slightly. In fact, from an experimental point of view, we would even prefer to work with a slightly red-detuned drive because, under these conditions, the experiment is much more stable and therefore easier to operate (especially at higher input powers). Therefore, this section is devoted to the question: Can we generate and detect entanglement also with a red-detuned laser drive?

We expect the basic idea of our entanglement detection protocol to also work with a moderate detuning: Even with a detuned drive—we still get the sidebands from the two-mode squeezing and the beamsplitter part of the interaction at $-\omega_m$ and $+\omega_m$ (with respect to our local oscillator). Hence, the extraction of the sidebands from our measurement data still works in the same way. The main difference is that, for a red-detuned laser drive, the sideband at $+\omega_m$ has a higher photon flux than the sideband at $-\omega_m$. This is due to the peak of the cavity transmission function being slightly shifted towards the upper sideband which leads to the well-known phenomenon of laser cooling of the mechanical oscillator [MK04; Mar+07; Wil+08; Grö+08]. But since we work with a relatively broad cavity ($\kappa \simeq 2.7\,\mathrm{MHz}$) and outside the resolved-sideband regime ($\kappa \gg \omega_m \lesssim 1\,\mathrm{MHz}$) , a moderate detuning of some 100 kHz only leads to a small sideband-asymmetry of less than 2 : 1.[42] Applied to our protocol, this means that the variances of the light modes targeting the upper sideband will be larger than that of its counterpart for the lower sideband, but they are still on the same order of magnitude.

sideband asymmetry

[42] *Using the expression* $\frac{S_{FF}(+\omega_m)}{S_{FF}(-\omega_m)} = \frac{(\omega_m-\Delta)^2+(\kappa/2)^2}{(\omega_m+\Delta)^2+(\kappa/2)^2}$ *from [Mar+07]*

Of course, even though the asymmetry between the sidebands in terms of photon flux is quite moderate, a red-detuned drive will still lead to significant cooling of the mechanical modes and thereby change the dynamics of the system drastically. The expected cooling factor (neglecting optical noise) can be as high as 10^4 for the parameters considered below.[43] The question is: Does this help or hinder the detection of entanglement?

laser cooling of mechanical modes

[43] *Cooling of* 6×10^3 *for the parameters of Figure 5.18.*

Below (Section 5.9.1 and Section 5.9.3), I show that a moderately red-detuned drive, generally, has a neutral to beneficial effect on the

entanglement. More specifically, it leads to a decreased sensitivity to higher-order mechanical modes as shown in Section 5.9.3.

Related to the cooling, we also expect a significant decrease in the autocorrelation time of the pulse quadratures. This is because the autocorrelation time is inversely proportional to the damping rate of the mechanical oscillator which increases due to the cooling. Since, in the case of membrane modes, we are dealing with very small intrinsic mechanical damping rates, the added optical damping can make a massive difference in this respect. For the parameters explored below, the difference in damping between the resonant and detuned case can be as large as 10^4. Since the autocorrelation time of the pulses determines the measurement time needed to gather significant statistics for our experiment, a drastic reduction of the autocorrelation time is, in general, quite beneficial. This aspect is discussed in section Section 5.9.2.

5.9.1 *Single-mode simulations*

To explore the effect of a red-detuned drive, we first consider the simple case of a single mechanical mode. Figure 5.16 shows the maximum logarithmic negativity $E_{\mathcal{N}}(\Gamma_{\text{opt}})$ (optimized with respect to the pulse width Γ) as a function of the optomechanical coupling g for three different mechanical quality factors. We contrast the curves resulting from simulations with a resonant drive (blue-greenish lines, square markers) to those for a 200 kHz-red-detuned drive (red-purplish lines, circle markers). In both cases, optical noise was included. Note that the chosen detuning $\Delta = 2\pi \times 200\,\text{kHz}$ is relatively small compared to both the mechanical frequency of $\omega_m = 2\pi \times 920\,\text{kHz}$ as well as the cavity linewidth $\kappa \simeq 2\pi \times 2.73\,\text{MHz}$.

We detect entanglement in both the resonant as well as in the detuned case if the mechanical quality factor exceeds 5×10^6. Hence, detuning the drive does not prevent us from generating and detecting entanglement. In the resonant case, however, the detected entanglement depends significantly on the exact value of the optomechanical coupling g. With a red-detuned drive, in contrast, we are much less sensitive to the exact value of the optomechanical coupling g.

In fact, the strong sensitivity to the exact coupling strength in the resonant case is related to the optical noise. This is demonstrated in Figure 5.17 which compares the optimal entanglement $E_{\mathcal{N}}^{(\text{opt})} = E_{\mathcal{N}}\left(\Gamma_{\text{opt}}\right)$ for a resonant and a red-detuned drive ($\Delta = 200\,\text{kHz}$) and with and without optical noise. For the detuned case (red curves), both noisy and noise-free simulations yield very smooth and monotonically increasing $E_{\mathcal{N}}^{(\text{opt})}(g)$-curves. In the resonant case (blue curves), on the other hand, there is a stark difference between the noise-free and noisy simulations: Without optical noise (solid line), $E_{\mathcal{N}}^{(\text{opt})}(g)$ is

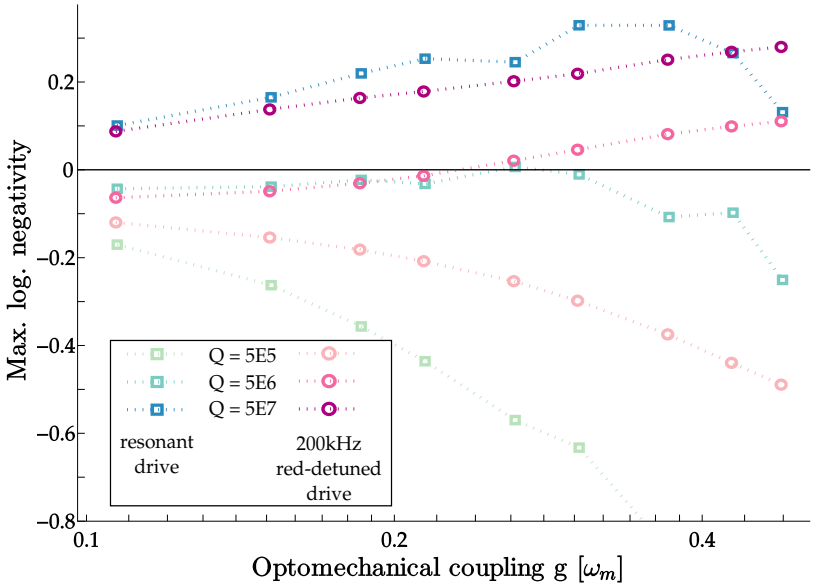

Figure 5.16. Maximum of logarithmic negativity $E_{\mathcal{N}}(\Gamma_{\text{opt}})$ versus optomechanical coupling g for resonant and red-detuned single-mode simulations with optical noise and different mechanical quality factors Q. Blue-greenish lines with square markers correspond to simulations with a resonant drive. Red-purplish lines with circle markers correspond to simulations with a drive which is red-detuned by 200 kHz. In both cases, entanglement is achieved if and only if $Q \geq 5 \times 10^6$. For the detuned simulations, entanglement is a monotone function of the input power, whereas, for the resonant simulations, its dependence on the input power is significantly more erratic.

Parameters:
with optical noise,
$\omega_m = 2\pi \times 0.92\,\text{MHz}$,
$\kappa \simeq 2.73 \times \omega_m$,
$g_0 \simeq 71 \times 10^{-6} \times \omega_m$,
$P_{\text{in}} = [2.5, \ldots, 50]\,\mu\text{W}$,
$g \simeq [0.1, \ldots, 0.48] \times \omega_m$,
$Q = 5 \cdot [10^5, 10^6, 10^7]$,
$\Delta = 2\pi \times [0, 200]\,\text{kHz}$,
$T = 5\,\text{K}$;
single-sideband eval.

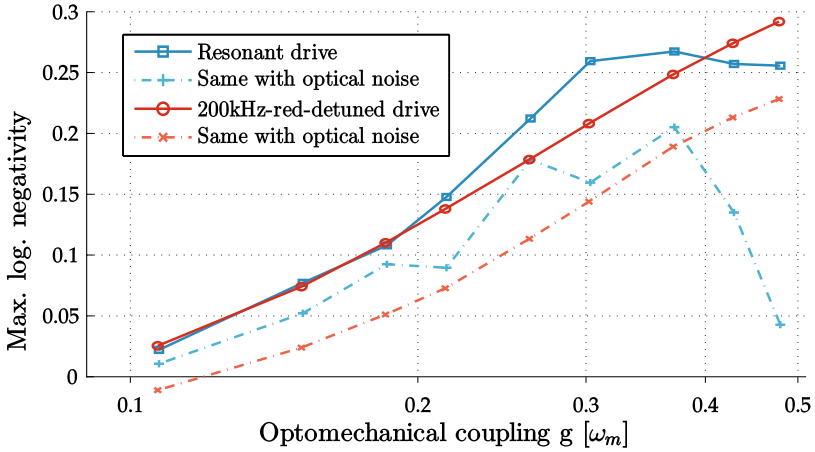

Parameters: with and without optical noise, $Q \simeq 15.8 \times 10^6$, rest as in Figure 5.16.

Figure 5.17. Maximum of logarithmic negativity $E_{\mathcal{N}}(\Gamma_{\text{opt}})$ versus optomechanical coupling g for single-mode simulations with optical noise (dashed lines) and without optical noise (solid lines) and for different laser detunings Δ. Blue (red) lines correspond to simulations with a resonant (200 kHz-red-detuned) drive, respectively.

a rather smooth function with a single local maximum for $g \simeq \omega_m/3$, whereas with optical noise (dashed line), $E_{\mathcal{N}}^{(\text{opt})}(g)$ shows several local maxima and drops quite drastically for $g > 0.4 \times \omega_m$.

It is quite interesting, that both with and without optical noise, the red-detuned drive yields monotonically increasing functions $E_{\mathcal{N}}^{(\text{opt})}(g)$ for all values of g considered here ($g < \omega_m/2$), while for a resonant drive, we obtain a maximum of $E_{\mathcal{N}}^{(\text{opt})}(g)$ at around $g \simeq \omega_m/3$. Hence, a slightly detuned drive allows to go to higher coupling strengths without negatively impacting the entanglement.

5.9.2 *Impact on the required measurement time*

To be able to reliably estimate entanglement for our experiment, we need to gather a significant number of statistically independent pulse pairs. Another way of saying this is: We need to measure orders of magnitude longer than the autocorrelation time of the pulse pairs. As demonstrated in the appendix in Section C.7, the autocorrelation time of the pulse quadratures is essentially given by the inverse mechanical line width. Since the mechanical linewidth can be well below 1 Hz for membrane modes, gathering 10^4 independent pulse pairs, takes at least 10^4 s $\simeq$ 2.8 h. Multiply this by the desired number of independent measurements (e.g. at different optical powers) and this requirement begins to look quite daunting.

optically broadened mechanical line-width

Fortunately, the mechanical line width can be increased drastically by optical cooling, i.e. by using a moderately red-detuned drive. This optical increase in line width is accompanied by a drastic reduction of autocorrelation times as demonstrated in Section C.7. We therefore

expect to be able to collect significant statistics much more quickly using a red-detuned drive. Can we verify that?

Recall that the time evolution of our optomechanical system is linear, all driving noise processes are Gaussian, and the transformations from the quadratures of the output light field to the pulse quadratures are linear too. Therefore, we expect the stationary joint distribution (and, a fortiori, also the stationary marginal distributions) of the pulse quadratures to be Gaussian. Since, we expect the distribution of the measured pulse quadratures to approach the stationary distribution with increasing measurement time, we also expect it to become more and more Gaussian.

stationary distribution of pulse quadratures is Gaussian

Therefore, by measuring the deviation from Gaussianity as a function of measurement time for the detuned and the resonant case, we can study the impact of detuning on our ability to collect significant statistics. Since a detuned drive reduces the autocorrelation time and thereby increases the effective number of independent samples per measurement time, it should yield a faster approach to stationarity and, correspondingly, a faster approach to Gaussianity for the pulse quadratures. Figure 5.18 confirms this expectation: With a resonant drive, the statistics only starts to approach Gaussianity for measurements longer than the inverse mechanical linewidth (black vertical line) because for shorter measurements all samples are strongly correlated. For a detuned drive, on the other hand, the trend towards a Gaussian distribution begins already for much shorter measurement times. Also, for any given measurement time, Gaussianity is better in the detuned case than in the resonant case.

approach to Gaussianity with increasing measurement time

As discussed in Section C.7, the increase in mechanical linewidth and decrease in autocorrelation time is expected to be on the order of four orders of magnitude. Correspondingly, we expect the minimum required measurement time to go down from $10^4\,\mathrm{s} \simeq 2.8\,\mathrm{h}$ to on the order of a second using a 200 kHz red-detuned drive. Hence, in this respect, we gain enormously by operating the experiment in a moderately red-detuned regime.

impact on measurement time

5.9.3 *Two-mode simulations*

To make sure detuning does not hurt our ability to detect entanglement in the presence of multiple mechanical modes, we also explored the effect of a detuned drive in multi-mode simulations. Below, I present the results of two-mode simulations with varying detuning. Results for a detuned simulation with 45 mechanical modes are presented in the appendix, in Section C.8.

The simulations presented below show that, surprisingly, a moderate drive detuning can increase the detected entanglement significantly. Importantly, this increase in detected entanglement is even

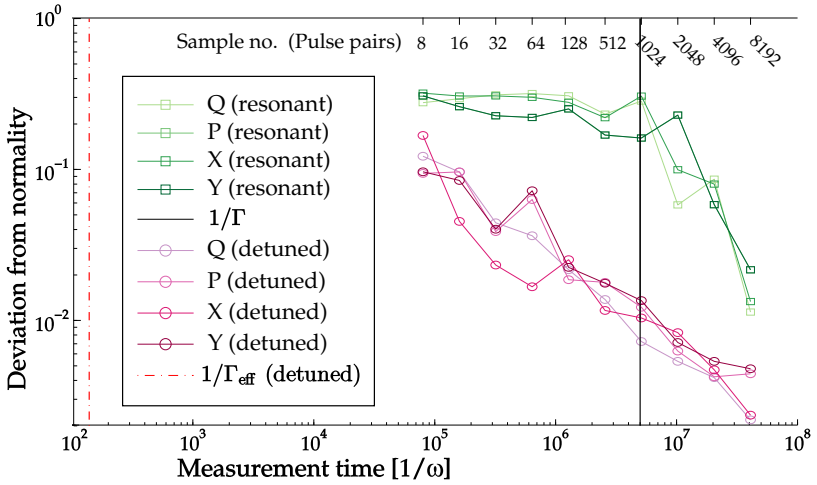

Parameters:
with optical noise,
$\omega_m = 2\pi \times 0.92\,\mathrm{MHz}$,
$\kappa \simeq 2.73 \times \omega_m$,
$g_0 \simeq 71 \times 10^{-6} \times \omega_m$,
$P_{\mathrm{in}} = 15\,\mu\mathrm{W}$,
$g \simeq 0.26 \times \omega_m$,
$Q = 5 \times 10^6$,
$\Delta = 2\pi \times [0, 200]\,\mathrm{kHz}$,
$T = 5\,\mathrm{K}$.

Figure 5.18. Approach of measured statistics of the pulse quadratures to Gaussianity for single-mode simulations with a resonant (greenish, square markers) and a 200 kHz red-detuned drive (red-purplish, circle markers). Plotted is the deviation from Gaussianity for each individual pulse quadrature as a function of measurement time. Deviation from Gaussianity is measured as a distance between the empirical cumulative distribution function (cdf) of the data and the cdf of a Gaussian distribution with the same mean and variance as the full simulated sample. For a resonant drive, Gaussianity is only approached for measurements longer than the inverse mechanical linewidth (black vertical line). For a detuned drive, in contrast, the trend towards Gaussianity begins already for much shorter measurement times. The red dashed-dotted vertical line marks the inverse of the effective (optically broadened) mechanical linewidth $\Gamma_{\mathrm{eff}} \simeq \Gamma_{\mathrm{opt}} \simeq 7.2 \times 10^{-2} \times \omega_m$ in the detuned case. Measurements can never be as short as $1/\Gamma_{\mathrm{eff}}$, however, since they must be longer than the duration of a single pulse-pair (see secondary x-axis for conversion of measurement time to pulse pairs).

more pronounced if we evaluate only one of the simulated mechanical modes. These advantages of detuning accrue in addition to the beneficial effect on the measurement statistics discussed in Section 5.9.2. Unfortunately, we do not yet have a good understanding of the detuning-induced entanglement increase. Therefore, this section is intended as an outlook in the hope that the results presented here might be valuable input to further investigations.

Figure 5.19 shows the maximum amount of entanglement which can be detected in two-mode simulations as a function of mode spacing (i.e. the frequency difference between first and second mode) for different drive detunings (color-coded) . Note that there are two sets of curves in this plot, those resulting from a two-mode evaluation (dashed lines, square markers) and those resulting from a single-mode evaluation (solid lines, circle markers).

two-mode evaluation

Let us first focus on the two-mode evaluations. As expected, they always yield more entanglement than the corresponding single-mode evaluations, (see Section C.3 for a discussion). As a function of frequency separation of the modes (x-axis of Figure 5.19), the entanglement detected in two-mode evaluations reaches an optimum at around a frequency difference of $\omega_2 - \omega_1 \simeq 20\,\%$. For increasing frequency separation, the entanglement decreases again to values comparable to those reached in a single-mode evaluation (solid lines in the same plot). Hence, with increasing frequency (increasing distance from the fundamental mode), the second mode seems to add less and less to the total entanglement. This behavior would be expected for very large frequencies of the second mode (for $\omega_2 \gg \kappa$). That it happens here already for $\omega_2 \lesssim \kappa$ is surprising and we do not have a good explanation for this effect at the moment.

entanglement as function of mode separation

entanglement as function of detuning

As a function of the detuning of the laser drive, the detected entanglement rises monotonically up until $\Delta = 2\pi \times 800\,\mathrm{kHz}$ (the largest simulated detuning). This suggests that we can gain considerably by using a red-detuned drive. Note however that, for fixed input power (as assumed in these simulations), there will be a finite optimum detuning. This is because, for increasing detuning, the intracavity light amplitude and therefore also the optomechanical coupling will eventually decrease significantly, which will limit the generation of entanglement.

single-mode evaluation

What happens if we only analyze the first of the two mechanical modes simulated here? The answer is provided by the solid lines (circle markers) in Figure 5.19. For decreasing frequency difference of the mechanical modes, the entanglement detected in a single-mode evaluation decreases and eventually disappears. This is the effect discussed in Section 5.7.1 which can destroy entanglement if mechanical modes are sufficiently close but not all of them are taken into account in the evaluation. For increasing frequency difference of the

entanglement as function of mode separation

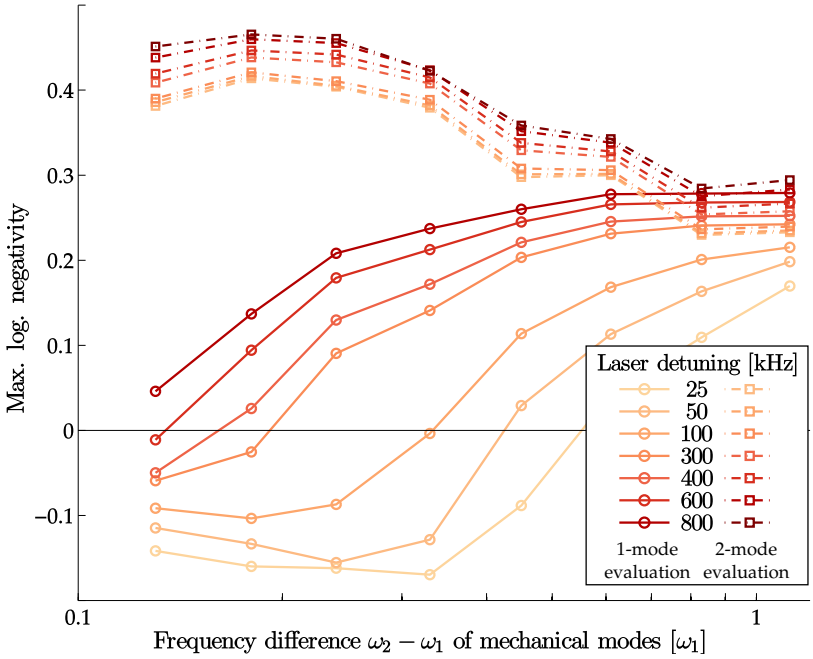

Parameters: without optical noise, $\omega_{m1} = 2\pi \times 920\,\mathrm{kHz}$, $\omega_{m2} \simeq \{1.1, \ldots, 2.1\} \times \omega_{m1}$, $\kappa \simeq 2.73 \times \omega_{m1}$, $g_0 \simeq 71 \times 10^{-6} \times \omega_{m1}$, $P_{\mathrm{in}} = 30\,\mu\mathrm{W}$, $g \simeq 0.37 \times \omega_{m1}$, $Q_1 = Q_2 = 15.8 \times 10^6$, $T = 5\,\mathrm{K}$, two-sideband evaluation.

Figure 5.19. Optimum of logarithmic negativity $E_{\mathcal{N}}\left(\Gamma_{\mathrm{opt}}\right)$ in two-mode simulations with different mode spacings and detunings. The y-axis shows the logarithmic negativity optimized with respect to the pulse width Γ. The x-axis is the frequency difference of the two simulated modes in units of ω_{m1} (hence, $x = 1$ corresponds to $\omega_{m2} = 2 \times \omega_{m1}$; ω_{m1} was fixed at $2\pi \times 920\,\mathrm{kHz}$). The different curves correspond to different red-detunings of the drive from 25 kHz (lightest) to 800 kHz (darkest). Contrasted are two different types of evaluations: Single-mode evaluations which take only the first mechanical mode into account (solid lines, circle markers) and two-mode evaluations which take both mechanical modes into account (dashed lines, square markers). Note that, in these simulations, the optical input power was fixed. This means that the intracavity power and hence also the optomechanical coupling g changed with the detuning Δ. Because of the large cavity linewidth $\kappa \gg \Delta$ this effect is negligibly small, however.

simulated modes, on the other hand, the entanglement approaches a steady value. Hence, if the frequency spacing is large enough, the second mode stops to negatively impact the entanglement detected in the single-mode evaluation. As explained above, this effect would be expected for very large frequencies ω_{m2} of the second mode but happens here already for surprisingly small values of ω_{m2}.

entanglement as function of detuning

For increasing detuning, on the other hand, the detected entanglement rises significantly. Interestingly, this effect—while in principal similar to what happens for the two-mode evaluations (dashed lines, square markers in Figure 5.19)—is much stronger than in the case of the two-mode evaluations. In fact, the added entanglement due to the increased detuning can make the difference between entangled and separable in the case of the single-mode evaluations.

"forgetting" higher mechanical modes

The conclusion is that, in some cases, a moderate detuning of the drive will allow us to "forget" some of the mechanical modes in the evaluation. Obviously, this could be advantageous in experiments where it may not always be possible to include all mechanical modes in the evaluation—either because of computational constraints or because it may not be possible to characterize the optomechanical system sufficiently well.

5.9.3.1 *Outlook*

As mentioned above, we do not currently understand why detuning is so beneficial in the multi-mode case. An analysis of the correlations between different light modes as a function of detuning seems to be required. How could this problem be approached theoretically? An exact and general analysis of the correlation of different light modes in the multi-mode case is difficult and will likely not yield much insight.

It might therefore be better to start with a very simple toy model of the light modes analyzed in the experiment. One could, for example, assume the quadratures of the different mechanical sidebands to be roughly constant within one pulse. This should allow to write the covariance matrix for the pulse quadratures as a function of the covariances of the sideband quadratures (which depend on the detuning and coupling) and the parameters defining the light modes (central frequency and pulse width). Maybe such a simple model could already help to gain some insights into the effects of detuning and of additional mechanical modes.

5.10 INTER-PULSE DELAYS

Much of the beauty—and some of the headache—of our entanglement protocol comes from the fact that all the action is shifted to post-processing. The headache is in the huge amounts of raw data

we need to handle: Whereas [Pal+13b] needed to record only 4 pulse quadratures times 10^4 repetitions to show entanglement, we need to record continuous time traces at high sampling rates which can add up to hundreds of gigabytes of data. The beauty, however, is that this raw data contains much more information than only one particular set of pulse quadratures. This means that we can explore correlations between many different light modes simply by reevaluating the same raw data.

This section illustrates this advantage of the pulsed-continuous entanglement protocol using the example of a variable "dead-time" or delay Δt in between the entangling and the readout pulse. In [Pal+13b] such a delay[44] was implemented by switching off the microwave drive for a time Δt. Therefore, in experiments such as [Pal+13b], analyzing the effect of a different delay means redoing the measurement.

[44] *In their case,* $\Delta t = 10\,\mu$s.

In our protocol, on the other hand, analyzing the effect of a different delay means simply redoing the evaluation of the same raw data with a different set of mode functions. A suitable redefinition of the mode functions for exploring inter-pulse delays is the following:

$$\hat{a}_{t,\Delta t} \equiv \int_{-\infty}^{t-\Delta t/2} \alpha\left(\tau - t\right)\, \hat{a}_{\mathrm{sig}}(\tau)\mathrm{d}\tau, \tag{5.74}$$

$$\hat{b}_{t,\Delta t} \equiv \int_{t+\Delta t/2}^{+\infty} \beta\left(\tau - t\right)\, \hat{a}_{\mathrm{sig}}(\tau)\mathrm{d}\tau. \tag{5.75}$$

In the application to data from measurements or simulations, this redefinition simply amounts to skipping $\Delta t \times f_{\mathrm{sample}}$ samples (rounded to the nearest integer) in between the two pulses.

5.10.1 *Application 1: Measuring mechanical decoherence*

By increasing the inter-pulse delay Δt, we can "watch" decoherence degrade the entanglement between the two pulses (as shown in Figure 5.20 for simulated data). Hence, evaluation of the same measurement data with different inter-pulse delays yields a measurement of mechanical decoherence.

Figure 5.20 shows an application of this idea to simulated data. The time scale over which entanglement is lost is defined by the mechanical decoherence time $(\bar{n}\gamma)^{-1}$. In this simulation, $(\bar{n}\gamma)^{-1} \simeq 7.6\,\mu$s for all mechanical modes which agrees well with the observed disappearance of entanglement for inter-pulse delays of more than a few µs.

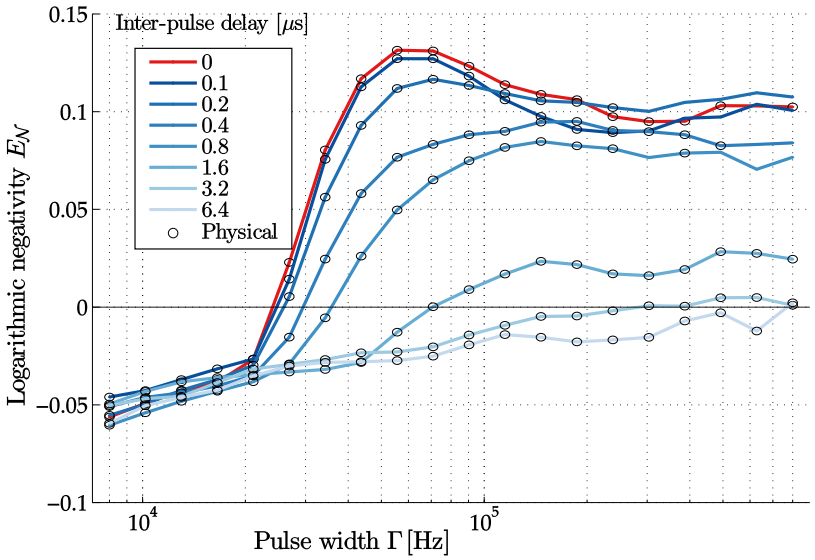

Figure 5.20. Logarithmic negativity E_N versus pulse width Γ for a 45-mode simulation for different inter-pulse delays Δt. The evaluation with $\Delta t = 0$, i.e. directly adjacent pulses (red solid line; same as in Figure 5.14) yields the highest value of the logarithmic negativity. The maxima of the entanglement curves with non-zero inter-pulse delay (blue solid lines) decrease monotonically with increasing inter-pulse delay (towards lighter blues).

Parameters: same as in Figure 5.14; two-sideband eval.; $\Delta t = [0\,\mu s, \ldots, 6.4\,\mu s]$.

5.10.2 *Application 2: Preventing spurious correlations*

eliminating spurious inter-pulse correlations

Note that, in the experiment, small dead-times in between the pulses can also be used to exclude potential spurious inter-pulse correlations. Spurious correlations can arise, for example, due to low-pass filters in the detector circuits which act as integrators in the time domain. In contrast to legitimate quantum correlations, such correlations due to imperfect detection will occur even for shot noise measurements. To check that the inter-pulse delay was chosen sufficiently large to eliminate these effects we can therefore analyze shot noise measurements: Assume there is some $\Delta t_{\text{critical}}$, such that, for all inter-pulse delays $\Delta t > \Delta t_{\text{critical}}$, we do not observe systematic correlations between the entangling and readout pulse for shot noise measurements. Then, we have good reasons to believe that, for the same delays $\Delta t > \Delta t_{\text{critical}}$, any correlations in the signal are not caused by the detector circuits.

Unfortunately, this idea cannot solve *all* problems related to filters in the detector circuit. The problem is that filters will not only lead to spurious *inter-pulse* correlations, but also to spurious *intra-pulse* correlations. That is, if there are several light modes per pulse, filters will introduce correlations between these light modes even for shot noise measurements. These spurious inter- and intra-pulse correlations can lead to strongly unphysical covariance matrices[45] and unrealistically large entanglement values.

spurious intra-pulse correlations remain

[45] *As mentioned before, "unphysical" covariance matrices are those which do not satisfy generalized Heisenberg uncertainty relations.*

We actually see this problem in our experimental data and it is not yet clear how to best deal with it. Therefore, I discuss this problem in some more depth in the following Section 5.11. It is important to realize that the problem is not specific to our setup. In fact, no detector has a perfectly flat response in frequency (equivalently, a δ-function response in time). The main exacerbating factor in our experiment is the need to analyze several mechanical modes. This means, as discussed, that the problem cannot be solved completely by introducing an inter-pulse delay.

The main asset of our protocol, on the other hand, is its enormous flexibility. Because, everything is done in post-processing, we can explore the effect of the detector response much more thoroughly. And there might well be ways to adapt our protocol to cleanly account for a non-flat detector response.

5.11 NON-FLAT DETECTOR RESPONSE

In the theory and simulations presented so far, I assumed that the detector response is independent of frequency. Unfortunately, this is not true in our experiment, since the detection electronics includes a high-pass filter with a cut-off frequency of roughly 200 kHz and a low-pass filter with a cut-off at roughly 12 MHz (see Section 3.2.2). Hence, two questions arise:

1. How does a non-flat detector response affect our entanglement detection protocol? The answer, as already hinted at, is that it can lead to spurious correlations which, in turn, can lead to unphysical covariance matrices and nonsensical entanglement values. This problem is discussed in Section 5.11.1, together with some ideas how to tackle it.

2. Is this only an in-principle problem? Or is our current experimental setup actually affected by it? The answer, unfortunately, is that it actually is a problem for our experiment and we see clear indications of it in our measurement data. This is discussed in Section 5.11.2 and Section 5.11.3.

5.11.1 *Analytic toy example*

To better understand the implications of a non-flat detector response, I resort to a simple analytic model. In our experimental setup, a frequency-dependent detector response arises (amongst others) due to a 12 MHz low-pass filter in the detection signal paths. This filter (as well as any other filters occurring in our detectors) can be modeled as an infinite impulse response (IIR) filter with an impulse response function $h(t)$. The signal $\tilde{c}(t)$ which we actually measure in

the presence of the filter is therefore related to the ideal, unfiltered measurement signal $c(t)$ by a convolution:

$$\tilde{c}(t) \equiv (h * c)(t) \equiv \int_{-\infty}^{+\infty} h(t-\tau) \times c(\tau)\, \mathrm{d}\tau. \tag{5.76}$$

Since the filter is causal, the impulse response $h(t)$ is non-zero only for positive t. Therefore, we could also write the above as

$$\tilde{c}(t) = \int_{-\infty}^{t} h(t-\tau) \times c(\tau)\, \mathrm{d}\tau. \tag{5.77}$$

The calculation of the pulse modes according to (5.65) then yields

$$a_t^{(\mathrm{i})} = \int_{-\infty}^{t} \alpha^{(\mathrm{i})}(\tau - t)\, \tilde{c}(\tau)\, \mathrm{d}\tau, \tag{5.78}$$

$$b_t^{(\mathrm{i})} = \int_{t}^{+\infty} \beta^{(\mathrm{i})}(\tau - t)\, \tilde{c}(\tau)\, \mathrm{d}\tau. \tag{5.79}$$

Since $\alpha^{(\mathrm{i})}(t) = 0$ for $t > 0$ and $\beta^{(\mathrm{i})}(t) = 0$ for $t < 0$ we have

$$a_t^{(\mathrm{i})} = \int_{-\infty}^{+\infty} \alpha^{(\mathrm{i})}(\tau - t)\, \tilde{c}(\tau)\, \mathrm{d}\tau, \tag{5.80}$$

$$b_t^{(\mathrm{i})} = \int_{-\infty}^{+\infty} \beta^{(\mathrm{i})}(\tau - t)\, \tilde{c}(\tau)\, \mathrm{d}\tau. \tag{5.81}$$

Re-expressing the filtered signal $\tilde{c}(\tau)$ according to (5.76) yields

$$a_t^{(\mathrm{i})} = \int_{-\infty}^{+\infty} \mathrm{d}\tau\, \alpha^{(\mathrm{i})}(\tau - t) \left\{ \int_{-\infty}^{+\infty} \mathrm{d}\tau'\, h(\tau - \tau') \times c(\tau') \right\} \tag{5.82}$$

$$= \int_{-\infty}^{+\infty} \mathrm{d}\tau'\, c(\tau') \left\{ \int_{-\infty}^{+\infty} \mathrm{d}\tau\, \alpha^{(\mathrm{i})}(\tau - t) \times h(\tau - \tau') \right\} \tag{5.83}$$

$$= \int_{-\infty}^{+\infty} \mathrm{d}\tau'\, c(\tau') \times \alpha_h^{(\mathrm{i})}(\tau', t), \tag{5.84}$$

where we defined a new "filtered mode function" *filtered mode functions*

$$\alpha_h^{(\mathrm{i})}(\tau', t) \equiv \int_{-\infty}^{+\infty} \mathrm{d}\tau\, \alpha^{(\mathrm{i})}(\tau - t) \times h(\tau - \tau'). \tag{5.85}$$

Analogously, we obtain

$$b_t^{(\mathrm{i})} = \int_{-\infty}^{+\infty} \mathrm{d}\tau'\, c(\tau') \times \beta_h^{(\mathrm{i})}(\tau', t), \text{ with} \tag{5.86}$$

$$\beta_h^{(\mathrm{i})}(\tau', t) \equiv \int_{-\infty}^{+\infty} \mathrm{d}\tau\, \beta^{(\mathrm{i})}(\tau - t) \times h(\tau - \tau'). \tag{5.87}$$

(5.84) and (5.86) show that applying our original mode functions $\alpha^{(\mathrm{i})}$ and $\beta^{(\mathrm{i})}$ to filtered measurement data has the same effect as applying the filtered mode functions $\alpha_h^{(\mathrm{i})}$ and $\beta_h^{(\mathrm{i})}$ to ideal measurement data.

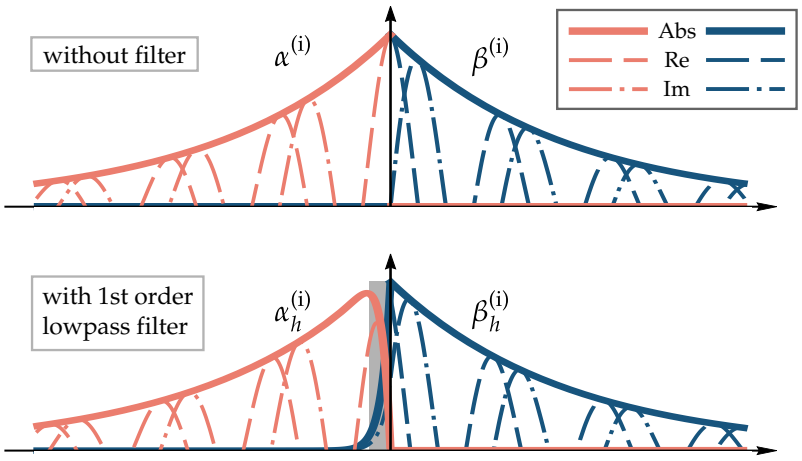

Figure 5.21. Comparison of the mode functions $\alpha^{(i)}$ and $\beta^{(i)}$ (upper panel) to the effective mode functions $\alpha_h^{(i)}$ and $\beta_h^{(i)}$ in the presence of a first-order low pass filter (lower panel). The gray bar in the lower panel indicates times for which the filtered mode functions overlap. Note that, for the sake of visual clarity, only positive values are plotted.

Note that the filtered mode functions $\alpha_h^{(i)}$ and $\beta_h^{(i)}$ are identical to the original mode functions $\alpha^{(i)}$ and $\beta^{(i)}$ exactly if $h(\tau - \tau') = \delta(\tau - \tau')$, i.e. exactly if the detector has a flat response. Otherwise, $\alpha_h^{(i)}$ and $\beta_h^{(i)}$ are "smeared out" versions of the original mode functions. We can illustrate this for the simple example of a first-order low pass filter with impulse response $h(t) \propto \exp(-t/t_c)\,\Theta(t)$.[46]

[46] $\Theta(t)$ *is the Heaviside theta function.*

Figure 5.21 shows the mode functions $\alpha^{(i)}$ and $\beta^{(i)}$, defined as in (5.1) and (5.2), and the corresponding filtered mode functions $\alpha_h^{(i)}$ and $\beta_h^{(i)}$ for a first-order low pass filter with cutoff frequency t_c^{-1}. I assume $t_c^{-1} > \Gamma^{(i)}$, i.e. a filter response time which is shorter than the decay time of the pulse modes (satisfied in our experiment). For this simple toy example, analytic expressions for $\alpha_h^{(i)}$ and $\beta_h^{(i)}$ can be found:

$$\alpha_h^{(i)}(t) \propto \left(\underbrace{\Theta(-t)\, e^{\left(i\omega_m{}^{(i)} + \Gamma^{(i)}\right)t}}_{\equiv (A1) \propto \alpha^{(i)}(t)} - \underbrace{\Theta(-t)\, e^{t/t_c}}_{\equiv (A2)} \right) \cdot c_+, \tag{5.88}$$

$$\beta_h^{(i)}(t) \propto \left(\underbrace{\Theta(+t)\, e^{\left(i\omega_m{}^{(i)} - \Gamma^{(i)}\right)t}}_{\equiv (B1) \propto \beta^{(i)}(t)} - \underbrace{\Theta(-t)\, e^{t/t_c}}_{\equiv (B2)} \right) \cdot c_-, \text{ with} \tag{5.89}$$

$$c_\pm \equiv \frac{\sqrt{\Gamma^{(i)}}}{t_c^{-1} - \left(i\omega_m{}^{(i)} \pm \Gamma^{(i)}\right)}. \tag{5.90}$$

The first terms $(A1)$ and $(B1)$ of the above expressions are proportional to the original mode functions; hence, $(A1)$ and $(B1)$ do not have overlap in time and are orthogonal. The second terms $(A2)$ and

$(B2)$, however, do have overlap in time: $(B2)$ is proportional to $\Theta(-t)$ which describes a "leakage" of the readout mode into the entangling mode; this is apparent in the lower panel of Figure 5.21 (emphasized by the gray bar). Because of the additional terms $(A2)$ and $(B2)$, the filtered mode functions $\alpha_h^{(\mathrm{i})}$ and $\beta_h^{(\mathrm{i})}$ are not orthogonal to each other. In our toy example, we can find an analytic expression for the overlap:[47]

non-orthogonality of filtered mode functions

$$\int_{-\infty}^{+\infty} \alpha_h^{(\mathrm{i})}(t) \cdot \beta_h^{(\mathrm{i})^*}(t)\, \mathrm{d}t = \frac{\Gamma^{(\mathrm{i})} t_c \left(1 + \left(\Gamma^{(\mathrm{i})} - i\omega_m{}^{(\mathrm{i})}\right) t_c\right)}{\left(1 + \Gamma^{(\mathrm{i})} t_c\right)\left(1 + \left(\Gamma^{(\mathrm{i})} + i\omega_m{}^{(\mathrm{i})}\right) t_c\right)}. \quad (5.91)$$

[47] *Note that (5.88) and (5.89) must be normalized to arrive at this expression. In the experiment, this happens implicitly via the calibration to shot noise.*

This undesired overlap tends to zero if $\Gamma^{(\mathrm{i})} t_c$ goes to zero, i.e. in the limits of a flat detector response or a very narrow pulse. We can expand (5.91) around $\Gamma^{(\mathrm{i})} t_c = 0$ and obtain:

$$\int_{-\infty}^{+\infty} \alpha_h^{(\mathrm{i})}(t) \cdot \beta_h^{(\mathrm{i})^*}(t)\, \mathrm{d}t = \Gamma^{(\mathrm{i})} t_c + \mathcal{O}\left(\left(\Gamma^{(\mathrm{i})} t_c\right)^2\right). \quad (5.92)$$

This means that, in the limit of small t_c, i.e. large cut-off frequencies of the filter, the overlap is proportional to the pulse width $\Gamma^{(\mathrm{i})}$. We therefore expect potential problems introduced by the filter to become more prevalent with increasing pulse width.

How does the filter affect the overlap of modes belonging to the *same* pulse, e.g. two modes $\alpha^{(\mathrm{i})}$ and $\alpha^{(\mathrm{j})}$? For our simple toy example, the problem can again be solved analytically. We define $\alpha^{(\mathrm{i})}$ as above; hence, $\alpha_h^{(\mathrm{i})}(t)$ is still given by (5.88). We define a second mode $\alpha^{(\mathrm{j})}$—with the same functional form as $\alpha^{(\mathrm{i})}$ (see (5.1)) and the same pulse width $\Gamma = \Gamma^{(\mathrm{i})} = \Gamma^{(\mathrm{j})}$ but with a different central frequency $\omega_m{}^{(\mathrm{j})} \neq \omega_m{}^{(\mathrm{i})}$—and orthogonalize it with respect to $\alpha^{(\mathrm{i})}$. Then, we apply (5.85) to $\alpha^{(\mathrm{j})}$ and derive $\alpha_h^{(\mathrm{j})}(t)$. The resulting expression is lengthy and not very insightful but it allows us to derive an expression for the mode overlap between the filtered mode functions $\alpha_h^{(\mathrm{i})}$ and $\alpha_h^{(\mathrm{j})}$. The full expression is rather lengthy but, as with (5.91), it tends to zero for $\Gamma t_c \to 0$ and it has a compact expansion for small Γt_c:

intra-pulse overlap

$$\begin{aligned} &\int_{-\infty}^{+\infty} \alpha_h^{(\mathrm{i})}(t) \cdot \alpha_h^{(\mathrm{j})^*}(t)\, \mathrm{d}t = \quad (5.93)\\ &= i\,\mathrm{sgn}(\Delta\omega_m)\, \frac{2\Gamma - i\Delta\omega_m}{\sqrt{4\Gamma^2 + \Delta\omega_m{}^2}} \times \Gamma t_c + \mathcal{O}\left(\left(\Gamma t_c\right)^2\right), \end{aligned}$$

where $\Delta\omega_m \equiv \omega_m{}^{(\mathrm{j})} - \omega_m{}^{(\mathrm{i})}$ and $\mathrm{sgn}(\Delta\omega_m)$ is the sign of $\Delta\omega_m$. We are most interested in the absolute value of the mode overlap (5.93), which is a measure of the amount of spurious correlations introduced by the filter. It is again given by

$$\left|\int_{-\infty}^{+\infty} \alpha_h^{(\mathrm{i})}(t) \cdot \alpha_h^{(\mathrm{j})^*}(t)\, \mathrm{d}t\right| = \Gamma t_c + \mathcal{O}\left(\left(\Gamma t_c\right)^2\right). \quad (5.94)$$

We conclude that, in the limit of large cut-off frequencies t_c^{-1}, the undesired overlap between modes of the same pulse is proportional to the pulse width Γ.

rephrasing the problem

With the help of (5.85) and (5.87), we can therefore express the problem introduced by a non-flat detector response very succinctly as follows. The filtered mode functions—the mode functions we *effectively* apply to our signal—are, in general, not mutually orthogonal. This problem manifests in two different ways:

1. An overlap between $\alpha_h^{(\mathrm{i})}$ and $\beta_h^{(\mathrm{j})}$, i.e. an overlap between modes of the entangling pulse and the readout pulse as demonstrated in (5.91). This leads to *spurious inter-pulse correlations*.

2. An overlap between $\alpha_h^{(\mathrm{i})}$ and $\alpha_h^{(\mathrm{j})}$ ($\beta_h^{(\mathrm{i})}$ and $\beta_h^{(\mathrm{j})}$), i.e. an overlap between modes within the entangling (readout) pulse as demonstrated in (5.93). This leads to *spurious intra-pulse correlations*.

In the remaining subsections, I will show for simulated data (Section 5.11.2) and measurement data (Section 5.11.3) that both types of spurious correlations, inter-pulse and intra-pulse, can cause unphysicality and diverging entanglement values. I conclude in Section 5.11.4 by discussing some possible solutions.

5.11.2 *Simulations*

Let us explore the effect of a non-flat detector response in single-mode simulations, by comparing simulations with and without the low-pass filter. Note that, in the simulations presented below, I do not use the ideal first-order low pass used as a toy example in Section 5.11.1. Instead, I use a realistic model (deduced from shot noise measurements) of the actual 12 MHz low-pass filter employed in the experiment. This filter rolls off much more steeply than the first-order low pass considered earlier.

5.11.2.1 *Spurious inter-pulse correlations*

First, let us look at a single-sideband evaluation of single-mode simulations. In this case, we deal with only one light mode per pulse. Hence, there can be no intra-pulse correlations, but only (inter-pulse) correlations between the entangling and the readout pulse. In this sense, it is the simplest possible scenario. The results are presented in Figure 5.22.[48] Unfortunately, even in this simplest possible case, the presence of the low pass filter significantly changes the detected entanglement.

[48] *Figure 5.24 shows the same data, but evaluated using a two-sideband evaluation. Interestingly, this exacerbates the problem quite drastically.*

Can we really blame the difference in entanglement between the two different simulations on the low-pass filter? The analytical toy model of Section 5.11.1 suggested that the effect of the filter should

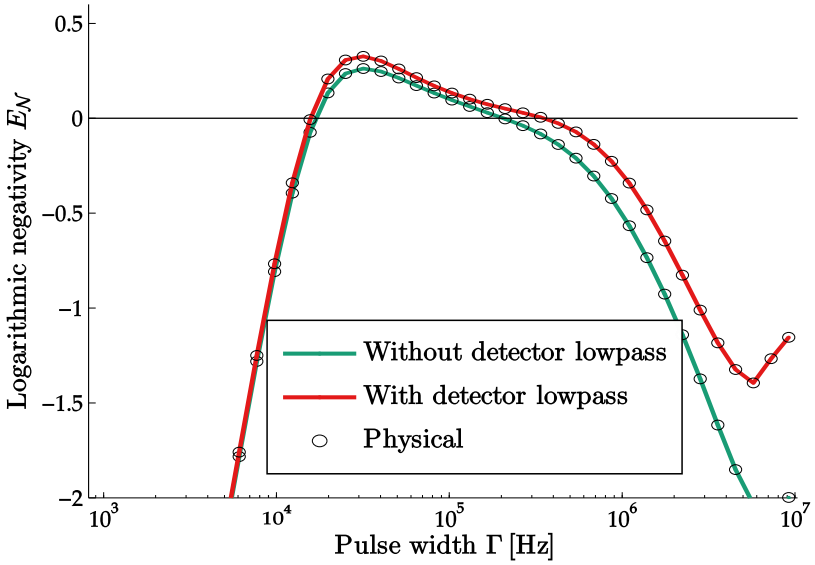

Figure 5.22. Logarithmic negativity E_N versus pulse width Γ from single-mode simulations with flat and frequency-dependent detector response. The data was evaluated using a single-sideband evaluation. The simulation assuming a flat detector response (green solid line) and the one assuming a 12 MHz low-pass filter (red solid line) yield similar entanglement values for small pulse widths, but diverge more and more with increasing pulse widths. All pulse widths yield physical covariance matrices (circle markers).

Parameters: single-sideband eval., without optical noise, $\omega_m = 2\pi \times 920\,\mathrm{kHz}$, $\kappa \simeq 2.73 \times \omega_m$, $g_0 \simeq 7.1 \times 10^{-5} \times \omega_m$, $g \simeq 0.30 \times \omega_m$, $Q = 5 \times 10^7$, $T = 5\,\mathrm{K}$,$\mathcal{C} \simeq 14.9$.

become more problematic with increasing pulse widths. And, indeed, the difference in entanglement between the simulations with and without the filter becomes larger with increasing pulse width.

deviation grows with increasing pulse width

The "smoking gun" that the difference in entanglement is due to the filter, however, is presented in Figure 5.23. The plot shows the absolute value of the covariance between different pulse quadratures *for simulated shot noise measurements*. Ideally, these covariances should all be zero. But in practice, due to limited statistics, we will always observe a small non-zero covariance. For small pulse widths Γ, the measured covariances are indeed non-zero but small, in line with the assumption of statistical fluctuations. Furthermore, there is no obvious systematic difference for small pulse widths between the simulation with and without the low-pass filter.

correlations between shot noise quadratures due to limited statistics

For large pulse widths, however, a clear difference between the simulations with and without the filter appears. For the simulation without the filter, all covariances remain small. For the simulation including the filter, however, some inter-pulse covariances (between the Q- and $X-$ as well as the $P-$ and $Y-$quadratures) grow far beyond what would be reasonably expected on purely statistical grounds. This behavior is consistent with the results of Section 5.11.1 which predict a large effective overlap of the readout and entangling pulse for large pulse widths.

spurious inter-pulse correlations grow with pulse width

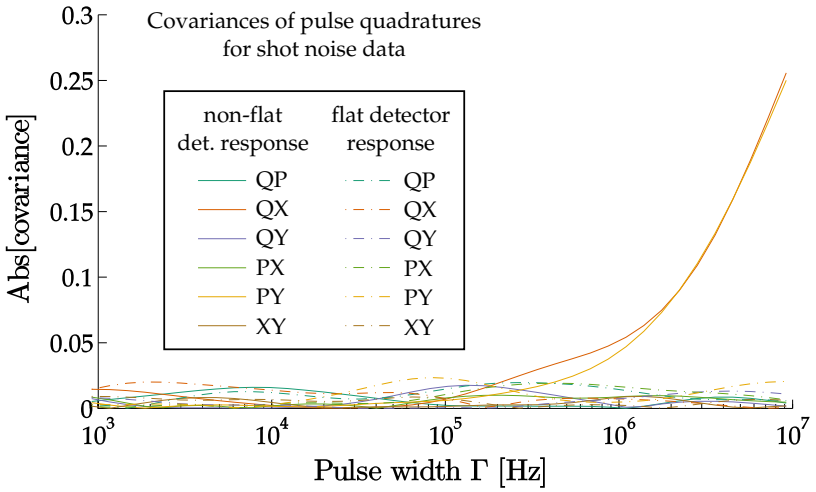

Parameters: as in Figure 5.22.

Figure 5.23. Absolute value of covariances between pulse quadratures for simulated shot noise measurements (with and without a frequency-dependent detector response) as a function of pulse width Γ. For small pulse widths, the simulation with the detector low pass (solid lines) yields similar correlations as the simulation with a flat detector response (dashed lines). For large pulse widths, however, the simulation assuming a non-flat detector response yields very strong inter-pulse correlations (between Q and X, and between P and Y), while the correlations between quadratures belonging to the same pulse (Q and P, as well as X and Y) remain small.

implications for entanglement

Note that already at $\Gamma \simeq 1\,\mathrm{MHz}$, the spurious off-diagonal correlations for simulated shot noise measurements are on the order of 0.05, i.e. a tenth of the theoretically expected shot noise variance. This means that already at these pulse widths, the entangling and the readout mode have a very significant effective overlap. Thus, entanglement values calculated for these pulse widths must definitely not be trusted. Figure 5.22 showed, however, that even for much smaller pulse widths, the measured entanglement starts to change significantly due to the presence of the filter. This suggests that even much smaller effective mode overlaps (of 1 % or less)—which we cannot distinguish from purely statistical correlations given our limited sample sizes—can influence the amount of entanglement inferred from the data.

5.11.2.2 *Spurious intra-pulse correlations*

What happens if the filter also introduces spurious *intra-pulse* correlations? This is explored in Figure 5.24 which shows results for the simulations presented above in Figure 5.22, but this time evaluated using a two-sideband evaluation. Hence, in this case we analyze two light modes per pulse. Ideally, these light modes are orthogonal and, therefore, constitute a legitimate set of quantum modes. But (5.93) showed that also the modes within a single pulse can become

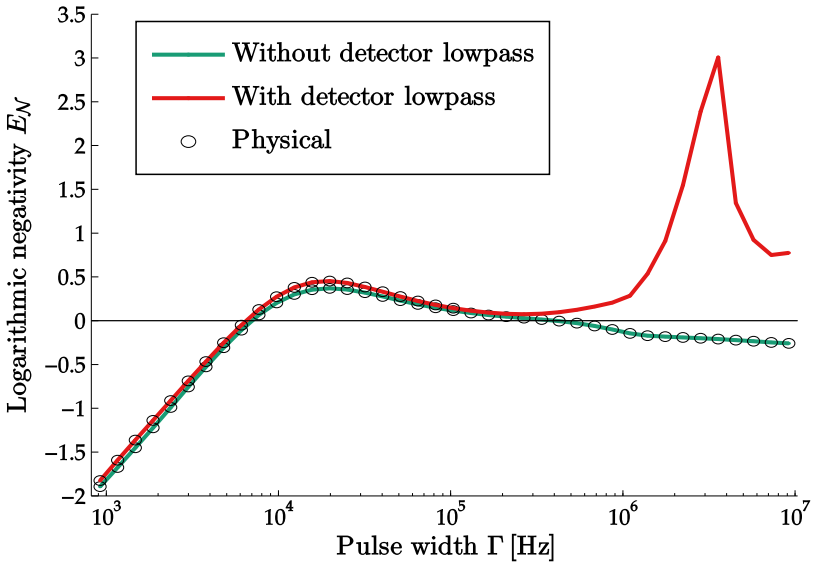

Figure 5.24. Logarithmic negativity E_N versus pulse width Γ from single-mode simulations with and without a frequency-dependent detector response. The simulation assuming a flat detector response (green solid line) yields physical covariance matrices for all pulse widths considered here. The simulation using a non-flat detector response (red solid line) coincides reasonably well for very small pulse widths, but diverges drastically from the ideal curve for $\Gamma > 200\,\mathrm{kHz}$, yielding entanglement values which are much too large. It also fails to deliver physical covariance matrices for pulse widths $\Gamma > 100\,\mathrm{kHz}$.

Parameters: two-sideband eval., rest as in Figure 5.22.

effectively non-orthogonal due to filtering, which can lead to unphysicality and deviations of the measured entanglement from the true value.

In fact, the difference in entanglement between the simulations with and without the filter are much more drastic for the two-sideband (Figure 5.24) than for the single-sideband evaluation (Figure 5.24). In addition, the simulation including the low-pass filter does not yield physical covariance matrices for pulse widths $\Gamma > 100\,\mathrm{kHz}$, for the two-sideband evaluation.

unphysicality and drastically different entanglement values for large pulse widths

Figure 5.25 shows that the filter does indeed lead to strong spurious correlations between some quadratures belonging to the same pulse. This is in addition to the spurious inter-pulse correlations which were already present in the single-sideband evaluation (see Figure 5.23). These spurious correlations demonstrate unambiguously that the corresponding modes are effectively not orthogonal. It is plausible that the combined effect of the spurious correlations between the pulses and within a single pulse explains the unphysicalities and strongly differing entanglement values at large pulse widths in the presence of the filter.

strong intra-pulse correlations for large pulse widths

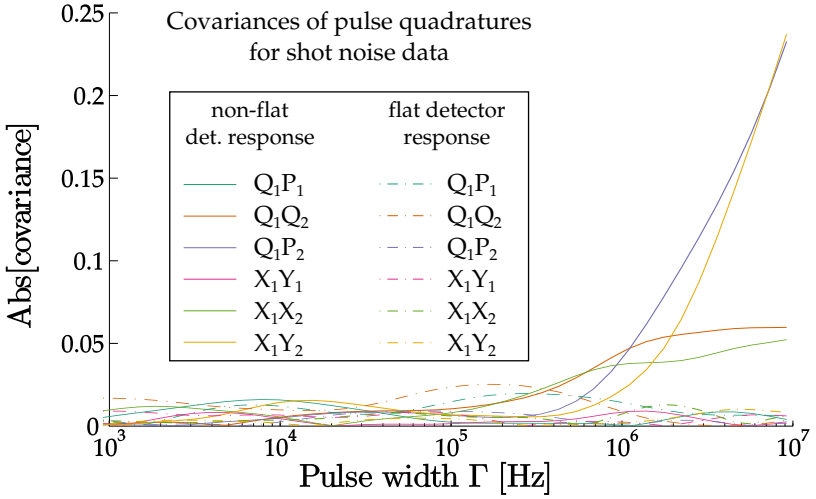

Parameters: as in Figure 5.24.

Figure 5.25. Absolute value of intra-pulse covariances between some of the pulse quadratures for simulated shot noise measurements (with and without frequency-dependent detector response) as a function of pulse width Γ. For small pulse widths, the simulation with the detector low pass (solid lines) yields similar correlations as the simulation with a flat detector response (dashed lines). For large pulse widths, however, the simulation assuming a non-flat detector response yields much stronger intra-pulse correlations (compared to the simulation with a flat detector response) for some pairs of quadratures, chiefly for the pairs Q_1 and P_2 and X_1 and Y_2.

5.11.3 *Experimental results*

Let us finally look at experimental data recorded at liquid Helium temperatures $T \simeq 5\,\mathrm{K}$.[49] The mechanical element was a commercial square SiN membrane (by Norcada) with a fundamental frequency $\omega_1 \simeq 675\,\mathrm{kHz}$, which we drove with an optical input power of $P_{\mathrm{in}} \simeq 50\,\mu\mathrm{W}$. Figure 5.26 shows the result of a two-sideband evaluation of this data taking into account 47 mechanical modes. The resulting entanglement curve shows some resemblance to the red curve in Figure 5.24 which resulted from a single-mode simulation taking the non-flat detector response into account. In particular, it also features unphysicality and implausibly large entanglement values for large pulse widths.

[49] *An estimate based on a low-temperature sensor placed close to the membrane. We do not have a direct measurement of the mode temperature for this data set.*

unphysicality and large entanglement for large Γ

To better understand the origin of the diverging entanglement values and unphysicalities in our experimental data, we can again look for potential spurious correlations introduced by the non-flat detector response. Figure 5.27 looks again at the absolute value of covariances between different pulse quadratures for shot noise data (in the spirit of Figure 5.23 and Figure 5.25). But, given that each covariance matrix has now 376×376 entries, it does not make sense anymore to look at individual covariances. Instead, the maximum, mean, median and

spurious correlations due to non-flat detector response?

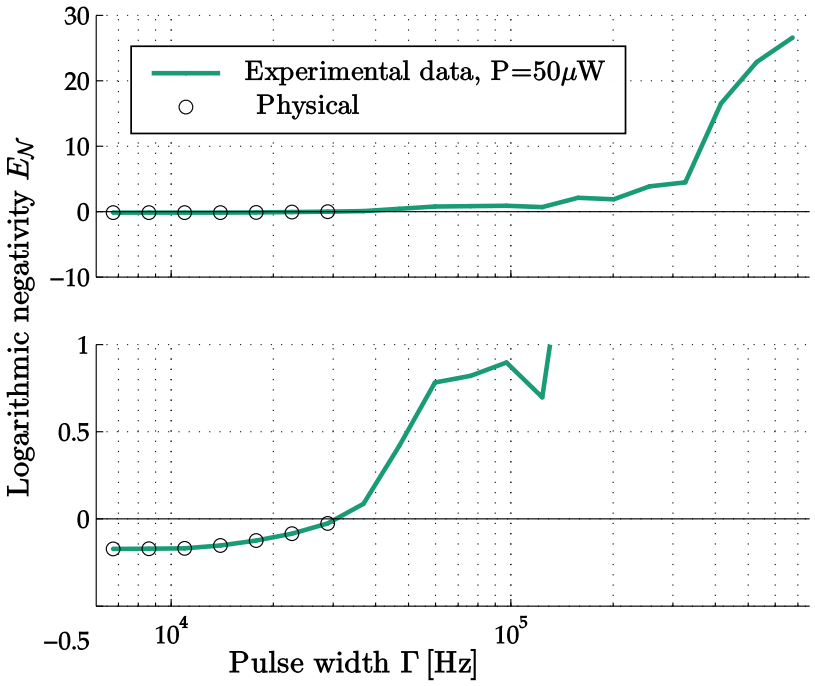

Figure 5.26. Logarithmic negativity $E_{\mathcal{N}}$ versus pulse width Γ for preliminary experimental data recorded using a commercial SiN membrane at liquid Helium temperatures with an optical input power of $P_{\text{in}} \simeq 50\,\mu\text{W}$. The lower panel is a zoom-in of the upper panel. For small pulse widths $\Gamma < 30\,\text{kHz}$, the evaluation yields physical covariance matrices (circle markers); the covariance matrices for all other pulse widths are unphysical. There is a strong divergence of the measured entanglement starting roughly at $\Gamma \simeq 120\,\text{kHz}$.

Parameters:
two-sideband eval.
using 47 modes,
$\omega_1 \simeq 675\,\text{kHz}$,
$\omega_2 \simeq 1.07\,\text{MHz}, \ldots$
$T \simeq 5\,\text{K}$,
$P_{\text{in}} \simeq 50\,\mu\text{W}$.

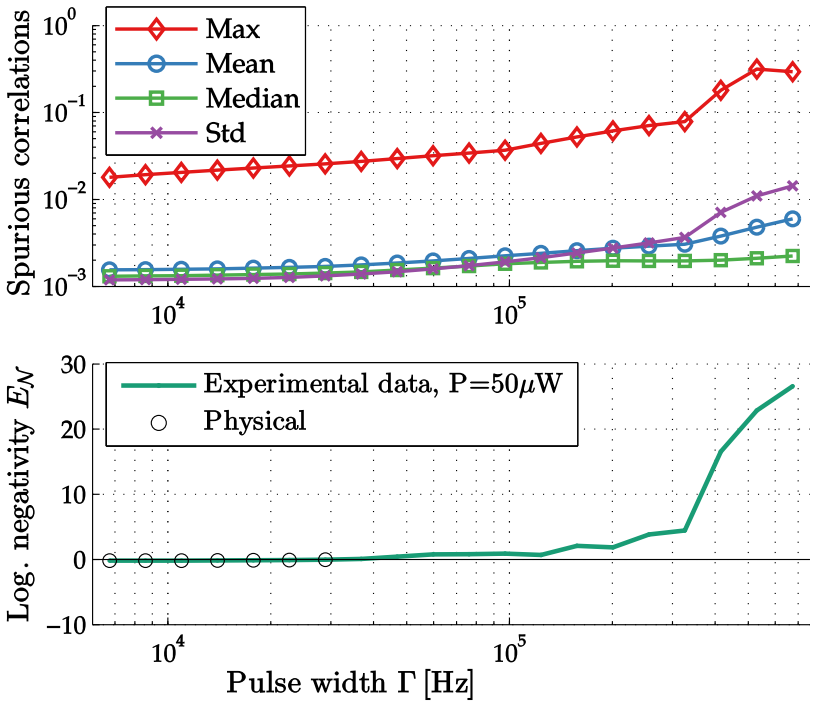

Same evaluation as in Figure 5.26, applied to experimentally recorded shot noise.

Figure 5.27. Spurious correlations between different pulse quadratures for experimentally recorded shot noise data (upper panel). Plotted are the maximum, mean, median and standard deviation of the absolute values of the covariances between different pulse quadratures calculated using measured shot noise. The lower panel shows, as a visual reference, the inferred entanglement for $P_{\text{in}} \simeq 50\,\mu\text{W}$ (see Figure 5.26).

standard deviation of the covariances are plotted to characterize the typical size and range of these unwanted correlations.

Recall that, ideally, these covariances between different quadratures for shot noise data should be zero up to statistical fluctuations; in particular, there should be no systematic dependence on the pulse width Γ. Unfortunately, Figure 5.27 paints a very different picture. There is a clear systematic growth of correlations with increasing pulse width. For the largest pulse width, the maximum of these off-diagonal correlations for the shot noise measurements becomes comparable in size to the shot noise variance (=1/2). This means that, for these largest pulse widths, some of the analyzed modes—instead of being orthogonal—are effectively almost collinear.

systematic growth of spurious correlations with increasing pulse width

5.11.4 *Possible solutions*

The frequency dependence of our detectors turned out to be serious problem for our experiment. Recall the basic "ingredients" for this problem:

1. Short mechanical coherence times on the order of µs. This requires us to use pulses which are broad in frequency space (on the order of 100 kHz). It also prevent us from introducing long inter-pulse delays.

2. A detector response which is not flat in the frequency windows of interest—windows of some 100 kHz width around the mechanical resonances.

3. As an exacerbating factor: The necessity to analyze the contribution of several closely spaced mechanical modes.

None of these challenges are unique to our experiment. Ideas to tackle this issue might therefore be applicable to a wider range of experiments. Let me very briefly sketch some potential "lines of attack".

5.11.4.1 *Improvements in the experiment*

In the experiment, there are two obvious knobs for improvements—the detectors themselves and the mechanical coherence times. Regarding the detectors, we could push their cut-off frequencies further away from the mechanical resonances. In our case, this would require new photodiodes, as well as changes to locking electronics and electro-optics. The reason for the latter is the following: The 12 MHz low-pass filter is necessary to prevent a strong modulation at 20 MHz (required for locking the optomechanical cavity) from saturating our AD-cards. Shifting this low-pass filter to higher frequencies therefore also requires shifting the modulation tone to higher frequencies.

improving detection

Alternatively, we can try to increase mechanical coherence times. A factor of ten could plausibly be gained by moving the experiment from a liquid Helium flow cryostat to a dilution refrigerator. By lowering decoherence by a factor of ten, the optimal pulse widths will also be shifted downwards by a factor of ten. This would help because, as discussed in the previous sections, the non-flat detector response matters less for pulses which are narrower in frequency space.

increasing coherence times

5.11.4.2 *Improvements in post-processing*

A different way of counteracting the frequency-dependent effect of the detectors by modeling the effect of the detectors and defining a filter to undo the effect of the detectors. Such an "inverse filter" (undoing the effect of the frequency-dependent detection) could be applied directly to the raw data and should yield the data we would have measured for an ideal detector.[50] This is the route we are currently exploring. The main difficulty here is to obtain model of the detector response which is sufficiently accurate such that we can trust any entanglement we might detect.

"undoing" the frequency-dependent response

[50] *Alternatively, such a correction step could be incorporated in the definition of the pulse modes.*

post-selecting a subset of pulse modes

Alternatively, we could use the fact that not *all* mechanical modes need to be taken into account in the evaluation (as demonstrated using simulations in Section 5.7.2.1). Maybe there are subset of modes which are not so sensitive to the frequency-dependence of the detection and still show entanglement? This idea seems to work in simulations (for certain parameters), but has not yet allowed us to extract reliable entanglement curves from the experimental data.

effective single-mode case plus inter-pulse delays

The extreme case of the above idea is when only a single mechanical mode needs to be taken into account. This happens if the mechanical coherence time is so large, and correspondingly the optimal pulse width so small, that the overlap between neighboring pulse modes is negligible. In this case, we can detect entanglement by analyzing only a single mechanical mode. If, in addition, we analyze only a single optical sideband per pulse, the frequency-dependent detection can only cause spurious correlations in between the pulses. But, for sufficiently high coherence times, these inter-pulse correlations can be eliminated by a sufficiently long delay in between the two pulses (as discussed in Section 5.10).

5.12 CONCLUSION

In this chapter, I have systematically analyzed the feasibility of a novel entanglement detection protocol for cavity optomechanical systems, referred to as the pulsed-continuous protocol. For suitable experimental parameters, this protocol detects entanglement between different light modes in a laser beam reflected from an optomechanical cavity. The pulsed-continuous entanglement detection protocol offers two main advantages compared to the pulsed protocol proposed by [Hof+11] and implemented by [Pal+13b]. First, it is experimentally relatively simple since it does not require active pulsing but works for an optomechanical cavity which is driven continuously with a resonant or moderately red-detuned beam. Second, the pulsed light modes whose correlations are analyzed are only defined in post-processing. In principle, this allows a more systematic analysis of how entanglement is shared among different modes of the reflected light field.

main advantages for the pulsed-continuous protocol

feasibility of entanglement detection in the presence of laser noise and multiple mechanical modes

The main objective of this chapter was to demonstrate, using extensive computer simulations, that this protocol can detect optomechanically induced entanglement for realistic experimental parameters. In particular, I demonstrated that the residual classical laser noise in our experiment does not prevent entanglement generation and detection. More importantly, I have shown that this protocol is well adapted to optomechanical systems with multiple significantly interacting mechanical modes (such as membrane-in-the-middle cavities).

main challenges for the pulsed-continuous protocol

In the course of this analysis, also the challenges have become quite clear. One challenge is that the protocol requires large amounts of raw data (on the order of several tens of gigabytes) and is computationally expensive, if the number of analyzed modes becomes large. This makes a systematic analysis of the correlations among a large number of different light modes difficult in practice. Another challenge, and the main current roadblock in our experiment, is the sensitivity of the protocol to the frequency-dependence of the detectors (for current experimental parameters). Different solutions to this problem have been sketched in the previous section and are currently investigated.

take-away message

The most important take away message from this study, which generalizes beyond this particular protocol, is the following. The presence of multiple significantly interacting and closely spaced mechanical modes can prevent the observation of optomechanically induced quantum correlations in the reflected light field. But such quantum correlations *can* be observed by suitably extending the set of light modes to be analyzed. Extending the correlation analysis to a larger number of light modes is particularly convenient in the pulsed-continuous protocol, in which the light modes are defined entirely in post-processing.

APPENDIX

A

NOTATION

A.1 GENERAL

SYMBOL / EQN.	MEANING
x	Scalar variable
$\boldsymbol{x}$ [bold face]	Column vector
$\boldsymbol{\sigma}, \boldsymbol{\Sigma}, \boldsymbol{A}$ etc. [bold face]	Matrix
$A \equiv B$	A is defined as B
$A \overset{!}{=} B$ ($A \overset{!}{>} B$,...)	A must be equal to (larger than,...) B
$\lvert\boldsymbol{\Sigma}\rvert = \det \boldsymbol{\Sigma}$	Determinant of matrix $\boldsymbol{\Sigma}$
$\delta_{ij} = \begin{cases} 1 & i = j \\ 0 & i \neq j \end{cases}$	Kronecker delta
$\delta(t) = \begin{cases} \infty & t = 0 \\ 0 & t \neq 0 \end{cases}$, s.th. $\int_{-\infty}^{+\infty} f(t)\,\delta(t - t_0)\mathrm{d}t = f(t_0)$	Dirac delta distribution
$\Theta(t) = \begin{cases} 1 & t \geq 0 \\ 0 & t < 0 \end{cases}$	Heaviside theta function
$\lfloor x \rfloor \equiv \max\{n \in \mathbb{Z} \lvert n \leq x\}$	Floor of x
$\mathbb{N}_0, \mathbb{N}$	Natural numbers with / without zero
$\mathbb{Z}, \mathbb{R}, \mathbb{C}$	Whole / real / complex numbers

Table A.1. General typographic conventions and definitions of some standard functions and sets.

A.2 QUANTUM MECHANICS

SYMBOL / EQN.	MEANING
$\hat{x}$ ($\hat{\boldsymbol{x}}$)	Scalar (vector-valued) quantum operator
$\left[\hat{a}, \hat{b}\right] \equiv \hat{a}\hat{b} - \hat{b}\hat{a}$	Commutator of $\hat{a}$ and $\hat{b}$
$\left\{\hat{a}, \hat{b}\right\} \equiv \hat{a}\hat{b} + \hat{b}\hat{a}$	Anti-commutator of $\hat{a}$ and $\hat{b}$
$\left[\hat{b}, \hat{b}^\dagger\right] = 1$	Canonical commutator of mode operators $\hat{b}, \hat{b}^\dagger$
$\hat{q} = \left(\hat{b} + \hat{b}^\dagger\right)/\sqrt{2}$	Position / amplitude quadrature
$\hat{p} = \left(\hat{b} - \hat{b}^\dagger\right)/i\sqrt{2}$	Momentum / phase quadrature
$[\hat{q}, \hat{p}] = i$	Canonical commutator of quadratures $\hat{q}, \hat{p}$
ρ	Quantum state (in general, mixed)
$\langle \hat{O} \rangle \equiv \mathrm{tr}\left(\rho \hat{O}\right)$	Expectation value of operator $\hat{O}$ in state ρ
$\sigma_{\hat{q}}^2 \equiv \left\langle 0 \middle\vert \hat{q}^2 \middle\vert 0 \right\rangle = \frac{1}{2}$	Ground state momentum variance
$\sigma_{\hat{p}}^2 \equiv \left\langle 0 \middle\vert \hat{p}^2 \middle\vert 0 \right\rangle = \frac{1}{2}$	Ground state position variance
$\sigma_{\hat{q}}\sigma_{\hat{p}} \geq 1/2$	Heisenberg uncertainty relation
$\hat{\boldsymbol{R}}$	Vector of quadrature operators
$\boldsymbol{\sigma} \equiv \langle \{\hat{\boldsymbol{R}}, \hat{\boldsymbol{R}}^\mathsf{T}\} \rangle - \langle \hat{\boldsymbol{R}} \rangle \langle \hat{\boldsymbol{R}}^\mathsf{T} \rangle$	Ensemble covariance matrix (CM)
$\boldsymbol{\sigma}^{(\mathrm{PT})}$	Partially transposed CM
$\tilde{\boldsymbol{\sigma}}$	Sample CM of measured pulse quadratures

Table A.2. Notation and definitions related to quantum mechanics.

A.3 OPTOMECHANICS

SYMBOL / EQN.	MEANING
$q_0 \equiv \sqrt{\hbar/2m\omega_m}$, $p_0 = m\omega_m q_0$	Ground state uncertainties (in SI-units) of position and momentum
ω_m	Mechanical frequency
γ_m	Mechanical linewidth
$Q \equiv \omega_m/\gamma_m$,	Mechanical quality factor
ω_c	Resonance frequency of optomechanical cavity
ω_l	Frequency of driving laser
$\Delta \equiv \omega_l - \omega_c$	Detuning of laser with respect to OM-cavity
κ	Cavity HWHM
κ_1	Cavity linewidth due to input coupler
α_1^{in}	Mean amplitude of driving laser field
$\alpha = \frac{2\kappa_1}{\kappa^2+\Delta^2}\alpha_1^{in}$	Mean amplitude of intra-cavity field
g_0	Single-photon coupling
$g \equiv \sqrt{2}\lvert\alpha\rvert g_0$	Linearized optomechanical coupling

Table A.3. Conventions and formulas regarding optomechanics.

A.4 STATISTICS AND STATE ESTIMATION

SYMBOL / EQN.	MEANING
x ($\boldsymbol{x}$)	Scalar (vector-valued) random variable
$\hat{x}$ ($\hat{\boldsymbol{x}}$)	Estimate of x ($\boldsymbol{x}$)
$\mathcal{P}(x; p_1, \ldots, p_n)$	Prob. distribution $\mathcal{P}$ for random var. x parametrized by $p_1, \ldots, p_n$
$\mathcal{N}\left(x; \mu_x, \sigma^2\right) \equiv \frac{1}{\sqrt{2\pi\sigma_x^2}} \exp\left(-\frac{(x-\mu_x)^2}{2\sigma_x^2}\right)$	Normal distribution of x with mean μ_x and variance σ^2
$\mathcal{N}(\boldsymbol{x}; \boldsymbol{m}, \boldsymbol{\Sigma}) \equiv \frac{1}{\sqrt{2\pi\lvert\boldsymbol{\Sigma}\rvert}} \exp\left(-\boldsymbol{x}'^{\mathsf{T}}\boldsymbol{\Sigma}^{-1}\boldsymbol{x}'/2\right)$, with $\boldsymbol{x}' \equiv \boldsymbol{x} - \boldsymbol{m}$.	Multivariate normal distribution of $\boldsymbol{x}$ with mean $\boldsymbol{m}$ and covariance matrix $\boldsymbol{\Sigma}$
$x \sim \mathcal{P}(x; p_1, \ldots, p_n)$	x is distributed according to $\mathcal{P}$
$\{x_i\}_{i=1,\ldots N}$	Measurement sample of random var. x
$\overline{x_i} \equiv \frac{1}{N}\sum_{i=1}^{N} f(x_i)$	Sample mean of $f(x)$
$\mathbb{E}[f(x)] \equiv \int_{\mathbb{R}} f(x)\,\mathcal{P}(x; p_1, \ldots, p_n)\,\mathrm{d}x$	Ensemble mean of a function $f(x)$ with respect to distribution $\mathcal{P}$

Table A.4. Conventions regarding statistics and state estimation.

Note that, for brevity, I often talk about "probabilities" when we are actually dealing with probability densities. Also, I use the same symbols to denote a random variable and its value at a specific time. The intended meaning should be clear from the context.

A.4.1 *Calculation rules for Gaussian distributions*

product of Gaussians

The product of two Gaussian distributions is proportional to another Gaussian [P+08, sec. 8.1.8]:

$$\mathcal{N}(\boldsymbol{x}; \boldsymbol{m}_1, \boldsymbol{\Sigma}_1) \times \mathcal{N}(\boldsymbol{x}; \boldsymbol{m}_2, \boldsymbol{\Sigma}_2) \propto \mathcal{N}(\boldsymbol{x}; \boldsymbol{m}, \boldsymbol{\Sigma}), \tag{A.1}$$

$$\boldsymbol{\Sigma}^{-1} = \boldsymbol{\Sigma}_1^{-1} + \boldsymbol{\Sigma}_2^{-1}, \tag{A.2}$$

$$\boldsymbol{m} = \boldsymbol{\Sigma}\left(\boldsymbol{\Sigma}_1^{-1}\boldsymbol{m}_1 + \boldsymbol{\Sigma}_2^{-1}\boldsymbol{m}_2\right). \tag{A.3}$$

To derive the Kalman filter, I need to rewrite a Gaussian distribution $\mathcal{N}(\boldsymbol{y}; \boldsymbol{C}\boldsymbol{x}, \boldsymbol{V})$ of a variable $\boldsymbol{y}$ which depends linearly on another variable $\boldsymbol{x}$ as a distribution of $\boldsymbol{x}$. In this context, the matrix $\boldsymbol{C}$ will

be the so-called *measurement matrix* relating the system state $\boldsymbol{x}$ to the measured output $\boldsymbol{y}$. $\boldsymbol{C}$ satisfies two conditions in our case:

measurement matrices & inversion of distributions

1. $\boldsymbol{C}$ is a $m \times n$-matrix with m (number of measurement variables) smaller than n (number of state variables).
2. I assume that all our measurement variables are independent, such that all rows of $\boldsymbol{C}$ are linearly independent. Hence, $\boldsymbol{C}$ has full rank.

Under these conditions—even though we cannot directly invert $\boldsymbol{C}$ to rewrite $\mathcal{N}(\boldsymbol{y}; \boldsymbol{C}\boldsymbol{x}, \boldsymbol{V})$ as a distribution of $\boldsymbol{x}$—we can use the "right pseudoinverse" $\boldsymbol{C}^\mathsf{T}\left(\boldsymbol{C}\boldsymbol{C}^\mathsf{T}\right)^{-1}$ of $\boldsymbol{C}$ [Ste94, pp. 50-51] to obtain

right pseudoinverse

$$\mathcal{N}(\boldsymbol{y}; \boldsymbol{C}\boldsymbol{x}, \boldsymbol{V}) \propto \mathcal{N}\left(\boldsymbol{x}; \boldsymbol{C}^\mathsf{T}\left(\boldsymbol{C}\boldsymbol{C}^\mathsf{T}\right)^{-1}\boldsymbol{y}, \left(\boldsymbol{C}^\mathsf{T}\boldsymbol{V}^{-1}\boldsymbol{C}\right)^{-1}\right). \tag{A.4}$$

A.5 FOURIER ANALYSIS AND NOISE POWER

SYMBOL / EQN.	MEANING
$x(t)$	Random signal
$\dot{x}(t) \equiv \frac{\partial x(t)}{\partial t}$	Time derivative of $x(t)$
$\tilde{x}(\Omega) \equiv \int_{-\infty}^{+\infty} x(t)\, e^{-i\Omega t} \mathrm{d}t$	Fourier transform of $x(t)$
$x(t) \equiv \int_{-\infty}^{+\infty} \tilde{x}(\Omega)\, e^{+i\Omega t} \frac{\mathrm{d}\Omega}{2\pi}$	Inverse Fourier transform of $\tilde{x}(\Omega)$
$\tilde{\dot{x}}(\Omega) = i\Omega\tilde{x}(\Omega)$	Time derivative in Fourier domain
$G_{xx}(\tau) \equiv \mathbb{E}[x(t)\, x(t+\tau)]$	Autocorrelation function (ACF) of random signal $x(t)$
$S_{xx}(\Omega) = \int_{-\infty}^{+\infty} G_{xx}(\tau)\, e^{-i\Omega\tau} \mathrm{d}\tau$	Two-sided noise power spectral density NPS of $x(t)$
$S_x(\Omega) \equiv 2 \times S_{xx}(\Omega)$	One-sided NPS of $x(t)$
$S_{(\alpha x)(\alpha x)}(\Omega) = \alpha^2 S_{xx}(\Omega)$ $S_{\alpha x}(\Omega) = \alpha^2 S_x(\Omega)$	Scaling of NPS with constant α
$S_{\dot{x}\dot{x}}(\Omega) = \Omega^2 S_{xx}(\Omega)$ $S_{\dot{x}}(\Omega) = \Omega^2 S_x(\Omega)$	NPS of the time derivate $\dot{x} \equiv \frac{\partial x(t)}{\partial t}$
$G_{xx}(\tau) = \alpha\delta(\tau)$	ACF of a white-noise process $x(t)$
$S_{xx}(\Omega) = \alpha$	NPS for a white-noise process $x(t)$
$\mathbb{E}[x^2(t)] = \int_{-\infty}^{\infty} S_{xx}(\Omega) \frac{\mathrm{d}\Omega}{2\pi}$ $= \int_0^{\infty} S_x(\Omega) \frac{\mathrm{d}\Omega}{2\pi}$	Variance from NPS

Table A.5. Notation and formulas regarding Fourier analysis and noise power spectral densities etc. Following the definitions and notation in [Cle+10] and [Wil12, sec.2.1].

Note that writing down the integrals defining Fourier and inverse Fourier transformations in Table A.5 does not guarantee their existence. Note also that the definition for the NPS relies on the Wiener–Khinchin theorem [Cle+10, eq. (A4)] which assumes wide-sense stationarity.

B

NOISE MEASUREMENTS

Below, I provide more information on the laser noise measurements: Some additional plots of the filtered amplitude noise (Section B.1) and frequency noise (Section B.2), as well as a detailed explanation of how the frequency measurements were obtained (Section B.3).

B.1 AMPLITUDE NOISE

B.1.1 *Single-pass filtering*

noise suppression at high frequencies

Figure B.1 shows the classical amplitude noise of the laser beam after a single pass through the filter cavity in low-finesse and high-finesse mode. The filter cavity reduces classical amplitude noise for sideband frequencies above 200 kHz (100 kHz) for the low-finesse (high-finesse) mode. Below 100 kHz, however, the filter cavity increases classical amplitude noise, probably because of an unstable lock of the filter cavity to the laser at low sideband frequencies. An unstable lock could cause additional amplitude noise in two different ways:

increased noise at low frequencies

1. Whenever the laser is not exactly resonant with filter cavity, classical frequency noise of the laser is converted to amplitude noise. The induced amplitude noise has the same spectral characteristics as the classical frequency noise, which increases strongly towards low sideband frequencies.

2. Even without classical frequency noise, a fluctuating detuning leads to fluctuations in the transmitted intensity, hence amplitude noise. If the fluctuations of the detuning are stronger at low frequencies (which they usually are), so are the fluctuations of amplitude.

Note that the magnitude of both effects depends strongly on the mean detuning. For zero mean detuning, both effects are zero to first order in the detuning—for non-zero mean detuning, they are not.

I have not explored the added low-frequency noise further, because our optomechanical devices have mechanical frequencies of at least 400 kHz and noise below 100 kHz is therefore not an issue for us (this is confirmed by simulations; see Section 5.4.2.2). It is highly relevant, however, for experiments with smaller mechanical frequencies such as optical levitation experiments in which trap frequencies are typically on the order of 100 kHz. For such experiments, it would be interesting to estimate the amount of low-frequency amplitude noise

relevant for optical levitation

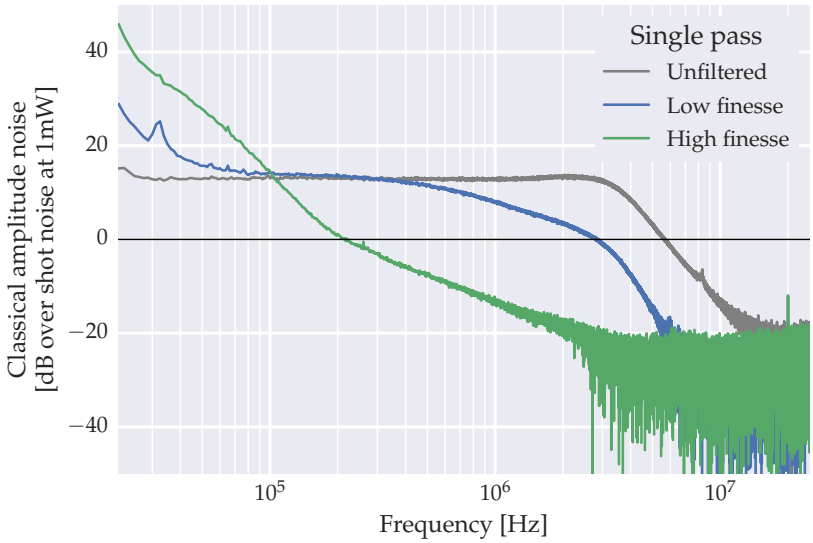

Figure B.1. Classical amplitude noise after single-pass filtering for the low finesse (blue) and high finesse filter cavity (green), as well as for the unfiltered laser (gray). Below 100 kHz, filtering increases classical amplitude noise, probably due to an unstable lock of the filter cavity to the laser.

added by the two mechanisms discussed above and compare it to the measurements.

B.1.2 *Double-pass filtering*

Figure B.2 shows the classical amplitude noise after double pass filtering. The main features—noise suppression at high frequencies and added noise at low frequencies—are similar to single-pass filtering. After double-pass filtering in high-finesse (low-finesse) mode, the beam is shot noise limited above 200 kHz (1 MHz) for 1 mW optical power.

Figure B.3 shows the measured and expected noise suppression for double pass filtering. The expected suppression for double-pass filtering is the square of the suppression for single-pass filtering and depends only on the filter cavity linewidth κ_{FC}. The linewidth was derived from the measured single-pass suppressions (see Figure 3.4), yielding $\kappa_{\mathrm{FC}} \simeq 2\pi \times 650\,\mathrm{kHz}$ ($2\pi \times 48\,\mathrm{kHz}$) for the low-finesse (high-finesse) filter cavity.

good fit of expected and observed suppression in low-finesse mode...

For the low-finesse mode, expected and measured noise suppression agree well at high frequencies, which confirms that the double pass filter does indeed work as expected. The deviation at lower frequencies is likely due to an unstable lock of the filter cavity to the laser, as discussed in Section B.1.1.

...but clear deviation in high-finesse mode

For the high-finesse mode, however, the measured noise suppression is much smaller than expected. At low frequencies ($< 150\,\mathrm{kHz}$),

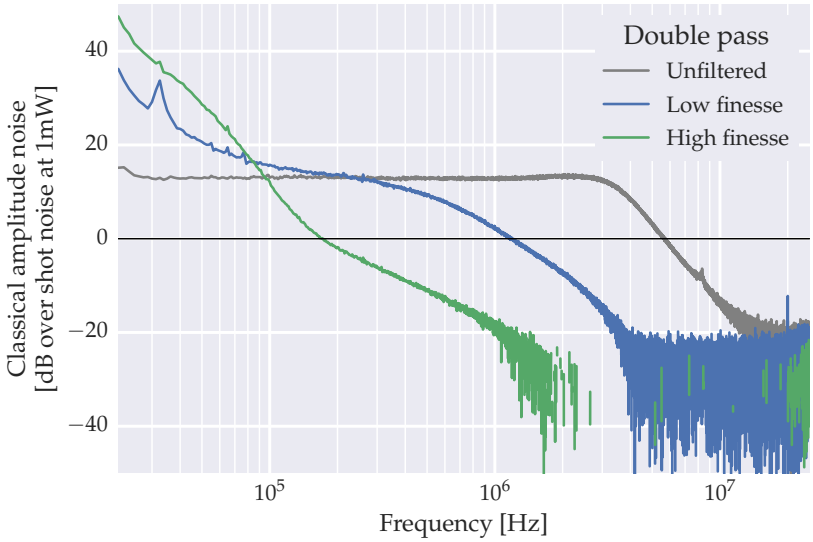

Figure B.2. Classical amplitude noise after double-pass filtering using the low-finesse (blue) and high-finesse filter cavity (green). For comparison, the unfiltered noise is shown in gray. Above 200 kHz (100 kHz), classical amplitude noise is reduced by low-finesse (high-finesse) filtering. As in the single-pass case, the filter cavity adds low-frequency noise (below 100 kHz).

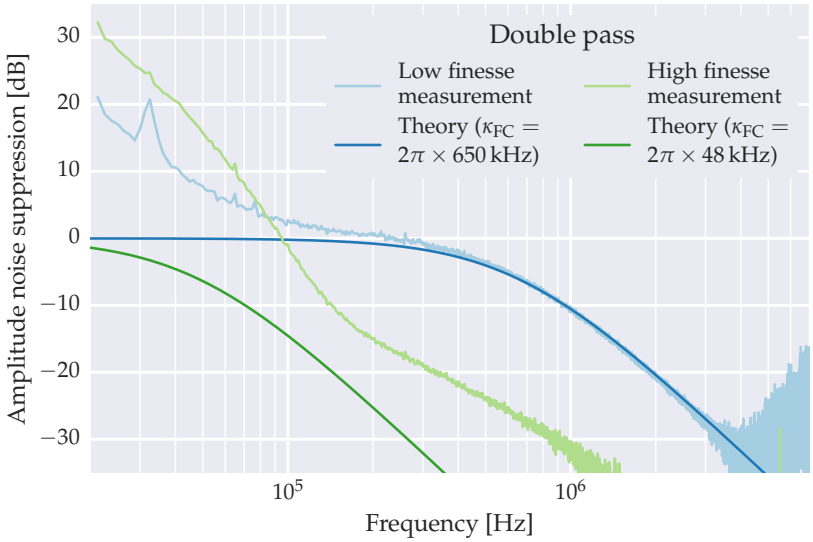

Figure B.3. Amplitude noise suppression due to double-pass filtering with the low finesse (blue) and high finesse (green) filter cavity. Measurements are shown in light colors, theory in dark. As in the single-pass case (Figure 3.4), the measured noise suppression deviates from the expectation at low frequencies (below 150 kHz), likely due to an unstable filter cavity lock (see Section 3.1.3.3). The deviation of the measured suppression for the double-pass in high-finesse mode above 150 kHz is currently not understood.

this is likely again due to an unstable filter cavity lock (compare Figure 3.3 which shows that low frequency amplitude noise for double-pass and single-pass filtering has very similar spectral characteristics, both in low-finesse and high-finesse mode). For frequencies above 150 kHz, however, the measured noise level itself (see Figure B.2), shows a frequency-dependence which is clearly different from the dependence below 150 kHz. This suggests that deviations from the expected suppression at these higher frequencies have a different cause.

possible explanations for deviations from expected suppression

Note that the deviation cannot be explained by the measurement noise floor: For frequencies between 150 kHz and 1 MHz, we are comfortably above the measurement noise floor; Figure B.2 shows that the measurement noise floor is at less than -20 dB, which is only reached at frequencies above 1 MHz in the high-finesse double-pass measurement. Possible explanations for the added amplitude noise might be:

- Air density fluctuations along the beam path inside the filter cavity (the filter cavity is currently not operated in vacuum)
- Backscattering from the intra-cavity mode which is pumped on the first pass into the (counter-propagating) mode which is pumped on the second pass (in Figure 3.1: From the mode indicated by red to the one indicated by yellow). Effectively, this would mean the measured light is a mixture of single-pass and double-pass-filtered light. At high sideband frequencies, the noise would then eventually be dominated by the single-pass-filtered component since its noise power decreases less rapidly with increasing sideband frequency.

I chose to not investigate this further since, even with the suboptimal noise suppression, the classical laser noise levels are sufficiently low for generation and detection of entanglement. This is shown by simulations of our entanglement protocol which include a realistic laser noise model based on our measurements (see Section 5.4.2.2).

B.2 FREQUENCY NOISE

Note that frequency noise was measured and independently calibrated for up to three different lengths of the delay fiber in the imbalanced Mach–Zehnder-interferometer (see Section B.3.2). What is plotted in the following are bands of uncertainty spanned by the minima and maxima of these measurements at the given frequency.

B.2.1 *Single-pass filtering*

Figure B.4 shows the measured frequency noise after a single-pass through the filter cavity in both low-finesse and high-finesse mode.

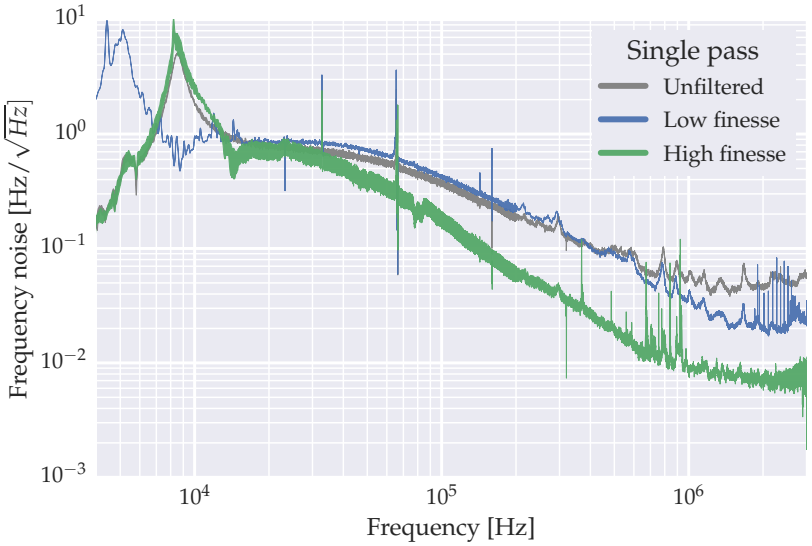

Figure B.4. Classical frequency noise after single-pass filtering for the low finesse (blue) and high finesse filter cavity (green). The frequency noise of the unfiltered laser is shown in gray.

Figure B.5 shows the corresponding measured noise suppressions, together with the expected noise suppression, based on the filter cavity linewidth κ_{FC}. κ_{FC} itself is derived from measured suppressions of amplitude noise (see Figure 3.4).

For very low frequencies (below 10 kHz), there are large deviations between measured and expected noise suppression due to strong and broad noise peaks of unknown origin which seem to have shifted in between the measurements for the different filter modes (see Figure B.4). At intermediate frequencies, below 2 MHz (200 kHz) for the low-finesse (high-finesse) mode, the measurements agree reasonably well with the expectations. At higher frequencies, there are clear deviations of the measured and expected suppression.

In the case of the high-finesse mode, this high-frequency deviation of the measured suppression from the expectation is likely due to the measurement noise floor. This is suggested by the fact that the single-pass and double-pass measurements for high-finesse start to coincide above 200 kHz (see Figure 3.6). Most likely, this measurement noise floor is set by phase noise caused by the delay fiber. For the low-finesse mode, I have no explanation for the observed excess frequency noise.

B.2.2 *Double-pass filtering*

Figure B.6 shows the measured frequency noise after double-pass filtering. Figure B.7 shows the corresponding measured noise suppressions and contrasts them with the expectations. As in the case of the

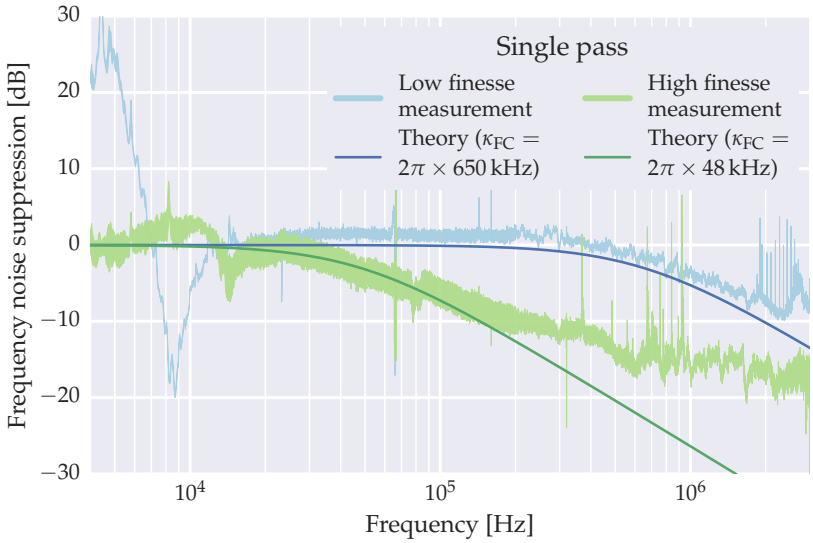

Figure B.5. Frequency noise suppression after single-pass filtering with the low finesse (blue) and high finesse (green) filter cavity. Measurements and theory are shown in light and dark colors, respectively.

amplitude noise, expectations for the double-pass noise suppression are derived from the measured filter cavity linewidth.

Qualitatively, the agreement of measured and expected noise suppression is similar to the single-pass case: Poor at low frequencies (below 20 kHz) due to strong and broad noise peaks which seem to shift for different filter modes. Somewhat reasonable at intermediate frequencies. And poor again at high frequencies above 1 MHz (200 kHz) for the low-finesse (high-finesse) mode. As in the single-pass case, the high-frequency deviation in the high-finesse mode is likely caused by the measurement noise floor (due to noise caused by the delay fiber), whereas I have no reasonable explanation for the high-frequency deviation in the low-finesse mode.

B.3 MEASURING FREQUENCY AND PHASE NOISE

B.3.1 *Relation of phase and frequency noise*

The phase of a laser field is given by

$$\phi(t) = \omega_1 t + \delta\phi(t) + \phi_0, \tag{B.1}$$

where $\omega_1 t$ is the time evolution of the carrier, and $\delta\phi$ are small, zero-mean fluctuations around it. ϕ_0 is an arbitrary offset, which we are not concerned with since we cannot measure it.

direct measurement of phase noise

A direct measurement of the phase noise $\delta\phi(t)$ requires a phase-reference at least as stable as the device under test. Since the filtered laser we are using for the entanglement experiment is the most stable

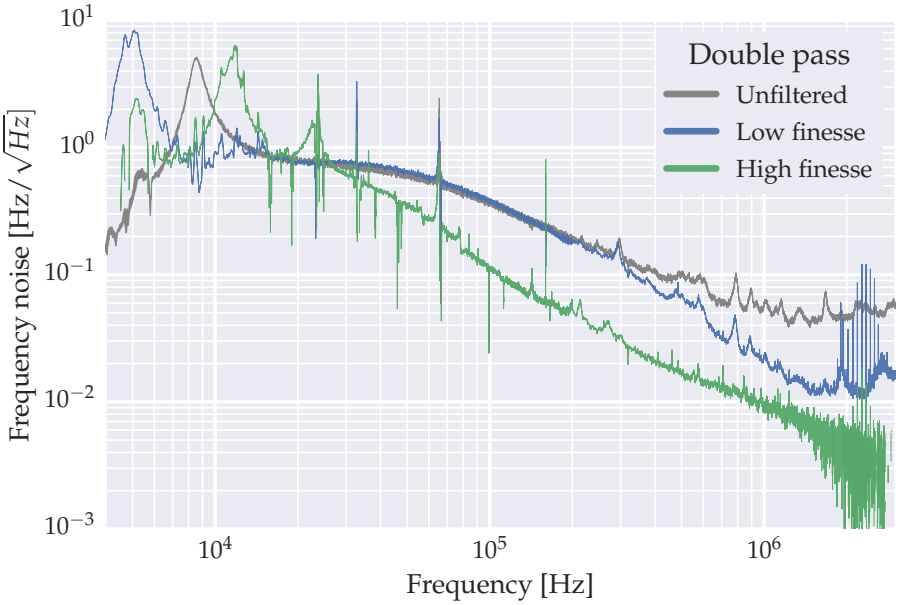

Figure B.6. Classical frequency noise after double-pass filtering for the low finesse (blue) and high finesse filter cavity (green). The unfiltered noise is shown in gray.

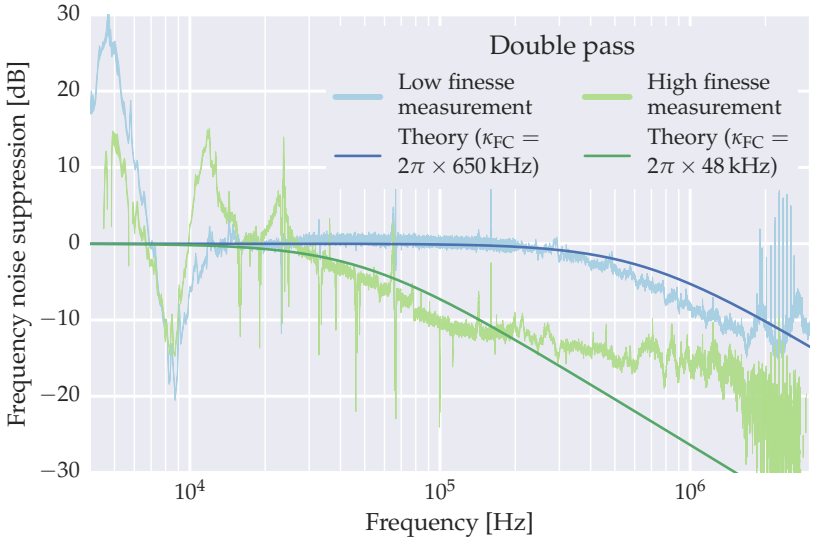

Figure B.7. Frequency noise suppression after double-pass filtering with the low finesse (blue) and high finesse (green) filter cavity. Measurements and theory are shown in light and dark colors, respectively.

source in our lab, we cannot perform a direct phase noise measurement in this way. But we can infer the phase noise spectrum $S_{\delta\phi}$ from the frequency noise $S_{\delta\omega}$, which can be measured as explained in Section B.3.2.

instantaneous optical frequency

The instantaneous optical frequency $\omega(t)$ is defined as the rate of change of optical phase $\phi(t)$:

$$\omega(t) \equiv \dot{\phi}(t) = \omega_l + \delta\dot{\phi}(t) \equiv \omega_l + \delta\omega(t). \tag{B.2}$$

$\omega(t)$ has a large DC component—the carrier frequency ω_l—and small fluctuations $\delta\omega(t)$ around it.

In Fourier space, we have $\delta\tilde{\omega}(\Omega) = i\Omega\delta\tilde{\phi}(\Omega)$ and, therefore,

$$S_{\delta\omega}(\Omega) = \Omega^2 S_{\delta\phi}(\Omega) \tag{B.3}$$

Since we are only ever interested in the *fluctuations* $\delta\omega$ and $\delta\phi$ of the frequency and phase, I drop the δ from here on, and denote them simply by ω and ϕ, respectively.

B.3.2 *Imbalanced Mach–Zehnder interferometer*

[51] *Imbalanced MZI:*

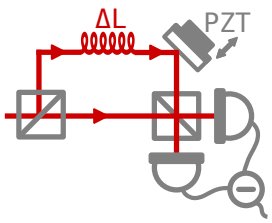

Frequency noise S_ω can be measured using a MZI,[51] where one of the interferometer arms is prolonged with respect to the other by a fiber of length ΔL (this measurement is also discussed in [Rie13]). The arm length difference ΔL leads to a relative time delay for optical signals between the two arms of

$$\Delta T = \frac{\Delta L \cdot n}{c}, \tag{B.4}$$

where n is the refractive index of the fiber.

The difference ΔP in optical power at the two outputs of the MZI is proportional to the phase difference $\Delta\phi(t)$ between the two arms. This is true for small phase differences $\Delta\phi \ll 1$, which is enforced experimentally by locking the interferometer to a relative phase difference $\Delta\phi \simeq 0$. For a laser with fluctuating instantaneous optical frequency $\omega(t)$, the phase difference $\Delta\phi(t)$ is time-dependent and given by the following integral over the instantaneous frequency:

phase difference = optical frequency integrated over time period ΔT

$$\Delta P(t) \propto \Delta\phi(t) = \int_t^{t+\Delta T} \omega(\tau)\, \mathrm{d}\tau. \tag{B.5}$$

To get the interferometer transfer function, we take the Fourier transform of this equation and obtain

$$\begin{aligned}
\tilde{\Delta P}(\Omega) &\propto \int_{-\infty}^{+\infty} \mathrm{d}t\, e^{-i\Omega t} \int_{t}^{t+\Delta T} \omega(\tau)\, \mathrm{d}\tau && \text{(B.6)}\\
&= \int_{-\infty}^{+\infty} \mathrm{d}t\, e^{-i\Omega t} \int_{0}^{\Delta T} \omega(t+\tau)\, \mathrm{d}\tau && \text{(B.7)}\\
&= \int_{0}^{\Delta T} \left(\int_{-\infty}^{+\infty} \mathrm{d}t\, e^{-i\Omega t} \omega(t+\tau) \right) \mathrm{d}\tau && \text{(B.8)}\\
&= \int_{0}^{\Delta T} \left(e^{i\Omega\tau} \tilde{\omega}(\Omega) \right) \mathrm{d}\tau && \text{(B.9)}\\
&= i\frac{1-e^{i\Omega\Delta T}}{\Omega} \cdot \tilde{\omega}(\Omega) && \text{(B.10)}\\
&= \left(e^{i\Omega\Delta T} - 1 \right) \tilde{\phi}(\Omega), && \text{(B.11)}
\end{aligned}$$

where the last line follows from $\tilde{\omega}(\Omega) = \dot{\tilde{\phi}}(\Omega) = i\Omega\tilde{\phi}(\Omega)$.

Hence, the magnitude $\left|T_{\phi\to\Delta P}(\Omega)\right|$ of the interferometer transfer function from phase fluctuation ϕ at the input to power difference ΔP at the outputs is:

$$\left|T_{\phi\to\Delta P}(\Omega)\right| \equiv \left|\tilde{\Delta P}(\Omega)/\tilde{\phi}(\Omega)\right| \propto \left|e^{i\Omega\Delta T} - 1\right| \propto \left|\sin(\Omega\Delta T/2)\right|. \tag{B.12}$$

We measure the optical power difference ΔP between the outputs of the MZI with two photodetectors, which yields a difference current ΔI. The photodetectors themselves also have a frequency-dependent response $|T_{P\to I}(\Omega)|$, which we need to take into account. Hence, the full measurement is described (up to dark noise and shot noise) by the following transfer function:

$$\begin{aligned}
\left|T_{\phi\to\Delta I}(\Omega)\right| &= \left|T_{\phi\to\Delta P}(\Omega)\right| \times \left|T_{\Delta P\to\Delta I}(\Omega)\right| && \text{(B.13)}\\
&\propto \left|\sin(\Omega\Delta T/2\right| \times \left|T_{P\to I}(\Omega)\right|. && \text{(B.14)}
\end{aligned}$$

To accurately deduce the NPS of phase or frequency fluctuations from the the measured NPS of the difference current $S_{\Delta I}(\Omega)$, we apply the following post-processing steps, which are explained in the following sections:

1. Correct the measured spectra for dark and shot noise (Section B.3.3)
2. Correct for the detector response $|T_{\Delta P\to\Delta I}(\Omega)|$ (Section B.3.4)
3. Measure the actual delay ΔT of the interferometer and correct for its transfer function $\left|T_{\phi\to\Delta P}(\Omega)\right| \propto |\sin(\Omega\Delta T/2)|$ (Section B.3.5).
4. Calibrate the resulting spectra (Section B.3.6)

B.3.3 *Dark noise and shot noise*

The detector dark noise is easy to take care off: We measure it independently and directly subtract it from all measured spectra. Other significant sources of noise in this measurement are shot noise and noise from differential fluctuations in the two arms of the interferometer.

B.3.3.1 *Different types of interferometer dark noise*

"$\Delta L = 0$-dark noise": shot noise plus dark noise from interferometer instabilities

Most of the noise sources which remain after subtraction of detector dark noise can be measured directly by setting the arm length difference ΔL to close to zero (by removing the additional delay fiber). Let us call the noise measured in this mode "$\Delta L = 0$-dark noise". For $\Delta L \simeq 0$, the sensitivity to external phase noise is negligible in the frequency range of interest (confirmed by a direct measurement of the interferometer transfer function). Hence, any remaining noise measured for $\Delta L \simeq 0$ is not caused by classical phase noise of the laser, and should therefore be subtracted. This remaining noise includes both classical fluctuations of the relative phase due to interferometer instabilities, as well as shot noise. Both of these contributions depend only on the optical power at the detectors and not on the arm length difference.

"$\Delta L \neq 0$-dark noise": additional dark noise from the delay fiber

Note however, that there are also classical fluctuations of the relative phase between the interferometer arms which *do* depend on the arm length difference: If we add a fiber of length L to the interferometer, we will measure additional noise due to fluctuations of the effective optical path length inside the added fiber, which could arise from temperature fluctuations (at very low frequencies) or from acoustic fluctuations of the fiber length (at MHz frequencies). Let us call this contribution to the measured noise "$\Delta L \neq 0$-dark noise". This contribution cannot be measured as easily, since, once a fiber delay has been introduced, the measurements are always dominated by the phase noise of the laser. Therefore, I neglected the $\Delta L \neq 0$-dark noise in the measurements presented here, which should therefore be considered upper limits on the phase and frequency noise of the laser. Note that, for low levels of external phase noise, we are indeed limited by a background noise the size of which is consistent with rough expectations for the size of the $\Delta L \neq 0$-dark noise. In future measurements, it would therefore be desirable to independently measure this contribution and correct for it. For the sake of brevity, I will from now on refer to $\Delta L = 0$-dark noise, which includes shot noise and noise arising from instabilities of the interferometer, simply as "dark noise", in the understanding that it does not account for all dark noise contributions.

B.3.3.2 *Correcting for interferometer dark noise*

subtracting the "$\Delta L = 0$-dark noise"

Note that the measured dark noise $S_I^{(\Delta L=0)}(\Omega)$ fluctuates slightly in between different measurement runs. Such fluctuations could be due to fluctuations of the interferometer visibility or of the optical powers in the interferometer arms. To account for these fluctuations, I added a 160 kHz-calibration peak to all measurements by modulating a piezo-mounted mirror in one of the interferometer arms. This peak completely dominates the external phase noise at 160 kHz; it can therefore be used to rescale the measured dark noise to the level appropriate for a given measurement. To correct a measured spectrum $S_I(\Omega)$, I first scale the measured dark noise $S_I^{(\Delta L=0)}(\Omega)$ such that its band power at 160 kHz matches the band power of the target spectrum $S_I(\Omega)$ at 160 kHz. Then I subtract the scaled dark noise from $S_I(\Omega)$. The net effect is a perfect cancellation of the artificial dark noise peak at 160 kHz and, hopefully, of most other dark noise contributions. Note that, in fact, the band powers at 160 kHz fluctuated by a only few percent in between different measurements.

Figure B.8 shows an example spectrum before and after dark noise subtraction. We see that dark noise is not limiting the measurement below 3 MHz. In the range from 4 to 16 MHz, $\Delta L = 0$-dark noise is, in fact, the limiting broadband noise. This is evidenced by the fact that the zeros of the transfer function are well resolved in this frequency range after dark noise subtraction, which shows that no other noise source contributes significantly. Comparison with measurements for other delays, however, reveals a rather broad noise peak between 7.2 MHz and 8.2 MHz which is not due to $\Delta L = 0$-dark noise. Above 16 MHz, dark noise subtraction is not sufficient to resolve the zeros of the transfer function. This implies that, at these frequencies, other noise contributions—potentially due to the delay fiber—are significant.

B.3.4 *Detector response*

I define the detector response as the magnitude of the transfer function from optical power P at the diode to photo-current I after all filtering and amplification

$$|T_{P\to I}(\Omega)| \equiv \left|\tilde{I}(\Omega)/\tilde{P}(\Omega)\right|. \tag{B.15}$$

Shot noise is characterized by a flat power fluctuation spectrum, hence for shot noise $|\tilde{P}(\Omega)| = \text{const}$. We can therefore determine the detec-

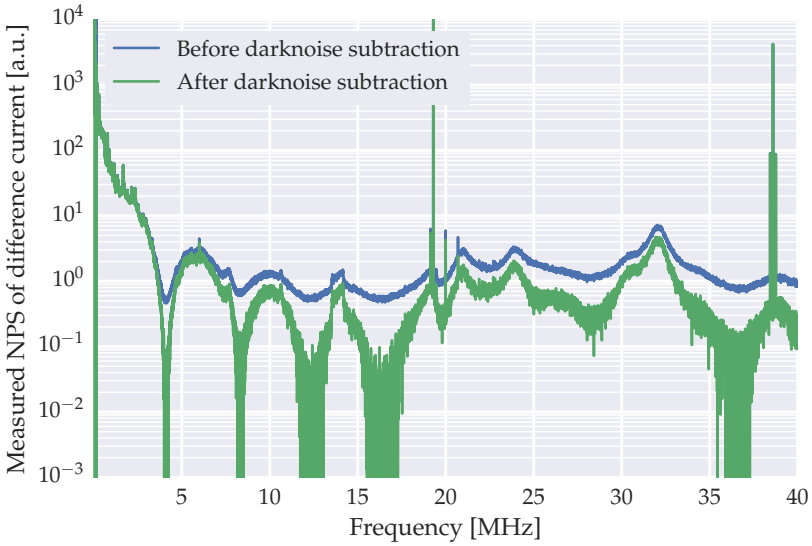

Measurement parameters: $\Delta L \simeq 50\,\mathrm{m}$, $\Delta T \simeq 0.24\,\mu\mathrm{s}$, free-running laser, single pass through high finesse filter cavity.

Figure B.8. Example spectrum before (blue) and after (green) dark noise subtraction. This measurement was done for a single pass through the high finesse filter cavity. Zeros of the transmission functions are at $\Omega_n \simeq n \times 2\pi \times 4.1\,\mathrm{MHz}$ ($n = 0, 1, \ldots$). Hence, the time delay between the two interferometer arms is $\Delta T = 2\pi/\Omega_1 \simeq 0.24\,\mu\mathrm{s}$. With the nominal fiber delay of $\Delta L = 50\,\mathrm{m}$, we obtain an effective refractive index of the fiber of $n = \Delta T \cdot c/\Delta L \simeq 1.46$.

tor response from the NPS $S_I^{(o)}(\Omega)$ for shot noise (which is measured using the difference output of two balanced detectors:

$$|T_{P\to I}(\Omega)| \propto \sqrt{S_I^{(o)}(\Omega)}. \tag{B.16}$$

The details are described in Figure B.9.

B.3.5 *Interferometer response*

measuring the interferometer transfer function

The next step, after correcting for dark noise and the detector response, is the correction for the transfer function (B.12) of the interferometer. This transfer function can, in principle, be measured directly by connecting a broadband fiber EOM (in the laser beam path before the interferometer) to the output of a network analyzer. The fiber EOM produces a phase modulation of the input light. This phase modulation is translated by the interferometer into intensity fluctuations at the detectors. The measured intensity fluctuations are then fed back into the network analyzer. By sweeping the modulation frequency, we obtain a frequency dependent measurement of the transfer function from modulation voltage at the fiber EOM to optical

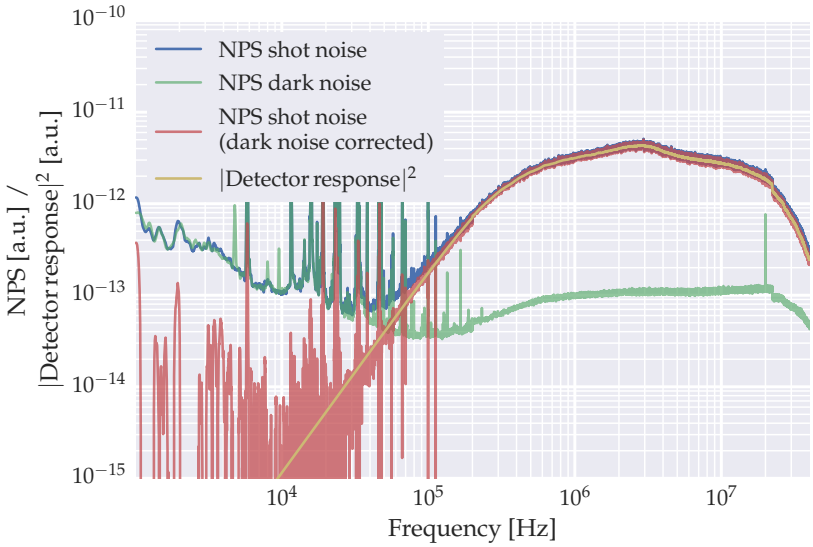

Figure B.9. Measurement of the detector response: A shot noise measurement (blue) is corrected for dark noise (green) yielding a corrected shot noise spectrum (red). We smooth the corrected spectrum for frequencies above 200 kHz, and extend the observed frequency-dependence to frequencies below 200 kHz assuming a near-quadratic roll-off (manually adjusted to yield a reasonable fit to the measurement) to obtain the square $|T_{P\to I}(\Omega)|^2$ of the detector response (yellow). The latter can then be used to correct measured spectra for the detector response (by dividing them by $|T_{P\to I}(\Omega)|^2$).

Measurement parameters: $P_{\text{opt}} \simeq 15\,\text{mW}$ for the shot noise measurement

power fluctuation at the output of the interferometer. Hence, we can measure the product

$$|T_{V\to\Delta P}(\Omega)| = |T_{V\to\phi}(\Omega)| \times |T_{\phi\to\Delta P}(\Omega)| \tag{B.17}$$

of the interferometer response

$$|T_{\phi\to\Delta P}(\Omega)|, \tag{B.18}$$

and the response of the fiber EOM, defined as the magnitude of the transfer function from modulation voltage V to phase modulation ϕ:

$$|T_{V\to\phi}(\Omega)| \equiv |\tilde{\phi}(\Omega)/\tilde{V}(\Omega)|. \tag{B.19}$$

Unfortunately, the response $|T_{V\to\phi}(\Omega)|$ of the fiber EOM is not known precisely. Therefore, we cannot infer the interferometer transfer function (B.18) directly from the measured transfer function (B.17). Instead we use the theory expression (B.12), which depends only on the relative time delay ΔT of the interferometer arms. ΔT can, in

ΔT from zeros of measured transfer function

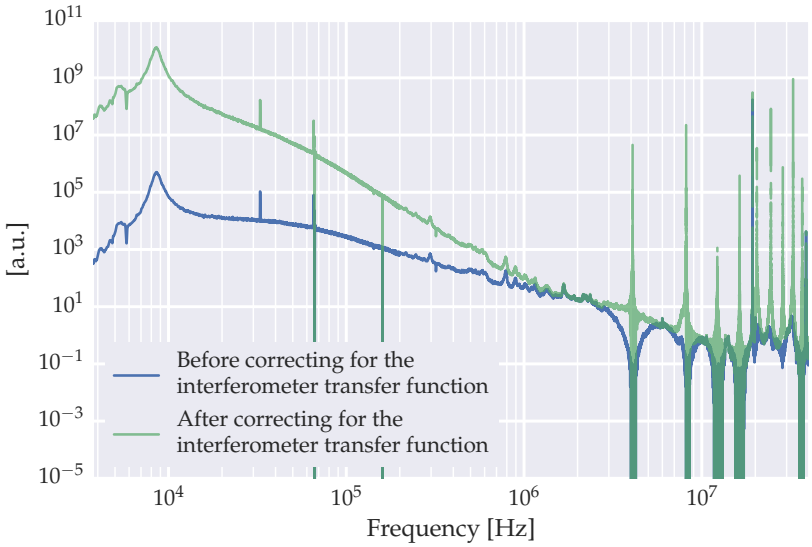

Measurement parameters: $\Delta L \simeq 50\,\mathrm{m}$, $\Delta T \simeq 0.24\,\mu\mathrm{s}$, free-running laser, unfiltered.

Figure B.10. Example spectra demonstrating the correction for the interferometer transfer function. Before correction (blue), the measured spectrum has zeros at $\Omega_n \simeq n \times 2\pi/\Delta T$ (for $\Delta T \simeq 0.24\,\mu\mathrm{s}$, $n = 0, 1, \ldots$) as predicted by the interferometer transfer function (B.12). After the correction (green, semi-transparent), these zeros disappear but at their frequencies the noise power fluctuates wildly. In the next step, the measurement values close to zeros of the transfer functions are excluded and replaced by values obtained from measurements with a different delay time ΔT (hence, different locations of the zeros).

turn, be inferred from the evenly spaced zeros Ω_n ($n = 1, 2, \ldots$) of the measured transfer function (B.17):

$$\Delta T = n \times \frac{2\pi}{\Omega_n}. \tag{B.20}$$

B.3.5.1 *Correction for interferometer transfer function*

points of zero sensitivity

Figure B.10 shows an example trace before and after correcting for the interferometer transfer function (B.12). Close to the zeros of the transfer function, the sensitivity of the measurement is close to zero. This is reflected in wildly fluctuating noise power of the corrected spectra at these frequencies.

"stitching together" measurements for different delays ΔL

In order to obtain reliable measurements at all frequencies, we must therefore measure for different delay fiber lengths ΔL (i.e. different delays ΔT). We chose to measure for $\Delta L \simeq 50\,\mathrm{m}$, $53\,\mathrm{m}$, and $100\,\mathrm{m}$. For each sideband frequency Ω of interest (10 kHz to 10 MHz), at least one of these measurements has sufficiently non-zero sensitivity. Therefore, we can cut the regions of low sensitivity from each measured spectrum, stitch the three resulting spectra together, and obtain a spectrum without any gaps caused by low sensitivity.

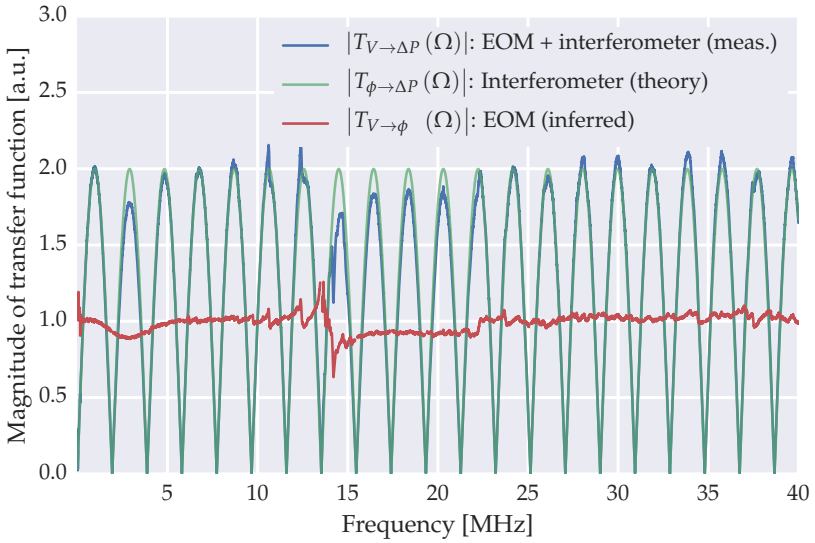

Figure B.11. Example measurement of the combined transfer function of EOM plus interferometer (blue). From this, we obtain the theoretical interferometer transfer function (green, semi-transparent) by estimating ΔT from the zeros of the measured transfer function. Dividing the measured by the theoretically expected transfer function yields the transfer function of the fiber EOM (red).

Measurement parameters: $\Delta L \simeq 100\,\mathrm{m}$, $\Delta T \simeq 0.52\,\mu\mathrm{s}$.

B.3.5.2 *Fiber EOM response*

inferring the response of the fiber EOM

The response of the fiber EOM $\left|T_{V\to\phi}(\Omega)\right|$ can be inferred from the comparison of the measured interferometer transfer function (B.17) to the theoretically expected one (B.12):

$$\left|T_{V\to\phi}(\Omega)\right| = \left|T_{V\to\Delta P}(\Omega)\right| \,/\, \left|T_{\phi\to\Delta P}(\Omega)\right| \tag{B.21}$$

An example measurement and estimated EOM response is shown in Figure B.11.

We perform the measurement of the transfer function $|T_{V\to\Delta P}(\Omega)|$ and estimate (B.21) of the fiber EOM response before each noise measurement (in particular, also for each different delayΔT) to ensure the interferometer is functioning as desired. The standard deviation between the resulting 18 different estimates of the fiber EOM response is, on average across all frequencies, on the order of a percent. The fact that we get highly consistent estimates for the fiber EOM response for all measurements shows that the interferometer response was, in fact, close to the theoretical expectation for each measurement.

consistent estimates across different measurements

B.3.6 *Calibration of phase noise spectra*

The spectra which result from division by the interferometer transfer function—let us denote them by $S_{\tilde{\phi}}$—are proportional to the actual phase noise spectra S_ϕ:

$$S_{\tilde{\phi}} = S_{\alpha\cdot\phi} = \alpha^2 \cdot S_\phi, \tag{B.22}$$

with an unknown calibration factor α. If we know the actual phase noise power $S_\phi(\nu_{\text{cal}})$ for some frequency ν_{cal}, we can determine the calibration factor α by comparing the expected phase noise power $S_\phi(\nu_{\text{cal}})$ to the measured phase noise power $S_{\tilde{\phi}}(\nu_{\text{cal}})$:

$$\alpha = \sqrt{S_{\tilde{\phi}}(\nu_{\text{cal}}) / S_\phi(\nu_{\text{cal}})}. \tag{B.23}$$

We produce such a strong known phase modulation by inserting a fiber EOM and driving it harmonically at $\nu_{\text{cal}} = 19.3\,\text{MHz}$ with a function generator (modulation depth $50\,\text{mV}_{\text{pp}}$). The resulting phase modulation $S_\phi(\nu_{\text{cal}})$ can be independently calibrated as follows.

B.3.6.1 *Calibration of EOM phase modulation*

Consider a mono-chromatic laser beam (frequency ω_1) phase-modulated at frequency $\omega_{\text{cal}} = 2\pi \cdot \nu_{\text{cal}}$ with a peak phase deviation of β:

$$\begin{aligned} E(t) &\propto \exp\left(i\omega_1 t + i\beta \sin\left(\omega_{\text{cal}} t\right)\right) \\ &= \exp\left(i\omega_1 t\right) \cdot \exp\left(i\beta \sin\left(\omega_{\text{cal}} t\right)\right). \end{aligned} \tag{B.24}$$

The last expression can be expressed as a sum of harmonics of $\sin\left(\omega_{\text{cal}} t\right)$ using the Jacobi-Anger expansion [17]:

$$\exp\left(i\beta \sin\left(\theta\right)\right) = \sum_{n=-\infty}^{\infty} J_n(\beta) \exp\left(in\theta\right). \tag{B.25}$$

This leads to

$$\begin{aligned} E(t) &\propto \exp\left(i\omega_1 t\right) \cdot \sum_{n=-\infty}^{\infty} J_n(\beta) \exp\left(in\omega_{\text{cal}} t\right) \\ &= \sum_{n=-\infty}^{\infty} J_n(\beta) \exp\left(i\left(\omega_1 + n\omega_{\text{cal}}\right) t\right) \equiv \sum_{n=-\infty}^{\infty} E_n(t), \end{aligned} \tag{B.26}$$

where J_n is the n-th Bessel function of the first kind. E_n is the field amplitude of the n-th sideband, the corresponding optical power is proportional to $|E_n|^2$. Hence, the phase modulation of angular frequency ω_{cal} adds optical side-bands at angular frequencies $\omega_1 \pm n \cdot \omega_{\text{cal}}$ whose amplitude $J_n(\beta)$ is determined by the peak modulation depth β of the phase modulation. We can use (B.26) to infer the peak phase devia-

tion β from the ratio of the amplitude of the first sideband to the amplitude of the carrier.

phase modulation depth from sideband amplitude

We measure this ratio (call it r) by mixing the modulated beam with an unmodulated laser with optical frequency ω_{LO} (some GHz away from ω_{l}) on a beam splitter and detecting the beat note with a fast photodetector. The resulting photocurrent is proportional to the square of the sum of the fields which gives a DC part proportional to the optical power of the two beams and an AC part ("beat note") proportional to the product of the fields. The noise power spectrum of the photocurrent I is therefore

measuring power in optical sidebands

$$S_I(\Omega) \propto \sum_{n=-\infty}^{\infty} \left(J_n(\beta)\right)^2 \delta\left(\Omega - (\Delta\omega_{\mathrm{l}} + n \cdot \omega_{\mathrm{cal}})\right), \tag{B.27}$$

where $\Delta\omega_{\mathrm{l}} \equiv \omega_{\mathrm{LO}} - \omega_{\mathrm{l}}$. We measure the band powers

$$\mathrm{BP}_0 \equiv \int_{\Omega \simeq \Delta\omega_{\mathrm{l}}} S_I(\Omega)\,\mathrm{d}\Omega \tag{B.28}$$

$$\mathrm{BP}_1 \equiv \int_{\Omega \simeq \Delta\omega_{\mathrm{l}} + \omega_{\mathrm{cal}}} S_I(\Omega)\,\mathrm{d}\Omega \tag{B.29}$$

of the carrier contribution (at frequency $\Delta\omega_{\mathrm{l}}$) and of the first upper sideband (at frequency $\Delta\omega_{\mathrm{l}} + \omega_{\mathrm{cal}}$), respectively, we obtain the ratio r of their field amplitudes

$$r = \sqrt{\mathrm{BP}_1 / \mathrm{BP}_0} = J_1(\beta)/J_o(\beta), \tag{B.30}$$

from which we can deduce β. Note that, for small phase modulations β, r increases monotonically with β such that β can be uniquely determined. For our calibration peak, we extract a peak phase modulation depth of

peak phase modulation

$$\beta = \delta\phi_{\mathrm{pk}} = 9.86\,\mathrm{mrad}_{\mathrm{pk}}. \tag{B.31}$$

The band power of the calibration phase and frequency modulation are therefore given by

calibration band power

$$\int_{\nu \approx \nu_{\mathrm{cal}}} S_\phi(\nu)\mathrm{d}\nu = \delta\phi^2_{\mathrm{rms}} = \left(\delta\phi_{\mathrm{pk}}/\sqrt{2}\right)^2 \tag{B.32}$$

$$= 4.86 \times 10^{-5}\,\mathrm{rad}^2 \tag{B.33}$$

$$\int_{\nu \approx \nu_{\mathrm{cal}}} S_\nu(\nu)\mathrm{d}\nu = \nu^2_{\mathrm{cal}} \cdot \delta\phi^2_{\mathrm{rms}} = 1.81 \times 10^{10}\,\mathrm{Hz}^2. \tag{B.34}$$

Note that the calibration tone used for the phase noise measurements was produced by a $50\,\mathrm{mV_{pp}}$-modulation at $\nu_{\mathrm{cal}} = 19.3\,\mathrm{MHz}$ using a function generator. We sweeped the modulation depth over a wide range around the $50\,\mathrm{mV_{pp}}$ using a network analyzer to verify that we are deeply in a regime of small phase modulation, where measured sideband power is perfectly proportional to applied mod-

ulation voltage. We also checked that the detector response was flat enough in the measured frequency range by comparing the measured values for the upper and lower sideband power. These should be equal ideally and differed only slightly in the measurements (standard deviation from the mean less than 3 % for 9 different measurements spanning more than two decades in modulation power). To increase accuracy, we used the mean of upper and lower sideband power to determine β.

C

PULSED-CONTINUOUS ENTANGLEMENT

C.1 DEFINITION OF THE LOGARITHMIC NEGATIVITY

In this thesis, we quantify entanglement using the logarithmic negativity $E_\mathcal{N}$ because it can be calculated straight-forwardly even for multi-mode Gaussian states. For an N-mode covariance matrix σ and a bipartition $A \equiv \{1, \dots M\}$ and $B \equiv \{M+1, \dots N\}$ of the N modes,[52] the logarithmic negativity between A and B is defined as follows [for details see e.g. AI07]: We first calculate the partially transposed covariance matrix $\sigma^{(\mathrm{PT})}$, i.e. we transpose only the B-modes (basically, changing the sign of the p-quadratures for all modes in B). Next, we calculate the so-called symplectic spectrum $\left\{\nu_k^{(\mathrm{PT})}\right\}_{k=1,\dots,N}$ of the partially transposed covariance matrix $\sigma^{(\mathrm{PT})}$. Then, we define the logarithmic negativity between A and B as follows [AI07, eq. 68]:

[52] *In this thesis, I am only interested in the entanglement between the entangling and the readout pulse. This defines the bipartition of interest.*

$$E_\mathcal{N} \equiv \begin{cases} -\sum_k \log\left(\nu_k^{(\mathrm{PT})}/\nu^{(0)}\right), & \text{for } k:\ \nu_k^{(\mathrm{PT})} < \nu^{(0)}, \\ 0, & \text{if all } \nu_k^{(\mathrm{PT})} \geq \nu^{(0)}, \end{cases} \tag{C.1}$$

where $\nu^{(0)}$ is the shot noise variance (variance of a quadrature in a coherent state; in our case, $\nu^{(0)} = 1/2$). If the state σ is entangled, the partially transposed state $\sigma^{(\mathrm{PT})}$ is unphysical which implies that at least one of the $\nu_k^{(\mathrm{PT})}$ drops below $\nu^{(0)}$ [Simoo]. Hence, $E_\mathcal{N}$ becomes positive. If the state is separable, on the other hand, we have $\nu_k^{(\mathrm{PT})} \geq \nu^{(0)}$ (for all k) and, therefore, $E_\mathcal{N} = 0$.

The latter, however, proves inconvenient in practice: Obtaining the value 0 for all separable states is simply too uninformative. In practice, if the state is not entangled, we at least want to get a sense of how far we are from entanglement. To this end, we modify the definition of the logarithmic negativity such that it yields different negative values for different separable states. How to achieve this modified definition, however, depends on the number of (light) modes: For two light modes (hence, a single mechanical mode evaluated with the single-sideband evaluation), there is a natural way to modify the definition (Section C.1.1). For more than two light modes (multiple mechanical modes and/or two-sideband evaluation), however, there is no single natural modified definition: Which definition is chosen in the multi-mode case is therefore a matter of convenience and depends on the quantum states to be analyzed (Section C.1.2).

C.1.1 *Single-mode case*

In the simplest case, we deal with only a single mechanical mode and only one mechanical sideband per pulse. Hence, there are only two (light) modes to be analyzed: The entangling mode centered on the lower mechanical sideband and confined to times $t < 0$, and the readout mode centered on the upper mechanical sideband and confined to times $t > 0$. In this case, at most one of the partially transposed symplectic eigenvalues $\nu_k^{(\mathrm{PT})}$ can drop below $\nu^{(0)}$ [AI07, eq. 69]. Therefore, (C.1) can be simplified to

$$E_{\mathcal{N}} \equiv \max\left(0, -\log\left(\nu_-^{(\mathrm{PT})}/\nu^{(0)}\right)\right), \tag{C.2}$$

where $\nu_-^{(\mathrm{PT})}$ is the smallest symplectic eigenvalue of the partially transposed covariance matrix [AI07, eq. 82].

In this case, it is clear how to extend the definition of the logarithmic negativity in order to obtain different negative values for different separable states. We simply define

$$E_{\mathcal{N}} \equiv -\log\left(\nu_-^{(\mathrm{PT})}/\nu^{(0)}\right), \tag{C.3}$$

irrespective of whether $\nu_-^{(\mathrm{PT})} < \nu^{(0)}$ or not.

For $\nu_-^{(\mathrm{PT})} < \nu^{(0)}$, the state is entangled and (C.3) yields the same (positive) values as the standard definition. For $\nu_-^{(\mathrm{PT})} > \nu^{(0)}$, on the other hand, the state is separable and (C.3) yields negative values while the standard definition (C.1) yields 0.

C.1.2 *Multi-mode case*

If we take several mechanical modes into account in our evaluation and/or if we consider a two-sideband evaluation, then the resulting covariance matrix comprises more than two (light) modes. In this case, an ambiguity arises when we try to modify the definition (C.1) to allow for negative values for separable states in analogy to (C.3).

In the single-mode case, at most one of the $\nu_k^{(\mathrm{PT})}$ can drop below the shot noise variance $\nu^{(0)}$. This allows us to modify the definition of the logarithmic negativity in a natural way: We simply let the logarithmic negativity "track" $\nu_-^{(\mathrm{PT})}$ (the smallest symplectic eigenvalue of the partially transposed covariance matrix), irrespective of whether $\nu_-^{(\mathrm{PT})} < \nu^{(0)}$ or not.

For more than two light modes, however, there may be several $\nu_k^{(\mathrm{PT})}$ for which $\nu_k^{(\mathrm{PT})} < \nu^{(0)}$. But, if several symplectic eigenvalues could potentially contribute to entanglement: Which subset of symplectic

eigenvalues should we track when no entanglement is present? I.e., what is the best choice for the index set K in the following definition?

$$E_{\mathcal{N}} \equiv \begin{cases} -\sum_k \log\left(\nu_k^{(\mathrm{PT})}/\nu^{(0)}\right), & \text{for } k:\ \nu_k^{(\mathrm{PT})} < \nu^{(0)}, \\ -\sum_{k\in K} \log\left(\nu_k^{(\mathrm{PT})}/\nu^{(0)}\right), & \text{if all } \nu_k^{(\mathrm{PT})} \geq \nu^{(0)}. \end{cases} \tag{C.4}$$

Assuming that the $\nu_k^{(\mathrm{PT})}$ are in ascending order, two reasonable definitions could be

1. $K = \{1\}$, i.e. only the smallest symplectic eigenvalue is taken into account.
2. $K = \{1, \ldots, N/2\}$, with N the number of (light) modes. Since at most $N/2$ of the $\nu_k^{(\mathrm{PT})}$ can be below the shot noise variance [AI07, eq. 69], this means summing over all symplectic eigenvalues which could potentially contribute to entanglement.

Since we are always interested in entanglement as a function of some other parameter p (such as the pulse width Γ or the coupling g), a reasonable requirement on our definition of $E_{\mathcal{N}}$ is that $E_{\mathcal{N}}$ should be continuous across zero as a function of p for the quantum states we are interested in. Continuity of $E_{\mathcal{N}}(p)$ depends on the number of symplectic eigenvalues which contribute to the entanglement (for those values of p which yield entanglement): If only one symplectic eigenvalue contributes, then definition 1 above will yield continuous curves. If more than one symplectic eigenvalues contribute, then definition 1 will not yield continuous curves but definition 2 or some other definition might.

In our case, simulations show that only one symplectic eigenvalue contributes. Hence, definition 1 is the most convenient choice for us. Figure C.1 illustrates this for the case of a two-mode simulation. Therefore, we define the logarithmic negativity as follows:

$$E_{\mathcal{N}} \equiv \begin{cases} -\sum_k \log\left(\nu_k^{(\mathrm{PT})}/\nu^{(0)}\right), & \text{for } k:\ \nu_k^{(\mathrm{PT})} < \nu^{(0)}, \\ -\log\left(\nu_-^{(\mathrm{PT})}/\nu^{(0)}\right), & \text{if all } \nu_k^{(\mathrm{PT})} \geq \nu^{(0)}. \end{cases} \tag{C.5}$$

where $\nu_-^{(\mathrm{PT})}$ is defined as the smallest symplectic eigenvalue of the partially transposed state.

C.2 MODE FUNCTIONS IN THE MULTI-MODE CASE

As explained in Section 5.6, we need to ensure that all mode-functions used in a multi-mode evaluation are orthonormal to each other. However, for any two mechanical mode frequencies ${\omega_m}^{(\mathrm{i})}$ and ${\omega_m}^{(\mathrm{j})}$, the

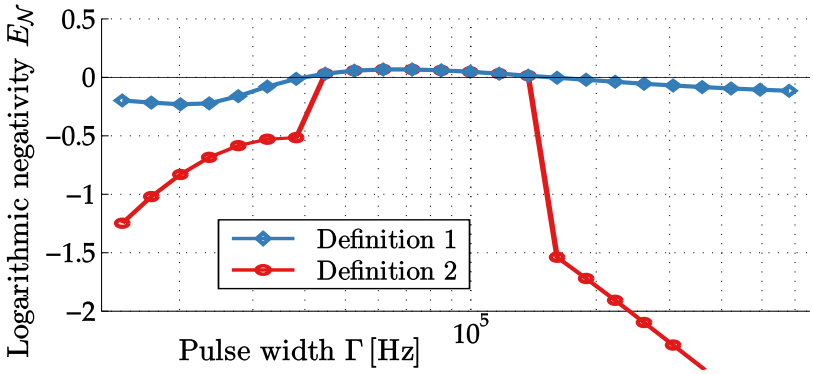

Parameters: with optical noise, $\omega_{m1} = 2\pi \times 920\,\text{kHz}$, $\omega_{m2} = 1.4 \times \omega_{m1}$, $\kappa \simeq 2.73 \times \omega_{m1}$, $g \simeq 0.30 \times \omega_{m1}$, $Q = 5 \times 10^6$, $T = 5\,\text{K}$.

Figure C.1. Comparison of two different definitions of the logarithmic negativity $E_{\mathcal{N}}$ (discussed in the main text) in a two-mode simulation. For pulse widths Γ for which entanglement is present, the two definitions agree. If no entanglement is present, they differ markedly. Definition 1 (blue, diamond markers) relies on only the smallest symplectic eigenvalue of the partially transposed covariance matrix and yields an entanglement curve which is continuous across zero. Definition 2 (red, circle markers) takes the smallest $N/2$ symplectic eigenvalues into account and yields discontinuous behavior across zero.

ideal mode functions $\tilde{\alpha}^{(i)}(t)$ and $\tilde{\alpha}^{(j)}(t)$ for the entangling pulse, defined by

$$\tilde{\alpha}^{(i)}(t) \equiv \exp\left(i\omega_{mi}t\right) \times \exp\left(\Gamma_i t\right) \text{ (for } t \leq 0\text{)}\,, \tag{C.6}$$

are not orthogonal to each other (and the same holds true for the mode functions $\tilde{\beta}^{(i)}(t)$ and $\tilde{\beta}^{(j)}(t)$ of the readout pulse). Therefore, it is clear that the orthonormalization procedure will introduce deviations from the ideal mode shape (C.6).

mode functions in time domain

Figure C.2 shows an example of two mode functions resulting from the orthonormalization. These mode functions correspond to the two-mode evaluation presented in Figure 5.6 (for the optimal pulse width $\Gamma_{\text{opt}} \simeq 40\,\text{kHz}$). The upper panel shows a mode function for the fundamental mode at $\omega_1 = 2\pi \times 920\,\text{kHz}$. This mode function is a complex harmonic oscillation with an exponentially decaying envelope, hence it has not changed due to the orthonormalization.

The lower panel shows the corresponding mode function for the next higher-order mode at $\omega_2 = 2\pi \times 1.3\,\text{MHz}$. Clearly, the envelope of the second mode function in the time domain is not a simple exponential decay anymore but is additionally modulated as a result of the orthonormalization procedure. The envelope is now of the form $(1 + \delta \sin(\omega_{\text{mod}} t + \phi)) \times \exp(-\Gamma_i t)$ with $\omega_{\text{mod}} = \omega_2 - \omega_1$.

Figure C.3 shows noise power spectra of the real and imaginary part of these two mode functions. We see that, compared with mode 1, the mode shape for mode 2 in the frequency domain is slightly altered as a result of the orthonormalization procedure (small bumps

mode functions in frequency domain

around ω_1). Nevertheless, the noise power for both mode functions is still strongly concentrated in a frequency interval of width $\Gamma_{1/2} \simeq 40\,\mathrm{kHz}$ around the central frequencies $\omega_1 = 2\pi \times 920\,\mathrm{kHz}$ and $\omega_2 = 2\pi \times 1.3\,\mathrm{MHz}$, respectively. This is reassuring, because it means that the mode functions continue to act as bandpass filters around the mechanical frequency (as desired) even after the orthonormalization.

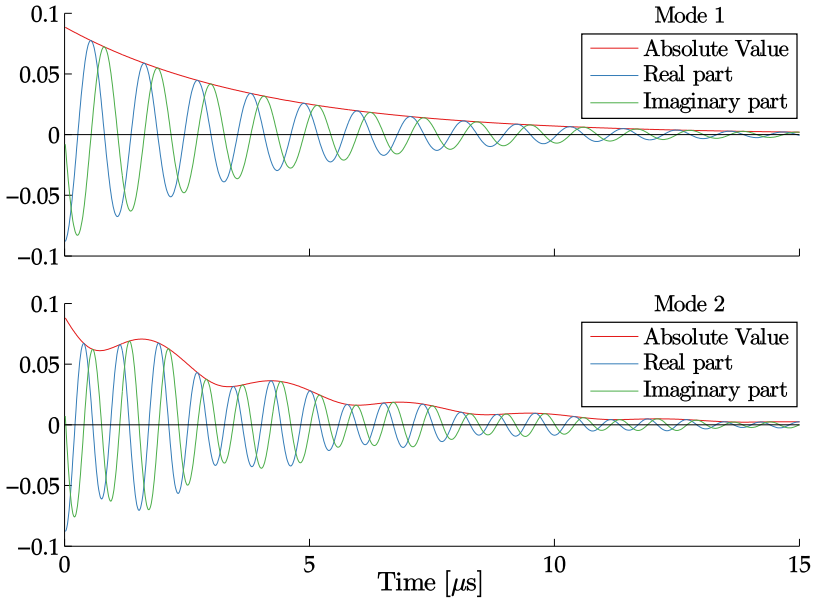

Figure C.2. Readout mode functions in a two-mode evaluation. The absolute value (red solid line) decays exponentially for mode 1 (upper panel), while, for mode 2 (lower panel), the exponential decay is modulated due to the orthonormalization. The real and imaginary parts (blue and green solid lines) oscillate at ω_1 and ω_2, respectively.

Parameters:
$\omega_1 = 2\pi \times 920\,\mathrm{kHz}$,
$\omega_2 = 2\pi \times 1.3\,\mathrm{MHz}$,
$\Gamma_{1/2} \simeq 40\,\mathrm{kHz}$.

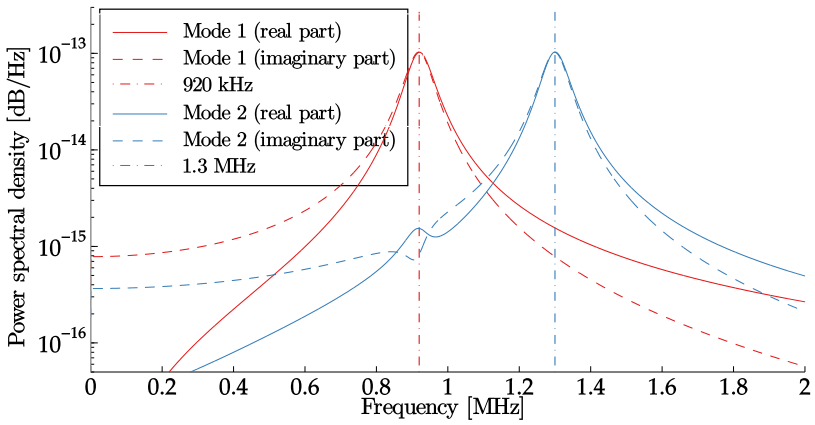

Figure C.3. Noise power spectral densities of the real and imaginary parts of the readout mode functions depicted in Figure C.2.

Parameters as in Figure C.2.

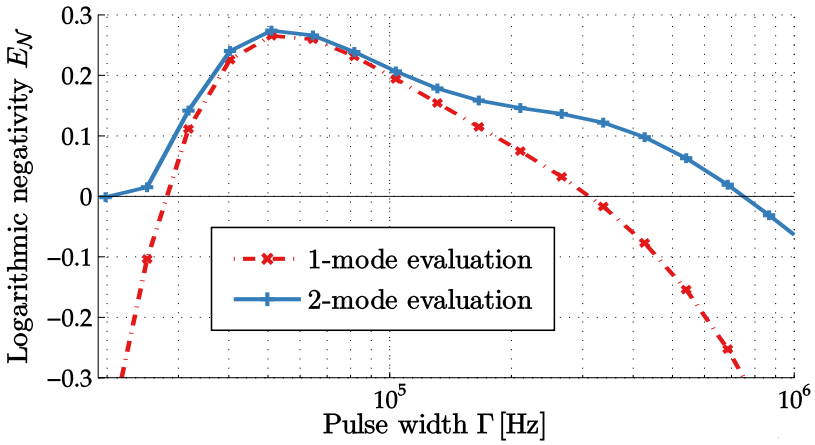

Parameters: without optical noise, $\omega_1 = 2\pi \times 920\,\mathrm{kHz}$, $\kappa \simeq 2.73 \times \omega_{m1}$, $g \simeq 0.37 \times \omega_{m1}$, $Q = 15.8 \times 10^6$, $T = 5\,\mathrm{K}$; for 2-mode eval.: $\omega_2 = 2\pi \times 1.3\,\mathrm{MHz}$.

Figure C.4. Logarithmic negativity $E_{\mathcal{N}}$ versus pulse width Γ for single- and two-mode evaluations of a single-mode simulation. The central frequency ω_1 in the single-mode evaluation (red, dashed line) corresponds to the mechanical frequency of the simulated mode. For the two-mode evaluation (blue, solid line), a second mode function at frequency ω_2 has been added (ω_2 does not correspond to any frequency of the simulation). The two-mode evaluation always yields at least as much entanglement as the single-mode evaluation (as expected) but does not significantly improve the maximally detected entanglement.

C.3 CAN MULTIMODE EVALUATIONS HURT?

Can we "go wrong" with a multimode evaluation? That is: Can we fail to detect entanglement because our evaluation assumes mechanical modes which are not present in the system we are studying?

Let us consider the example of a single-mode simulation which has (unnecessarily) been evaluated assuming two mechanical modes. Figure C.4 demonstrates that the two-mode evaluation "does not hurt": The two-mode evaluation yields values for the logarithmic negativity which are equal to or larger than the ones obtained by the single-mode evaluation. This is actually true in general because going from a multimode evaluation to a single-mode evaluation corresponds to tracing out (this is clear from the way the multimode evaluation is defined; see Section 5.6). And tracing out can only decrease the entanglement.

On the other hand, the maximum amount of entanglement which can be extracted does not increase markedly by adding the second mode in the evaluation. This can be understood as follows. Most of the correlations created in this simulation are concentrated at sideband frequencies which are very close to $\pm\omega_1 = \pm 2\pi \times 920\,\mathrm{kHz}$. Signals at these sideband frequencies are efficiently extracted by the first mode in the evaluation. But they do not contribute much to the signal extracted by the second pulse mode (with central frequencies at $\pm\omega_2 = \pm 2\pi \times 1.3\,\mathrm{MHz}$).

Note that the choice $\omega_2 = 2\pi \times 1.3\,\mathrm{MHz}$ in the two-mode evaluation is completely arbitrary; it does not correspond to any frequency in the simulation. But see Figure 5.6 for a corresponding plot where the same evaluation has been applied to a simulation with two mechanical modes at $\omega_1 = 2\pi \times 920\,\mathrm{kHz}$ and $\omega_2 = 2\pi \times 1.3\,\mathrm{MHz}$.

C.4 MODE FUNCTIONS FOR THE TWO-SIDEBAND EVALUATION

Figure C.5 depicts example mode functions for the two-sideband evaluation as defined in Section 5.8.1. The mode functions $\tilde{\alpha}_{(+)}(t)$ and $\tilde{\beta}_{(-)}(t)$ in the upper panel are the ones used in the "single-sideband protocol" (discussed before Section 5.8). The mode functions $\tilde{\alpha}_{(-)}(t)$ and $\tilde{\beta}_{(+)}(t)$ in the lower panel are the ones added in the two-sideband evaluation.

Ideally, $\tilde{\alpha}_{(-)}(t)$ and $\tilde{\beta}_{(+)}(t)$ would be defined as the complex conjugates of $\tilde{\alpha}_{(+)}(t)$ and $\tilde{\beta}_{(-)}(t)$. But, then they would not be orthonormal. The orthonormalization introduces deviations from the ideal mode shape in the form of modulations of the exponential envelope of $\tilde{\alpha}_{(-)}(t)$ and $\tilde{\beta}_{(+)}(t)$ (see lower panel). This is completely analogous to the discussion in Section C.2 for light modes corresponding to multiple mechanical modes.

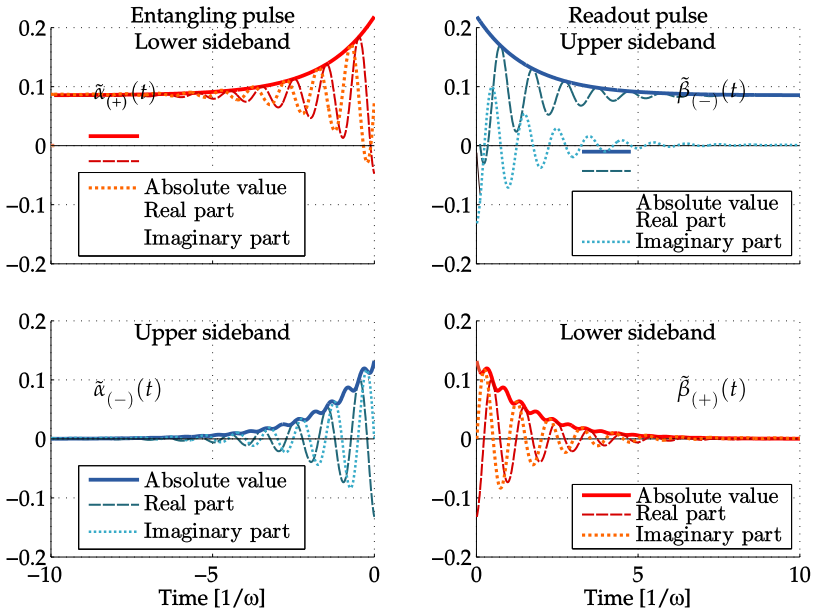

Figure C.5. Time domain plots of the mode functions in a two-sideband evaluation. Left are the mode functions for the first pulse (entangling pulse), right for the second pulse (readout pulse). The upper panels show the mode functions $\tilde{\alpha}_{(+)}(t)$ and $\tilde{\beta}_{(-)}(t)$ carrying most of the entanglement. $\tilde{\alpha}_{(+)}(t)$ targets the lower sideband in the first pulse, $\tilde{\beta}_{(-)}(t)$ targets the upper sideband in the second pulse. The lower panels show the mode functions $\tilde{\alpha}_{(-)}(t)$ and $\tilde{\beta}_{(+)}(t)$ which target the opposite sidebands (upper sideband in first pulse, lower sideband in second pulse).

Parameters:
$\omega = 2\pi \times 920\,\mathrm{kHz}$,
$\Gamma \simeq 0.1 \times \omega$.

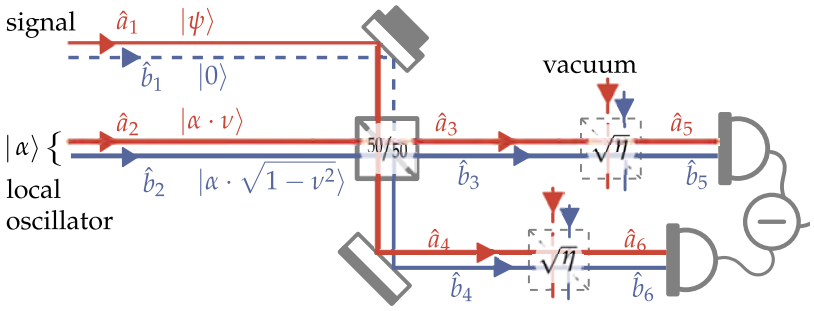

Figure C.6. Mode operator naming convention for homodyning with sub-unit visibility ν and detector efficiency η.

C.5 CORRECTION OF MEASURED COVARIANCE MATRICES FOR SUB-UNIT VISIBILITY AND DETECTOR EFFICIENCY

In the following, I expand on the discussion of the effects of sub-unit efficiency and visibility in Section 5.3.3, respectively.

Let η be the detector efficiency and ν the homodyne visibility. In our experiment, we have $\eta \simeq 95\,\%$ and, typically, $\nu \simeq 90\,\%$ due to imperfect spatial mode matching. We now consider the effect of these imperfections on homodyne detection of the state ρ_1 of signal mode $\hat{a}_1$ using a local oscillator in a coherent state $|\alpha\rangle$ with a large coherent amplitude $|\alpha| \gg 0$ (see Figure C.6 for naming conventions).

VISIBILITY Sub-unit homodyne interference visibility $\nu < 1$ means (in our case) that the signal mode and the local oscillator mode are not perfectly spatially mode-matched, i.e. these modes do not overlap fully at the 50/50-beamsplitter. To account for this effect, we need to decompose the local oscillator mode into two orthogonal spatial modes, $\hat{a}_2$ and $\hat{b}_2$ such that $\hat{a}_2$ has perfect overlap with the signal mode $\hat{a}_1$ on the 50/50-beamsplitter and $\hat{b}_2$ has zero overlap with it. Such a decomposition is always possible since it simply amounts to a projection of the spatial mode profile of the local oscillator mode onto a mode with perfect overlap with the signal mode; the remainder is then automatically orthogonal to the signal mode. For convenience, we use $\hat{b}_1$ as the label for that mode in the signal path which overlaps perfectly with the auxiliary local oscillator mode $\hat{b}_2$. Figure C.6 depicts schematically all spatial modes required to analyze the effects of visibility and efficiency. The modes $\hat{a}_i$ (depicted in red) are those which have overlap with the signal, while the modes $\hat{b}_i$ (depicted in blue) are those which have no overlap with the signal mode, hence which only contribute noise to the measurement.

Let ρ_1 be the quantum state of the signal mode $\hat{a}_1$. Since the signal is (by definition) only in mode $\hat{a}_1$, the mode $\hat{b}_1$ is actually in the vacuum state $|0\rangle$. It is easy to check that a homodyne visibility of ν implies that the states of the two local oscillator modes, $\hat{a}_2$ and $\hat{b}_2$ are

given by $|\alpha \cdot \nu\rangle$ and $|\alpha \cdot \sqrt{1-\nu^2}\rangle$, respectively (assuming the coherent amplitude of the local oscillator to be given by α).

Combining these modes on the 50/50-beamsplitter yields four new modes $\hat{a}_3, \hat{a}_4, \hat{b}_3, \hat{b}_4$ defined by:

$$\begin{pmatrix} \hat{a}_3 \\ \hat{a}_4 \end{pmatrix} = \frac{1}{\sqrt{2}} \begin{pmatrix} 1 & 1 \\ 1 & -1 \end{pmatrix} \begin{pmatrix} \hat{a}_1 \\ \hat{a}_2 \end{pmatrix}, \tag{C.7}$$

$$\begin{pmatrix} \hat{b}_3 \\ \hat{b}_4 \end{pmatrix} = \frac{1}{\sqrt{2}} \begin{pmatrix} 1 & 1 \\ 1 & -1 \end{pmatrix} \begin{pmatrix} \hat{b}_1 \\ \hat{b}_2 \end{pmatrix}. \tag{C.8}$$

EFFICIENCY The modes emerging from the 50/50-beamsplitter are sent to two photodetectors which measure the sum of the intensities in the $\hat{a}$- and $\hat{b}$-modes (there are no interference effects between these modes since they are orthogonal by definition). Since the detectors are not perfectly efficient, however, not every photon in these modes is actually detected. We can model the inefficiency by including (for each of the modes $\hat{a}_3, \hat{a}_4, \hat{b}_3, \hat{b}_4$) another beam splitter with transmissivity η before the detectors. These beam splitters model the scattering of $\sqrt{1-\eta^2}$ of the photons out of the detected mode. We can therefore define the modes $\hat{a}_5, \hat{a}_6, \hat{b}_5, \hat{b}_6$ which are actually detected as follows:

$$\hat{a}_5 = \sqrt{\eta} \cdot \hat{a}_3 + \sqrt{1-\eta} \cdot \hat{a}_{30}, \tag{C.9}$$

$$\hat{a}_6 = \sqrt{\eta} \cdot \hat{a}_4 + \sqrt{1-\eta} \cdot \hat{a}_{40}, \tag{C.10}$$

$$\hat{b}_5 = \sqrt{\eta} \cdot \hat{b}_3 + \sqrt{1-\eta} \cdot \hat{b}_{30}, \tag{C.11}$$

$$\hat{b}_6 = \sqrt{\eta} \cdot \hat{b}_4 + \sqrt{1-\eta} \cdot \hat{b}_{40}. \tag{C.12}$$

$\hat{a}_{30}, \hat{a}_{40}, \hat{b}_{30}, \hat{b}_{40}$ are vacuum modes which are mixed with the signal modes on the beam splitters which model the inefficient detection.

The photocurrent is proportional to the number difference operator

$$\hat{N}_- \equiv \left(\hat{a}_5^\dagger \hat{a}_5 + \hat{b}_5^\dagger \hat{b}_5\right) - \left(\hat{a}_6^\dagger \hat{a}_6 + \hat{b}_6^\dagger \hat{b}_6\right). \tag{C.13}$$

A lengthy but simple calculation yields the following variance of $\hat{N}_-$:

$$\langle \hat{N}_-^2 - \langle \hat{N}_- \rangle^2 \rangle = \eta \Sigma^{(o)} + \eta^2 \nu^2 \Sigma^{(sig)}, \text{ with} \tag{C.14}$$

$$\Sigma^{(sig)} \equiv \left(\alpha^2 \langle \hat{a}_1^\dagger \hat{a}_1^\dagger \rangle + (\alpha^*)^2 \langle \hat{a}_1 \hat{a}_1 \rangle + 2 |\alpha|^2 \langle \hat{a}_1^\dagger \hat{a}_1 \rangle\right) \tag{C.15}$$

$$\Sigma^{(o)} \equiv |\alpha|^2 + \langle \hat{a}_1^\dagger \hat{a}_1 \rangle \simeq |\alpha|^2, \tag{C.16}$$

where the expectation values $\langle \ldots \rangle \equiv \mathrm{tr}\,(\rho_1 \ldots)$ are with respect to the quantum state ρ_1 of the signal field. For vacuum input $\rho_1 = |0\rangle\langle 0|$, we obtain simply $\eta\Sigma^{(o)}$, hence $\Sigma^{(o)}$ is the variance we would have measured in in an ideal ($\nu = 1, \eta = 1$) shot noise measurement. With a non-vacuum signal, on the other hand, we measure $\eta\Sigma^{(o)} +$

$\eta^2\nu^2\Sigma^{(\mathrm{sig})}$, therefore $\Sigma^{(\mathrm{sig})} + \Sigma^{(\mathrm{o})}$ would have been measured for the signal in an ideal measurement.

Since our calculation of pulsed quadratures is simply a linear transformation of the measured photo-currents, the above equations are directly applicable to the sample covariance matrices of pulsed quadratures. Explicitly, we have the following relations between measured and ideal covariance matrices $\tilde{\sigma}^{(\mathrm{o})}{}_{(\mathrm{meas})}, \tilde{\sigma}^{(\mathrm{o})}{}_{(\mathrm{ideal})}$ for shot noise and $\tilde{\sigma}^{(\mathrm{sig})}{}_{(\mathrm{meas})}, \tilde{\sigma}^{(\mathrm{sig})}{}_{(\mathrm{ideal})}$ for signal measurements, respectively:

$$\tilde{\sigma}^{(\mathrm{o})}{}_{(\mathrm{meas})} = \eta\tilde{\sigma}^{(\mathrm{o})}{}_{(\mathrm{ideal})}, \tag{C.17}$$

$$\tilde{\sigma}^{(\mathrm{sig})}{}_{(\mathrm{meas})} = \eta^2\nu^2\tilde{\sigma}^{(\mathrm{sig})}{}_{(\mathrm{ideal})} + (\eta - \eta^2\nu^2)\tilde{\sigma}^{(\mathrm{o})}{}_{(\mathrm{ideal})} \tag{C.18}$$

$$= \eta^2\nu^2\tilde{\sigma}^{(\mathrm{sig})}{}_{(\mathrm{ideal})} + (1 - \eta\nu^2)\tilde{\sigma}^{(\mathrm{o})}{}_{(\mathrm{meas})}. \tag{C.19}$$

Therefore the corrections for inefficiency and visibility are given by:

$$\tilde{\sigma}^{(\mathrm{sig})}{}_{(\mathrm{ideal})} = \frac{\tilde{\sigma}^{(\mathrm{sig})}{}_{(\mathrm{meas})} - (1 - \eta\nu^2)\tilde{\sigma}^{(\mathrm{o})}{}_{(\mathrm{meas})}}{\eta^2\nu^2}, \tag{C.20}$$

$$\tilde{\sigma}^{(\mathrm{o})}{}_{(\mathrm{ideal})} = \tilde{\sigma}^{(\mathrm{o})}{}_{(\mathrm{meas})}/\eta. \tag{C.21}$$

C.6 OPTIMAL PULSE WIDTH Γ_{OPT}

In Section 5.4.2, I presented systematic single-mode studies of the dependence of the entanglement on two key parameters, the optomechanical coupling g and the mechanical quality factor Q. For the plots presented in Section 5.4.2, I optimized the logarithmic negativity $E_{\mathcal{N}}$ with respect to the pulse width Γ. Below, I provide contour plots which show how the pulse width Γ_{opt}, for which the maximum amount of logarithmic negativity is detected, depends on g and Q.

C.6.1 *Without optical noise*

Figure C.7a shows the optimal pulse width Γ_{opt} for a single mechanical mode at $\omega_m = 2\pi \times 920\,\mathrm{kHz}$ without optical noise (Figure 5.5a shows the corresponding values of logarithmic negativity). Almost everywhere, Γ_{opt} decreases with increasing mechanical quality factor Q. This makes sense because entanglement is only expected for pulse widths larger than the mechanical decoherence rate $\bar{n}\gamma \propto 1/Q$. If Q increases, mechanical decoherence decreases and the pulses can become longer in time and, correspondingly, narrower in the frequency domain.

Γ_{opt} decreases with Q

On the other hand, the optimal pulse width increases with increasing coupling g. This also makes senses, since there is an upper limit of roughly g^2/κ for the pulse widths for which entanglement can still be detected. Hence, the upper limit on the Γ-values suitable for entanglement detection increases with g.

Γ_{opt} increases with g

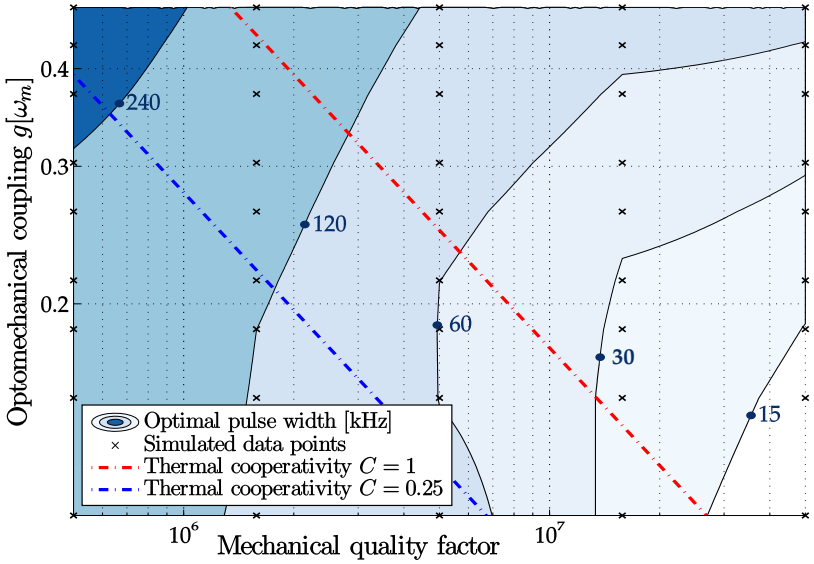

(a) Optimal pulse width Γ_{opt} (in kHz) versus quality factor Q and optical input power P_{in} for single-mode simulations *without optical noise*. The corresponding amount of entanglement is shown in Figure 5.5a.

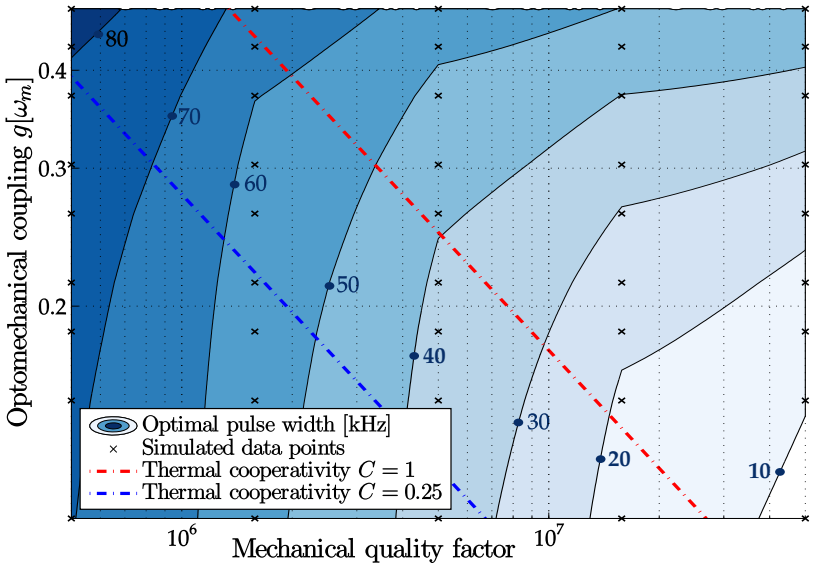

(b) Optimal pulse width Γ_{opt} (in kHz) versus quality factor Q and optical input power P_{in} for single-mode simulations *with optical noise* as measured for our setup. The corresponding amount of entanglement is shown in Figure 5.5b.

Figure C.7. Optimal pulse width Γ_{opt} (in kHz) versus quality factor Q and optical input power P_{in} for single-mode simulations with optical noise (Figure C.7b) and without it (Figure C.7a). Crosses mark the parameters which were simulated. For these parameters, the pulse width Γ has been optimized with respect to the logarithmic negativity. In between these parameters, values for the optimal pulse width Γ_{opt} were interpolated linearly.

Parameters:
$\omega_m = 2\pi \times 920\,\text{kHz}$,
$\kappa \simeq 2.73 \times \omega_m$,
$g_0 = 65 \times 10^{-6} \times \omega_m$,
$T = 5\,\text{K}$.

C.6.2 *Including optical noise*

Γ_{opt} decreases with Q and increases with g

Figure C.7b shows the same plot for an analogous simulation including optical noise. The general trend of decreasing Γ_{opt} for increasing quality factor is the same as for the noise-free case. Also the increase of Γ_{opt} with increasing coupling is similar to the noise-free case.

better signal-to-noise for narrower pulses

The main difference to the noise-free case is that, for all parameters considered here, the optimal pulse widths are significantly smaller (by around a factor of two). This is because for pulses which are broader (in frequency space) the signal to noise ratio is worse: they collect more optical noise (which is broad-band) compared to mechanical signal (which is comparatively narrow-band). In the presence of noise, pulses which are more well-defined in frequency space (longer in the time domain) are therefore advantageous.

C.7 AUTOCORRELATION OF PULSE QUADRATURES

In Section 5.9.2, I discussed the role of the autocorrelation time of the pulse quadratures in determining the minimum required measurement time for our experiment. In this section, I provide some additional information regarding the dependence of the autocorrelation time of the pulse quadratures on the mechanical coherence time and on the detuning of the laser drive.

[53] defined as $1/e$-time of the autocorrelation fct.

Figure C.8 shows the autocorrelation time[53] of pulse quadratures as a function of mechanical quality factor in resonant single-mode simulations (for different optical input powers). The plot shows that the autocorrelation time is roughly proportional to the mechanical quality factor. If measured in mechanical periods, the autocorrelation time is on the order of the mechanical quality factor. In other words, the autocorrelation time of the pulse quadratures is on the order of the inverse mechanical line width.

resonant case: autocorrelation time roughly equal to inverse mechanical line width

Since the mechanical line width can be increased drastically via optical damping, we expect to see a drastic reduction in the autocorrelation time of the pulse quadratures for a red-detuned drive. This is demonstrated in Figure C.9, where autocorrelation functions of pulse quadratures are shown side-by-side for the resonant and the detuned case. In stark contrast to the resonant case, the pulse quadratures are all essentially delta-correlated for a red-detuned drive.

reduced autocorrelation due to optical damping

In fact, for the considered parameters ($Q \in [5\times10^5, \ldots, 5\times10^7]$ and $P_{\mathrm{in}} \in [2.5\,\mu\mathrm{W}, \ldots, 50\,\mu\mathrm{W}]$), detuned simulations yield delta-correlated pulse quadratures. Hence, the corresponding autocorrelation time is smaller than the duration of one pulse pair, in this case 1×10^4 mechanical periods. Contrasting this with autocorrelation times as large as 3×10^7 mechanical periods in the resonant case, we conclude that the red-detuning (by $2\pi\times200\,\mathrm{kHz}$) yields a suppression of the

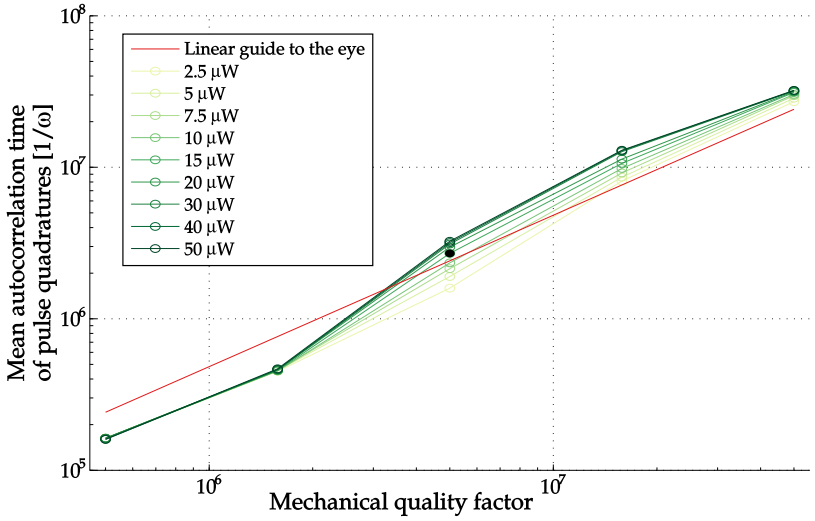

Figure C.8. Mean autocorrelation time of pulse quadratures for single-mode simulations with a resonant drive as a function of mechanical quality factor. The different curves correspond to different values of the optical input power (with darker colors corresponding to higher input powers). The autocorrelation times have been extracted from single-mode simulations by estimating the $1/e$-time for the autocorrelation function. Figure C.9 shows exemplary autocorrelation functions of pulse quadratures for $Q = 5 \times 10^6$ and $P_{\mathrm{in}} = 15\,\mu\mathrm{W}$ (these parameters are marked with a black dot in the current plot). As expected, the autocorrelation time of the pulse quadratures (measured in mechanical periods) is roughly given by the mechanical quality factor.

Parameters:
with optical noise,
$\omega_m = 2\pi \times 0.92\,\mathrm{MHz}$,
$\kappa \simeq 2.73 \times \omega_m$,
$g_0 \simeq 71 \times 10^{-6} \times \omega_m$,
$P_{\mathrm{in}} = [2.5, \ldots, 50]\,\mu\mathrm{W}$,
$g \propto \sqrt{P_{\mathrm{in}}} \simeq$
$[0.1, \ldots, 0.48] \times \omega_m$,
$Q = 5 \cdot [10^5, \ldots, 10^7]$,
$\Delta = 0\,\mathrm{kHz}$, $T = 5\,\mathrm{K}$;
for the evaluation:
$\Gamma \simeq 82\,\mathrm{kHz}$.

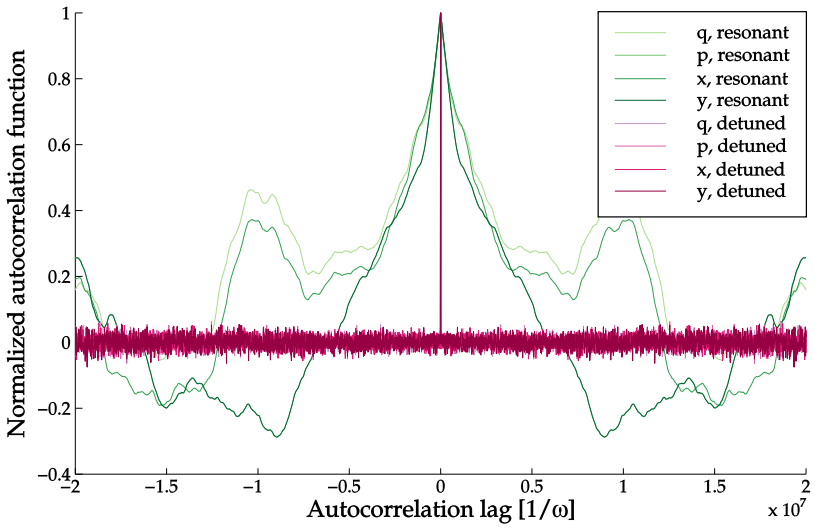

Figure C.9. Normalized autocorrelation function of pulse quadratures for resonant (greenish lines) and red-detuned (red-purplish lines) single-mode simulations. The mechanical quality factor was $Q = 5 \times 10^6$ in both cases. The resonant simulation corresponds to the one marked with a black dot in Figure C.8.

Parameters:
with optical noise,
$\omega_m = 2\pi \times 0.92\,\mathrm{MHz}$,
$\kappa \simeq 2.73 \times \omega_m$,
$g \simeq 0.26 \times \omega_m$,
$\Delta = 2\pi \times [0, 200]\,\mathrm{kHz}$,
$Q = 5 \times 10^6$, $T = 5\,\mathrm{K}$.

autocorrelation time by at least 3 orders of magnitude. This is consistent with the assumption that autocorrelation times are essentially given by the inverse mechanical line width since the latter is roughly 4 orders of magnitude smaller for the red-detuned case considered here compared to the resonant case.

This drastic decrease in autocorrelation time due to the detuned drive yields a significant decrease in the minimally required measurement time, as discussed in Section 5.9.2.

C.8 DETUNED MULTI-MODE SIMULATIONS

Figure C.10 shows the effect of moderate red-detuning on entanglement in a multi-mode situation with 45 modes. For narrow pulse widths (on the order of 10 kHz), the detuning seems to shift the entanglement curve upwards. This is consistent with the results from two-mode simulations presented in Section 5.9.3. For increasing pulse width, however, the covariance matrices for the detuned simulation fail to be physical and it becomes unclear up to which pulse width the entanglement curve for the detuned case can be trusted. We currently do not understand the reason for this "loss of physicality" in the detuned multi-mode case. In particular, it is unclear whether this is a contingent feature of this specific simulation or a general effect. The fact that, in two-mode simulations, covariance matrices were always physical in the detuned case gives hope that there is no in-principle problem with detuning in a multi-mode setting.

C.9 COMPARISON OF DIFFERENT NOISE MODELS

In the simulations presented in this thesis, I explored the possibility of entanglement detection both with and without optical noise. The noise model used in these simulations is based on the noise measurements for our setup described in Section 3.1.3 and Section 3.1.4. Here, I want to briefly touch upon the following two questions with respect to the role of the optical noise:

1. How sensitive are our results with respect to the noise model?
2. How much could we improve our results by improving the optical noise?

I cannot answer these questions systematically but want to at least discuss them for one specific example. Figure C.11 shows results from two-mode simulations for different models of the laser noise and for the noise-free case.

The different noise models are based on the measurements described in Section 3.1.3 and Section 3.1.4. Taking these measurements

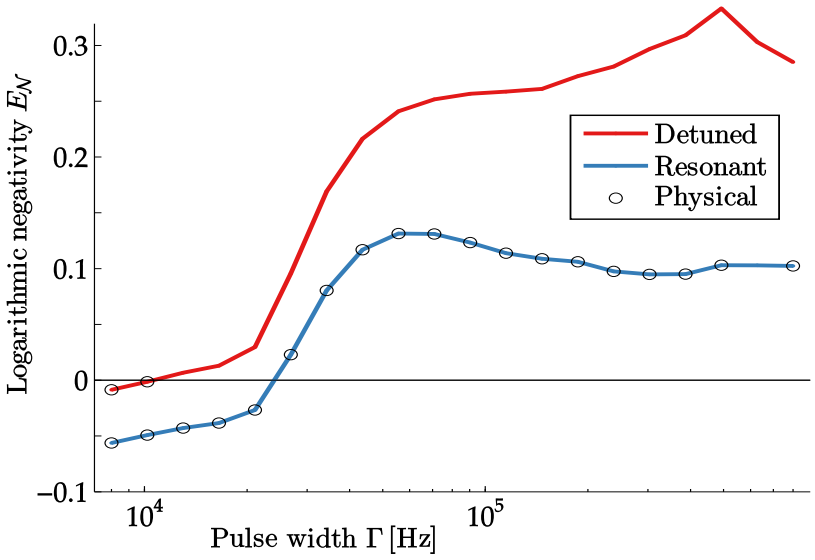

Figure C.10. Logarithmic negativity $E_{\mathcal{N}}$ versus pulse width Γ for a simulation of the first 45 modes of a SiN membrane of roughly 490 µm side length. Plotted are the results of a two-sideband evaluation of a simulation with a resonant drive (blue solid line; same as in Figure 5.14) and a simulation with a 200 kHz red-detuned drive (red solid line). For the resonant simulation, almost all pulse widths considered in the evaluation yield physical covariance matrices (marked by circle markers in the plot). For the detuned simulation, on the other hand, only two out of twenty pulse widths lead to physical covariance matrices. Note that both curves result from a two-sideband evaluation.

Parameters:
with optical noise,
$\Delta = 2\pi \times [0, 200]$ kHz,
$\omega_1 = 2\pi \times 800$ kHz,
$\omega_{2,\ldots,45}/(2\pi \cdot \text{MHz}) \simeq \{1.26, \ldots, 4.56\}$,
$Q = 5 \times 10^6$ (all modes),
$g_1 \simeq 0.37 \times \omega_1$,
$g_{2,\ldots,45}/\omega_1 \in [7.4 \times 10^{-3}, \ldots, 0.22]$
$\kappa \simeq 2.73 \times \omega_1$,
$P_{\text{in}} = 20\,\mu\text{W}$, $T = 5\,\text{K}$.

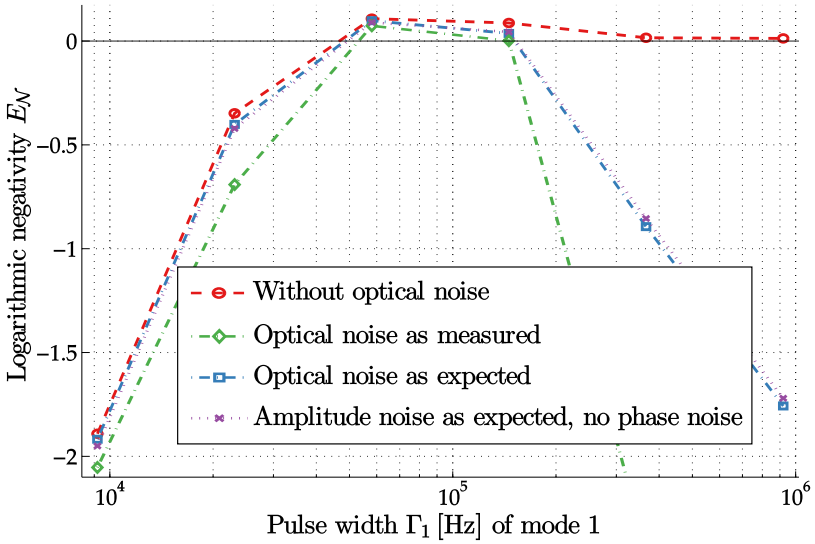

Figure C.11. Logarithmic negativity $E_{\mathcal{N}}$ versus pulse width Γ for a two-mode simulation using different models for the optical noise. The assumptions behind the different noise models are explained in the main text. Note that, in this plot, only the pulse width Γ_1 of mode 1 is varied; the pulse width for mode 2 is kept fixed at its optimum value $\Gamma_2 \simeq 58$ kHz. The evaluations presented here are single-sideband evaluations.

Parameters:
with optical noise,
$\omega_1 = 2\pi \times 920$ kHz,
$\omega_2 = 1.4 \times \omega_1$,
$Q_1 = Q_2 = 5 \times 10^6$,
$g_{0_1} = g_{0_2} = 2\pi \times 65$ Hz,
$g_1 = g_2 \simeq 0.31 \times \omega_1$,
$\kappa \simeq 2.73 \times \omega_1$,
$P_{\text{in}} = 20\,\mu\text{W}$, $T = 5\,\text{K}$.

measured versus expected laser noise

at face value yields the curve labeled "optical noise as measured" (green, diamond marker). This is the worst case scenario. As discussed in Section 3.1.4, we have good reasons to believe, that in the noise measurements (with the high-finesse filter cavity operated in the double pass configuration) the actual laser noise drops below the noise floor of the noise measurement itself. By assuming that the filter cavity actually yields the expected performance in double pass and applying that filter performance to the single-pass noise measurements we arrive at a significantly more optimistic noise model which yields the curves labeled "optical noise as expected" (blue, diamond markers).

sensitivity to the noise model

These two significantly different noise models (and their corresponding entanglement curves) provide a preliminary answer to question 1: How sensitive are our results to how exactly we model the optical noise? We see in Figure C.11 that the curves resulting from "noise as expected" and "noise as measured" differ significantly. As expected, the more conservative noise model ("as measured"), which is the one used throughout this thesis, performs worse than the model with "noise as expected". More importantly, however, the maximum of the entanglement is relatively similar in both cases. This suggests that our choice of noise model is benign in the sense of being conservative but not overly pessimistic.

amplitude versus phase noise

Figure C.11 also shows another curve labeled "amplitude noise as expected, no phase noise" (purple, cross markers). The noise model behind this curve is the same as "optical noise as expected" but with phase noise completely switched off. Quite surprisingly, the resulting entanglement curve is not significantly better than the curve for "optical noise as expected". But both curves are significantly worse than the curve resulting from a noise-free simulation (red, circle markers). This suggests the following preliminary answer to question 2: If our expectation regarding the phase noise (as encoded in the "optical noise as expected"-model) are correct, then we are not limited by phase noise, but only by amplitude noise. Furthermore, by eliminating the amplitude noise, we could significantly improve the entanglement.

BIBLIOGRAPHY

[Abd+11] M. Abdi, Sh. Barzanjeh, P. Tombesi, and D. Vitali. "Effect of phase noise on the generation of stationary entanglement in cavity optomechanics." In: *Phys. Rev. A* 84.3 (Sept. 19, 2011), p. 032325. DOI: 10.1103/PhysRevA.84.032325 (cit. on p. 27).

[AI07] Gerardo Adesso and Fabrizio Illuminati. "Entanglement in continuous-variable systems: recent advances and current perspectives." In: *Journal of Physics A: Mathematical and Theoretical* 40.28 (2007), pp. 7821–7880 (cit. on pp. 99, 104, 129, 183–185).

[AKM14] Markus Aspelmeyer, Tobias J. Kippenberg, and Florian Marquardt. "Cavity optomechanics." In: *Rev. Mod. Phys.* 86.4 (Dec. 30, 2014), pp. 1391–1452. DOI: 10.1103/RevModPhys.86.1391 (cit. on pp. 1, 3, 4, 7, 12, 16, 18–21).

[Bel80] VP Belavkin. "Optimal filtering of Markov signals with quantum white noise." In: *Radio Eng Electron Physics* 25 (1980), pp. 1445–1453 (cit. on p. 78).

[Bia14] Ciro Biancofiore. "Cavity Optomechanics with Membranes in Optical Resonators." PhD thesis. SCHOOL OF ADVANCED STUDIES-Doctoral course in Physics (XXVI cycle), 2014 (cit. on p. 7).

[Bie+09] F. Bielsa, A. Dupays, M. Fouché, R. Battesti, C. Robilliard, and C. Rizzo. "Birefringence of interferential mirrors at normal incidence." In: *Appl. Phys. B* 97.2 (Aug. 6, 2009), pp. 457–463. DOI: 10.1007/s00340-009-3677-7 (cit. on p. 15).

[BTD01] Joshua C. Bienfang, Russell F. Teehan, and Craig A. Denman. "Phase noise transfer in resonant optical cavities." In: *Review of Scientific Instruments* 72 (Aug. 2001), pp. 3208–3214. DOI: 10.1063/1.1387251 (cit. on p. 36).

[Bla01] Eric D. Black. "An introduction to Pound–Drever–Hall laser frequency stabilization." In: *American Journal of Physics* 69.1 (2001), p. 79. DOI: 10.1119/1.1286663 (cit. on p. 46).

[Böh07] Hannes René Böhm. "Radiation-pressure cooling of a mechanical oscillator." PhD thesis. Vienna, 2007 (cit. on pp. 32, 43, 45, 48).

[BJK97] S. Bose, K. Jacobs, and P. L. Knight. "Preparation of nonclassical states in cavities with a moving mirror." In: *Physical Review A* 56.5 (1997), p. 4175 (cit. on p. 4).

[BM67] V. B. Braginski and A. B. Manukin. "Ponderomotive effects of electromagnetic radiation." In: *Sov. Phys.—JETP* 25 (1967), p. 653 (cit. on p. 3).

[BMT70] V. B. Braginskii, Anatoli B. Manukin, and M. Yu Tikhonov. "Investigation of dissipative ponderomotive effects of electromagnetic radiation." In: *Soviet Journal of Experimental and Theoretical Physics* 31 (1970), p. 829 (cit. on p. 3).

[Bre+08] Ferdinand Brennecke, Stephan Ritter, Tobias Donner, and Tilman Esslinger. "Cavity Optomechanics with a Bose-Einstein Condensate." In: *Science* 322.5899 (Oct. 10, 2008), pp. 235–238. DOI: 10.1126/science.1163218 (cit. on p. 91).

[Bri+03] T. Briant, P.F. Cohadon, M. Pinard, and A. Heidmann. "Optical phase-space reconstruction of mirror motion at the attometer level." In: *The European Physical Journal D - Atomic, Molecular and Optical Physics* 22.1 (Jan. 1, 2003), pp. 131–140. DOI: 10.1140/epjd/e2002-00217-9 (cit. on pp. 89–91).

[Bro99] Oliver Sascha Brozek. "Frequenzstabilisierung eines Nd:YAG-Hochleistungs-Laser-Systems für den Gravitationswellendetektor GEO 600." PhD thesis. Hannover: Hannover, 1999 (cit. on p. 31).

[Bye88] Robert L. Byer. "Diode Laser—Pumped Solid-State Lasers." In: *Science* 239.4841 (Feb. 12, 1988), pp. 742–747. DOI: 10.1126/science.239.4841.742 (cit. on p. 30).

[CW51] Herbert B. Callen and Theodore A. Welton. "Irreversibility and generalized noise." In: *Physical Review* 83.1 (1951), pp. 34–40 (cit. on p. 9).

[Cav80] Carlton M. Caves. "Quantum-Mechanical Radiation-Pressure Fluctuations in an Interferometer." In: *Phys. Rev. Lett.* 45.2 (July 14, 1980), pp. 75–79. DOI: 10.1103/PhysRevLett.45.75 (cit. on p. 3).

[Cha+14] S. Chakram, Y. S. Patil, L. Chang, and M. Vengalattore. "Dissipation in Ultrahigh Quality Factor SiN Membrane Resonators." In: *Phys. Rev. Lett.* 112.12 (Mar. 24, 2014), p. 127201. DOI: 10.1103/PhysRevLett.112.127201 (cit. on pp. 55, 57, 112).

[Cha+11] Jasper Chan, T. P. Mayer Alegre, Amir H. Safavi-Naeini, Jeff T. Hill, Alex Krause, Simon Gröblacher, Markus Aspelmeyer, and Oskar Painter. "Laser cooling of a nanomechanical oscillator into its quantum ground state." In: *Nature* 478.7367 (Oct. 5, 2011), pp. 89–92. DOI: 10.1038/nature10461 (cit. on p. 1).

[CK91] E. A. P. Cheng and T. J. Kane. "High-power single-mode diode-pumped Nd: YAG laser using a monolithic nonplanar ring resonator." In: *Optics letters* 16.7 (1991), pp. 478–480 (cit. on p. 31).

[Cle+10] A. A. Clerk, M. H. Devoret, S. M. Girvin, Florian Marquardt, and R. J. Schoelkopf. "Introduction to quantum noise, measurement, and amplification." In: *Reviews of Modern Physics* 82.2 (Apr. 2010), pp. 1155–1208. DOI: 10.1103/RevModPhys.82.1155 (cit. on p. 164).

[CHP99] P. F. Cohadon, A. Heidmann, and M. Pinard. "Cooling of a Mirror by Radiation Pressure." In: *Phys. Rev. Lett.* 83.16 (Oct. 18, 1999), pp. 3174–3177. DOI: 10.1103/PhysRevLett.83.3174 (cit. on pp. 4, 91).

[Col+14] Garrett D. Cole et al. "Tensile-strained InxGa1-xP membranes for cavity optomechanics." In: *Applied Physics Letters* 104.20 (May 19, 2014), p. 201908. DOI: 10.1063/1.4879755 (cit. on pp. 54, 112).

[Dor+83] A. Dorsel, J. D. McCullen, P. Meystre, E. Vignes, and H. Walther. "Optical Bistability and Mirror Confinement Induced by Radiation Pressure." In: *Phys. Rev. Lett.* 51.17 (Oct. 24, 1983), pp. 1550–1553. DOI: 10.1103/PhysRevLett.51.1550 (cit. on pp. 4, 24).

[Dre+83a] R. W. P. Drever, G. M. Ford, J. Hough, I. M. Kerr, A. J. Munley, J. R. Pugh, N. A. Robertson, and H. Ward. "A gravity-wave detector using optical cavity sensing." In: *General Relativity and Gravitation 1980*. Vol. 1. 1983, p. 265 (cit. on p. 46).

[Dre+83b] R. W. P. Drever, John L. Hall, F. V. Kowalski, J. Hough, G. M. Ford, A. J. Munley, and H. Ward. "Laser phase and frequency stabilization using an optical resonator." In: *Applied Physics B* 31.2 (1983), pp. 97–105 (cit. on p. 46).

[Ein09] Albert Einstein. "On the Development of Our Views Concerning the Nature and Constitution of Radiation (Deutsche Physikalische Gesellschaft, Verhandlungen 7, 1909, pp. 482-500, and Physikalische Zeitschrift, vol. 10, 1909, pp. 817-826)." In: *The Collected Papers of Albert Einstein, trans.*

Anna Beck and Peter Havas 2 (1909), pp. 1900–1909 (cit. on p. 3).

[FM01] Lee Samuel Finn and Soma Mukherjee. "Data conditioning for gravitational wave detectors: A Kalman filter for regressing suspension violin modes." In: *Phys. Rev. D* 63.6 (Feb. 23, 2001), p. 062004. DOI: 10.1103/PhysRevD.63.062004 (cit. on p. 77).

[Fre+93] I. Freitag, I. Kröpke, A. Tünnerman, and H. Welling. "Electrooptically fast tunable miniature diode-pumped Nd:YAG ring laser." In: *Optics Communications* 101.5 (Sept. 1, 1993), pp. 371–376. DOI: 10.1016/0030-4018(93)90732-K (cit. on p. 31).

[FTW95] I Freitag, A Tünnermann, and H Welling. "Power scaling of diode-pumped monolithic Nd:YAG lasers to output powers of several watts." In: *Optics Communications* 115.5 (Apr. 1, 1995), pp. 511–515. DOI: 10.1016/0030-4018(95)00020-9 (cit. on p. 31).

[GC85] C. W. Gardiner and M. J. Collett. "Input and output in damped quantum systems: Quantum stochastic differential equations and the master equation." In: *Phys. Rev. A* 31.6 (June 1, 1985), pp. 3761–3774. DOI: 10.1103/PhysRevA.31.3761 (cit. on p. 18).

[Gmb03] InnoLight GmbH. *Prometheus Product Line - User's Manual*. Version 4.5. Hannover, Germany.: InnoLight, Oct. 30, 2003 (cit. on p. 31).

[GA10] M.S. Grewal and A.P. Andrews. "Applications of Kalman Filtering in Aerospace 1960 to the Present [Historical Perspectives]." In: *IEEE Control Systems* 30.3 (June 2010), pp. 69–78. DOI: 10.1109/MCS.2010.936465 (cit. on p. 77).

[Grö+08] S. Gröblacher, S. Gigan, H. R. Böhm, A. Zeilinger, and M. Aspelmeyer. "Radiation-pressure self-cooling of a micromirror in a cryogenic environment." In: *EPL (Europhysics Letters)* 81.5 (Mar. 2008), p. 54003. DOI: 10.1209/0295-5075/81/54003 (cit. on p. 131).

[Grö10] Simon Gröblacher. "Quantum opto-mechanics with micromirrors." PhD thesis. Vienna: Vienna, 2010 (cit. on pp. 16, 44, 46, 47, 51).

[Grö+09a] Simon Gröblacher, Klemens Hammerer, Michael R. Vanner, and Markus Aspelmeyer. "Observation of strong coupling between a micromechanical resonator and an optical cavity field." In: *Nature* 460.7256 (Aug. 6, 2009), pp. 724–727. DOI: 10.1038/nature08171 (cit. on p. 1).

[Grö+09b] Simon Gröblacher, Jared B. Hertzberg, Michael R. Vanner, Garrett D. Cole, Sylvain Gigan, K. C. Schwab, and Markus Aspelmeyer. "Demonstration of an ultracold micro-optomechanical oscillator in a cryogenic cavity." In: *Nature Physics* 5.7 (June 7, 2009), pp. 485–488. DOI: 10.1038/nphys1301 (cit. on p. 38).

[Had+99] Y Hadjar, P. F Cohadon, C. G Aminoff, M Pinard, and A Heidmann. "High-sensitivity optical measurement of mechanical Brownian motion." In: *Europhysics Letters (EPL)* 47.5 (Sept. 1, 1999), pp. 545–551. DOI: 10.1209/epl/i1999-00422-6 (cit. on pp. 4, 91).

[HR05] Jan Hald and Valentina Ruseva. "Efficient suppression of diode-laser phase noise by optical filtering." In: *JOSA B* 22.11 (2005), pp. 2338–2344 (cit. on p. 32).

[HC80] T. W. Hansch and B. Couillaud. "Laser frequency stabilization by polarization spectroscopy of a reflecting reference cavity." In: *Optics Communications* 35.3 (Dec. 1, 1980), pp. 441–444. DOI: 10.1016/0030-4018(80)90069-3 (cit. on p. 46).

[Hei04] Ferdinand van der Heijden. *Classification, parameter estimation, and state estimation: an engineering approach using MATLAB*. Chichester, West Sussex, Eng.; Hoboken, NJ: Wiley, 2004 (cit. on p. 85).

[Heu+04] Michèle Heurs, Volker M. Quetschke, Benno Willke, Karsten Danzmann, and Ingo Freitag. "Simultaneously suppressing frequency and intensity noise in a Nd:YAG nonplanar ring oscillator by means of the current-lock technique." In: *Optics Letters* 29.18 (2004), p. 2148. DOI: 10.1364/OL.29.002148 (cit. on p. 31).

[Hof15] Sebastian G. Hofer. "Quantum Control of Optomechanical Systems." PhD thesis. Vienna: Vienna, 2015 (cit. on pp. 7, 12, 16, 24, 25, 27, 93).

[HH15] Sebastian G. Hofer and Klemens Hammerer. "Entanglement-enhanced time-continuous quantum control in optomechanics." In: *Phys. Rev. A* 91.3 (Mar. 17, 2015), p. 033822. DOI: 10.1103/PhysRevA.91.033822 (cit. on pp. 1, 5, 90, 91).

[Hof+13] Sebastian G. Hofer, Denis V. Vasilyev, Markus Aspelmeyer, and Klemens Hammerer. "Time-Continuous Bell Measurements." In: *Phys. Rev. Lett.* 111.17 (Oct. 22, 2013), p. 170404. DOI: 10.1103/PhysRevLett.111.170404 (cit. on pp. 1, 5).

[Hof+11] Sebastian G. Hofer, Witlef Wieczorek, Markus Aspelmeyer, and Klemens Hammerer. "Quantum entanglement and teleportation in pulsed cavity optomechanics." In: *Phys. Rev. A* 84.5 (Nov. 2011). DOI: 10.1103/PhysRevA.84.052327 (cit. on pp. 1, 4, 94, 95, 116, 154).

[17] *Jacobi–Anger expansion*. In: *Wikipedia*. Page Version ID: 764050877. Feb. 6, 2017 (cit. on p. 180).

[Jay+08] A. M. Jayich, J. C. Sankey, B. M. Zwickl, C. Yang, J. D. Thompson, S. M. Girvin, A. A. Clerk, F. Marquardt, and J. G. E. Harris. "Dispersive optomechanics: a membrane inside a cavity." In: *New J. Phys.* 10.9 (Sept. 1, 2008), p. 095008. DOI: 10.1088/1367-2630/10/9/095008 (cit. on pp. 54, 62).

[Jöc+11] Andreas Jöckel, Matthew T. Rakher, Maria Korppi, Stephan Camerer, David Hunger, Matthias Mader, and Philipp Treutlein. "Spectroscopy of mechanical dissipation in micromechanical membranes." In: *Appl. Phys. Lett.* 99.14 (Oct. 3, 2011), p. 143109. DOI: 10.1063/1.3646914 (cit. on p. 57).

[KB61] R. E. Kalman and R. S. Bucy. "New Results in Linear Filtering and Prediction Theory." In: *J. Fluids Eng.* 83.1 (Mar. 1, 1961), pp. 95–108. DOI: 10.1115/1.3658902 (cit. on p. 76).

[Kal60] Rudolph Emil Kalman. "A new approach to linear filtering and prediction problems." In: *Journal of basic Engineering* 82.1 (1960), pp. 35–45 (cit. on p. 75).

[KB85] Thomas J. Kane and Robert L. Byer. "Monolithic, unidirectional single-mode Nd: YAG ring laser." In: *Optics Letters* 10.2 (1985), pp. 65–67 (cit. on pp. 30, 31).

[KNB87] Thomas J. Kane, Alan C. Nilsson, and Robert L. Byer. "Frequency stability and offset locking of a laser-diode-pumped Nd: YAG monolithic nonplanar ring oscillator." In: *Optics letters* 12.3 (1987), pp. 175–177 (cit. on p. 31).

[Kep19] Johannes Kepler. *De cometis libelli tres*. Augustae Vindelicorum: A. Apergerum, 1619 (cit. on p. 3).

[KL66] H. Kogelnik and Tingye Li. "Laser beams and resonators." In: *Proceedings of the IEEE* 54.10 (1966), pp. 1312–1329 (cit. on pp. 14, 15).

[Leb01] Peter Lebedew. "Untersuchungen über die Druckkräfte des Lichtes." In: *Ann. Phys.* 311.11 (Jan. 1, 1901), pp. 433–458. DOI: 10.1002/andp.19013111102 (cit. on p. 3).

[Leo97] Ulf Leonhardt. *Measuring the Quantum State of Light*. 1st ed. Cambridge University Press, July 13, 1997 (cit. on p. 102).

[MMT97] S. Mancini, V. I. Man'ko, and P. Tombesi. "Ponderomotive control of quantum macroscopic coherence." In: *Phys. Rev. A* 55.4 (Apr. 1, 1997), pp. 3042–3050. DOI: 10.1103/PhysRevA.55.3042 (cit. on p. 4).

[Mar+07] Florian Marquardt, Joe P. Chen, A. A. Clerk, and S. M. Girvin. "Quantum Theory of Cavity-Assisted Sideband Cooling of Mechanical Motion." In: *Phys. Rev. Lett.* 99.9 (Aug. 28, 2007), p. 093902. DOI: 10.1103/PhysRevLett.99.093902 (cit. on p. 131).

[Max73] James Clerk (1831-1879) Auteur du texte Maxwell. *A treatise on electricity and magnetism.* Vol. 2. ark:/12148/bpt6k95176j. Oxford: Clarendon press, 1873 (cit. on p. 3).

[MK04] Constanze Höhberger Metzger and Khaled Karrai. "Cavity cooling of a microlever." In: *Nature* 432.7020 (2004), pp. 1002–1005 (cit. on p. 131).

[Mur+08] Kater W. Murch, Kevin L. Moore, Subhadeep Gupta, and Dan M. Stamper-Kurn. "Observation of quantum-measurement backaction with an ultracold atomic gas." In: *Nat Phys* 4.7 (July 2008), pp. 561–564. DOI: 10.1038/nphys965 (cit. on pp. 3, 91).

[NH01] E. F. Nichols and G. F. Hull. "A Preliminary Communication on the Pressure of Heat and Light Radiation." In: *Phys. Rev. (Series I)* 13.5 (Nov. 1, 1901), pp. 307–320. DOI: 10.1103/PhysRevSeriesI.13.307 (cit. on p. 3).

[NMG16] R. A. Norte, J. P. Moura, and S. Gröblacher. "Mechanical Resonators for Quantum Optomechanics Experiments at Room Temperature." In: *Phys. Rev. Lett.* 116.14 (Apr. 5, 2016), p. 147202. DOI: 10.1103/PhysRevLett.116.147202 (cit. on p. 112).

[Pal+13a] T. A. Palomaki, J. W. Harlow, J. D. Teufel, R. W. Simmonds, and K. W. Lehnert. "Coherent state transfer between itinerant microwave fields and a mechanical oscillator." In: *Nature* 495.7440 (2013), pp. 210–214 (cit. on p. 115).

[Pal+13b] T. A. Palomaki, J. D. Teufel, R. W. Simmonds, and K. W. Lehnert. "Entangling Mechanical Motion with Microwave Fields." In: *Science* 342.6159 (2013), pp. 710–713 (cit. on pp. 1, 4, 94, 115, 140, 154).

[Pas] Rüdiger Paschotta. *Article on 'nonplanar ring oscillators' in the Encyclopedia of Laser Physics and Technology*. URL: https://www.rp-photonics.com/nonplanar_ring_oscillators.html (visited on 08/25/2016) (cit. on p. 30).

[Pat+06] M Paternostro, S Gigan, M S Kim, F Blaser, H R Böhm, and M Aspelmeyer. "Reconstructing the dynamics of a movable mirror in a detuned optical cavity." In: *New Journal of Physics* 8.6 (June 23, 2006), pp. 107–107. DOI: 10.1088/1367-2630/8/6/107 (cit. on p. 92).

[P+08] Kaare Brandt Petersen, Michael Syskind Pedersen, et al. "The matrix cookbook." In: *Technical University of Denmark* 7 (2008), p. 15 (cit. on pp. 75, 162).

[PHH99] Michel Pinard, Y. Hadjar, and Antoine Heidmann. "Effective mass in quantum effects of radiation pressure." In: *The European Physical Journal D-Atomic, Molecular, Optical and Plasma Physics* 7.1 (1999), pp. 107–116 (cit. on p. 23).

[Pol] Mikhail Polyanskiy. *Refractive index of Si3N4 (Silicon nitride)*. URL: https://refractiveindex.info/?shelf=main&book=Si3N4&page=Philipp (visited on 08/07/2017) (cit. on p. 22).

[PPR13] T. P. Purdy, R. W. Peterson, and C. A. Regal. "Observation of Radiation Pressure Shot Noise on a Macroscopic Object." In: *Science* 339.6121 (Feb. 15, 2013), pp. 801–804. DOI: 10.1126/science.1231282 (cit. on pp. 3, 91).

[Pur+12] T. P. Purdy, R. W. Peterson, P.-L. Yu, and C. A. Regal. "Cavity optomechanics with Si 3 N 4 membranes at cryogenic temperatures." In: *New J. Phys.* 14.11 (2012), p. 115021. DOI: 10.1088/1367-2630/14/11/115021 (cit. on p. 61).

[Pur+13] T. P. Purdy, P.-L. Yu, R. W. Peterson, N. S. Kampel, and C. A. Regal. "Strong optomechanical squeezing of light." In: *Physical Review X* 3.3 (2013), p. 031012 (cit. on p. 1).

[Que03] Volker Quetschke. "Korrelationen von Rauschquellen bei Nd:YAG Lasersystemen." PhD thesis. Hannover: Universität Hannover, 2003 (cit. on p. 31).

[RA09] P. Rabl and M. Aspelmeyer. "Phase-noise induced limitations on cooling and coherent evolution in optomechanical systems." In: *Physical Review A* 80.6 (Dec. 2009). DOI: 10.1103/PhysRevA.80.063819 (cit. on p. 38).

[Rei+16] Christoph Reinhardt, Tina Müller, Alexandre Bourassa, and Jack C. Sankey. "Ultralow-Noise SiN Trampoline Resonators for Sensing and Optomechanics." In: *Phys. Rev. X* 6.2 (Apr. 1, 2016), p. 021001. DOI: 10.1103/PhysRevX.6.021001 (cit. on p. 112).

[Rie13] Ralf Riedinger. "Optomechanical State Reconstruction and Optical Noise Reduction for Cavity Optomechanics Experiments." Master Thesis. Marburg: Marburg, 2013 (cit. on p. 172).

[Saf+13] Amir H. Safavi-Naeini, Simon Gröblacher, Jeff T. Hill, Jasper Chan, Markus Aspelmeyer, and Oskar Painter. "Squeezed light from a silicon micromechanical resonator." In: *Nature* 500.7461 (Aug. 8, 2013), pp. 185–189. DOI: 10.1038/nature12307 (cit. on p. 1).

[San+10] J. C. Sankey, C. Yang, B. M. Zwickl, A. M. Jayich, and J. G. E. Harris. "Strong and tunable nonlinear optomechanical coupling in a low-loss system." In: *Nat Phys* 6.9 (Sept. 2010), pp. 707–712. DOI: 10.1038/nphys1707 (cit. on p. 59).

[Sau90] Peter R. Saulson. "Thermal noise in mechanical experiments." In: *Phys. Rev. D* 42.8 (Oct. 15, 1990), pp. 2437–2445. DOI: 10.1103/PhysRevD.42.2437 (cit. on pp. 9–11).

[Sim00] R. Simon. "Peres-Horodecki Separability Criterion for Continuous Variable Systems." In: *Phys. Rev. Lett.* 84.12 (2000). Copyright (C) 2009 The American Physical Society; Please report any problems to prola@aps.org, p. 2726. DOI: 10.1103/PhysRevLett.84.2726 (cit. on p. 183).

[Sou+09] D. R. Southworth, R. A. Barton, S. S. Verbridge, B. Ilic, A. D. Fefferman, H. G. Craighead, and J. M. Parpia. "Stress and silicon nitride: A crack in the universal dissipation of glasses." In: *Physical review letters* 102.22 (2009), p. 225503 (cit. on pp. 54, 55, 57).

[Ste94] Robert F. Stengel. *Optimal control and estimation*. Dover books on advanced mathematics. New York: Dover Publications, 1994. 639 pp. (cit. on pp. 71–73, 76, 77, 163).

[Teu+11a] J. D. Teufel, T. Donner, Dale Li, J. W. Harlow, M. S. Allman, K. Cicak, A. J. Sirois, J. D. Whittaker, K. W. Lehnert, and R. W. Simmonds. "Sideband cooling of micromechanical motion to the quantum ground state." In: *Nature* 475.7356 (July 6, 2011), pp. 359–363. DOI: 10.1038/nature10261 (cit. on p. 1).

[Teu+11b] J. D. Teufel, Dale Li, M. S. Allman, K. Cicak, A. J. Sirois, J. D. Whittaker, and R. W. Simmonds. "Circuit cavity electromechanics in the strong-coupling regime." In: *Nature* 471.7337 (Mar. 10, 2011), pp. 204–208. DOI: 10.1038/nature09898 (cit. on p. 1).

[Tho+08] J. D. Thompson, B. M. Zwickl, A. M. Jayich, Florian Marquardt, S. M. Girvin, and J. G. E. Harris. "Strong dispersive coupling of a high-finesse cavity to a micromechanical membrane." In: *Nature* 452.7183 (Mar. 6, 2008), pp. 72–75. DOI: 10.1038/nature06715 (cit. on p. 54).

[Tit+99] I. Tittonen, G. Breitenbach, T. Kalkbrenner, T. Müller, R. Conradt, S. Schiller, E. Steinsland, N. Blanc, and N. F. De Rooij. "Interferometric measurements of the position of a macroscopic body: Towards observation of quantum limits." In: *Physical Review A* 59.2 (1999), p. 1038 (cit. on pp. 4, 91).

[Trö+09] M. Tröbs, S. Barke, J. Möbius, M. Engelbrecht, D. Kracht, L. d'Arcio, G. Heinzel, and K. Danzmann. "Lasers for LISA: Overview and phase characteristics." In: *J. Phys.: Conf. Ser.* 154.1 (2009), p. 012016. DOI: 10.1088/1742-6596/154/1/012016 (cit. on p. 38).

[VCP08] Scott S. Verbridge, Harold G. Craighead, and Jeevak M. Parpia. "A megahertz nanomechanical resonator with room temperature quality factor over a million." In: *Applied Physics Letters* 92.1 (2008), pp. 13112–13112 (cit. on pp. 54, 55, 112).

[Ver+06] Scott S. Verbridge, Jeevak M. Parpia, Robert B. Reichenbach, Leon M. Bellan, and H. G. Craighead. "High quality factor resonance at room temperature with nanostrings under high tensile stress." In: *Journal of Applied Physics* 99.12 (2006), p. 124304 (cit. on pp. 54, 55, 112).

[Vit+07] D. Vitali, S. Gigan, A. Ferreira, H. Böhm, P. Tombesi, A. Guerreiro, V. Vedral, A. Zeilinger, and M. Aspelmeyer. "Optomechanical Entanglement between a Movable Mirror and a Cavity Field." In: *Phys. Rev. Lett.* 98.3 (Jan. 2007). DOI: 10.1103/PhysRevLett.98.030405 (cit. on p. 4).

[Wal87] N. G. Walker. "Quantum Theory of Multiport Optical Homodyning." In: *Journal of Modern Optics* 34.1 (Jan. 1, 1987), pp. 15–60. DOI: 10.1080/09500348714550131 (cit. on p. 101).

[Wie+15] Witlef Wieczorek, Sebastian G. Hofer, Jason Hoelscher-Obermaier, Ralf Riedinger, Klemens Hammerer, and Markus Aspelmeyer. "Optimal State Estimation for Cavity Optomechanical Systems." In: *Phys. Rev. Lett.* 114.22 (June 4, 2015), p. 223601. DOI: 10.1103/PhysRevLett.114.223601 (cit. on pp. 1, 2, 4, 16, 25, 34, 42–44, 48–54, 66, 79–81, 83, 84, 86, 87, 89, 92).

[Wil+15] D. J. Wilson, V. Sudhir, N. Piro, R. Schilling, A. Ghadimi, and T. J. Kippenberg. "Measurement-based control of a mechanical oscillator at its thermal decoherence rate." In: *Nature* 524.7565 (Aug. 20, 2015), pp. 325–329. DOI: 10.1038/nature14672 (cit. on p. 91).

[Wil+09] D. Wilson, C. Regal, S. Papp, and H. Kimble. "Cavity Optomechanics with Stoichiometric SiN Films." In: *Physical Review Letters* 103.20 (Nov. 2009). DOI: 10.1103/PhysRevLett.103.207204 (cit. on pp. 16, 21, 54, 55).

[Wil12] Dalziel Joseph Wilson. "Cavity optomechanics with high-stress silicon nitride films." PhD thesis. California Institute of Technology, June 15, 2012 (cit. on pp. 7, 10, 12, 16, 21, 22, 57, 62, 164).

[Wil+11] I. Wilson-Rae, R. A. Barton, S. S. Verbridge, D. R. Southworth, B. Ilic, H. G. Craighead, and J. M. Parpia. "High-Q Nanomechanics via Destructive Interference of Elastic Waves." In: *Phys. Rev. Lett.* 106.4 (Jan. 27, 2011), p. 047205. DOI: 10.1103/PhysRevLett.106.047205 (cit. on p. 57).

[Wil+08] I. Wilson-Rae, N. Nooshi, J. Dobrindt, T. J. Kippenberg, and W. Zwerger. "Cavity-assisted backaction cooling of mechanical resonators." In: *New J. Phys.* 10.9 (Sept. 1, 2008), p. 095007. DOI: 10.1088/1367-2630/10/9/095007 (cit. on p. 131).

[Yan11] Cheng Yang. "Progress toward observing quantum effects in an optomechanical system in cryogenics." PhD thesis. Yale University, 2011 (cit. on p. 14).

[Zaw+02] I. Zawischa, M. Brendel, K. Danzmann, C. Fallnich, M. Heurs, S. Nagano, V. Quetschke, H. Welling, and B. Willke. "The GEO 600 laser system." In: *Class. Quantum Grav.* 19.7 (Apr. 7, 2002), p. 1775. DOI: 10.1088/0264-9381/19/7/374 (cit. on p. 31).